Titre: Title:	Slow Light in Waveguide Bragg Gratings Direct-Written by Femtosecond Laser in Bulk Glass
Auteur: Author:	Qingtao Chen
Date:	2025
Type:	Mémoire ou thèse / Dissertation or Thesis
Référence: Citation:	Chen, Q. (2025). Slow Light in Waveguide Bragg Gratings Direct-Written by Femtosecond Laser in Bulk Glass [Thèse de doctorat, Polytechnique Montréal]. PolyPublie. https://publications.polymtl.ca/65828/

URL de PolyPublie: PolyPublie URL:	https://publications.polymtl.ca/65828/
Directeurs de recherche: Advisors:	Raman Kashyap, & Mohammad S. Sharawi
Programme: Program:	Génie électrique

POLYTECHNIQUE MONTRÉAL

affiliée à l'Université de Montréal

Slow Light in Waveguide Bragg Gratings Direct-Written by Femtosecond Laser in Bulk Glass

QINGTAO CHEN

Département de génie électrique

Thèse présentée en vue de l'obtention du diplôme de *Philosophiæ Doctor*

Génie électrique

Mai 2025

POLYTECHNIQUE MONTRÉAL

affiliée à l'Université de Montréal

Cette thèse intitulée :

Slow Light in Waveguide Bragg Gratings Direct-Written by Femtosecond Laser in Bulk Glass

présentée par **Qingtao CHEN**

en vue de l'obtention du diplôme de *Philosophiæ Doctor*

a été dûment acceptée par le jury d'examen constitué de :

Ke WU, président

Raman KASHYAP, membre et directeur de recherche

Mohammad S. SHARAWI, membre et codirecteur de recherche

Elham BALADI, membre

François LÉGARÉ, membre externe

DEDICATION

To my beloved wife, parents, and elder brother.

ACKNOWLEDGEMENTS

First and foremost, I would like to express my heartfelt gratitude to my supervisor, Prof. Raman Kashyap, for his unwavering support and guidance throughout this entire journey. I could not have completed this work without his patience, invaluable advice, and belief in me. I am also deeply grateful to my co-supervisor, Prof. Mohammad S. Sharawi, for his insightful input and constant encouragement, which were crucial in refining my ideas and overcoming challenges.

A sincere thank you also goes to my thesis committee members, Prof. Ke Wu, Prof. François Légaré, Prof. Elham Baladi, and Prof. Denis Seletskiy, for their thoughtful feedback and suggestions, which significantly improved my work. I truly appreciate the time they dedicated to reviewing my research and helping me grow as a scholar.

I would like to extend a special thanks to Dr. Jean-Sébastien Boisvert for his continuous support and guidance throughout my time in the Fabulas lab. From teaching me how to use various equipment to help me tackle technical challenges, his assistance has been essential to my growth as a researcher. I am incredibly grateful for his unwavering help. I would also like to thank Foroogh Jafari for her invaluable contributions to device fabrication and for our insightful discussions. Her expertise and support were instrumental in refining my work, and I truly appreciate the time and effort she dedicated to assisting me.

I am thankful to Prof. Sébastien Loranger for his assistance with article modifications and excellent Fabulas lab management, to Dr. Frédéric Monet for his help with the OBR measurements, and to Dr. Louis-Philippe Carigan for his support with sample cutting. My thanks also go to Dr. Pascal Burasa, Zhiyong Dong, Jianzhao Gou, and Dr. Yuxuan Xie for their assistance and discussions related to the time delay experiment. I would like to acknowledge Prof. John Xiupu Zhang, Dr. Huijuan Niu, and Dr. Wenjing Fang for their collaborations in optoelectronics, metasurfaces, and antenna domains. I would also like to thank the administrative and IT staff at the Poly-Grames Research Center, especially Rachel Lorie and Jean-Sébastien Decarie, for their invaluable assistance with various matters.

My heartfelt thanks go to my amazing colleagues and friends, both in the Fabulas lab—Dr. Amirhossein Tehranchi, Dr. Jyothis Thomas, Dr. Yalina Garcia Puente, Dr. Antsar Rih Hlil, Pierre

Lorre, Antoine Roberge, Yannick Cuerno, Jacynthe Francoeur, Olivier Bédanger, Mathurin Iannone, and Arthur Poiffaut—and at the Poly-Grames Research Center—Dr. Wentao Lin, Erjun Zhang, Dr. Nhu Huan Nguyen, Dr. Desong Wang, Dr. Dongze Zheng, Dr. Xiaoyi Wang, Dr. Ben You, Dr. Chunmei Liu, Dr. Kang Zhou, Dr. Xiaoqiang Gu, Jie Deng, Dr. Bengeng Cai, Dr. Reza Shamsaee Malfajani, Dr. Amirhossein Askarian Bajestani, Dr. Chandan Roy, Jianye Mai, and others. Your support, whether through brainstorming ideas, lending a hand with experiments, or offering a listening ear during stressful times, has made my PhD journey far more enjoyable.

On a personal note, I owe everything to my family, especially my wife Joanna Qingqing Wu, my parents Zhaohua Chen and Meishan Song, my elder brother Qingdong Chen, and my parents-in-law. Their unconditional love, constant support, and sacrifices have made all the difference. Without them, I would not be where I am today. A huge thank you to my friends, Dr. Junlong Zhu, Dr. Kaixuan Wang, Fengjie Sun, Yingxin Wang, Qin Xue, Wei He, Dr. Tianling Peng, Keyin Tang, and Dr. Jingrui Chen, for always being there for me, offering encouragement, and for just making life a little bit easier when things got tough.

To everyone who has supported me along the way—thank you, from the bottom of my heart. This thesis would not have been possible without you.

RÉSUMÉ

La lumière lente fait référence au phénomène dans lequel la vitesse de la lumière est significativement réduite lorsqu'elle traverse un milieu, une structure périodique ou un système. Cet effet peut être réalisé à des températures ultra-basses ou ambiantes en utilisant des techniques basées sur la dispersion induite par les matériaux ou les structures. En pratique, les dispositifs de lumière lente sont généralement fabriqués à l'aide de photolithographie dans des salles blanches, où des changements d'indice de réfraction (IR) supérieurs à 1 sont obtenus dans des matériaux solides, ou par des techniques d'écriture directe au laser femtoseconde (FSL) dans des matériaux transparents tels que les fibres et les lamelles de verre, entraînant des changements d'IR allant de 10^{-4} à 10^{-2}. La lumière lente a permis de nombreuses applications dans les communications optiques, l'optique linéaire et non linéaire, l'informatique quantique et l'industrie émergente des capteurs.

Cependant, les effets de la lumière lente dans les réseaux de Bragg à base de verre massif créés à l'aide de techniques d'écriture directe au laser femtoseconde n'ont pas été largement explorés. Pour combler cette lacune et exploiter le potentiel des dispositifs de lumière lente dans les technologies intégrées transparentes, cette thèse propose une exploration préliminaire et une démonstration expérimentale de la lumière lente dans les réseaux de Bragg à guide d'ondes par des techniques d'écriture directe au laser femtoseconde. Cette recherche comprend : 1) l'exploration d'un nouveau modèle de guide d'ondes et l'étude des effets de la lumière lente dans deux types de réseaux de Bragg basés sur ce modèle ; 2) la dérivation de la formule du facteur de ralentissement (SDF) et l'application de l'ingénierie de décalage aux réseaux de Bragg à lignes ; 3) l'application du SDF dans les réseaux de Bragg à points de Modèle-I et Modèle-II avec ingénierie de décalage, ainsi qu'une analyse de la manière dont l'ajustement de la distance centre-à-centre dans le guide d'ondes affecte la performance de la lumière lente des réseaux de Bragg à points Modèle-II.

Tout d'abord, les effets de lumière lente dans deux types de réseaux de Bragg à guide d'ondes sont démontrés expérimentalement à l'aide du nouveau modèle de guide d'ondes, mis en œuvre par des techniques d'écriture directe FSL. Lors du processus de réglage du guide d'ondes, les paramètres optimaux sont obtenus après des centaines d'itérations, en ajustant finement des variables telles que la puissance du laser, la fréquence de répétition et la vitesse d'écriture. Cela est réalisé grâce à une

analyse approfondie des variations de l'indice de réfraction (RI), des pertes de propagation, des modes de propagation et de l'efficacité de guidage de la lumière. Le nouveau modèle de guide d'ondes repose sur un régime thermique accumulé qui évolue d'un guide d'ondes à noyau et coquille, à deux guides d'ondes à noyau et coquille avec une grande distance centrale, et enfin à une structure de guide d'ondes parfaite formée par deux guides d'ondes à noyau et coquille avec des régions de coquilles partiellement superposées (appelées PO-WGs) qui présentent des performances de guidage de la lumière par coquille. Ces PO-WGs présentent un changement de RI de l'ordre de 10^{-3}, de faibles pertes de propagation et une bonne efficacité de guidage de la lumière. La création réussie de réseaux de Bragg à points et à lignes démontre davantage la performance non saturée des PO-WGs. Les caractéristiques de lumière lente des deux types de réseaux de Bragg sont étudiées expérimentalement et théoriquement en détail, montrant un petit facteur de dispersion de groupe (SDF) pour le réseau de Bragg à points en raison de son faible creux de transmission, tandis qu'un SDF plus grand est observé pour le réseau de Bragg à lignes, qui présente un creux de transmission plus important mais avec plusieurs lobes secondaires. Ces résultats suggèrent que les PO-WGs sont un excellent candidat pour la création de réseaux de Bragg, bien que le faible creux de transmission dans les réseaux de Bragg à points et la présence de plusieurs lobes secondaires dans les réseaux de Bragg à lignes perdants indiquent la nécessité d'une optimisation supplémentaire des PO-WGs et de leur interaction avec les réseaux de Bragg.

Deuxièmement, les effets améliorés de la lumière lente sont largement explorés dans les réseaux de Bragg à guide d'onde à passage unique (SLPWG) à ligne-grille, grâce à l'application de l'ingénierie de décalage. L'utilisation du SLPWG avec des paramètres d'écriture optimisés permet d'éviter efficacement la nécessité de multiples guides d'onde ou de faisceaux de guides d'onde, ce qui peut entraîner des lobes secondaires indésirables et augmenter les pertes dans les réseaux de Bragg. En appliquant l'ingénierie de décalage avec une distance calibrée pour l'inscription des réseaux de ligne au-dessus du SLPWG, l'interaction entre le SLPWG et les réseaux de lignes est considérablement augmentée. Cette conception entraîne un creux de transmission étroit et profond, résolvant efficacement les problèmes de pertes et de lobes secondaires, et permet d'obtenir un facteur de dispersion (SDF) plus élevé – avec une amélioration d'au moins 12% par rapport aux réseaux de Bragg à ligne mentionnés précédemment. Il est important de noter que la polarisation de la lumière incidente peut influencer le creux de transmission et doit être prise en compte. De plus, une investigation théorique est menée, avec la formule SDF dérivée de la théorie des modes

couplés, offrant une approche efficace pour évaluer les caractéristiques de lumière lente de tout type de réseau de Bragg en utilisant uniquement la constante de couplage.

Troisièmement, le phénomène amélioré de lumière lente est démontré dans deux types de réseaux de Bragg à points (Model-I et Model-II DBG) grâce à l'ingénierie de décalage et à l'ajustement de la distance centre-à-centre dans le modèle de guide d'ondes. Dans le Model-I DBG, basé sur le SLPWG, le creux de transmission s'améliore avec un décalage ajusté, entraînant une augmentation du SDF de 16% par rapport aux DBG de PO-WGs mentionnés précédemment. Cependant, la position relative du point par rapport au SLPWG affecte davantage l'amélioration de la caractéristique du SDF. Pour résoudre ce problème, le Model-II DBG est proposé, basé sur un guide d'ondes à double passage laser (DLPWG), avec des ajustements apportés à la fois au décalage et à la distance centre-à-centre. Le DLPWG utilisé dans le Model-II DBG est adapté avec un taux de répétition plus faible et une vitesse d'écriture plus lente, mais une puissance laser plus élevée que l'inscription PO-WGs, ce qui entraîne un changement de l'indice de réfraction du noyau qui est 2 à 3 fois plus grand que celui du SLPWG et des PO-WGs. En tenant compte de la polarisation de la lumière incidente, le Model-II DBG présente d'excellents effets de lumière lente, avec une augmentation du SDF de 20% et de 40% par rapport aux DBG SLPWG et PO-WGs, respectivement. De plus, l'effet de lumière lente surestimé dans le Model-II DBG est étudié à travers des traces de signal à des longueurs d'onde ajustées au pic de réflexion et près des bords de réflexion.

En résumé, cette thèse fournit une exploration préliminaire des effets de lumière lente dans plusieurs types de réseaux de Bragg à base de verre massif, en utilisant de nouveaux modèles de guides d'ondes et des recettes d'inscription optimisées par les techniques d'écriture directe FSL. Les résultats expérimentaux du SDF démontrent le potentiel des réseaux de Bragg conçus pour de futures applications, y compris le développement de structures à onde lente pour la gestion du trafic de données, la miniaturisation des dispositifs et l'intégration sur puce. Ces réseaux de Bragg pourraient également être appliqués dans des verres durcis pour les écrans de téléphones portables avec capteurs intégrés, améliorer les interactions lumière-matière lorsqu'ils sont intégrés à des antennes optiques, et contribuer au développement de fenêtres intelligentes pour les bâtiments et les automobiles.

ABSTRACT

Slow light refers to the phenomenon in which the speed of light is significantly reduced as it travels through a medium, periodic structure, or system. This effect can be achieved at ultra-low or room temperatures using techniques based on material-induced or structure-induced dispersion. In practice, slow light devices are typically fabricated using photolithography in clean rooms, where refractive index (RI) changes greater than 1 are achieved in solid materials, or through femtosecond laser (FSL) direct-writing techniques in transparent materials such as fibers and glass slides, resulting in RI changes ranging from 10^{-4} to 10^{-2}. Slow light has enabled numerous applications across optical communications, linear and nonlinear optics, quantum computing, and the emerging sensor industry.

However, slow-light effects in bulk glass-based waveguide Bragg gratings created using FSL direct-writing techniques have not been extensively explored. To address this gap and unlock the potential applications of slow light devices in transparent integrated technologies, this thesis provides a preliminary exploration and experimental demonstration of slow light in waveguide Bragg gratings by FSL direct-writing techniques. This research includes: 1) the exploration of a novel waveguide model and the study of slow-light effects in two types of Bragg gratings based on this model; 2) the derivation of the slow-down factor (SDF) formula and the application of offset engineering to line-Bragg gratings; 3) the application of the SDF in Model-I and Model-II dot-Bragg gratings with offset engineering, along with an analysis of how adjusting the center-to-center distance in the waveguide affects the slow-light performance of Model-II dot-Bragg gratings.

First, the slow-light effects in two types of waveguide Bragg gratings are experimentally demonstrated using the novel waveguide model, implemented through FSL direct writing techniques. During the waveguide tailoring process, the optimal parameters are achieved after hundreds of iterations, fine-tuning variables such as laser power, repetition rate, and writing speed. This is done through a comprehensive analysis of RI changes, propagation loss, propagation modes, and light-guiding efficiency. The novel waveguide model is based on a thermally accumulated regime that evolves from a core-shell waveguide, to two core-shell waveguides with a large center distance, and finally to a perfect waveguide structure formed by two core-shell waveguides with partially overlapping shell regions (referred to as PO-WGs) that showcase a shell-guided light

performance. These PO-WGs exhibit an RI change on the order of 10^{-3}, low propagation loss, and good light-guided efficiency. The successful creating of dot-Bragg and line-Bragg gratings further demonstrates the unsaturated performance of PO-WGs. The slow-light characteristics of the two types of Bragg gratings are studied experimentally and theoretically in detail, showing a small SDF for the dot-Bragg grating due to its low transmission dip, while a larger SDF is observed for the line-Bragg grating, which exhibits a higher transmission dip but with multiple side lobes. These findings suggest that PO-WGs are an excellent candidate for creating Bragg gratings, though the weak transmission dip in dot-Bragg gratings and the presence of multiple side lobes in lossy line-Bragg gratings, which indicate the need for further optimization of the PO-WGs and their interaction with the gratings.

Second, the enhanced slow-light effects are thoroughly explored in single-laser-pass waveguide (SLPWG) line-Bragg gratings through the application of offset engineering. The use of SLPWG with optimized writing parameters effectively avoids the need for multiple waveguides or waveguide bundles, which can lead to unwanted side lobes and increase losses in Bragg gratings. By employing offset engineering with a calibrated distance for line grating inscription atop the SLPWG, the interaction between the SLPWG and the line gratings is significantly increased. This design results in a narrow and deep transmission dip, successfully addressing the issues of losses and side lobes, and yields a larger SDF — achieving at least a 12% improvement compared to the previously mentioned line-Bragg gratings. It is important to note that the polarization of incident light can influence the transmission dip and should be considered. Additionally, a theoretical investigation is conducted, with the SDF formula derived based on coupled-mode theory, offering an effective approach for evaluating the slow-light characteristics of any type of Bragg grating using only the coupling constant.

Third, the enhanced slow-light phenomenon is demonstrated in two types of dot-Bragg gratings (Model-I and Model-II DBGs) through offset engineering and the adjustment of the center-to-center distance within the waveguide model. In Model-I DBG, based on SLPWG, the transmission dip improves with an adjusted offset, resulting in an SDF increase of 16% compared to the previously mentioned PO-WGs DBG. However, the relative position of the dot to the SLPWG affects further enhancement of the SDF characteristic. To address this, Model-II DBG is proposed, based on double-laser-pass waveguide (DLPWG), with adjustments made to both the offset and the center-to-center distance. The DLPWG used in Model-II DBG is adapted with a smaller

repetition rate and writing speed, but a higher laser power than the PO-WGs inscription, leading to a core RI change that is 2 to 3 times greater than that of SLPWG and PO-WGs. Considering the polarization of incident light, the Model-II DBG exhibits excellent slow-light effects, with an SDF increase of 20% and 40% compared to the SLPWG DBG and PO-WGs DBG, respectively. Additionally, the overestimated slow-light effect in Model-II DBG is investigated through signal traces at wavelengths tuned to the reflection peak and near the reflection edges.

In summary, this thesis provides a preliminary exploration of slow-light effects in several types of bulk glass-based Bragg gratings, utilizing novel waveguide models and optimized inscription recipes through FSL direct writing techniques. The experimental SDF results demonstrate the potential of the designed Bragg gratings for future applications, including the development of slow-wave structures for data traffic management, device miniaturization, and on-chip integration. These Bragg gratings could also be applied in hardened glass for cellphone screens with embedded sensors, enhance light-matter interactions when integrated with optical antennas, and contribute to the development of smart windows for buildings and automobiles.

TABLE OF CONTENTS

LIST OF TABLES

LIST OF FIGURES

LISTE OF SYMBOLS AND ABBREVIATIONS

BW	Bandwidth
CMT	Coupled-mode theory
C-to-C	Center-to-center
DBG(s)	Dot-Bragg grating(s)
DBP	Delay-bandwidth product
DC	Duty cycle
DFB	Distributed-feedback laser
DLPWG	Double-laser-pass waveguide
EIT	Electromagnetically induced transparency
FWHM	Full width at half maximum
FSL	Femtosecond laser
GD(s)	Group delay(s)
GI(s)	Group index (indices)
h-pol	Horizontal polarization
MFD	Mode field diameter
MZM	Mach-Zehnder Modulator
NA	Numerical aperture
NI-MAX	NI Measurement & Automation Explorer
NDBP	Normalized delay-bandwidth product
OBR	Optical Backscatter Reflectometer
OSA	Optical spectrum analyzer
PA-WGs	Parallel adjacent waveguides

PC	Polarization controller
PD	Photodiode
PIC	Photonic integrated circuit
PO-WGs	(Parallel) Partially overlapping waveguides
RI	Refractive index
RIs	Refractive indices
SDF(s)	Slow-down factor(s)
v-pol	Vertical polarization
SLPWG	Single-laser-pass waveguide
WBG(s)	Waveguide Bragg grating(s)
WLBG	Waveguide line-Bragg grating

LIST OF APPENDICES

CHAPTER 1 INTRODUCTION

The propagation of light is an old topic. Yet when one mentions the velocity of light is 3×10^8 m/s, it actually refers to the phase velocity of light in a vaccum. The phase velocity is the speed at which the phase oscillation of the electromagnetic plane wave propagates in a vacuum. Excepting vacuum or laser technologies for the light source, almost all the velocity of light measurements in any medium involves a light pulse (optical signal) in propagationg a certain distance. This velocity of light pulse is indeed the group velocity of light, which indicates the light propagation with an envelope of the wave packet. However, how to operate a light in media (refractive indices not 1) with a slower speed for more light-matter interactions is an interesting topic. Slow light device is a good choice, which involves exploring of light propagation mechanism in dispersion media at ulta-low or room temperature.

1.1 Motivation and problem

The advancement of photonic integrated circuit (PIC) components that offer compact device sizes, high-speed data transmission, substantial data storage capacity, and fabricated in transparent materials, presents a considerable challenge in today's communication systems [1]. In recent years, slow light technologies [2]–[4] have gained considerable attention, offering a promising opportunity for optical signal manipulation and energy compression [5]. These technologies enable smaller devices and enhanced light-matter interactions, making them particularly valuable for applications in optical communication, sensing, and nonlinear optics [6], [7]. Slow light refers to the situation in which the group velocity of light is reduced within a medium (i.e. group velocity is much less than the speed of light), typically at ultra-low or room temperature, thereby enhancing interactions between light and matter [2]. This effect is vital for enhancing the performance of photonic devices by delaying and temporarily storing light.

To date, methods for generating slow light typically rely on material dispersion engineering and structural (waveguide) dispersion engineering [7], [8]. Most slow light devices based on materials are fabricated at ultra-low temperatures or using specialized materials, which introduce high experimental costs, complex experimental setups, and limitations for practical applications. In contrast, slow light generated through structural dispersion engineering at room temperature—

using photonic crystal structures [9]–[11], coupled resonator structures [12], [13], metamaterial structures [14]–[16], semiconductor structures [17]–[19], and waveguide structures [20], [21]—offers broader potential for applications and greater design flexibility. Compared to slow light created in conventional solid materials with a refractive index (RI) change larger than 1 in clean room environments, those formed in transparent materials using waveguide structures in fibers [3], [22] by femtosecond laser (FSL) direct-writing techniques, with RI changes ranging from 10^{-4} to 10^{-3}, have gained more attention from researchers due to their promising advantages. Further, integrating the aforementioned slow light technologies with transparent bulk materials by FSL direct-writing techniques, which may have applications in future regular windows, car windshields, and smartphone screens, presents significant challenges and has not been extensively explored.

Despite slow light has been demonstrated in a variety of photonic structures, slow-light effects in waveguide Bragg gratings in bulk glass using FSL direct writing have not been extensively explored. Furthermore, it is crucial to optimize the writing parameters and the design of waveguides and Bragg gratings to achieve effective slow light characteristics, such as a reduced group index and slow-down factor, while minimizing material defects. It is also important to ensure high-quality waveguide structures, maintain high efficiency, and minimize loss in the Bragg grating structures operating in the C-band.

Based on those challenges, this thesis focuses on how to efficiently and successfully inscribe waveguide Bragg gratings (WBGs) by FSL direct writing technique in bulk glass slides with the aim of achieving slow-light effects. Comparing with the traditional photolithography in clean room or other complex techniques at ultra-low temperature, FSL direct writing has emerged as a promising technique for fabricating high-quality waveguide and WBG structures within bulk glass with unique advantages, such as flexibility and three-dimensional structures. The precision of FSL direct writing techniques allows for the accurate fabrication of these slow light Bragg gratings at the microscopic level. This capability opens up new possibilities for innovative photonic devices in bulk glasses that can operate at slower velocity and offer enhanced light-matter performance in future optical communication, optical information storage, optical buffers, quantum computing, and sensing applications.

1.2 Research objectives

The objectives of this research are centered on investigating slow-ight effects in waveguide Bragg gratings inscribed using FSL direct writing technique in bulk glass slides. Building on the motivation and problem statements outlined above, the general objective can be divided into five specific goals, as follows.

(1) Develop a reproducible novel waveguide within a bulk glass slide with high-efficiency light guiding.

The first objective is to develop a novel waveguide with high light guiding efficiency and low propagation loss, suitable for waveguide Bragg grating preparation. To achieve this, hundreds or even thousands of waveguides need to be inscribed within the bulk glass slides. The relevant writing parameters, such as femtosecond laser power, repetition rate, writing speed, and waveguide position, must be carefully calibrated until an optimal process is established in preparation for the next step of grating inscription.

(2) Develop two types of waveguide Bragg gratings based on the novel waveguide model and investigate their slow-light effects.

The second objective is to further refine the writing parameters for grating fabrication, based on the previously developed waveguide model. In this objective, two types of Bragg gratings (dot-Bragg grating and line-Bragg grating) resonaning in the optical C-band will be fabricated. Additionally, slow light metrics, such as group delay (GD) and group index (GI), will be analyzed through measurements and numerical simulations.

(3) Derive a slow-down factor (SDF) equation to evaluate the slow-light effects of waveguide Bragg gratings.

The third objective is to derive an equation to evaluate the slow-light effects in any type of waveguide Bragg gratings. This equation, derived using the coupled-mode theory (CMT), will be specifically related to the coupling constant of Bragg gratings. It will offer a detailed theoretical framework for assessing the slow light performance of any type of waveguide Bragg gratings.

(4) Develop offset-enhanced line-Bragg gratings and evaluate the slow-light effects using the SDF formula.

The goal of this objective is to design and fabricate single-laser-pass waveguide (SLPWG) line-Bragg gratings with enhanced slow-light effects through offset engineering. Different offset configurations will be explored between the waveguide and the line grating array. The line-Bragg grating with the largest transmission dip strength resulting from this offset engineering will be identified as having the most enhanced slow-light effects. Additionally, theoretical evaluations of the slow light performance (using SDF formula) of the offset line-Bragg grating will be provided.

(5) Develop slow light phenomona in two types of dot-Bragg gratings through "offset engineering" and evaluate them theoretically using the SDF formula.

The fifth objective is to inscribe two types of dot-Bragg gratings with different offsets, aimed at enhancing the slow-light effect. These gratings will be fabricated using both SLPWG and double-laser-pass waveguide (DLPWG) configurations. The center-to-center distances in the DLPWG will also be studied to further optimize the slow-light effects. In addition, the SDF formula will also be employed to further assess the slow-light effects in dot-Bragg gratings.

1.3 Thesis outline

This thesis mainly focuses on exploring the underlying mechanisms of slow light and enhanced slow light phenomena in bulk glass-based waveguide Bragg gratings through "offset engineering" by FSL direct writing techniques. Based on this research topic, a series of FSL inscription and exploration experiments, experimental measurements, theoretical calculations, and data processing were carried out. The specific chapters are shown below:

Chapter 1 first provides a brief overview of the background of the research topic, followed by the motivation and problem statement. The research objectives and key contributions (chapters 4~6) are then presented, and the chapter concludes with a description of the thesis structure.

Chapter 2 is devoted to a comprehensive literature review on the research topic. It begins with an overview of slow light theory and key metrics, including group velocity, GI, GD, delay-bandwidth product (DBP), and slow-down factor (SDF). Next, the phenomena of slow light observed in various media, such as atomic vapors, rare-earth-doped materials, semiconductors, metamaterials, photonic crystals, fibers, and transparent bulk glass slides (the focus of this research), are reviewed. The chapter then explores simulations of slow light metrics in uniform Bragg gratings using coupled-mode theory, with GI computed from the phase's first derivative derived from the

amplitude reflection coefficient of the grating. Finally, potential applications of slow-light effects in Bragg gratings are discussed.

Chapter 3 offers an overview of the methodology related to FSL inscription and the measurement characterization techniques used to assess the waveguide Bragg grating metrics in this thesis. It then outlines how these methods are applied in the three articles that form the core of this research work. The following three chapters (i.e. chapters 4~ 6) will primarily present these three articles.

Chapter 4 presents the first article, which introduces a novel waveguide model (i.e. parallel partially-overlapping waveguides, PO-WGs) and demonstrates the detailed inscription of two Bragg gratings using this model. The **first objective**, which aims to successfully inscribe an innovative waveguide with effectively light guiding and low propagation loss within a 75 mm long glass slide, was accomplished. Building on this new waveguide model, the **second objective** was achieved by inscribing two different Bragg gratings and measuring their slow-light effects. Finally, the third objective was partially addressed using the Bloch wave and coupled mode theory to analyze the slow-light effects.

Chapter 5 introduces the second article, which explores the use of "offset engineering" to exploit slow-light effects in a second-order SLPWG line-Bragg grating through enhanced transmission dip strength. The **third objective** was fully achieved in this article by developing a specific formula for the SDF using CMT. This formula demonstrates how to use the coupling constant to evaluate the slow-light characteristics of any Bragg grating. The article also addresses the **fourth objective** by demonstrating how to introduce "offset" in SLPWG line-Bragg gratings to enhance slow-light effects. Four different offset configurations were explored, with the most effective one highlighted.

Chapter 6 discusses the third article, which investigates enhanced slow-light phenomena in two types of dot-Bragg gratings through "offset engineering", i.e. the **fifth objective**. Two models of first-order dot-Bragg gratings (DBGs) (i.e. Model-I DBG and Model-II DBG) are introduced, based on the SLPWG and DLPWG models, respectively. The chapter explores the slow-light effects in these dot-Bragg gratings by applying “offset engineering”. The advantages of both the core refractive index change and the center-to-center distances in the DLPWG are addressed in detail, aiming to further improve transmission strength and enhance slow-light effects in Model-II DBGs. The time delay of the Model-II DBG is investigated and observed through experimental setups using a fast photodiode and an oscilloscope, thoroughly addressing the fifth objective.

Chapter 7 provides a general discussion, offering an overview (key findings and contributions) of the work displayed throughout the thesis and reflecting on the challenges and difficulties encountered while achieving the five objectives set out at the beginning. Further, the directions for future research, along with the practical applications and significance of this study, are outlined.

Chapter 8 concludes the thesis and outlines potential theoretical benefits and applications based on the research conducted.

CHAPTER 2 LITERATURE REVIEW

This chapter provides a comprehensive review of slow light and enhanced slow light in FSL-inscribed waveguide Bragg gratings. First, the fundamental theory of slow light is introduced, covering its key characteristics, including group velocity, group index (GI), group delay (GD), and the slow-down factor (SDF), along with simulations of slow light in uniform Bragg gratings. Second, the mechanism of refractive index (RI) change/modification in waveguides and schemes of waveguide inscription techniques are examined. Third, various types of inscription techniques for waveguide Bragg gratings are discussed in detail. Finally, potential applications of slow light in Bragg gratings are explored.

2.1 Slow light theory and its metrics

Slow light means that the light pulse propagates with a very small group velocity in media [23], in which the light pulse (optical signal) is substantially slowed due to the light-matter interaction. The slow light metrics, namely group velocity, GI, GD, delay-bandwidth product (DBP), and normalized delay-bandwidth product (NDBP) [23], [24], will be discussed as follows. For convenience, the group delay and group index are used to representing by the SDF in many cases.

2.1.1 Group velocity

The propagation of slow light is in the form of a small group velocity, v_g, which describes the propagation speed and direction of a pulse envelop (red dashed curve in Figure 2.1). It is given by

$$v_g = \frac{d\omega}{dk} = \frac{\Delta\omega}{\Delta k} \tag{2.1}$$

where k and ω are the wavenumber and angular frequency, respectively.

The group index, n_g, also referred to as SDF, is defined as the product of the velocity of light in free space and the reciprocal of group velocity, as shown by

$$n_g = \frac{c}{v_g} = c\frac{dk}{d\omega} \tag{2.2}$$

where c is velocity of light in free-space with the value of $3 \times 10^8\ m/s$.

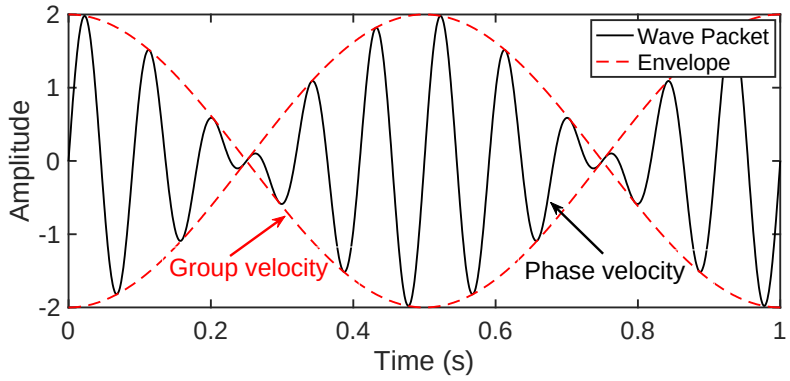

Figure 2.1 The envelope of the wave packet moves at the group velocity.

In a dispersive material, the variable refractive index, n, relies on ω or k. The dispersive relation is given by

$$\omega n = ck\,, \tag{2.3}$$

and the differential of equation (2.3) is

$$\omega dn + nd\omega = cdk. \tag{2.4}$$

Rewrite equation (2.4) to arrive at

$$\frac{c}{n} = \frac{\omega}{n}\frac{dn}{dk} + \frac{d\omega}{dk}\,, \tag{2.5}$$

where the phase velocity is

$$v_p = \frac{c}{n} = \frac{\omega}{k}. \tag{2.6}$$

Therefore, from equations (2.5) and (2.6), the relationship between group velocity and phase velocity is

$$v_g = v_p - \frac{\omega}{n}\frac{dn}{dk}. \tag{2.7}$$

Equation (2.7) describes that v_g deviates from v_p and dn/dk is responsible for the relation between v_p and v_g. The two quantities will be equal each other if the medium has no dispersion, namely the differential term dn/dk is zero. In contrary, the refractive index is not constant in a dispersion medium, which means dn/dk will not be zero, so the group velocity v_g is a bit smaller

than the phase velocity v_p. Therefore, the group velocity is always a little slower than the phase velocity. The relation between group velocity and phase velocity is shown in Figure 2.1. It is observed that the group velocity of a light signal (plane wave) represents the speed at which the overall envelope of the wave packet propagates through a medium, whereas the phase velocity describes the speed at which the individual wave crests and troughs travel within the medium.

2.1.2 Group index

According to equations (2.2) and (2.3), we have another form of group index given by

$$n_g = c\frac{dk}{d\omega} = n + \omega\frac{dn}{d\omega}. \tag{2.8}$$

So in a dispersive material with variable refractive index, the group velocity can be represented as

$$v_g = \frac{c}{n_g} = \frac{c}{n + \omega\frac{dn}{d\omega}}. \tag{2.9}$$

From equation (2.9) we can see, a wave will be stopped if v_g approaches to zero. In other words, this needs group index n_g with positive infinity, which means $dn/d\omega$ should be as large as possible due to the variation range of n is finite. It is also equivalent to the reciprocal of $dn/d\omega$, i.e. $d\omega/dn$ should be as small as possible.

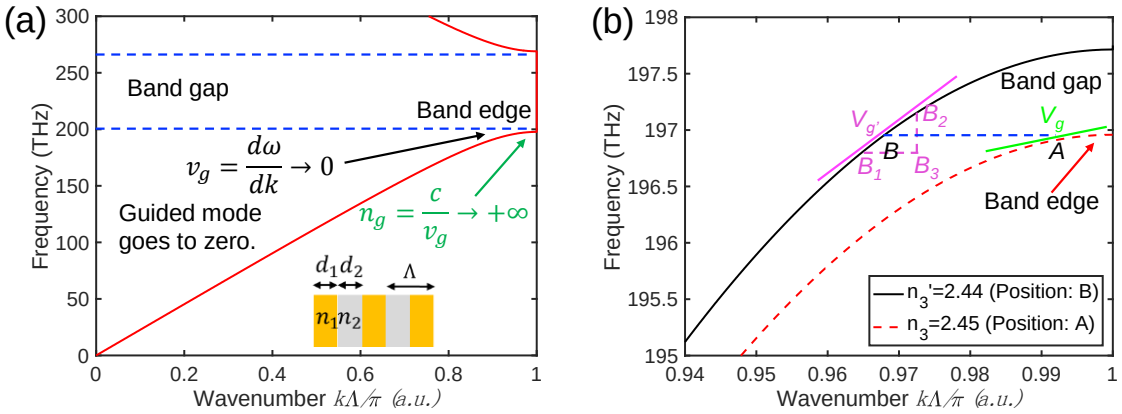

Figure 2.2 (a) Band structure and (b) the magnified view of band stucture near the band edge.

For example, there is a periodic structure shown in the inset of Figure 2.2(a). The relevant parameters are given, where the width is $d_1 = d_2 = 165\ nm$, the corresponding refractive index is $n_1 = 2.44$, $n_2 = 1.44$, the periodicity is $\Lambda = 330\ nm$ and the duty cycle (DC) is $d_1/\Lambda = 50\%$.

It can be seen that the group velocity $d\omega/dk$ approaches 0 near the band edge position, which means that the guided mode goes to zero and there is almost no light to be propagated, so the slow wave/light is formed. Further, the slow light has anther figure of merit: time delay tunability. Close to the band edge (Figure 2.2(b), magnified view), when the refractive index (RI) $n_3 = 2.45$ decreases to $n_3' = 2.44$ ($n_2 = 1.44$, showing no change), a small RI change of 10^{-2} results a significant shift in the group velocity (i.e. the slope from band structure) from point A to point B. This causes the group velocity to increase from $v_g = 6.92 \times 10^6$ m/s to $v_g' = 3.12 \times 10^7$ m/s. Consequently, the corresponding group index decreases from 43.3 at position A to 9.6 at position B, where the time delay (Δt) tunability can be calculated as 112 ns, using the formula $\Delta t = 1/v_g - 1/v_g{}'$. This phenomonon can be interpreted as a small RI change leading to a significant change in both group velocity and group index, which in turn results in a time delay, reduced device size, lower power consumption, and easier integtation with other devices [18].

Besides, if the refractive index n is simultaneous related to ω and k, that is $n(\omega, k)$, the equation (2.3) can be rewritten as the form of

$$\omega n(\omega, k) = ck \tag{2.10}$$

and the corresponding derivative form of equation (2.10) to ω can be described as [25]

$$\begin{aligned} \frac{\partial k}{\partial \omega} &= \frac{1}{c}\frac{\partial [n(\omega,k)\omega]}{\partial \omega} \\ &= \frac{n}{c} + \frac{\omega}{c}\left(\frac{\partial n}{\partial \omega} + \frac{\partial n}{\partial k}\frac{\partial k}{\partial \omega}\right). \end{aligned} \tag{2.11}$$

Hence, another form of group velocity can be given by

$$\begin{aligned} v_g &= \frac{1}{\partial k/\partial \omega} \\ &= \frac{c - \omega\frac{\partial n}{\partial k}}{n + \omega\frac{\partial n}{\partial \omega}}. \end{aligned} \tag{2.12}$$

It can be seen from equation (2.12), the group velocity of a slow light/wave can be controlled by changing v_g, i.e. changing n, $\frac{\partial n}{\partial \omega}$ or $\frac{\partial n}{\partial k}$. Meanwhile, this will introduce a large index mismatch and insertion loss if we use a larger refractive index to produce slow-light effect. However, the refractive index n is usually not changed too much for a fixed medium, so it is only to change the

other two quantities $\frac{\partial n}{\partial \omega}$ or $\frac{\partial n}{\partial k}$ to realize a slow-light effect. The specific method is shown as follows [25]: **Method (a):** Keep n unchanged and make $\frac{\partial n}{\partial \omega}$ large and positive, and **Method (b):** Keep n unchanged and make $\frac{\partial n}{\partial k}$ large and positive.

Method (a) is regarded as material dispersion engineering (material induced dispersion), while Method (b) is the characteristic of spatial variation of n and is referred to as structural dispersion engineering (structure induced dispersion) [8]. Those are the two common slow light schemes.

2.1.3 Delay-bandwidth product

Because the group velocity is determined by dispersion, so we should analyze dispersion relation if we want to slow or stop a wave. In general, both materials and structures can be induced to produce dispersion so as to realize slow-light effect. Provided that we can stop a wave, i.e. $n_g \gg n$, so equation (2.8) can be changed as

$$n_g \approx \omega \frac{dn}{d\omega} \approx \omega \frac{\Delta n}{\Delta \omega} = \frac{\Delta n}{\Delta \omega / \omega}$$
$$= 2\pi f \frac{\Delta n}{2\pi \Delta f} = f \frac{\Delta n}{\Delta f} \tag{2.13}$$

and another changed form of equation (2.13) is

$$\Delta f = \Delta n \frac{f}{n_g}. \tag{2.14}$$

Meanwhile, the delay-bandwidth product (DBP) [4] represents how the highest slow-light or slow-wave capacity of the device can potentially provide and it is also a parameter to quantify the trade-off between bandwidth and delay. It can be obtained by multiplying Δt in equation (2.14) as given by

$$DBP = \Delta t \Delta f = \Delta t \Delta n \frac{f}{n_g} = \Delta t \Delta n \frac{c/\lambda}{c/v_g}$$
$$= \Delta t \Delta n \frac{v_g}{\lambda} = \frac{L \Delta n}{\lambda} \tag{2.15}$$

where L is the length of device, Δt is the time delay through the propagation length of L, λ is the operating wavelength, Δn is the change of n over the bandwidth, and Δf (or $\Delta \omega$) is the frequency

bandwidth (or an operating bandwidth, or an optical signal bandwidth) centred at a frequency $f = \omega/2\pi$ (or ω). Additionally, the relation $L = \Delta t \cdot v_g$ can also be derived from equation (2.15).

The trade off between dispersion (delay) and slow light bandwidth is shown in Figure 2.3 [26]. It is can be seen that the black line depicts the small dispersion Δt_1 corresponding to a large slow light bandwidth Δf_1 (Figure 2.3(a)), while the large dispersion Δt_2 inversely corresponds a small slow light/wave bandwidth Δf_2 shown by the red line (Figure 2.3(b)). Actually, the larger slow light/wave bandwidth means the device which can be used to handle more signals and the larger dispersion, on the contrary, will produce slower waves [26]. So it is useful to tune the relationship between them.

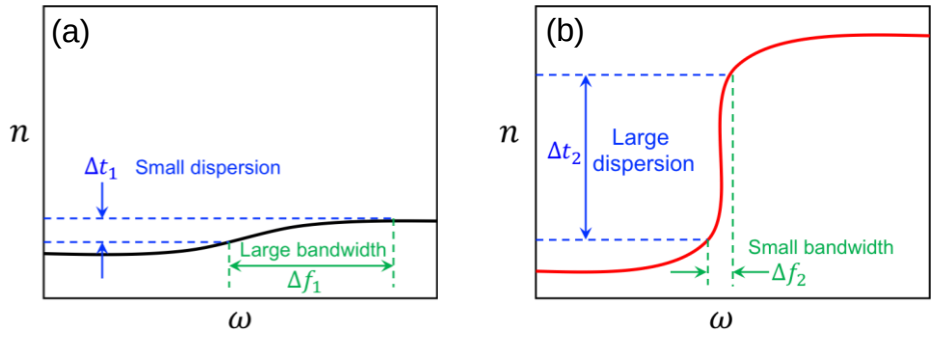

Figure 2.3 In a dispersion medium, the refractive index *n* varies as a function of ω and *k*.

In order to compare the devices of different lengths or operating at different wavelengths (with different operating frequencies), the normalized delay-bandwidth product (NDBP) [4] Δn is proposed, which is considered as a parameter to evaluate the slow light performance and defined as the product of group index and frequency range (slow light bandwidth) as shown by

$$NDBP = \Delta n = n_g \frac{\Delta f}{f} . \tag{2.16}$$

2.2 Slow light in Bragg gratings

A slow light device is an optical system or a two-port device with specific media (material induced dispersion) or designed structures (structure/waveguide induced dispersion). When an optical signal travels from input to the slow light device, it will be kept/controlled by this device for a certain time and then is released from the output port. This controlled amount of time indicates a delay and a significantly reduced group velocity of the optical signal, leading to slow light. The

generation of slow light depends on material/structural dispersion engineering [7], [8]. The material dispersion engineering [26], [29] usually is realized using complex equipment and ultra-low temperature, which includes electromagnetically induced transparency (EIT) [28], Bose-Einstein condensates [29], coherent population oscillation [30] and stimulated Brillouin scattering [31]. The structural/waveguide dispersion engineering usually can be implemented at room temperature and flexible to design, which comprises coupled resonator structures [13], [32]–[36], metamaterial structures [37]–[40], photonic crystal structures [4], semiconductor materials [21], [41], and waveguide structures in fibers [3], [22] and bulk glass slides [42], [43]. Besides, the slow light also can be achieved by employing longer devices or circular array to produce larger group delay [44]. Those devices leverage various physical mechanisms to achieve slow-light effects, enabling applications in optical communication, quantum computing, and enhanced light-matter interactions.

The primary focus of this thesis is slow light in waveguide Bragg gratings inscribed by FSL in bulk glass slides. A comprehensive review will be provided, covering the simulation and fabrication of these Bragg gratings, as well as an in-depth analysis of their slow-light effects.

2.2.1 Modeling slow light in uniform Bragg grating

The slow-light characteristics of Bragg gratings can be evaluated using various metrics, including group velocity, GI, GD, and SDF. Among these, the SDF is particularly useful, as it defines the ratio of GD in waveguide Bragg gratings to the GD in a standard waveguide. This section derives the SDF formula and provides an example to illustrate the slow-light characteristics of uniform Bragg gratings.

2.2.1.1 Slow-down factor formula

A Bragg grating is an optical device fabricated by a periodically modulated of refractive index in the light-guiding region (e.g. an optical fiber core or optical waveguide) on a subwavelength scale. Figure 2.4 shows the schematic of a waveguide Bragg grating in a glass slide, where part of the input spectrum is reflected at the Bragg condition while the rest is transmitted. The optical properties of Bragg gratings, such as reflection and transmission response, usually can be solved analytically by coupled-mode theory [45], [46]. The slow light characteristics, such as GD and SDF, can also be computed through the first derivative of phase from the amplitude reflection coefficient r_{ARC} or amplitude transmission coefficient t_{ATC}.

For uniform Bragg gratings, the amplitude reflection coefficient (r_{ARC}) and power reflection coefficient (R=$|r_{ARC}|^2$) [45], [46] can be given as

$$r_{ARC} = \frac{i\kappa \sinh(\alpha L)}{\alpha \cosh(\alpha L) - i\hat{\sigma} \sinh(\alpha L)}\,, \tag{2.17}$$

and

$$R = |r_{ARC}|^2 = \frac{\sinh^2(\alpha L)}{\cosh^2(\alpha L) - \frac{\hat{\sigma}^2}{\kappa^2}}\,. \tag{2.18}$$

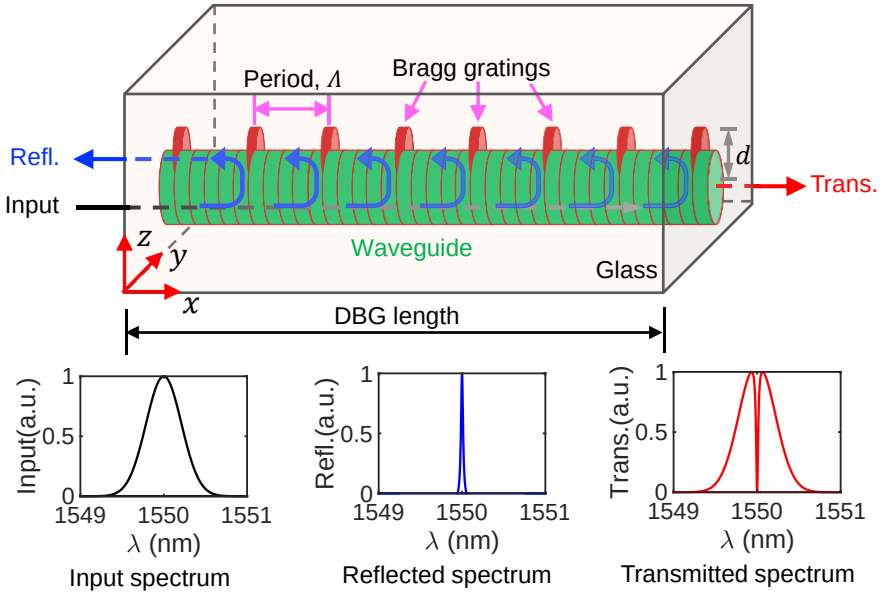

Figure 2.4 Schematic of a Bragg grating in a medium (e.g., a glass slide) illustrating the input, reflected, and transmitted spectra. Here, d represents the center distance between the waveguide and the dot, which is used to calibrate the resonance characteristics of the transmission.

From equation (2.18), the maximum/peak reflectivity R_{max} for a Bragg grating is

$$R_{max} = R|_{\hat{\sigma}=0} = \frac{\sinh^2(\alpha L)}{\cosh^2(\alpha L)} = \tanh^2(\kappa L)\,, \tag{2.19}$$

with $\hat{\sigma} = 0$, or at the wavelength λ_{max}, given by

$$\lambda_{max} = \left(1 + \frac{\Delta n}{n_{eff}}\right)\lambda_B. \tag{2.20}$$

The bandwidth between the main reflection peak and the first zero can be evaluated using $\alpha L = i\pi$. Therefore, the grating bandwidth between the first zeros (BW) becomes

$$\mathrm{BW} = \frac{\lambda_B^2}{\pi n_{eff} L}\sqrt{(\kappa L)^2 + \pi^2}\,. \tag{2.21}$$

From equation (2.21), if $(\kappa L)^2 \ll \pi^2$, the bandwidth can be estimated as

$$\mathrm{BW} \approx \frac{\lambda_B^2}{n_{eff} L}\,, \tag{2.22}$$

while if $(\kappa L)^2 \gg \pi^2$, the bandwidth is proportional to the ac coupling constant κL, leads to

$$\mathrm{BW} \approx \frac{\lambda_B^2 \kappa}{\pi n_{eff}}\,. \tag{2.23}$$

The parameters used in the derivation of the formulas are summarized in Table 2.1.

Table 2.1 The explanations of parameters used for the calculation of Bragg grating.

Symbol	**Expression**	**Explanation**
α	$\sqrt{\kappa^2 - \hat{\sigma}^2}$	Effective coupling coefficient
$\hat{\sigma}$	$\delta + \sigma = \beta - \beta_B + \sigma$	A general "dc" self-coupling coefficient
δ	$\beta - \beta_B$	Detuning
σ	$2\pi\Delta n/\lambda$	the "dc" coupling coefficient
β	$2\pi n_{\mathrm{eff}}/\lambda$	Propagation constant
β_B	$2\pi n_{\mathrm{eff}}/\lambda_B$	Propagation constant at λ_B
n_{eff}	$2\pi\Delta n/\lambda$	Effective index of the light-guiding media (e.g. core or optical waveguide)
λ_B	$2n_{\mathrm{eff}}\Lambda/m$	The designed Bragg wavelength
κ	$\pi v\Delta n/\lambda$	The "ac" coupling coefficient
v	[0, 1]	Fringe visibility
Δn	About 10^{-4}~10^{-3}	Refractive index change
Λ	---	Grating period
m	---	Grating order
L	---	Grating length
κL	---	The "ac" coupling constant

While the amplitude transmission coefficient t_{ATC} is given by

$$t_{ATC} = \sqrt{T} = \frac{\alpha}{\alpha\cosh(\alpha L) - i\hat{\sigma}\sinh(\alpha L)}$$
$$= \frac{\alpha^2\cosh(\alpha L) + i\alpha\hat{\sigma}\sinh(\alpha L)}{\alpha^2\cosh^2(\alpha L) + \hat{\sigma}^2\sinh^2(\alpha L)}$$
$$= \mathrm{Re}(t) + i\mathrm{Im}(t), \tag{2.24}$$

where T=1 − R=1 − r_{ARC}^2 is the power transmission coefficient.

The phase θ_t can be written

$$\theta_t = \tan^{-1}\left(\frac{Im(t)}{Re(t)}\right) = \tan^{-1}\left(\frac{\hat{\sigma}}{\alpha}tanh(\alpha L)\right). \tag{2.25}$$

Therefore, the grating group delay (GD), τ_g, can be calculated using the derivative of the phase θ_t, derived from the amplitude transmission coefficient t_{ATC} (Appendix B), and described as

$$\tau_g = -\frac{\lambda^2}{2\pi c}\frac{d\theta_t}{d\lambda} = \frac{L}{v_w}\left(1 + \frac{(\kappa L)^2}{\pi^2}\right). \tag{2.26}$$

Using the definition of slow-down factor (SDF), $S = \tau_g/\tau_w$, and consider the waveguide group delay (without a grating), $\tau_w = L/v_w$, where v_w is the group velocity of the waveguide. Thus, we have

$$S = 1 + \frac{(\kappa L)^2}{\pi^2}. \tag{2.27}$$

The equation (2.27) indicates that the SDF can be adjusted based on a given value of coupling constant κL. Specifically, a larger κL results in a higher SDF, leading to a narrower transmission bandwidth (if $(\kappa L)^2 \ll \pi^2$ [45]) in the Bragg grating. Similar to the group index, the SDF serves as an effective parameter for evaluating the slow-light effect of a device.

2.2.1.2 Simulation of slow light characteristics

An example is presented to illustrate the properties of a 50 mm long uniform Bragg grating with a designed Bragg wavelength (λ_B) of 1550 nm and two different coupling constants (κL) of 1.5 and 3.0. Based on equations (2.18) and (2.26), the reflection, transmission, and group delay characteristics are simulated, as shown in Figure 2.5. As observed, a smaller κL corresponds to a narrower bandwidth (Figure 2.5(a~b)), assuming the same grating length. Using equations (2.22) and (2.21), the bandwidths are calculated to be 32 pm and 45 pm for κL values of 1.5 and 3.0, respectively, which agree well with the simulation results (Figure 2.5(a)).

The group delay, determined using equation (2.26), exhibits distinct variations near the reflection edges, indicating the presence of slow-light effects (Figure 2.5(c)). At the right reflection edges (Figure 2.5(d)), the group delay profiles are normalized to eliminate the influence of the light-guiding medium, yielding values of 70 ps and 257 ps for κL of 1.5 and 3.0, respectively. Furthermore, the SDF, calculated using equation (2.27), is found to be 1.23 and 1.91 for κL values of 1.5 and 3.0, respectively, demonstrating the tunability of slow-light effects in Bragg gratings.

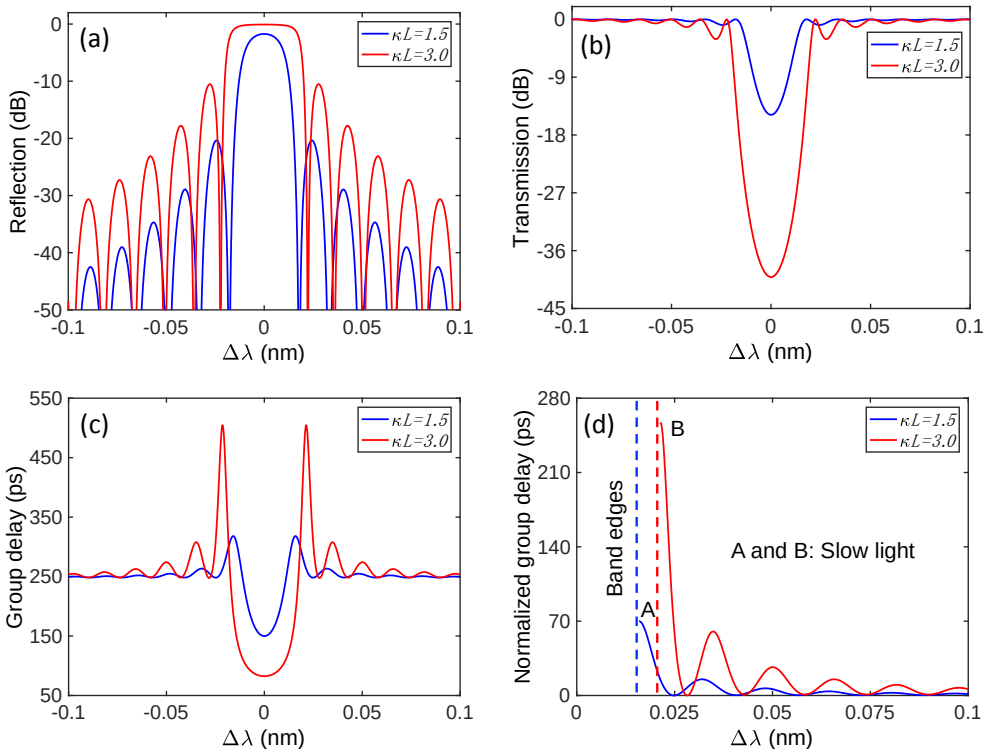

Figure 2.5 An example of a uniform Bragg grating with a grating length of L=50 mm, featuring two different coupling constants (κL) of 1.5 and 3.0. (a) Reflection spectrum, (b) Transmission spectrum, (c) Group delay in reflection, and (d) Normalized group delay, highlighting the slow light position near the band edge. Note that λ_{max} represents the central wavelength, as determined by equation (2.20).

2.2.2 Fabrication of uniform Bragg grating

There are various techniques for fabricating Bragg gratings. However, this thesis primarily focuses on slow light in waveguide Bragg gratings fabricated using FSL direct writing/inscription techniques in bulk glass slides. Therefore, this section will first review different types of FSL-induced refractive index (RI) changes/modifications, including isotropic, orthotropic, and hybrid modifications, which are utilized for fabricating subsurface and ridge waveguides. Following this,

three primary FSL-inscribed grating fabrication methods—point-by-point, line-by-line, and plane-by-plane—based on these waveguides will be discussed in detail.

2.2.2.1 Schemes of refractive index change

The use of ultrashort laser pluses to modify the RI within bulk glass for light guiding was first demonstrated by K. Hirao's group [47], [48]. Since then, this technique has been widely applied to fabricate various optical waveguides in different materlas and to enable three-dimensional optical storage [49], [50] in transparent materials. Over the years, RI changes in waveguides and related devices have been reported elsewhere [51]–[56]. One approach involves using FSL to inscribe modified tracks with isotropic RI changes, typically resulting in positive RI changes, known as type-I modifications [57], which support light guiding. Another approach utilizes FSL to inscribe parallel modified lines with orthotropic modifications, characterized by negative RI changes within the laser-modified tracks. This method, known as type-II modification [58], enables light guiding in the regions between the modified tracks.

Type-I modification is typically accompanied by induced lattice defects or structural changes, occurring at lower-energy focused pulses and with heat accumulation [57], [59], [60]. This laser-induced effect alters the lattice symmetry, resulting in localized RI changes and enabling the formation of optical waveguides. In contrast, Type-II modification involves the FSL-induced formation of parallel modified tracks or lines with decreased refractive indices (RIs). Meanwhile, the surrounding regions undergo compression due to the volume expansion at the focal plane, leading to an increase in RI, which acts as the light guiding medium (optical waveguide) [58], [61], [62]. Additionally, waveguides inscribed using multipass tracks—such as waveguide arrays [63] and waveguide bundles [64] have been reported. These structures enhance light-guiding efficiency but may introduce multimode characteristics.

In this thesis, several novel waveguide structures are inscribed within low-iron soda-lime glass slides. This type of glass is not only inexpensive, widely available, and highly transparent but also well-suited for fabricating waveguides and Bragg gratings. Using these glass slides, subsurface and ablated ridge waveguides [65] are reported via both Type-I and Type-II modifications. However, the induced RI change was relatively small, on the order of 10^{-4}, and no waveguide Bragg gratings had been reported. Here, through single-pass and double-pass laser inscription with optimized parameters (such as laser power, repetition rate, and writing speed), two distinct waveguide models

were inscribed, achieving a maximum RI change of up to 2×10^{-3} and a propagation loss of 0.2 dB/cm. The center-to-center distance perpendicular to the light-guiding direction in two-pass laser inscription was carefully examined to calibrate the RI change and improve overall light-guiding efficiency. Furthermore, offset between the waveguide and line/dot gratings was analyzed along the vertical direction to fine-tune and enhance Bragg resonance.

2.2.2.2 Schemes of Bragg grating inscription

FSL-inscribed waveguide-based devices have been successfully demonstrated in various glass materials, including couplers [66]–[71], amplifiers [72], lasers [73], Bragg gratings [74], [75], three-dimensional devices [64], [76], [77], and lab-on-a-chip applications [78]. A wide range of waveguide configurations and optical devices in transparent materials [60] have been developed, with M. Ams et al. providing a concise review of FSL-inscribed waveguide Bragg gratings, covering fabrication methods, characteristics, types, and potential applications [79]. The primary FSL direct writing techniques for waveguide Bragg gratings include the point-by-point or dot-by-dot method [74], the modulated burst techniques [80], the line-by-line approach [81], [82], and the plane-by-plane method [83]–[85], as shown in Figure 2.6.

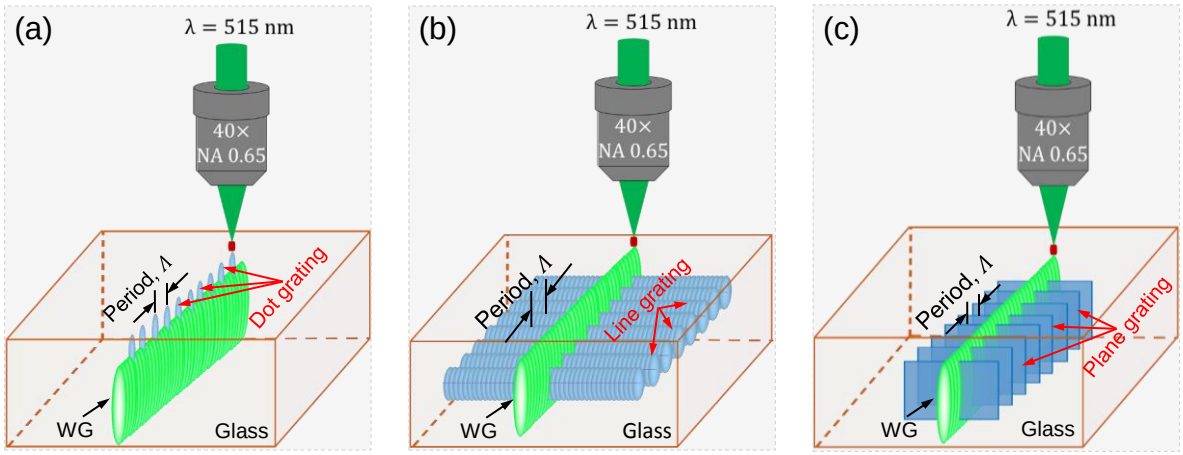

Figure 2.6 3D schematics of FSL inscription techniques: (a) Dot-by-dot (point-by-point), (b) Line-by-line, and (c) Plane-by-plane. It is important to note that the light-guiding waveguide can utilize different schemes, including single-pass, double-pass, array, or bundle configurations.

In the dot-by-dot or modulated burst method (Figure 2.6(a)), each dot is inscribed using either a single pulse [74] or a modulated burst pulse [80] with sufficient energy that is almost reaching or slightly exceeding the damage threshold of the sample substrates [79]. Compared to inscribed light-guiding structures such as optical waveguides, dot inscription typically requires a lower repetition

rate. This difference often results in larger light-guiding structures, smaller dot grating structures, and asymmetry between the guided light and the dots, which usually leads to weaker gratings. To address this, two-pass or multipass inscription techniques are employed for light-guiding structures. This not only enhances light-guiding efficiency, but also improves the interaction between the guided medium and the dots, producing a more pronounced transmission dip. However, excessive inscription passes [63], [64] can further increase the size disparity between the guided medium and the dots, leading to higher losses and broader Bragg gratings.

In the line-by-line method (Figure 2.6(b)), a two-step inscription process is required. First, the light-guiding structures are inscribed, followed by the line gratings. Notably, each line grating is oriented either perpendicular or tilted relative to the light-guiding medium. The short spacing between adjacent lines along the propagation direction determines the grating period. Additionally, the total grating length along this period significantly influences the transmission dip. Each inscribed line consists of a quasi-continuous structure with numerous overlapping pulses, ensuring a uniform RI modification. This results in larger modified regions, reduced phase noise and coupling loss, and lower insertion loss compared to point-by-point Bragg gratings [87].

In the plane-by-plane method (Figure 2.6(c)), a two-dimensional RI change is induced across the light-guiding regions (such as the fiber core or optical waveguide), enabling precise control over the width and depth of the modified area [86]. Additionally, this technique can incorporate elements such as a cylindrical lens [83], a cylindrical telescope [87], or a slit beam [88], [89] to introduce astigmatism within the focal volume, facilitating the formation of modified planes. These approaches effectively enlarge the modified region, enhancing mode coupling with the light-guiding medium, which results in strong Bragg gratings with minimal loss. Furthermore, by using a shorter focal length with rotating, tilted plane Bragg gratings can also be fabricated.

2.3 Applications of slow light in Bragg gratings

Slow light in Bragg gratings is increasingly utilized in various photonic applications due to its ability to enhance light-matter interactions by reducing the group velocity of light. Fiber Bragg grating-based slow light has demonstrated a growing range of applications [22], including (1) optical communications, where it serves as optical delay lines [90], [91], ultra-narrowband filters, and pulse shapers with large group delays and high dispersion [92], as well as enabling all-optical signal processing [93], [94]; (2) nonlinear optics and quantum electrodynamics [95], contributing

to nonlinear all-optical switches [96], high-intensity enhancement [97], [98], and large Purcell factors [95], [99], [100]; (3) sensing technologies [101], [102], assessed through metrics such as sensitivity, noise sources, resolution, dynamic range, and applications in strain and acoustic sensors [103]; and (4) environmental and mechanical detection, including temperature, humidity, chemical, and vibration sensing. Additionally, (5) future applications hold promise in next-generation communication systems, ultra-sensitive sensors, nonlinear optics, and quantum technologies [22].

Slow-light Bragg gratings, when integrated with various glass-based substrates, are expected to play a crucial role in photonic devices, such as photonic crystal waveguides for efficient filtering and sensing, optical delay lines for signal buffering, and biosensors for enhanced biomolecule detection. Furthermore, they offer improvements in hardened glass for cellphone screens, enable real-time monitoring in microfluidic devices, and contribute to the development of smart glass windows that optimize energy efficiency and indoor comfort.

CHAPTER 3 METHODOLOGY

This chapter introduces the methodology used in this project, covering fabrication and characterization for slow light in waveguide Bragg gratings, as well as the organization of the articles presented in the following chapters. Since theoretical calculations, design methods, simulations, fabrication, and characterization involve continuous iteration and refinement, many detailed procedures have been thoroughly described in the published articles (chapters 4~6) along with their appendices. Therefore, the methodology in this chapter will be discussed only briefly.

3.1 Methodology for the overall research

This thesis investigates slow light engineering in glass slide-based waveguide Bragg gratings. First, it explores slow light theory and related metrics (GI, GD, and SDF) with calculations and simulations. Next, the FSL inscription system is calibrated by analyzing parameters (writing speed, laser power, repetition rate, focal point position) for waveguide and grating preparation. Third, light guiding efficiency and phase change are measured to ensure waveguide quality, with polished end facets to minimize reflection losses. The fourth step involves Bragg grating inscription, fine-tuning parameters, and optimizing waveguide-dot/line grating offsets. Finally, polishing and characterization (RI change, cross-sectional view, transmission/reflection spectra, group delay) are conducted to ensure high-quality grating with a deep transmission dip.

Given that the fabrication and characterization steps typically require multiple rounds of adjustment and numerous iterations, and excluding the calculations and simulations shown in chapter 2, this chapter primarily focuses on the fabrication and characterization of slow light in waveguide Bragg gratings. Consequently, the methodology centers on three main aspects: discussion, fabrication, and characterization.

3.1.1 Slow light Bragg grating fabrication

The slow light in waveguide Bragg gratings are inscribed using the FSL direct writing system at the Fabulas Laboratory. This state-of-the-art experimental setup is capable of fabricating various waveguides, Bragg gratings, and couplers across a range of materials and polymers. Besides, a detailed introduction to the system can be found in previous theses [104]–[107], a book chapter

[59], or an article [108], completed by our Fabulas students. Therefore, this section provides a general description of the Fabulas laser fabrication system and the related fabrication processes used in my research project.

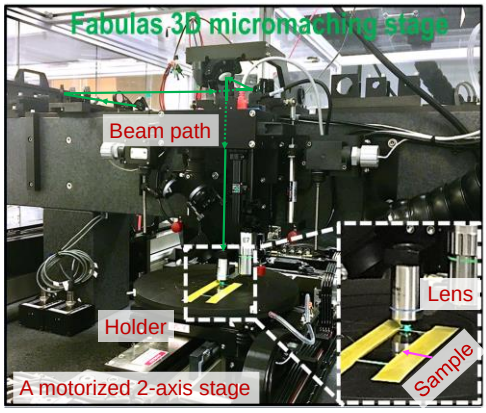

Figure 3.1 Fabulas laser fabrication system.

The femtosecond laser (FSL) used for the fabrication of slow light Bragg gratings is an 8 W Pharos laser system (Figure 3.1) from Light Conversion, with a pulse duration of 250 fs. This FSL operates at 1030 nm, which is doubled to 515 nm using the Orpheus system, and is coupled with an Aerotech 3200 precision translation stage for inscribing the waveguide and grating structures. The average inscription power used ranged from 100 mW to 1 W, with a repetition rate of 606 kHz, adjustable using a pulse picker to vary between 1 and 30 to conserve peak energy. The FSL pulse was focused through a 50×, 0.65 NA (numerical aperture) objective lens. The sample, a 75 mm long low-iron soda-lime glass (Fisherbrand, 75 mm × 25 mm × 1 mm, Catalog No.: 12-550-A3), was mounted on a sample holder stage. The writing speed was controlled by a computer and ranged from 1 mm/s to 20 mm/s.

During the above-mentioned FSL direct writing process in nonmetallic materials (such as glass and crystals) (see Figures 3.1 and 3.2(c)), electrons in the valence band (VB) absorb photon energy ($h\nu$) from the incident radiation field and gain sufficient energy to overcome the material's bandgap energy (E_g), allowing them to transition to the conduction band (CB) and become free electrons. However, a single photon from the incident (visible) FSL light typically does not possess enough energy to excite an electron across the bandgap. Therefore, nonlinear absorption processes are required. Meanwhile, it is worth noting that a different absorption mechanism—linear absorption (Figure 3.2(a))—commonly occurs under continuous-wave (CW) laser illumination in low-power

systems. In linear absorption, a single high-energy photon (with energy $h\nu$) is sufficient to excite an electron across the bandgap energy (E_g) in opaque materials (e.g., metals), promoting it from the valence to the conduction band (Figure 3.2(b)). This process occurs within the illuminated region and requires only a low photon density.

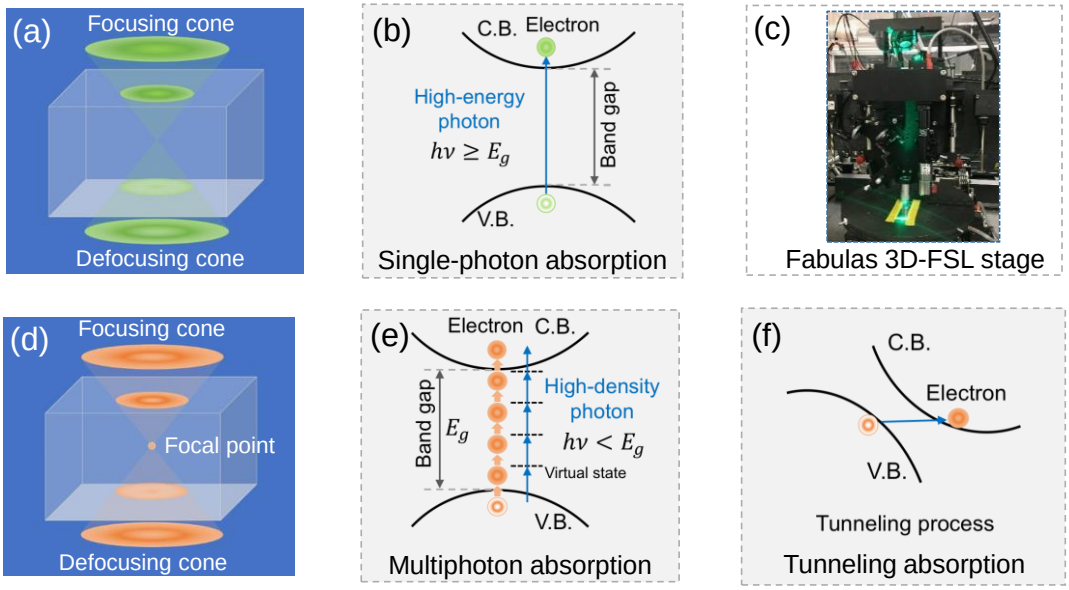

Figure 3.2 Linear excitation mechanisms include (a) the linear absorption model and (b) single-photon absorption processes. In contrast, nonlinear excitation mechanisms, implemented using the (c) Fabulas 3D femtosecond laser (FSL) system, involve (d) nonlinear absorption model, (e) multiphoton absorption, and (f) tunneling absorption processes.

For nonlinear absorption processes (Figure 3.2(d)), they are typically accompanied by photoionization and avalanche ionization, and are enabled by high-peak-power pulsed laser systems, such as our Fabulas 3D femtosecond laser (FSL) setup (Figure 3.2(c)). Photoionization is a laser-induced process where electrons absorb energy directly from the optical field and transition to the conduction band. There are two main mechanisms in photoionization process [45], [59], [109]: multiphoton ionization (Figure 3.2(e)), which depends on high laser frequency, and tunneling ionization (Figure 3.2(f)), which relies on strong laser intensity. In multiphoton ionization, a valence electron simultaneously absorbs multiple photons, and the total absorbed energy ($nh\nu$) exceeds the bandgap energy (E_g), allowing the electron to undergo an interband transition to the conduction band and become a free electron. In tunneling ionization, a bound electron is able to escape the Coulomb potential of its parent atom by quantum tunneling through the narrowed energy barrier between bands and becomes a free electron, even if the photon energy

is below the bandgap of material. This process typically occurs under a strong laser field and at relatively low laser frequencies. In addition, avalanche ionization [45], [59], [109], where field-accelerated electrons induce impact ionization, leading to carrier multiplication, may occur during the femtosecond laser (FSL) writing process. It typically acts as a secondary ionization mechanism, following multiphoton or tunneling ionization, especially under high laser intensities. It is important to note that nonlinear absorption confines the deposited energy to a localized focal volume, which enables true three-dimensional (3D) microstructuring in transparent materials.

3.1.1.1 Waveguide inscription

For waveguide fabrication, both single-pass and two-pass inscriptions are considered to ensure that the modified region within the bulk glass slides functions as an optical waveguide with higher light guiding efficiency. The inscription process involves careful consideration of various parameters, with gradual adjustments and optimization of each one, supported by extensive measurements. Additionally, in two-pass inscription, the center-to-center distance (0 μm, 1 μm, 2 μm, 3 μm, 4 μm, and 5 μm) is adjusted to enhance light-guiding efficiency and increase waveguide-dot interaction, thereby improving transmission characteristics.

Note that over-saturation in FSL-inscribed waveguides often occurs during this step, typically due to the following factors: (1) Excessive laser power can lead to nonlinear effects, causing unwanted modifications or damage to the material; (2) A high repetition rate can result in accumulated thermal effects before the material fully recovers from previous pulses; (3) Longer pulse durations release energy over a longer period, potentially leading to increased heat buildup and nonlinear effects; (4) A highly concentrated laser focus (small focus spot) can create a high energy density, leading to over-modification of the material; (5) The material's absorption characteristics must match the laser parameters, as mismatched absorption can cause over-saturation during the inscription process.

In summary, waveguide inscription is a complex process that depends on writing/scanning speed, pulse energy, and focus positions. Over-saturation of the waveguide can lead to inscribed gratings with no resonance or even failure.

3.1.1.2 Waveguide Bragg gratings inscription

The optical waveguide with high-efficiency light guiding features periodic dots or lines inscribed to form dot- or line-Bragg gratings. The dot array is aligned along the light-guided direction, while

the lines are oriented perpendicular to this direction. The inscription methods for dot-by-dot and line-by-line Bragg gratings have been discussed in Chapter 2. The primary focus of this research is the slow-light effect and its enhancement in these two types of Bragg gratings. Consequently, it is crucial to achieve Bragg gratings with larger transmission dips, as these dips indicate a higher coupling constant (κL), leading to a larger slow-down factor.

Through comprehensive analysis and investigation, offset engineering was introduced to enhance the transmission dips and slow-light effects in both dot- and line-based Bragg gratings. This offset was applied between the waveguide and the dots/lines along the vertical direction. It is important to note that excessively small offset intervals typically require extensive measurement work, due to the necessity of considering multiple writing parameters such as laser power, repetition rate, and writing speed. To balance these factors, four offset values (0 μm, 5 μm, 10 μm, and 15 μm) were selected for fabrication.

Additionally, for two-pass waveguide inscription, excluding offset engineering, six center-to-center distances ranging from 0 to 5 μm (with 1 μm steps) were also chosen to calibrate the overlap between the dot/line-waveguide interactions. This adjustment aims to achieve a higher coupling coefficient κ (i.e., coupling constant κL), thereby improving the transmission dips and further optimizing the slow-light effects.

3.1.2 Slow light Bragg grating characterization

The characterization of waveguides and waveguide Bragg gratings is a key aspect throughout the entire research project. In addition to the primary characterization methods outlined in published articles and the appendices, various practical experiences—such as sample polishing, experimental platform setup, fiber splicing, instrument usage, understanding the limitations of the measurement instruments, and ensuring personal safety—are also crucial for achieving accurate results. Here, we provide a brief overview of the main characterization methods used in the study.

3.1.2.1 Waveguide characterization

The primary characterization targets in this thesis are waveguides and waveguide Bragg gratings. For waveguides, the first focus is on RI change (Δn), including measurements of the phase profile and the effective affected height. The phase profile is measured using a non-invasive phase-refractive index profiler, "The Ripper™," as shown in Figure 3.3(a), developed by PhotoNova Inc.

[110]. The effective affected height is obtained from a cross-sectional (side view) analysis, which utilizes white light and NI-MAX (National Instruments Measurement & Automation Explorer) technology/software. The cross-sectional view images are then processed by the public software "ImageJ," which converts pixel measurements into microns. Figure 3.3(b) illustrates the femtosecond laser (FSL) direct writing process for waveguide fabrication within a bulk glass slide. When the FSL operates at a repetition rate of 606 kHz, a positive refractive index (RI) change is observed, as shown in Figure 3.3(c). In contrast, a lower repetition rate, such as 20.2 kHz, results in a negative RI change, as depicted in Figure 3.3(d).

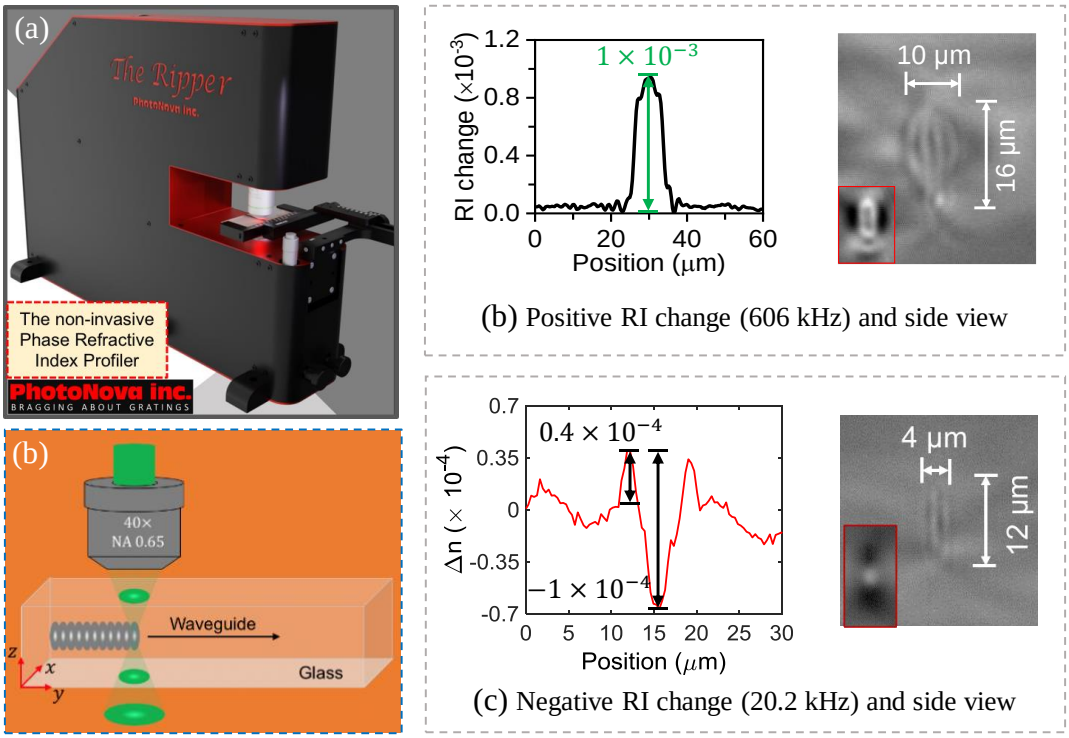

Figure 3.3 (a) The Ripper™ (Fabulas), (b) FSL direct writing waveguide within a bulk glass slide, (c) Waveguide with positive RI change at 606 kHz repetition rate and its side view, and (d) Waveguide with negative RI change at 20.2 kHz repetition rate and its side view.

The propagation loss of the waveguide, comprising both material absorption and scattering, is evaluated using the slope of the insertion loss through the segmental cutting method. A 75 mm-long sample is cut into four segments by a diamond saw with lengths of 10 mm, 15 mm, 20 mm, and 30 mm, as shown in the schematic and actual sample slabs in Figures 3.4(a) and (b). Before conducting measurements, the end facets of the slabs must be polished, and index-matching oil is applied to minimize multiple reflections between the waveguides and fibers during the

measurement process. The transmission power/spectrum of the waveguide with ($P_o(\lambda)$) and without ($P_{ref}(\lambda)$) the sample is measured using an optical spectrum analyzer (OSA, Ando, AQ6317B), as detailed in Appendix A (A.2). The insertion loss, $IR(dB)$, is then calculated using the equation (3.1).

$$IR(dB) = -10\log_{10}\frac{P_o(\lambda)\ (mW)}{P_{ref}(\lambda)\ (mW)} = P_{ref}(\lambda)\ (dBm) - P_o(\lambda)\ (dBm). \qquad (3.1)$$

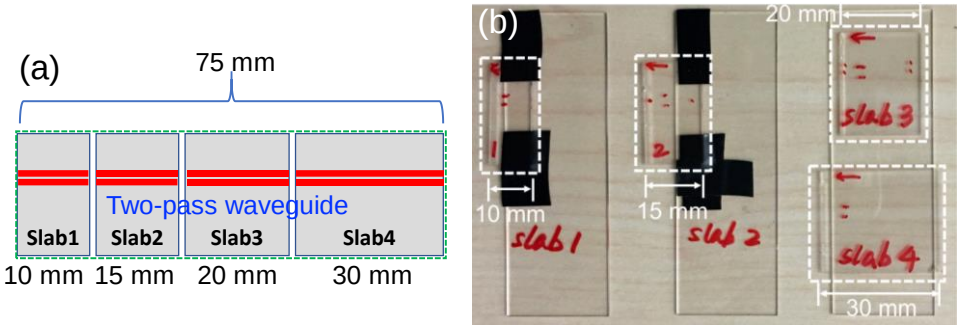

Figure 3.4 (a) Schematic diagram of the waveguide sample consisting of four slabs. (b) Photograph of the waveguide sample with four slabs, cut using a diamond saw for output power measurements.

It is important to note that several schematic experimental setups and methods for waveguide characterization, including output power measurements for evaluating light-guiding efficiency, light-guided position analysis (using the same setup as the cross-sectional view measurement), and mode near-field profiles, are described in Appendix A (A.3). Additionally, the use of V-number calculations to roughly estimate the LP modes for both waveguides and dot/line-Bragg gratings is presented in Appendix A (A.4). This will not be elaborated further here.

3.1.2.2 Waveguide Bragg gratings characterization

The characterization of waveguide Bragg gratings primarily involves measuring the reflection and transmission spectra, as well as the group delay in both reflection and transmission. For these spectrum measurements, this project employed two instruments: an OSA and an Optical Backscatter Reflectometer (Luna OBR 4600) system. The experimental setup schematics for the OSA and OBR are provided in Appendix A (A.4) and Appendix A (A.7) or Appendix B (B.2), respectively.

Before performing OSA or OBR measurements, it is essential to confirm the maximum light guiding efficiency (or output power) achievable for the waveguide Bragg gratings. This was done

using a supercontinuum laser (Fianium WhiteLase™ SC480) along with a polarization controller and a power meter. For reflection and transmission measurements, the OSA and a 3-dB coupler were employed, with a polarization controller used after the coupler to adjust the incident light to vertical polarization (v-pol) and horizontal polarization (h-pol).

For the OBR system, reflection can be directly measured by launching the optical signal into the waveguide Bragg gratings, while transmission measurements require the use of a circulator. A polarization controller is also employed to adjust the polarization to either v-pol or h-pol configurations. Additionally, to simplify the testing process, butt coupling was used between the SMF28 fiber and the end facets of the waveguide Bragg gratings. To minimize Fresnel reflections and potential Fabry-Pérot losses, the SMF28 fiber was intentionally tilted at an angle of less than 10 °, and index-matching oil was applied between the fiber and the waveguide.

Compared to the OSA, the OBR system not only offers higher resolution but also enables the extraction of group delay characteristics in both reflection and transmission of the Bragg gratings. Furthermore, the time delay can be measured using a time-domain method with a single-frequency DFB laser diode, a modulator, a fast photodiode, and an oscilloscope (as described in Chapter 6). Here, a super high-resolution OSA (APEX Technologies, with a resolution of 1.12 pm) was employed to accurately determine the positions of the reflection peak and reflection edges.

3.2 Organization of the articles

This thesis is structured around three articles that explore the slow-light effect and its enhancement in waveguide Bragg gratings fabricated using FSL direct writing techniques. The slow-light effect was initially discovered using complex equipment and ultra-low temperatures. Later, it was applied to solid materials such as silicon and silicon dioxide in semiconductor devices, photonic crystals, metamaterials combined with gold, and silica (fibers created with UV/FSL lasers), all at room temperature. These advancements have demonstrated significant potential for integration into compatible devices and for sensing applications. The three articles presented here specifically focus on the slow-light effect generated in waveguide Bragg gratings fabricated in bulk glass by FSL, which could have future applications in hardened glass for cellphone screens with embedded sensors, as well as in optical antennas for smart glass windows. These applications would enhance light-matter interactions, enabling real-time environmental monitoring and improving wireless communications.

The first article, published in Optics Express and titled **"Bragg gratings with novel waveguide models fabricated in bulk glass via fs-laser writing and their slow-light effects"**, focuses on waveguide Bragg gratings and slow-light effects. This article addresses the first and second objectives of this thesis, which involve the design, exploration, and fabrication of novel waveguides, waveguide Bragg gratings, and their associated slow-light effects. It serves as a preliminary investigation into slow light in waveguide Bragg gratings inscribed in bulk glass slides.

However, the dot-Bragg grating achieved only a transmission dip of less than 2 dB, centered around ~1630 nm (within the optical communication U band, primarily used for network monitoring), resulting in a small SDF of 1.04. The line-Bragg grating, centered at 1603 nm (in the L band), exhibited a transmission dip of less than 5 dB (measured by OSA, and ~11 dB measured by OBR), leading to an SDF of 1.12 (or 1.38 if using the ~11 dB transmission dip for calculation). However, the line-Bragg grating exhibited multiple side lobes and significant loss, which could be attributed to either the four-pass inscription process used for fabricating the waveguide or the excessive horizontal length (perpendicular to the light guiding direction) of the line grating (200 μm).

The second article, published in Optics Express and titled **"Offset-enhanced slow light in femtosecond laser-fabricated Bragg gratings"**, explores how to enhance slow-light effects in line-Bragg gratings through offset engineering. In this article, the formula for the SDF (Objective 3) was derived using coupled-mode theory, providing a means to evaluate slow-light effects in any type of Bragg grating simply by using the coupling constant κL.

To solve the lossy and side-lobe issues observed in the line-Bragg grating from Article 1, this study reduced the grating horizontal length (perpendicular to the light-guiding direction) to 15 μm and introduced vertical offsets between the line gratings and the waveguide to enhance both the transmission dip and slow-light effect (Objective 4). Additionally, the writing parameters for the waveguide were optimized, and a single-laser-pass inscription process was employed. These improvements enabled the inscribed line-Bragg gratings to achieve a narrow, deep transmission dip, effectively overcoming side-lobe effects. The result was a transmission dip of 12.5 dB and an SDF of 1.54, centered at ~1550 nm.

The third article, titled **"Enhanced slow-light phenomena in dot-Bragg gratings through offset engineering,"** was submitted to Journal of Lightwave Technology. In this study, two types of dot-Bragg gratings were fabricated with optimized writing parameters to enhance slow-light effects

(Objective 5): Model-I with a single-pass inscribed waveguide and Model-II with a two-pass inscribed waveguide. Further, offset engineering was applied to both models to further improve the slow-light effect (represented by SDF). Model-I achieved a transmission dip of 6.7 dB and an SDF of 1.21, centered at approximately 1550 nm.

For Model-II, a two-pass inscribed waveguide with a lower repetition rate was used, compared to Model-I, to mitigate potential waveguide oversaturation. The center-to-center distances were adjusted in Model-II's waveguide inscription to reduce dot position sensitivity to waveguide (observed in Model-I) and enhance dot-waveguide interaction, ultimately improving the transmission dip and SDF. Optimized Model-II demonstrated a 12.5 dB transmission dip and an SDF of 1.45, also centered at around 1550 nm. When compared to the dot-Bragg grating discussed in Article 1, the SDF values in Model-I and Model-II were improved by 16% and 39%, respectively. Furthermore, time delay measurements in Model-II, captured through signal pulse traces at the reflection peak and edges, revealed a relative delay of 7 ps, indicating an overestimated slow-light effect.

CHAPTER 4 ARTICLE 1: BRAGG GRATINGS WITH NOVEL WAVEGUIDE MODELS FABRICATED IN BULK GLASS VIA FS-LASER WRITING AND THEIR SLOW-LIGHT EFFECTS

Qingtao Chen, Jean-Sébastien Boisvert, Mohammad S. Sharawi, and Raman Kashyap

Published in: Optics Express

Publication date: Dec. 18, 2023

This article has been published in Optics Express (*Opt. Express*, vol. 32, no. 1, pp. 188–204, 2024, doi: 10.1364/oe.509482; Publication date: Dec. 18, 2023) and titled **"Bragg gratings with novel waveguide models fabricated in bulk glass via fs-laser writing and their slow-light effects"**. The article focuses on waveguide Bragg gratings and slow-light effects. The work demonstrates the design, exploration, and fabrication of novel waveguides, waveguide Bragg gratings, and their associated slow-light effects. It serves as a preliminary investigation into slow light in waveguide Bragg gratings inscribed in bulk glass slides. The supplement of this article is given in Appendix A of this thesis. *(It is important to note that: (1) The errors in Tables 4.1 and 4.2, as well as the associated analysis, have been corrected. (2) The y-axes in Figures 4.6~4.7 and 4.9~4.11 have been normalized to simplify the characterization and analysis of the Bragg gratings. (3) The TE and TM modes, in fact, equivalent to vertical (v-pol) and horizontal (h-pol) polarizations in this chapter, respectively.)*

Abstract: We present the experimental realization of an innovative parallel partially- overlapping waveguides (PO-WGs) model grounded in the thermal accumulated regime and fabricated using femtosecond (fs) laser direct-writing within low-iron bulk glass. The 75 mm long novel PO-WGs model was made by partially overlapping the shell parts of two core-shell types of waveguides via a back-and-forth single pass fs-laser inscription. The detailed evolution of the PO-WGs model from inception to completion was offered, accompanying by a thorough characterization, which unveils a substantial refractive index (RI) change, on the order of 10^{-3}, alongside low propagation loss (0.2 dB/cm) and distinctive features associated with the single mode and shell-guided light.

Notably, the unsaturated performance of PO-WGs model after the primary inscription paves the way for potential applications in the successful creation of two distinctive types of Bragg gratings: first-order dot-Bragg grating and second-order line-Bragg grating. The 75mm long dot-Bragg grating was written by a periodic dot array with a height of 6 μm atop the PO-WGs, and the birefringence was measured of 1.5×10^{-5} with a 16 pm birefringence-induced wavelength difference. The line-Bragg grating, which was inscribed with dual PO-WGs extending the line grating part to 40 mm in length along its period for increasing the transmission dip, exhibits a pronounced polarization dependence showcasing an effective birefringence of 4.2×10^{-4} at the birefringence-induced wavelength difference of 0.45 nm. We delved into the slow-light effects of the two Bragg gratings thoroughly, which the theoretical analysis (based on coupled-mode theory) revealed an effective group delay of 0.4 ns (group index 1.6) for the dot-Bragg grating. Similarly, the line-Bragg grating exhibited an effective group delay of 0.23 ns (group index 1.76), in good agreement with experimental measurements. These findings underscore the exciting potential of our gratings for creating optical slow-wave structures, particularly for future on-chip applications.

4.1 Introduction

With the development of large-scale photonic integrated circuits and the popularity of related applications, femtosecond (fs) laser (FSL) direct-writing waveguides [47] and waveguide-based photonic devices in bulk transparent materials, especially in bulk glass, have attracted significant attention [1], [111]. Due to the rapid precision-writing advantages by using FSL [112] for the refractive index (RI) change of bulk glasses to induce light guiding, several kinds of waveguides [60] and waveguide-based photonic devices, such as waveguide Bragg gratings [64], [74], [75], [113], amplifiers and lasers [114], three-dimensional devices [76], lab-on-a-chip applications [78], as well as some related fabrication techniques and characterizations [79], have been demonstrated.

The final induced RI modification forming the waveguide relies on the multiple writing parameters, such as laser power, repetition rate and writing speed to name of few, which are the cumulated result of different RI change mechanism. The maximum RI change in glasses, of order 10^{-2}, have been reported [115] at high repetition rate [55] resulting of the high heat accumulation. However, high thermal accumulation regime might make the RI change saturation, which renders the inscription of Bragg gratings difficult.

In this work, we propose a new waveguide model relying on heat accumulation mechanism at kHz repetition rates that allows the inscription of first-order dot and second-order line Bragg gratings in low-iron bulk glass. The new waveguide model is based on a simple tear-drop shell waveguide [116] that was achieved by partially overlapping the shells of two shell waveguides (i.e. partially overlap two tear drops) with a reasonable center-to-center distance formed within the thermal accumulation regime[54], in two FSL-written process steps with a single scan, herein referred to as PO-WGs. Compared with conventional double line waveguides with light guiding between lines [58], our PO-WGs model shows distinctive shell light-guided (or circular waveguiding) features, demonstrating the advantages of a high RI change, of order 10^{-3}, and low propagation loss of 0.2 dB/cm, which is also easy to implement rapidly with our tailored recipe. The successful inscription for two types of Bragg gratings with PO-WGs models ensures that the RI change in this low-iron glass was not saturated after the primary inscription. The 75mm long rapid-written dot-Bragg grating shows a full width at half maximum (FWHM) of 51 pm at resonance and a birefringence, of order 10^{-5} with 16 pm Bragg difference. The line-Bragg grating with dual PO-WGs was inscribed extending the grating part to 40 mm for increasing the transmission dip, which exhibits an FWHM-width of 55 pm, a strong birefringence, of order 10^{-4} with a 0.45 nm Bragg difference. In addition, the slow-light effects have been reported in fiber Bragg gratings [3], [22], but for bulk glasses, to our knowledge, it was not reported and could be of interest for on-chip telecommunications. Therefore, it is of great significance that the novel PO-WGs-based Bragg gratings have been further explored in an effort to generate slow light for creating slow-wave applications in terms of grating dispersion to enhance light-matter interaction in transparent materials.

4.2 New waveguide models (PO-WGs) inscription and characterization

A Pharos femtosecond laser (FSL), which operates at 1030 nm doubled to 515 nm with the Orpheus system couple with an Aerotech 3200 precisio translation stage was used to write the structure. The writing average power used was from 100 mW to 500 mW. The repetition rate was tuned from 101 kHz to 606 kHz with a pulse picker to conserve the peak energy. The writing speed was ranged from 1 mm/s to 20 mm/s with a lens of 0.65 of NA (numerical aperture). The 75mm long low-iron glass (Fisherbrand, 75 mm×25 mm×1 mm, Catalog No.: 12-550-A3) was chosen since it is not only cheap, available and highly transparent, but also easy for writing this

novel waveguide (PO-WGs) proposed by us. What counts is Bragg gratings also have been achieved demonstrating that the refractive index of this type of glass does not saturate after writing of this waveguide (PO-WGs). Compared with shorter glass slides, using longer ones for inscription provides easier and more precise waveguide loss characterization by cut-back method and Rayleigh scattering measurement from Bragg gratings. Moreover, our PO-WGs works in the weak guidance approximation due to the RI change, of order 10^{-3}, so longer ones ensure that the leaky modes excited at the injection can be eliminated. The detailed tailoring process and characterization for this waveguide model will be discussed in the following sections.

4.2.1 Partially-overlapping waveguides (PO-WGs) model

The subsurface and ridge waveguides [65] were realized in low-iron glass slides based on isotropic modification (i.e. same RI changes in all directions) [57] and orthotropic modification (i.e. negative RI change with guiding light in between the laser-modified parallel lines) [58]. However, that RI change was found to be very small, of order 10^{-4}, which directly affected the waveguide quality and the light guiding performance, even the optical devices based on it. Herein, our work shows a new waveguide model (PO-WGs) by FSL-written techniques[108] in similar glass, supporting light guidance at 1550 nm.

The exploration for the new PO-WGs model used three steps. Firstly, a tear drop type of 'shell waveguide' consisted of a super-continuous core-shell ellipsoid units along the light guiding direction (i.e.y-axis in Figure 4.1(a)) was inscribed with a single pass (step/fabrication process) by the preliminary writing parameters, which are 606 kH repetition rate, 150 mW laser power, 165 nJ pulse energy and 10 mm/s writing speed. However, the RI change is very small, of order 10^{-4} (Figure 4.1(d)), with a circular (shell) waveguiding measured by white light (inset in Figure 4.1(g)). Secondly, to further exploit a high quality waveguiding model with a higher RI change, the novelty of this study here is in the writing of the waveguide itself, which is achieved by parallel partially overlapping shell parts of two shell waveguides with a reasonable center-to-center distance to form a typical heat accumulation structure. During this process, one model, which consists of two parallel adjacent shell-waveguides with 8 or 10 μm center-to-center separation along x-axis (Figure 4.1(b)), is proposed and called as PA-WGs (Figure 4.1(h)) with a higher RI change, of order 10^{-3}, but a drop produced in between two peaks (Figure 4.1(e)). Thirdly, after further fine-tuning and exploration, the new writing scheme is proposed constituting two parallel shell-waveguides with

partial overlaps along x-axis (i.e. 6 μm center-to-center distance, (Figure 4.1(c)), forming a heat accumulation structure, referred to as PO-WGs (Figure 4.1(i)), whose RI change (Figure 4.1(f)) is higher just within a relative smaller drop compared to the RI map of PA-WGs.

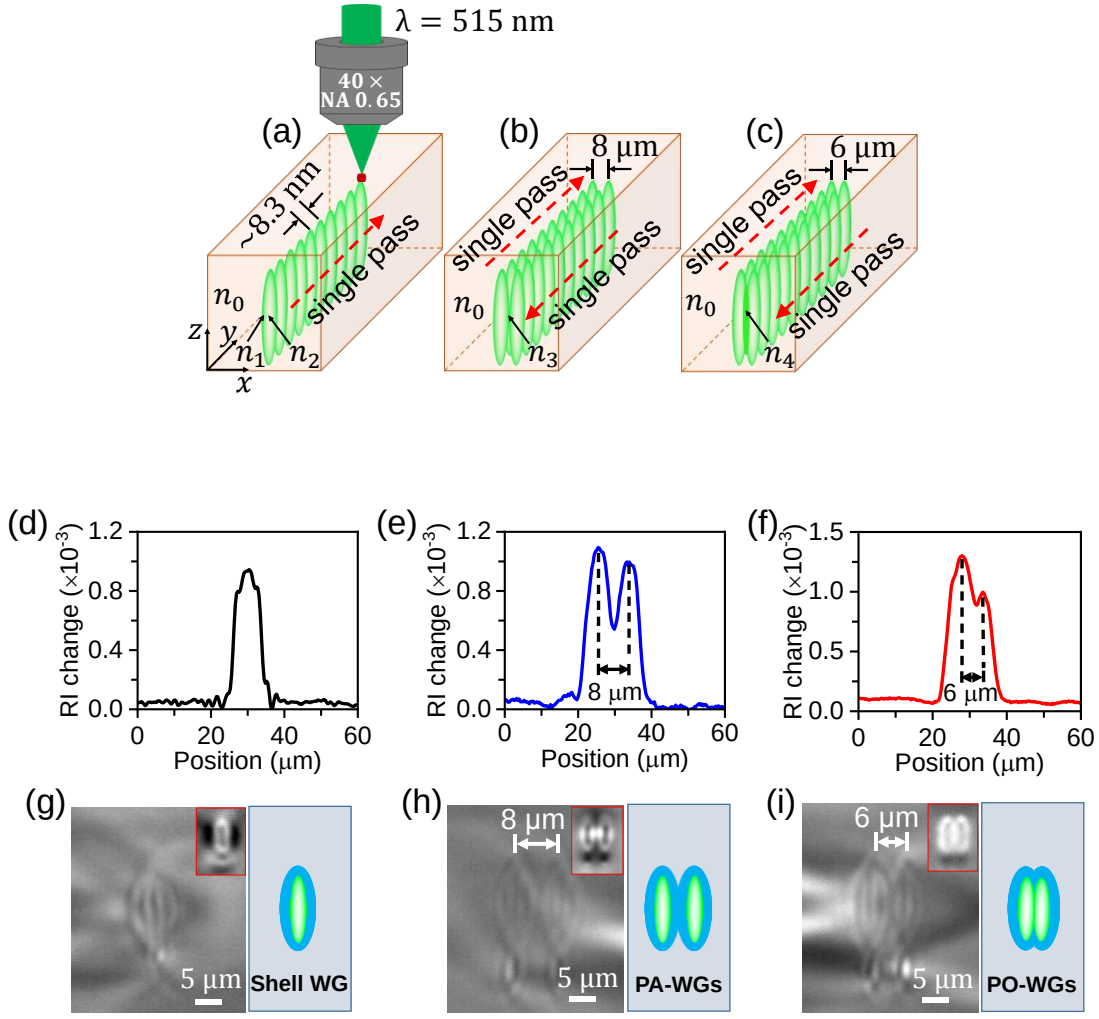

Figure 4.1 Evolution process of waveguide models and their characteristics. (a) Shell waveguide, (b) PA-WGs, and (c) PO-WGs. Note: The calculated period of ~8.3 nm among ellipsoid units along y-axis is not to scale. (d) and (g) RI change/contrast and side view of shell waveguide. (e) and (h) RI change and side view of PA-WGs with 8 μm center-to-center distance. (f) and (i) RI change and side view of PO-WGs. The insets in the red boxes in (g), (h) and (i) are measured by white light to show light guided positions, while the right side gives schematic diagrams of the three types of waveguide models. Note: The writing laser was incident from the top in (g), (h) and (i).

4.2.2 RI change of PO-WGs

The refractive index (RI) change, Δn, of waveguides in this paper is measured using an interferometric phase measurement technique and calculated by the following expression:

$$\Delta n = \frac{\Delta \phi \lambda}{2\pi h} \tag{4.1}$$

where $\Delta\phi$ is the phase change, h is the effective affected height, and λ is the measurement wavelength of 632 nm. The phase change based on a phase profile was obtained using a non-invasive phase-refractive index profiler—"The Ripper^{TM}" from PhotoNova Inc.[110]. The profiler features a phase noise of 10 mrad which corresponds to a RI change of only 10^{-5} [117]. The effective affected height was measured by NI-MAX (NI Measurement & Automation Explorer), and then a public software "ImageJ" was performed changing pixels of the side view into microns.

Figure 4.1(d) shows the RI change of shell waveguide with a positive RI change in the center, whereas most of the light is guided at the shell as shown in the inset of Figure 4.1(g). This suggests that the RI modification of the inner shell is less than the other shell where the light is confined. In Figure 4.1(e) the two shell waveguides are too far apart to allow a good overlap, contrary to Figure 4.1(f) where the light is confined in the center. Although the RI change of shell waveguide is up to the order 10^{-3} (Figure 4.1(d)), the output power is still limited due to the light guiding along the shell, not along the core, shown in the inset of Figure 4.1(g). For PA-WGs, the RI change is improved due to two adjacent shell waveguides, but a dip in RI change (Figure 4.1(e)) also affects the light guiding efficiency. The PO-WGs based on heat accumulation technique is proposed using partial overlaps of two shell waveguides to further increase the light guiding efficiency, such as higher RI change and higher output power. Additionally, the refractive indices of shell regions, n_1, adjacent shell regions, n_3 and shell overlapping regions, n_4 are larger than the refractive index of the glass substrate, n_0, while the core regions, n_2 also has a different value compared with n_0, as shown in Figures 4.1(a~c).

To further maximize the RI change of PO-WGs, we first coarsely and then finely adjust the preliminary writing parameters and center-to-center distance. The 64 recipes are carried out during finely adjustment with 6 μm and 8 μm center-to-center distance by changing the writing speed (1~20 mm/s), repetition rate (101 to 606 kHz) and laser power (100~250 mW), where the waveguide are all below the glass surface at a distance of 397 μm. The results of RI change for the 64 recipes are given in the Appendix A (Figure A.1), showing a best recipe for writing PO-WGs is 606 kHz repetition rate, 250 mW laser power, 165 nJ pulse energy, 5 mm/s writing speed and 6 μm center-to-center (C-to-C) distance, which resulted in a calculated period of ~0.83 nm. Based on

partial writing parameters of the best recipe, Figure 4.2(a) shows a set of RI change for PO-WGs varying with the writing speeds. We observed that the RI change gradually decreases with increasing writing speed, while the maximum values up to 1.5×10^{-3} (Max: $L4$) and 1.63×10^{-3} (Max: $L2$) are separately achieved with the writing speed of 5 mm/s when the PO-WGs are below glass surface of 397 μm and 55 μm. As one can observe that there is a difference of $(0.27\sim0.4) \times 10^{-3}$ in the RI change induced under the same illumination condition. Meanwhile, the corresponding depth of the structure is also increased by 44%~57% (that is from Figure 4.2(b) to Figure 4.2(c)), from glass surface to the bulk.

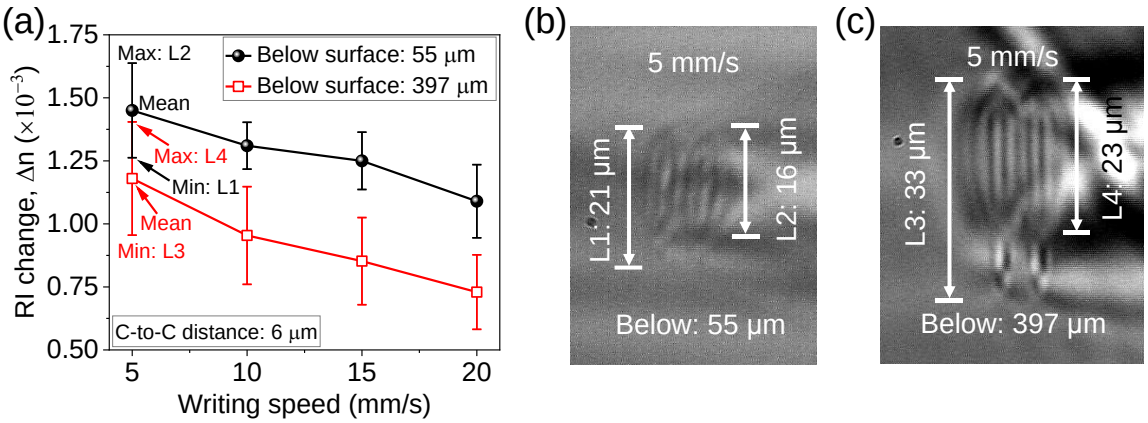

Figure 4.2 PO-WGs characterizations. (a) RI change (Min-, Max- and mean-values) versus writing speed. Note: C-to-C distance denotes the center-to-center distance. (b) and (c) Side views of PO-WGs below glass surfaces of 55 μm and 397 μm with 5 mm/s writing speed. The writing laser was incident from the top.

Multipass (or multi-scan numbers) can be used to increase the RI change of waveguides[85],but one needs to be careful not to reach saturation of the RI change which will be detrimental to Bragg grating inscription. However, our primary focus is on utilizing a single pass with a single scan to design a novel PO-WGs structure and explore its applications.

4.2.3 Propagation loss of PO-WGs

The propagation loss for PO-WGs below glass surface at 397 μm was measured by a segmental cutting method, where a 75 mm long glass is cut into 4 slabs by a diamond saw whose lengths are 1.0 cm, 1.5 cm, 2.0 cm, and 3.0 cm, and characterized using the slope of insertion loss. Both facets of each slab are polished before measurement to reduce most of the reflection and losses. The transmission power without and with waveguide samples are represented by $P_{ref}(\lambda)$ and $P_o(\lambda)$

and measured without using focusing lens and index matching oil (Appendix A.2), while the insertion loss is calculated by

$$IR(dB) = -10\log_{10}\frac{P_o(\lambda)}{P_{ref}(\lambda)} = P_{ref}(\lambda) - P_o(\lambda) \tag{4.2}$$

where the units of $P_{ref}(\lambda)$ and $P_o(\lambda)$ are numerical values (mW or W) and dBm for the middle and right parts of the equation, respectively.

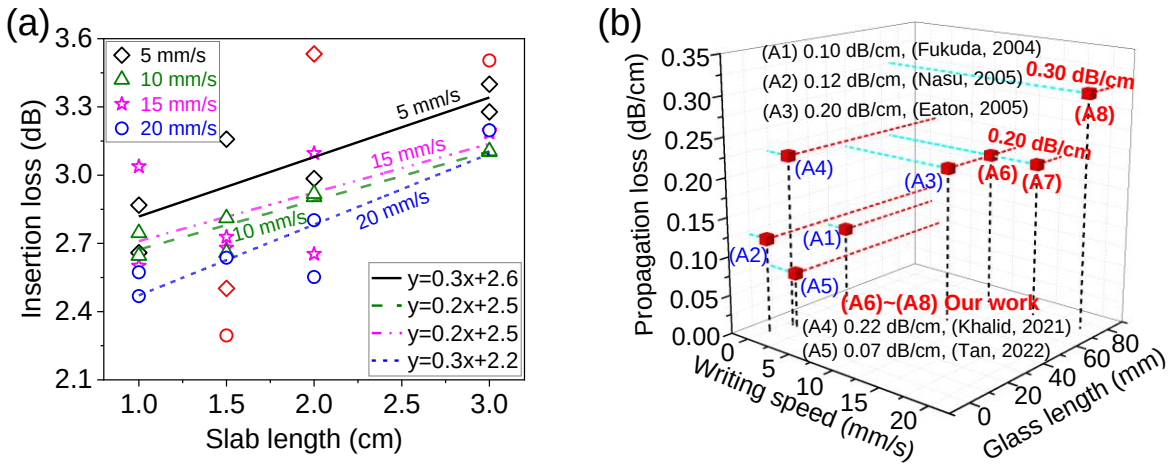

Figure 4.3 (a) PO-WGs insertion loss versus slab lengths with 4 different writing speeds. (b) Comparisons of propagation loss for PO-WGs at a 1550 nm wavelength, where (A2) and (A5) separately inscribed with multiscans and 8 scans, and others with 1 scan.

Figure 4.3(a) shows the obtained propagation loss (dB/cm) which is represented by the slope of linear fit (some outliers marked in red are excluded) while the intercept demonstrates the coupling loss. We can find the propagation losses are 0.2 dB/cm for a writing speed up to 15 mm/s and 0.3 dB/cm for 20 mm/s. Meanwhile, the comparison with the other waveguides[54], [118]–[121] is also given, as shown in Figure 4.3(b). We observed that some of them exhibit lower propagation losses with smaller RI change, and some are inscribed at MHz repetition rate limiting the inscription windows for Bragg gratings, while some have high RI change and low propagation loss, but short glass length are not suitable for the writing of long Bragg gratings. However, our waveguides are inscribed within a relatively longer glass substrate using a higher writing speed and a single scan for each ellipsoid unit, achieving a higher RI change, of order 10^{-3}, and a lower propagation loss, which is sufficient for large-scale integration of waveguide-based photonic devices and telecommunication applications.

4.2.4 Waveguiding efficiency of PO-WGs

The light guiding efficiency or light guiding ability of 75 mm waveguides is roughly estimated as the output power (Appendix A.3(a)) divided by the input power without considering the Fresnel loss, coupling loss and propagation loss. Figure 4.4 shows the writing speed versus the light guiding efficiency for PO-WGs below the glass surface at ~55 μm. In order to make the results precisely, we fabricated at least four samples for each writing speed. We observed that the average light guiding efficiency goes up to 59 % while the maximum value is up to 60% when the writing speed is 5 mm/s. However, the average light guiding efficiency reduces to approximately 36%, 35% and 34.9% when the writing speed is increased to 10 mm/s, 15 mm/s and 20 mm/s. Still, this trend in efficiency is not constant, while becoming somewhat smaller with higher stability (i.e. degree of aggregation of the measured points shown in the inset of Figure 4.4) when the writing speed is increased to 20 mm/s.

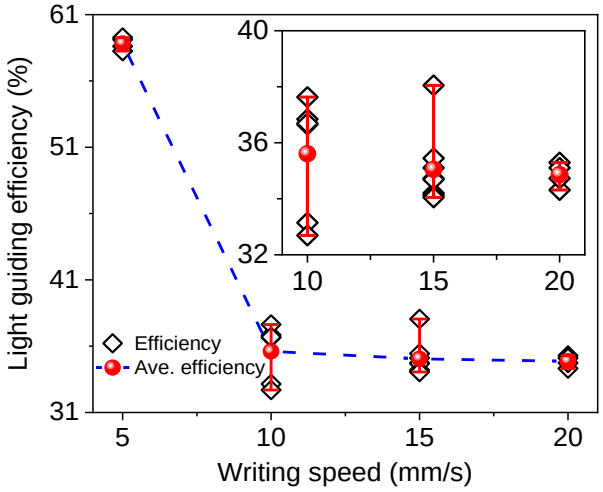

Figure 4.4 Light guiding efficiency of PO-WGs measured at 1550 nm.

Besides, the decrease of light guiding efficiency with higher writing speed also demonstrates a similar tendency to that of the corresponding RI change. We believe this trend on the one hand comes from the imperfect overlap and on the other hand might originate from irregularities and asymmetry of ellipsoid units comprising PO-WGs in the FSL-writing process with a higher speed that leads to a decrease in RI change. Besides, the shape asymmetry in the center along the horizontal or vertical of a single ellipsoid unit (Figure 4.1(g)) might induce scattering loss during light propagation, which would be another reason. In addition, the cross-sectional asymmetry of

PO-WGs might also have arisen from the single scan during writing, but multi-scans with the use of a cylindrical lens could solve the above-mentioned problems [59], [87], [122].

4.3 PO-WGs dot-Bragg grating

4.3.1 RI change of PO-WGs in dot-Bragg grating

The first-order dot-Bragg grating was inscribed in the 75 mm long low-iron glass in two steps. Firstly, the PO-WGs was first inscribed below the glass surface at ~ 55 μm using the above-mentioned best recipe. Secondly, a dot-by-dot periodic ellipsoidal array was written in the center along the length of the PO-WGs with a laser power of 100 mW, the pulse energy of 165 nJ, a single pass with the writing speed of $v = 3\ \mathrm{mm/s}$ and a repetition rate of $R = 5.51$ kHz, leading to a period of $\Lambda = v/R = 0.54$ μm. Compared to a 250 mW laser power for PO-WGs inscription, a lower laser power of 100 mW was used here for dot array due to a higher or identical power just only leads to the formation of an additional waveguide alongside the existing PO-WGs, essentially resulting in larger-sized PO-WGs. Also, less writing power results in a better writing resolution for dots array due to the nature of the non-linear interaction. It is to be noticed that a defined parameter, d, the vertical modulated distance (i.e. the depth of periodic ellipsoidal dot array located in between PO-WGs), was used to modulate the interaction between the PO-WGs mode and the periodic dot array, as shown in Figures 5(a~b). The measured value for d is roughly 6~7 μm to be used to modulate the resonant features for dot-Bragg grating. The resonance strength will become gradually weaker with increasing d value and will completely disappear when d value is equal to the vertical height of PO-WGs.

Figure 4.5(c) shows a peak RI change of 1.56×10^{-3} for the first-order dot-Bragg grating, while the average RI change is 1.3×10^{-3} obtained from several peaks. Also noticed is a center-drop from RI change leading to a little decrease in the peak and average values which might be attributed to the different writing parameters, especially the laser power and repetition rate, for dot array and PO-WGs. Further measurement of the light guiding efficiency of dot-Bragg grating exhibits a value of 55% at 1550 nm without considering the 3.4% Fresnel loss at both end-facets, coupling loss, propagation loss, and no focusing lens and index matching oil as well. A 4% decrease in the guiding efficiency compared to that of a single PO-WGs (59%) indicates that the possible impacts arise

from the center-drop of RI change, the scattering from the dot-Bragg grating itself as well as the writing parameters.

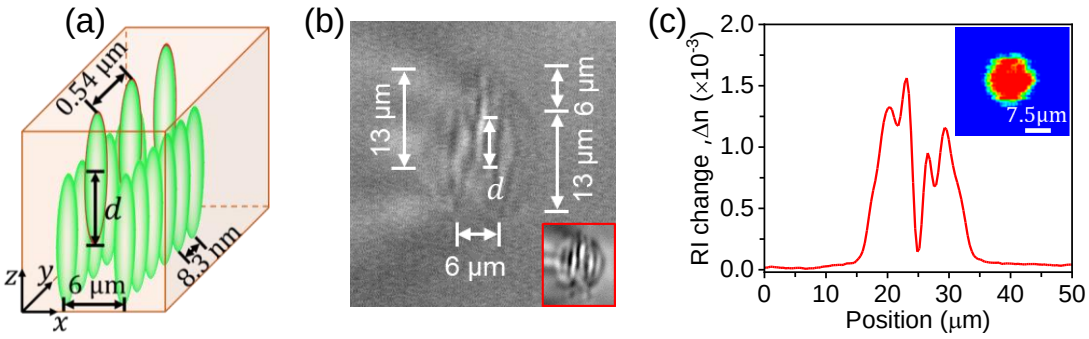

Figure 4.5 Dot-Bragg grating. (a) Schematic diagram but the dimensions are not to scale. (b) Side view (The inset in the red box shows the light guided position by white light). The writing laser was incident from the top. (c) RI change and an inset of mode near field measured at 1550 nm.

The light guiding position (the inset of Figure 4.5(b)) was measured by white light (Cold light source, intralux 6000-1, Appendix A.3(b)), which approximately indicates an effective diameter of 8~10 µm, a little larger than the center-to-center distance of 6 µm and roughly equals the horizontal distance of the peak position (10~12 µm) along 'Position' axis in the RI map (Figure 4.5(c)). Additionally, the mode near field (the inset of Figure 4.5(c)) was measured at 1550 nm wavelength (Appendix A.3(c)) with an estimated diameter of 15 µm which is calculated using the following mode field diameter (MFD) equation [123],

$$MFD = 2a\left(0.65 + \left(\frac{1.619}{V^{3/2}} + \frac{2.878}{V^{6}}\right)\right) \tag{4.3}$$

where a is the effective radii of 4 µm and 6 µm from side view (Figure 4.5(b)) of the PO-WGs, V is the normalized frequency (i.e. V-number, Appendix A.4) of 1.43 and 2.14 (with the calculated MFDs of 15 µm and 14 µm, respectively.), in which the dot-Bragg grating allows only the LP_{01} mode to propagate. In addition, the MFD can also be measured using the NanoScan (Appendix A.3(d)), with values of 16 µm and 15 µm along the effective radii of 4 µm and 6 µm, respectively. Consequently, we can draw the conclusion that the mode field position for dot-Bragg grating is approximately located at the light guiding position and that the light guides along the peaks with respect to the microscope image Figure 4.5(b) and the RI map Figure 4.5(c), with a diameter of 8~12 µm.

4.3.2 Dot-Bragg grating spectra

The transmission and reflection spectra for Bragg gratings were measured by supercontinuum laser (Fianium WhiteLase™ SC480) together with a 3dB coupler, a polarization controller and an optical spectrum analyzer (OSA, Ando, AQ6317B) shown in the Appendix A.5. The butt-coupling was used between a single mode fiber (SMF28) and waveguide end-facets, while we simultaneously tilted the SMF28 to form a less than 10° angle and added index matching oil between them to reduce the Fresnel reflection and possible Fabry-Pérot loss. All of the spectra were recorded by the OSA with a 10 pm resolution.

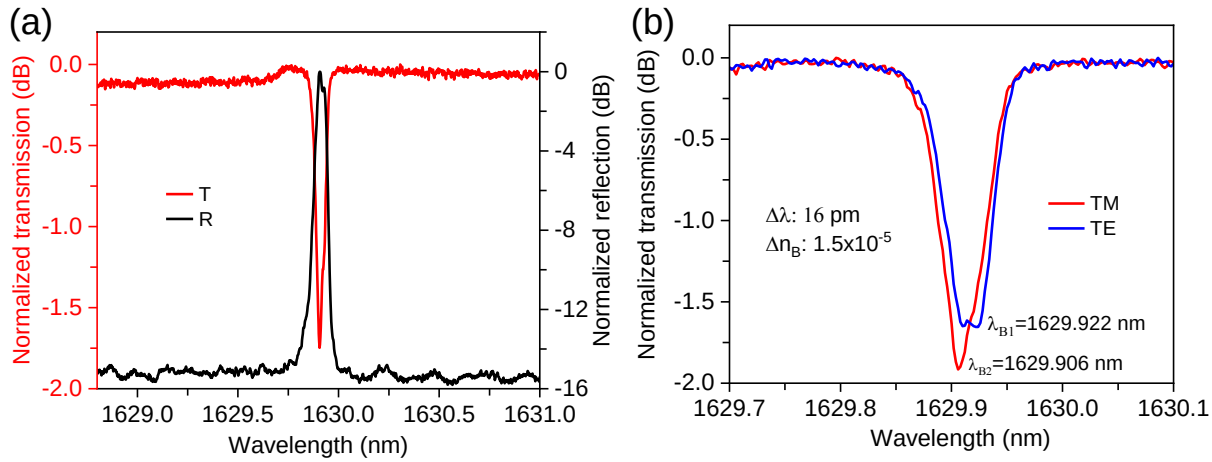

Figure 4.6 Dot-Bragg grating. Normalized (a) transmission (T) and reflection (R) spectra. (b) Polarization dependence measured by OSA with different polarization controller shapes. Note: (1) λ_{B1} and λ_{B2} represent the Bragg wavelengths, corresponding to 1629.922 nm and 1629.906 nm, respectively. (2) The TE and TM modes corresponds to vertical polarization (v-pol) and horizontal polarization (h-pol), respectively.

Figure 4.6(a) shows a narrowband transmission dip of 1.74 dB, with a full width at half maximum (FWHM) of 51 pm, and centered at the resonant wavelength (i.e. Bragg wavelength) of 1629.906 nm, i.e. supporting only a single mode and agreeing very well with the V-number estimation (Appendix A.4). The lower transmission dip strength is attributed to the vertical modulated distance, d, which can be adjusted during the FSL direct-writing process to induce sufficient interaction between the periodic dot array and PO-WGs modes for a strong transmission dip. The maximum reflectivity of Bragg grating, R_{max}, is given by using equation (4.4) with respect to the transmission dip strength, T, which is in unit of dB [45].

$$R_{max} = |\rho|^2 = 1 - 10^{-\frac{T}{10}} = \tanh^2(\kappa L) \tag{4.4}$$

where ρ is the amplitude reflection coefficient, $|\rho|^2$ is the power reflection coefficient which equals R_{max}, κ is the coupling coefficient, L is the grating length of 75 mm, and κL is the coupling constant. Using equation (4.4), we can calculate a maximum reflectivity of 33%, a coupling coefficient of 8.7 m^{-1}, and a coupling constant of 0.65.

Figure 4.6(b) shows the polarization dependence of dot-Bragg grating with 1.9 dB and 1.7 dB dips centered at different Bragg wavelengths measured under same conditions using OSA but with different settings of the polarization controller. The two dips (1.9 dB and 1.7 dB) correspond to the κL values of 0.69 and 0.65, which yield slow-down factor (SDF) values of 1.05 and 1.04, respectively, based on equation (2.27): $S = 1 + (\kappa L)^2/\pi^2$. The difference in Bragg wavelengths (i.e. Bragg difference) is defined as $\Delta\lambda$, which is obtained at 1629.922 nm (λ_{B1}) and 1629.906 nm (λ_{B2}) while separately correspond to TE and TM modes, with a value of 16 pm. Using the Bragg condition [45] given by

$$m\lambda_B = 2n_{eff}\Lambda \tag{4.5}$$

we can get $m\Delta\lambda = 2\Delta n_B \Lambda$, where λ_B is the Bragg wavelength, m is the grating order with a value of 1, n_{eff} is the effective refractive index of 1.49 estimated by femtosecond laser writing parameters, Λ is the grating period of 0.54 μm, and Δn_B is the effective birefringence. Therefore, a Bragg difference can be exhibited as 16 pm, which corresponds to an effective birefringence of 1.5×10^{-5}. This polarization phenomenon might arise largely from the asymmetry of RI change (Figure 4.5(c)), which results from the ellipsoid units in PO-WGs and dot-by-dot periodical array.

4.3.3 Slow-light effect of dot-Bragg grating

The slow-light performance, such as group delay and group index, of the dot-Bragg grating only has been calculated in theory because the grating resonant wavelengths at TM and TE modes are beyond the wavelength range (1525 nm~1610 nm) of our Luna Optical Backscatter Reflectometer (OBR) 4600. It is worth noting that the final calculated values for slow-light effect should be added to those values of the low-iron glass substrate itself (i.e. glass group delay, and glass group index).

In general, the wave propagation in our Bragg gratings can be equivalent to being guided in a periodic medium, like a Bloch wave in a one-dimensional crystal which is with invariance of lattice (i.e. periodicity) translations. According to the Bloch's theorem with a series of derivation, the

dispersion relation under normal incidence between frequency (ω) and Bloch wavenumber (K) for Bloch wave can be written as [124]

$$cos(K\Lambda) = cos(k_1 d_1)\, cos(k_2 d_2) - \frac{1}{2}\left(\frac{n_2}{n_1} + \frac{n_1}{n_2}\right) si\, n(k_1 d_1)\, si\, n(k_2 d_2) \tag{4.6}$$

where $k_1 = (\omega/c)n_1$ and $k_2 = (\omega/c)n_2$, n_1 and n_2 are the refractive indices while the corresponding d_1 and d_2 are the grating stack width and gap width between stacks. Figure 4.5(c) shows that the average RI change of the dot-Bragg grating is 1.3×10^{-3}, so we assume that the refractive index for dot grating stack is $n_1 = n_{eff} + \Delta n = 1.49 + (1.3 \times 10^{-3})$, while the value for the gap is $n_2 = n_{eff} - \Delta n = 1.49 - (1.3 \times 10^{-3})$. Moreover, the total reflections arise at the Bragg wavelengths of 1629.906 nm and 1629.922 nm for TM and TE modes, while the effective dot grating stacks and the gaps are assumed to be $d_1 = \lambda/(4n_1)$ and $d_2 = \lambda/(4n_2)$ with respect to the 50% duty cycle while the periodicity is given as $\Lambda = d_1 + d_2$. Then, we can easily calculate the group delay as $\tau = L(\partial K/\partial\omega)$, and then the group index by $n_g = c(\partial K/\partial\omega)$, as shown in Figure 4.7, where L=75 mm is the dot-Bragg length along light guiding direction. To make comparisons, the group delay was also calculated according to the coupled-mode theory (CMT) using the first derivative of phase (θ_ρ) from the amplitude reflection coefficient (ρ), i.e. $\tau = -(\lambda^2/(2\pi c))(d\theta_\rho/d\lambda)$ [46], and the results are also shown in Figure 4.7.

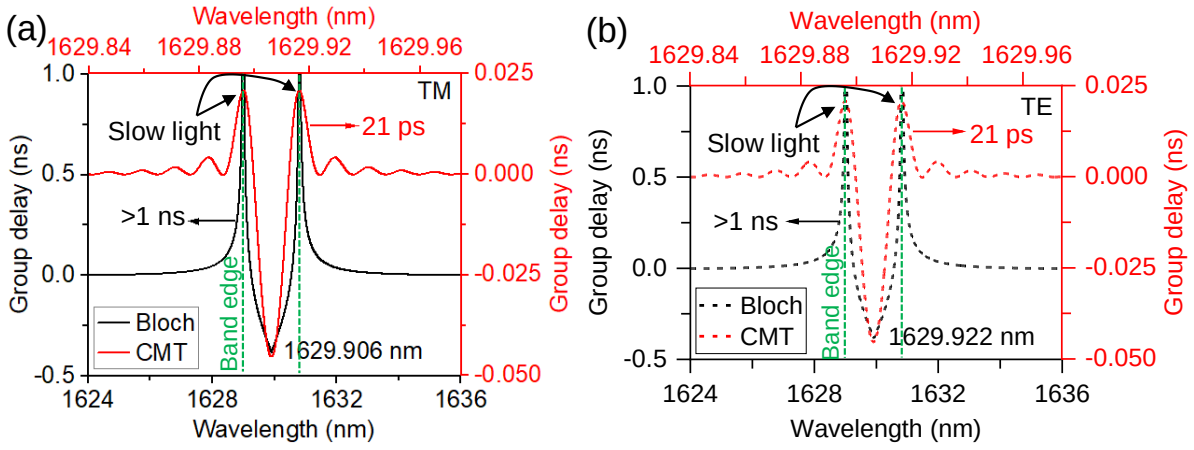

Figure 4.7 Simulated group delay at (a) TM (h-pol) and (b) TE (v-pol) modes using Bloch's theorem and coupled-mode theory (CMT) for dot-Bragg grating. Note: (1) The group delays of the waveguides (~0.38 ns) in the dot-Bragg gratings are normalized to zero on the y-axis to facilitate further analysis of the slow-light effect introduced by the grating. (2) The TE and TM modes correspond to v-pol and h-pol, respectively.

As is depicted in Figure 4.7, the group delay in TM and TE modes demonstrate similar symmetry shapes along the center positions of band gaps. The group delay calculated by Bloch's theorem is all >1.0 ns near the band edges for TM and TE modes, while the corresponding group index is all >4.0. More specifically, in equation (4.6), the wavenumber, K, of the light beam in the periodic medium obeys the Bragg law obtained by reflections added up in phase[124], while the normal incidence is taken into consideration during the equation derivation. Also, the obtained group delay based on CMT is ~0.021 ns for TM and TE modes, which corresponds to the effective value of 0.401 ns, resulting in the group index of 0.084. However, we need to acknowledge the disparities in the obtained 'bandgaps' based on the two theories, in which actually one value is the bandgap calculated by Bloch's theorem and the other value is the bandwidth computed by CMT, all in units of nm.

Notice that the group delay (GD) of the glass itself should not be ignored [101], while it can be calculated from the material itself, another related parameter, group index (GI), is defined as [45]

$$n_g = n - \lambda \frac{dn}{d\lambda} \tag{4.7}$$

where n is the refractive index of material itself, while its real part is described as [125]

$$n = 1.513 - 0.003169\lambda^2 + \frac{0.003962}{\lambda^2} \tag{4.8}$$

Table 4.1 The calculated group delay and group index in reflection (R) for dot-Bragg grating.

Name	**Effective group delay (GD) (ns)**			**Group index (GI)**		
Modes	GD of DBG	Glass GD	Final GD	GI of DBG	Glass GI	Final GI
TM (1629.906 nm) (Bloch)	> 1.0	0.38	> 1.38	> 4.0	1.53	> 5.53
TE (1629.922 nm) (Bloch)	> 1.0	0.38	> 1.38	> 4.0	1.53	> 5.53
TM (1629.906 nm) (CMT)	0.021	0.38	0.401	0.084	1.53	1.614
TE (1629.922 nm) (CMT)	0.021	0.38	0.401	0.084	1.53	1.614

So using equation (4.8), we calculated the refractive index of 1.506, while combining equation (4.7) and the derivation of the refractive index $n(\lambda)$ from equation (4.8) leads to the group index of 1.53 for low-iron glass at the wavelengths of 1629.906 nm and 1629.922 nm. In addition, the group

index, denoting the slow-down factor (SDF; Note that the formula for SDF is given in equation (2.27), $S = 1 + (\kappa L)^2/\pi^2$. It represents a relative value, defined as the ratio of the group delay of the grating (τ_g) to that of the waveguide (τ_w), i.e. $S = \tau_g/\tau_w$. Bloch-SDF=3.63, CMT-SDF=1.06), is also proportional to group delay but inversely proportional to group velocity and device length, and the maximum value is always obtained near the band edge, i.e. the falling edge of the transmission spectrum. The corresponding relation among them is given by [2]

$$n_g = \frac{c}{v_g} = \frac{c\tau}{L} \tag{4.9}$$

where $v_g = L/\tau$ is the group velocity, τ is the group delay, c is the light speed of 3×10^8 m/s, and L is the device length of 75 mm for the dot-Bragg grating. Considering the calculated group index for low-iron glass itself, and then substituting it into equation (4.9), it yields the corresponding group delay of 0.38 ns at the wavelengths of 1629.906 nm and 1629.922 nm (Note: These values (GI and GD) are approximately equal to the values of waveguide.). Therefore, the final effective group delay of TM and TE modes is >1.38 ns based on Bloch's theorem, including the group delay of the glass itself, while the corresponding effective group index is > 5.53. The effective group delay based on CMT is 0.401 ns in TM and TE modes, corresponding the effective group index of 1.614, as summarized in Tale 1. It should be noted that in theory, both group delay and group index can become arbitrarily large as the operating frequency approaches the band edge. However, in practice, this leads to several challenges. First, the dispersion becomes extremely strong and highly nonlinear. Second, the system becomes more sensitive to losses and fabrication imperfections due to the enhanced light-matter interaction. Additionally, scattering and absorption may become significant. Therefore, in practical applications, the operating frequency is typically chosen to be near—but not exactly at—the band edge, to balance the benefits of slow light with the limitations imposed by real-world conditions.

4.4 DO-WGs line-Bragg grating

The second-order line-Bragg grating was also written in two steps, i.e. first writing PO-WGs-based waveguides and then writing line gratings. However, for the second-order line-Bragg grating with PO-WGs, we found some small dips near the main resonant dip (Appendix A.6) which might be caused by cladding modes, or higher order modes, or the possible asymmetry of shell-waveguide cells within PO-WGs. Whereas, this problem was tackled by dual-overlapping PO-WGs (DO-WGs,

Figure 4.8(b)), in which the center-to-center distance is reduced to 3 μm to offset the possible asymmetry in PO-WGs while the average RI change is increased to 1.63×10^{-3} (Figure 4.8(d)), bigger than the average RI change of a single PO-WGs (black curve in Figure 4.2(a)). Based on DO-WGs, we ultimately achieved the second-order line-Bragg grating below the glass surface at 55 μm (Figure 4.8(a)) with the following writing parameters: the laser power of 100 mW, the pulse energy of 165 nJ, a single pass with the writing speed of 1 mm/s and a repetition rate of 20.2 kHz. Similar to the dot array inscription, a 100 mW laser power was still utilized for the creation of line gratings in this scenario. This choice not only achieves a superior writing resolution but also prevents the higher power from merely causing the emergence of an additional and larger-sized waveguide alongside the existing PO-WGs, without inducing any resonance.

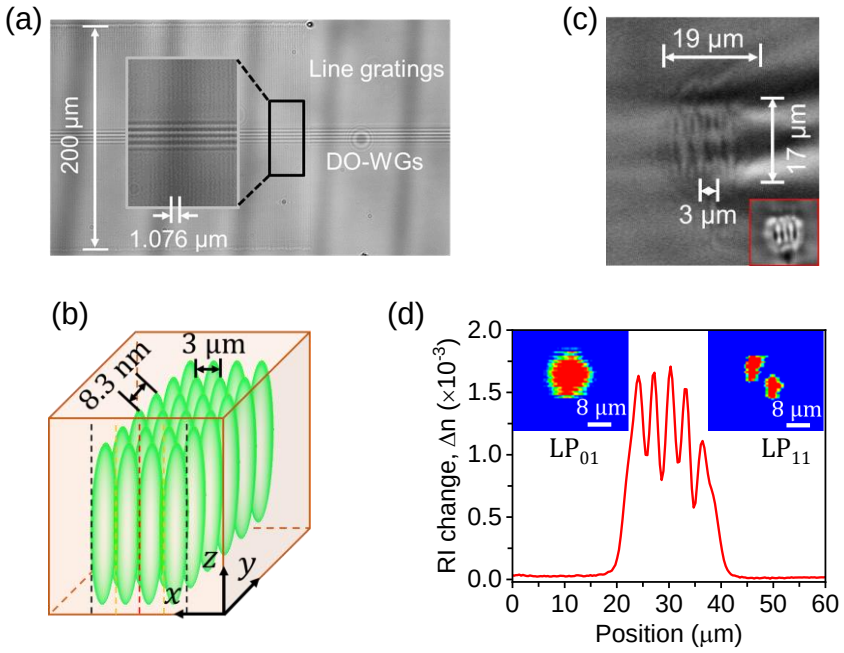

Figure 4.8 Line-Bragg grating. (a) Overhead view. (b) Schematic diagram of DO-WGs but the marked dimensions are not to scale. (c) RI change with the insets showing LP_{01} and LP_{11} mode near field at the 1550 nm wavelength. (d) Side view. (The inset in the red box shows the light guided position measured by white light). The writing laser was incident from the top.

4.4.1 RI change of DO-WGs in line-Bragg grating

Figure 4.8(d) shows RI change of DO-WGs with a maximum RI change of 1.71×10^{-3} while the light will propagate along the peak positions with an average RI change of 1.63×10^{-3}. Furthermore, the three overlapping regions among the four ellipsoid units (Figure 4.8(b)) also

should have the similar RI change with the average value of 1.63×10^{-3}, which indicates that the overlapping parts are induced by FSL direct writing with a similar and typical heat accumulation writing mechanism.

The mode near field, whose MFD is calculated to be 16 μm by using equation (4.3) with the effective radii of 8.15 μm and 9.2 μm (Figure 4.8(c) and its inset) and V-numbers of 3.26 and 3.68, was measured at 1550 nm wavelength as shown in the insets of Figure 4.8(d), representing that the LP_{01} and LP_{11} modes can be supported by DO-WGs. The two modes also can be confirmed by estimating the V-number to be 3.26 and 3.68, which are all larger than 2.405 but smaller than 3.832 (Appendix A.4). In addition, the MFDs can also measured using the NanoScan (Appendix A.3(d)), with values of 18 μm and 20 μm along the effective radii of 8.15 μm and 9.2 μm, respectively.

A 56% light guiding efficiency for DO-WGs in line-Bragg grating was achieved at 1550 nm using the same measurement method as PO-WGs (55%) in dot-Bragg grating. However, the 1% change seems not to be an actual increase, which is caused by the injected light leakage due to the dimensional mismatch between the fiber and the DO-WGs facet. Besides, the absorption and scattering from the line grating part with 40-mm-long and 200-μm-width might be another reason.

4.4.2 Line-Bragg grating spectra

Figure 9(a) shows the transmission and reflection spectra of the second-order ($m = 2$) line-Bragg grating measured by OSA. A 4.4 dB transmission dip strength (FWHM of 55 pm) centered at 1603.7 nm resonant wavelength is obtained. The line grating part in longitudinal length is 200 μm with a calculated period, Λ, of 1.706 μm by using equation (4.5) and a duty cycle of 50% along the propagation direction, as shown in Figure 4.8(a), where the horizontal length is extend to 40 mm for increasing the transmission dip strength.

The maximum reflectivity, R_{max}, for the line-Bragg grating is calculated to be 0.64 by using equation (4.4), where the coupling coefficient, κ, and the coupling constant, κL, are separately 27 m^{-1} and 1.1. However, there still exist some unexpected side lobes on the short wavelength side in the transmission spectrum (Figure 4.9(a)), which is because we did not use apodization for this grating. Moreover, we observed that this line-Bragg grating can work at LP_{01} (4.4 dB@1603.07 nm) and LP_{11} (2.1 dB@1602.31 nm) modes which are in good agreement with the two modes estimated by V-number calculation (Appendix A.4). Also noticed are the other two transmission

dips which are centered at 1602 nm and 1602.6 nm that might be cladding modes probably produced due to the asymmetry or polarization in the grating. In addition, some side-reflections near the resonant wavelength indicate that this line-Bragg grating shows a higher sensitivity to DO-WGs. Therefore, it still needs to solve the trade-off in this line-Bragg grating between transmission and reflection spectra by further optimizing the writing conditions to increase the transmission strength and reduce the sensitivity of reflection to DO-WGs.

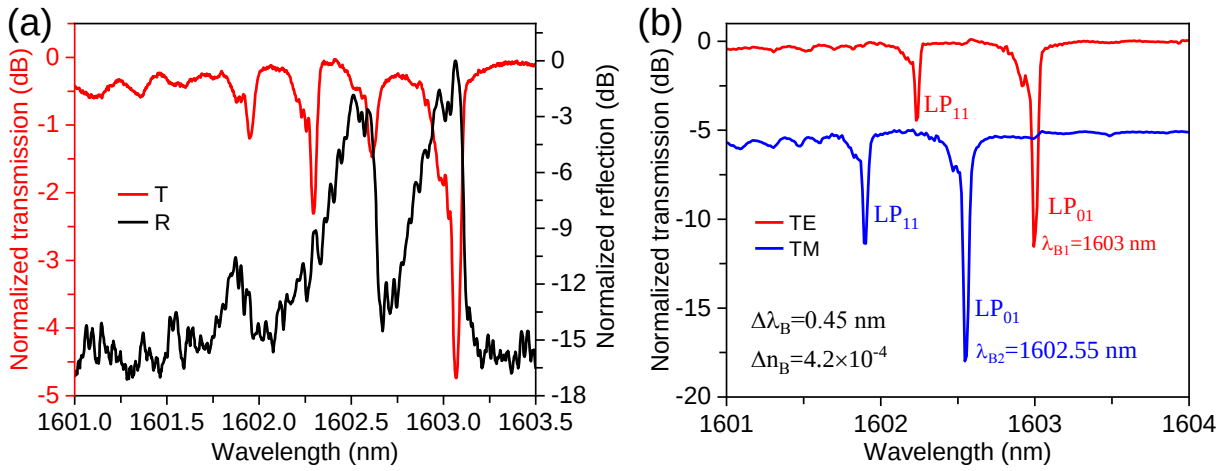

Figure 4.9 Line-Bragg grating. Normalized (a) transmission (T) and reflection (R) spectra measured by OSA. (b) Polarization dependence measured by OBR with different polarization controller shapes. Note: The TE and TM modes correspond to v-pol and h-pol, respectively.

The polarization dependence of the line-Bragg grating was measured by a Luna OBR 4600 with a polarization controller (Appendix A.7), as shown in Figure 4.9(b). The index matching oil was used between the fiber and sample facets to reduce Fresnel and Fabry-Pérot reflections. We observed that this line-Bragg grating has an obvious polarization dependence, which leads to an effective birefringence (Δn_B) value of 4.2×10^{-4} calculated from $m\Delta\lambda = 2\Delta n_B \Lambda$, where m is the grating order with a value of 2, $\Delta\lambda$ is the difference in Bragg wavelengths at TE and TM modes with a value of 0.45 nm, Λ is the grating period of 1.706 μm. Compared with the transmission spectrum with four transmission dips obtained by OSA as shown in Figure 4.9(a), two polarization states (TE and TM) have been observed apparently by OBR as shown in Figure 4.9(b). Each state has two dips, i.e. LP_{01} and LP_{11} modes, which could potentially be implemented in the fields of sensing and filtering [126]. At LP_{01} mode, the maximum dips are 11 dB (TE) and 12.5 dB (TM), corresponding to the κL values of 1.94 and 2.12, which yield SDF values of 1.38 and 1.45, respectively, based on equation (2.27): $S = 1 + (\kappa L)^2/\pi^2$. Furthermore, the two states exhibit a

~5.3 dB difference in transmission dips, which is mainly induced by the strong polarization dependence of line gratings and the birefringence of DO-WGs with respect to its RI change. Besides, the slight difference of refractive index between index matching oil and DO-WGs might produce a tiny cavity, which will affect the output power of the device under test and potentially have an impact on the difference in transmission dips.

4.4.3 Slow-light effect of line-Bragg grating

The slow-light effects (i.e. group delay, group index) in reflection for line-Bragg grating can be calculated by using equation (4.6). Here, the RI change for the line grating cannot be directly measured by "The Ripper^{TM}" owing to the limited resolution, but we can roughly estimate it by writing a single waveguide using the same recipe as written line gratings. Thus, we can get the estimated RI change (Δn) with the order of magnitude of $\sim 10^{-4}$. We assume that the refractive index for line grating stack and the gap are $n_1 = n_{eff} + \Delta n = 1.49 + 10^{-4}$ and $n_2 = n_{eff} - \Delta n = 1.49 - 10^{-4}$, where the widths for them are $d_1 = \lambda/(2n_1)$ and $d_2 = \lambda/(2n_2)$, considering the 50% duty cycle and the period of $\Lambda = d_1 + d_2$. Therefore, the group delay and group index of the L=40 mm line-Bragg grating can be easily obtained using $\tau = L(\partial K/\partial\omega)$ and $n_g = c(\partial K/\partial\omega)$ at the Bragg wavelengths of 1603 nm and 1602.55 nm for TE and TM modes, and also can be calculated by coupled-mode theory (CMT), as shown in Figure 4.10.

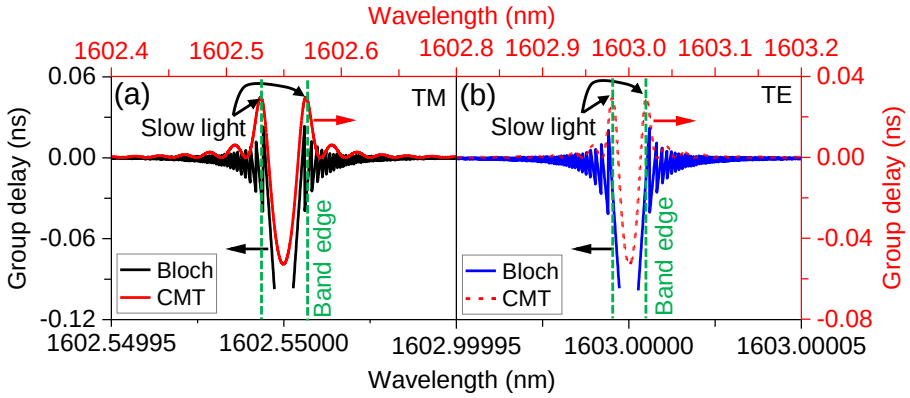

Figure 4.10 Simulated group delay at (a) TM mode (h-pol) and (b) TE mode (v-pol) using Bloch's theorem and coupled-mode theory (CMT) for line-Bragg grating. Note: (1) The group delays of waveguides (~0.2 ns) in the line-Bragg gratings are normalized to zero on the y-axes to simplify the analysis of the slow-light effect. (2) The TE and TM modes correspond to v-pol and h-pol, respectively.

We observed from Figure 4.10 that the group delays of line-Bragg grating are 23 ps (GI: 0.173) for TM and TE modes by Bloch's theorem and 30 ps (GI: 0.225) for CMT, respectively. Additionally, the group index and group delay of glass itself (Note: These values are approximately equal to the values of waveguide.) at the above-mentioned Bragg wavelengths can be calculated to be 1.53 and 0.2 ns (Note: The 0.2 ns is normalized to zero on the y-axis. The Bloch-SDF and CMT-SDF are 1.12 and 1.15, respectively.) by using equation (4.7~4.9). Therefore, the final group delay and group index for the line-Bragg grating in glass, in theory, are 0.223~0.23 ns and 1.703~1.755. Similarly, it is important to observe that the variations in the obtained 'bandgaps' from the two theories is attributed to two different parameters, i.e. bandgap and bandwidth separately calculated by Bloch and CMT (Appendix A.8).

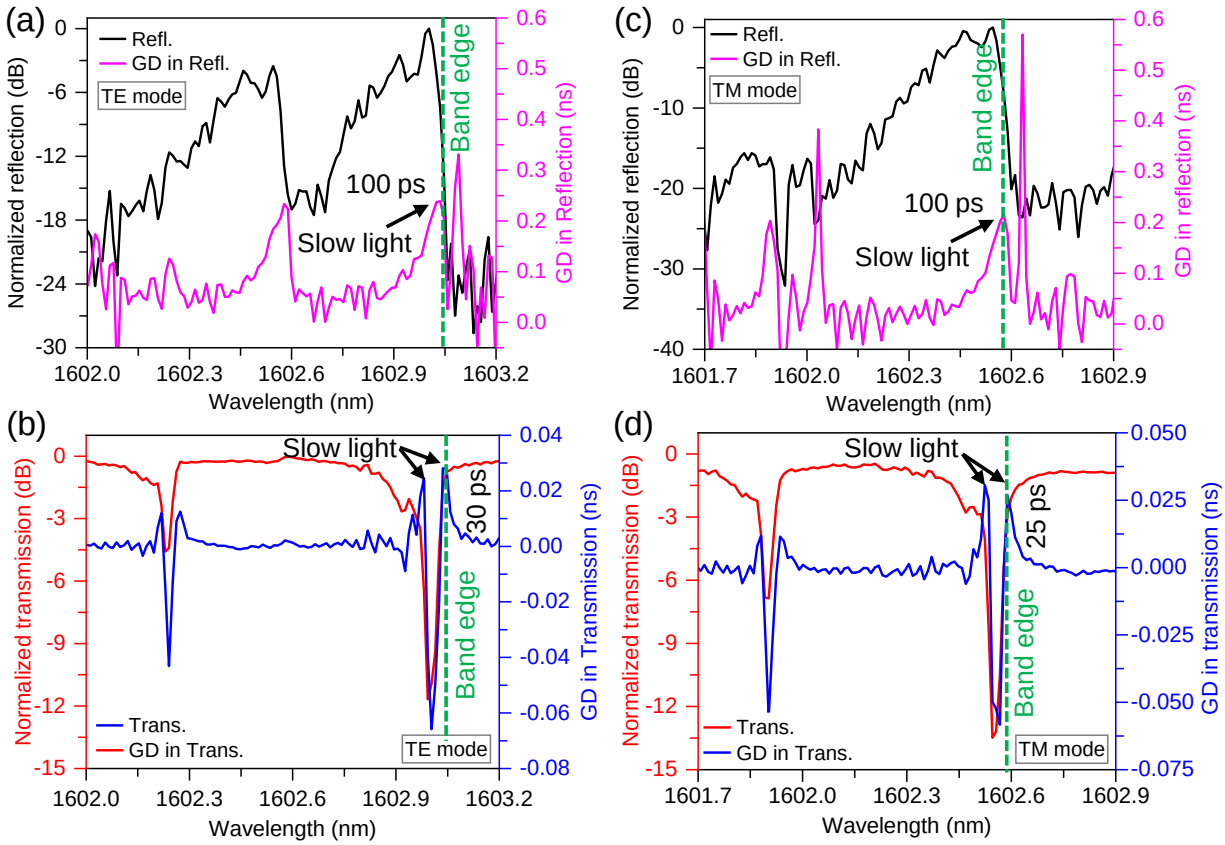

Figure 4.11 The measured normalized reflection (R) and transmission (T) spectra and the normalized group delay (GD) in reflection and transmission by Luna OBR for line-Bragg grating. (a) R and GD in R, and (b) T and GD in T with TE mode (v-pol) at 1603 nm. (c) R and GD in R, and (d) T and GD in T with TM mode (h-pol) at 1602.55 nm. Note: (1) The group delays of waveguides (~103.66 ns for GD in T) in the line-Bragg gratings are normalized to zero on the y-axes to simplify the analysis of the slow-light effect. (2) The TE and TM modes correspond to v-pol and h-pol, respectively.

The slow-light performance in reflection and transmission of the line-Bragg grating was also measured by a Luna OBR 4600 (Appendix A.6). Figure 4.11(a) shows the reflection (R), transmission (T), and group delay in reflection (τ_R) and transmission (τ_T) at TE and TM modes. It needs to be noticed that the reflection and transmission are represented by return loss (i.e. the ratio of output power and input power) in OBR measurements, which is equivalent to the spectra characteristics measured by OSA as shown in Figure 4.9(a). The group delay in reflection with TE mode, $\tau_{R,TE}$, is 0.1 ns at a wavelength of 1603 nm shown in Figure 4.11(a), where it demonstrates an approximate effective value of $0.5\tau_{R,TE}$ (i.e. ~50 ps), due to the reason that using OBR to measure reflection and group delay in reflection is actually a double pass measurement[127], [128]. The group delay in transmission with TE mode, $\tau_{T,TE}$, is as shown in Figure 4.11(b), yielding an approximate value of 30 ps (SDF=1.00029, attributed to the limited resolution of the experimental setup) which here is equivalent to the effective group delay owing to a single pass measurement for transmission and group delay in transmission by using OBR.

Table 4.2 Group delay and group index for line-Bragg grating.

Name	**Effective group delay (GD) (ns)**					**Group index (GI)**				
Modes	GD in R	GD in T	Glass GD	Final GD in R	Final GD in T	GI in R	GI in T	Glass GI	Final GI in R	Final GI in T
TE (1603 nm)	0.1	0.03	0.2	0.3	0.23	0.75	0.225	1.53	2.28	1.755
TM (1602.55 nm)	0.1	0.025	0.2	0.3	0.225	0.75	0.188	1.53	2.28	1.718

Likewise, we observed from Figure 4.11(c) that the group delay in reflection at TM mode, $\tau_{R,TM}$, is 0.1 ns at a wavelength of 1602.55 nm, which produces an approximate effective value of $0.5\tau_{R,TM}$, i.e. ~50 ps. Moreover, the corresponding group delay in transmission at TM mode, $\tau_{T,TM}$, as shown in Figure 4.11(d), presents a value around 25 ps (SDF=1.00024, attributed to the limited resolution of the experimental setup). Comparison of group delay obtained by OBR implies that the value in reflection is approximately twice than that in transmission, no matter what the mode is (Note: this is merely a matter of approximate interpretation). The group index in reflection and transmission for those Bragg wavelengths at TE and TM modes also can be obtained by using equation (4.9) based on the grating length, L, and the measured group delays. In addition, we still

consider the group delay and group index of the glass itself with the values of 0.2 ns and 1.53, while all of the values are summarized in Table 4.2.

We observed from Table 4.2 that the effective group delay (and group index) in reflection accords closely with the values in transmission at TE mode, while they also agree well for TM mode. It should be noted that the small group delay and group index could be based on the following reasons: (1) The small RI change. (2) The single writing pass for gratings. (3) The length of gratings along the guiding direction. (4) Loss during measurements. Correspondingly, we will further improve writing parameters of the femtosecond laser to write and fabricate with etching for Bragg gratings with higher group index in the future.

Therefore, the final effective group delay at TM and TE modes, in theory, is 0.23 ns while the corresponding effective group index is 1.76, including the group index of the glass, which agree very well with the experimental values.

4.5 Conclusion

We have proposed dot- and line-Bragg gratings in low-iron bulk glass with the length of 75 mm by femtosecond laser direct-writing schemes integrated separately with new parallel partially-overlapping waveguides (PO-WGs) model and dual PO-WGs (DO-WGs) expand these terms here in the conclusion. A detailed discussion for the evolution process of PO-WGs and RI change characterization is provided in this paper. Based on parallel overlapping, the PO-WGs achieve better light guiding efficiency, higher RI change of and 0.2 dB/cm propagation loss with up to 15 mm/s writing speed and 0.3 dB/cm at 20 mm/s. With PO-WGs, the periodic dot array in the dot-Bragg grating was realized at a writing speed of 3 mm/s, which demonstrated a weak dip strength and a narrow bandwidth. For line-Bragg grating, a writing speed of 1 mm/s for line gratings was adopted to integrate it with DO-WGs, where a 4.4 dB dip strength and 55 pm bandwidth were achieved. The polarization dependence of the two Bragg gratings is discussed demonstrating a large effective birefringence value of 4.2×10^{-4} for the line-Bragg grating. The slow-light generation by the dot-Bragg grating was discussed by a one-dimensional periodic medium model showing group delays of 0.4 ns and >1.38 ns using CMT and Bloch theories, respectively, corresponding to group indices of 1.614 and >5.53. The slow-light effect for the line-Bragg grating was measured by Luna OBR and theoretically analyzed, presenting a group delay of 0.23 ns, i.e. a group index of 1.76 under the weak transmission dip strength, which agrees very well with the

theoretical calculation. This value is already significant in increasing the transit time by more than a factor of 2 through the glass. Such weak dip strength of grating could be improved by chemical etching and writing parameters, while the grating dispersion can be used to create slow-wave structures to achieve high-efficiency light-matter interaction and optical applications.

4.6 Funding

This work was funded by the Natural Sciences and Engineering Research Council of Canada (NSERC), through the New Frontiers in Research Funding Fund (NFRF) with project number NFRFE-2020-00355.

4.7 Acknowledgments

The authors thank Dr. Frédéric Monet for the technical support with OBR measurements, Foroogh Jafari for the assistance with femtosecond laser writing, Dr. Louis-Philippe Carignan for cutting the sample by diamond saw, and their fruitful discussions.

4.8 Author contributions

Q.C. performed the optical characterization, including device polishing, experimental platform setup, measurements, data analysis, manuscript writing and revisions, as well as conducting the literature review. J.-S.B. and Q.C. collaborated on the Bragg grating inscription using FSL. R.K. and M.S. led the research and secured the funding. All authors contributed to the manuscript by providing feedback and comments.

This chapter covers Objectives 1 and 2.

CHAPTER 5 ARTICLE 2: OFFSET-ENHANCED SLOW LIGHT IN FEMTOSECOND LASER-FABRICATED BRAGG GRATINGS

Qingtao Chen, Jean-Sébastien Boisvert, Foroogh Jafari, Mohammad S. Sharawi, Sébastien Loranger, and Raman Kashyap

Published in: Optics Express

Publication date: Oct. 14, 2024

This article has been published in Optics Express (*Opt. Express*, vol. 32, no. 22, pp. 39257–39266, Oct. 2024, doi: 10.1364/OE.537736; Publication date: Oct. 14, 2024) and titled **"Offset-enhanced slow light in femtosecond laser-fabricated Bragg gratings"**. The article investigates enhancing slow-light effect in single-laser-pass waveguide (SLPWG) line-Bragg gratings through offset engineering. It derives a formula for the slow-down factor (SDF), allowing evaluation of slow-light effect in any Bragg grating using only the coupling constant. By optimizing the writing parameters in SLPWG, the issues of loss and side lobes observed in the line-Bragg grating observed in Article 1 were addressed. This was achieved by shortening the grating length perpendicular to the light-guiding direction and introducing offsets between the line gratings and the SLPWG. These improvements enabled the line-Bragg grating to exhibit both a narrow, deep transmission dip and an enhanced SDF, effectively mitigating side-lobe effects. The supplement of this article is given in Appendix B of this thesis.

Abstract: We report a strength-enhanced waveguide second-order line-Bragg grating (WLBG) directly written with femtosecond laser in bulk glass by using "offset" to exploit the slow-light effect. This design eschews the use of multiple waveguides and/or waveguide bundles for light guiding. Instead, it only employs a single-laser-pass waveguide (SLPWG) with a refractive index change of 1.1×10^{-3}, to achieve effective light propagation. The SLPWG is first written as a core-shell ellipsoid unit by a single-laser pass. Subsequently, a line-grating is written on top, with an offset to accommodate for the already modified refractive index from the waveguide along the vertical direction of different offset values 0 μm, 5 μm, 10 μm, and 15 μm. The enhanced slow-light effect for WLBG is studied theoretically and experimentally. Optimal performance occurs at

a 10 μm offset, exhibiting a maximum group delay of 35 ps and a derived slow-down factor (SDF) of up to 1.54, with a 12.5 dB transmission dip and a propagation loss of 1.16 dB/cm, in vertical polarization. The experimental SDF results demonstrate the potential of our design for future applications in creating slow-wave structures via grating dispersion for compact photonic integrated devices, applying it to microfluid devices that can increase the light-liquid interaction path for the detection of refractive index change caused by variations in fluid concentration and composition, directly incorporating it into the hardened glass of cellphone screens for embedded sensors, as well as integrating it into optical antennas within smart glass windows that can enhance light-matter interactions for enabling real-time monitoring of environmental changes and improving wireless communications.

5.1 Introduction

The development of photonic integrated circuit (PIC) components with small device footprints, high data-rate transmission, and large-capacity data storage, created in transparent materials, is a challenging goal in the current communication system [1]. Slow light is a good candidate for optical signals and optical energy compression, providing an opportunity for reducing device size and enhancing light-matter interactions [4]. Until now, a substantial periodic photonic structures [5], such as fiber-based Bragg gratings [22], [90], [129]–[132], Si-based waveguide Bragg gratings [21], [133], and planar photonic crystal waveguides [4], [134], have been used to generate slow light for further applications in optical nonlinearities, optical switching, quantum optics, optical storage, and on-chip integration [135]. Si-based and photonic crystal slow-light devices typically require complex photolithography techniques in the clean room. In contrast, the fiber-based and glass-based Bragg gratings are written by a femtosecond laser (FSL) which is lower in cost, faster, and easier to fabricate. The slow-light effects of fiber-based Bragg gratings have been reported by several researchers [22], [90], [129]–[132], but the slow-light effects on glass-based Bragg gratings, to the best of our knowledge, are only presented by our previous work [42]. Therefore, it is essential to further study the slow-light enhanced effect of Bragg gratings in bulk glass. This also will enable gratings with a higher group index to further enhance light-matter interactions. Such research could pave the way for the next generation of highly integrated PIC components in optics communication systems.

In this work, we report the fabrication and analysis of slow-light effect of an FSL-written waveguide line-Bragg grating (WLBG) with four different offsets (0 μm, 5 μm, 10 μm, and 15 μm) between the waveguide and line grating in bulk glass. The waveguide is written only with a single pass. The offset method between the grating and the waveguide is used to alleviate the issue of the already-femtosecond-laser-exposed area caused by the previous waveguide inscription. The enhanced slow-light effect is due to the offsets. Among them, a 10 μm offset produces the highest group delay of 35 ps, with a slow-down factor (SDF) of 1.0003 directly obtained from the measured group delay (GD), and the value of 1.54 derived from the coupling constant based on the measurements.

5.2 Principle of enhanced slow-light effect

The basic principle for the enhanced slow-light effect is shown in Figure 5.1, which is calculated using coupled-mode theory [46] and is representing by SDF. The SDF, S, is the ratio of grating group delay (τ_g) with the normal expected group delay of propagation in the same length without a grating, τ_w, i.e., $S = \tau_g/\tau_w = \tau_g c/(Ln_w)$, where c is the speed of light, L is the grating length and n_w is the group index of the waveguide. The transmission spectra of uniform Bragg gratings with coupling constants $\kappa L = 2$ and $\kappa L = 7$ are depicted in Figures 5.1(a, c). It can be found that the larger κL, the bigger transmission dip and wider is the stop band. Here, κ is denoted as the ac coupling coefficient with values of 40 m^{-1} and 140 m^{-1} for Figures 5.1(a, c), while L is the grating length of 50 mm.

Figures 5.1(b, d) show the S profiles, in which the magenta parts represent the slow-light regions. The two slow-light regions, symmetrically disposed around the central Bragg resonant wavelength of 1550 nm, are the results of the multiple back-and-forth coherent reflections of the incident light. This process leads to a decrease in the group velocity, generating slow light, also known as slow-light effect. As can be noted in Figures 5.1(b, d), a higher κL value leads to a higher SDF (S~3.55 in Figure 5.1(d) vs. S~1.22 in Figure 5.1(b)), but comes with a sacrifice in effective bandwidth, as the corresponding full width at half maximum (FWHM) of the SDF goes from 287 MHz (Figure 5.1(d)) to 749 MHz (Figure 5.1(b)).

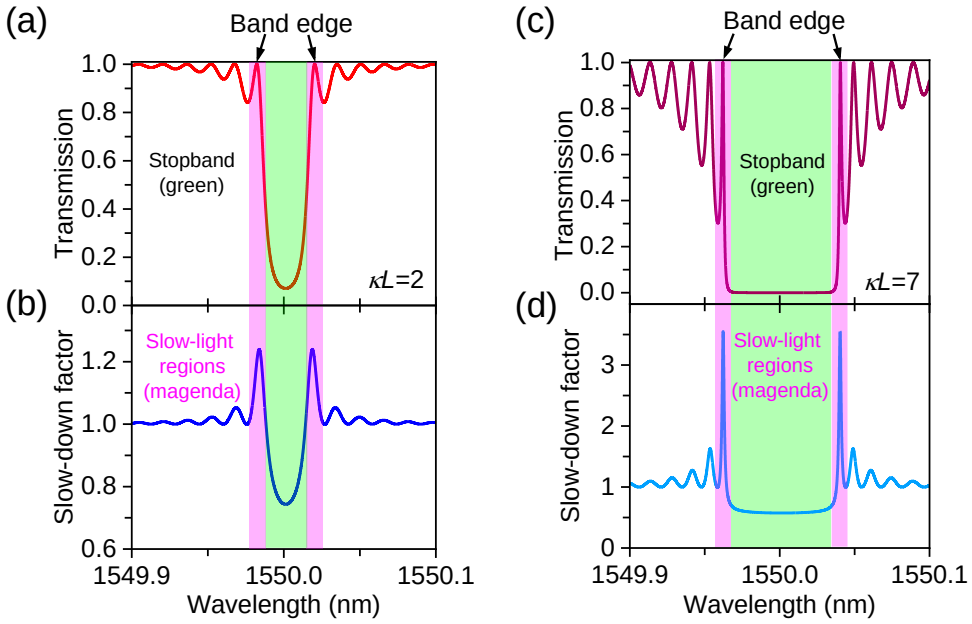

Figure 5.1 Principle of enhanced slow-light effect for uniform Bragg gratings. The transmission spectra and SDFs at coupling constants of (a) $\kappa L = 2$ and (b) $\kappa L = 7$. Note that the stop-band (in green) is not considered a usable region due to the high insertion loss.

5.3 Models and fabrication

Based on the principle of the enhanced slow-light effect, we exploit the "offset" between the waveguide and line gratings to increase the transmission dip. This also achieves a larger slow-down factor for more light-matter interactions. The designed waveguide line-Bragg grating (WLBG) and the single-laser-pass waveguide (SLPWG) models are shown in Figure 5.2. Using the same laser writing system [42], [108], the WLBG is written using a Pharos femtosecond laser (FSL) (wavelength 1030 nm, pulse duration 250 fs) with a frequency doubled to 515 nm by an Orpheus optical parametric amplifier (OPA). Other calibrating parameters during the whole fabrication process are shown below Figure 5.2(e). Additionally, an Aerotech 3000 precision stage with three-axis is used for translating samples relative to the focused laser beam.

The 75 mm long low-iron soda-lime glass (Fisherbrand, 75 mm length×25 mm width ×1 mm height, Catalog No.: 12-550-A3), offers exceptional transparency and cost-effectiveness, ideal for writing the WLBGs. The long glass substrate ensures precise writing of the waveguide and long-periodic line grating, while also minimizing most of the leaky modes excited at the light incident during measurements. What needs to be noted is that, unlike previous method [42], [63], [136] which involved two or four passes [42], or multi-passes [63], [136] for waveguide writing, the current

approach mainly employs single-laser-pass writing for each ellipsoid unit along the light guiding direction (y-axis), as depicted in Figure 5.2(e). Meanwhile, the length of each line of the grating is reduced from the previous 200 μm [42] to the current 15 μm (Figure 5.2(e)), while the total extent of the line grating along the light guiding direction (y-axis) is increased by 10 mm, i.e. from 40 mm [42] to 50 mm (Figure 5.2(e)). The ~×13 reduction in the grating line-length significantly decreases the inscription time for the line grating from approximately 3 hours to about 1.5 hours, while the increased grating-length along the y-axis boosts the transmission dip strength from 11 dB [42] to 12.5 dB, resulting in a derived SDF of 1.54.

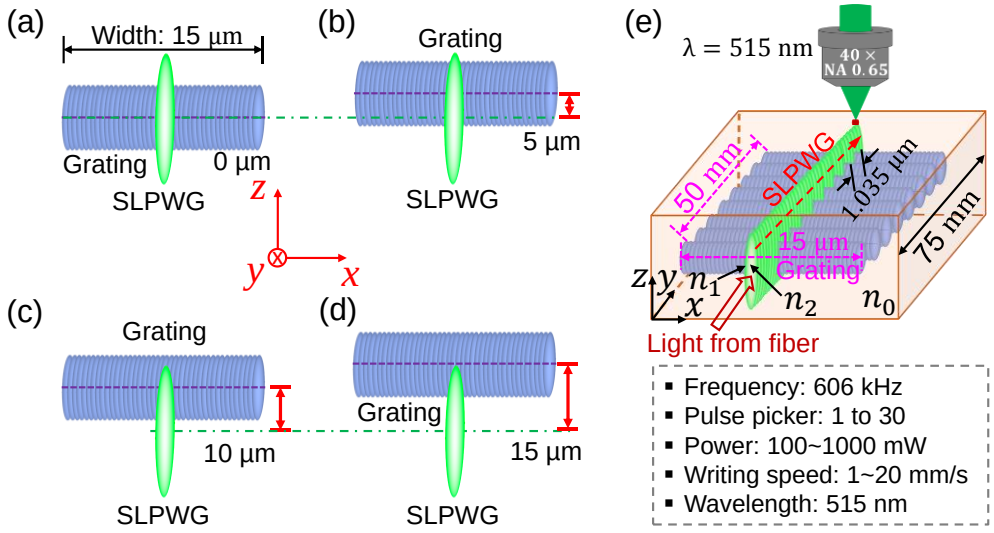

Figure 5.2 (a)~(d) Schematic diagrams of the WLBG cross-section showing four different offsets (0 μm, 5 μm, 10 μm and 15 μm) along the Z-direction between the SPLWG and line gratings. Note that overlaps exist between ellipsoidal units of both the single line grating along x-axis and the SLPWG along y-axis. (e) 3D schematic of the WLBG (0 μm offset), which includes a 75 mm long "continuous" SLPWG, line-Bragg gratings (Aspect ratio: 50 mm length × 15 μm width) with grating periods of 1.035 μm along the y-axis, and the writing parameters of the FSL. Here, n_0, n_1, and n_2 denote the refractive indices of the glass substrate, shell regions, and core regions, respectively. Note: The marked values and actual sizes are not to scale.

Two steps are employed for the WLBG fabrication, with the best recipe considering effective light guiding efficiency: (1) Inscribe a 75 mm long SLPWG below the glass surface (~118 μm), with writing parameters of 500 mW laser power, 101 kHz repetition rate selected with a pulse picker, 1 mm/s writing speed, and a numerical aperture (NA) of 0.65 for a microscope objective. (2) Inscribe a second-order (m=2) line-Bragg grating (Aspect ratio: 50 mm length × 15 μm width) with 100 mW laser power, 20.2 kHz repetition rate selected with a pulse picker, 1 mm/s writing speed, duty

cycle of 50%, grating period, Λ of 1.035 µm calculated by Bragg conditions [45]. Offset adjustments of the writing lens along the Z-direction were tested at 0 µm, 5 µm, 10 µm, and 15 µm, as shown in Figures 5.2(a~d).

5.4 Results and discussion

The refractive index (RI) change, Δn, of the ellipsoid core of the SLPWG achieves a peak of 1.1×10^{-3}, as shown in Figure 5.3(a), which is measured by "The Ripper™" from PhotoNova Inc. [110] and calculated using $\Delta n = \Delta\phi\lambda/(2\pi h)$. The $\Delta\phi$ is the phase change, h is the effective affected height, and λ is the measurement wavelength of 632 nm. It is important to note that we can utilize SLPWG with a larger RI change; however, the primary concern is that the larger RI change could cause greater scattering and absorption of the light, ultimately reducing overall transmission efficiency. Therefore, we must ensure that the RI change of the SLPWG is not saturated and maintains good light-guiding efficiency, which is essential for grating inscription. Figure 5.3(b) shows the light guiding profile (Side view of the xz cross-section as shown in Figure 5.3(c)) measured by the white light, where the effective part appears like an oval-shaped and transits most of the light. The operating modes of the SLPWG can be estimated using V-number, indicating that the single mode is supported along the radii of r_1 and r_2 directions (Appendix B.1) if only considering the effective light guiding position. Figure 5.3(c) illustrates the top view of WLBG with 0 µm offset, consisting of a "continuous" SLPWG and line gratings with a periodicity of 1.035 µm.

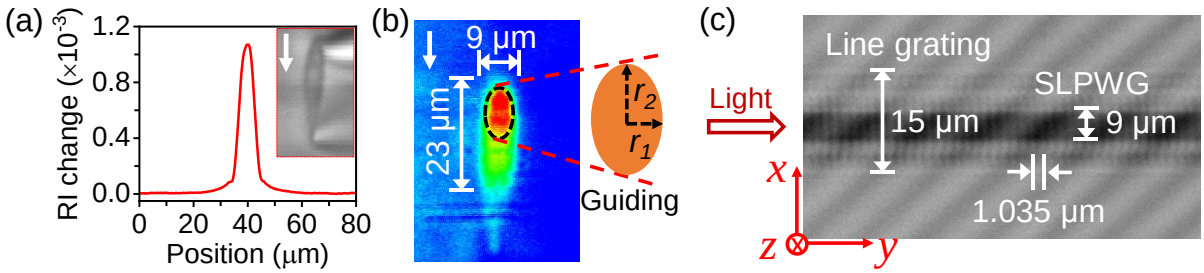

Figure 5.3 (a) The average RI change over waveguide height of the SLPWG. The inset shows the side view of SLPWG while the writing laser was incident from the top denoted by a white arrow. (b) The side view of SLPWG with an approximately oval-shaped light guided position measured by white light. The inset shows the effective enlarged light guiding position with the radii of r_1 and r_2. (c) The top view of WLBG consisting of a continuous SLPWG and line gratings. Note that the fringes are measurement artefact.

The transmission (T), reflection (R) spectra, and group delays (GDs) of WLBG with four offsets are measured by Luna OBR 4600 with a polarization controller (Appendix B.2). Index matching oil is used to reduce the reflections between the fiber and the facets of the sample. The spectra reveal that the fundamental resonant wavelengths of our WLBGs are all centered around 1550 nm. Hence, our analysis mainly focuses on examining the transmission spectra and their corresponding GDs in transmission (Appendix B.2).

Meanwhile, transmission dips are seriously affected by offset values, occurring for GDs as well. At a 0 μm offset (Figure 5.2(a)), the WLBG exhibits a mere 1 dB transmission dip, attributed to the overlaps between the SLPWG and line gratings, causing RI saturation in the previously written waveguide. By offsetting the values to 5 μm, 10 μm, and 15 μm, as depicted separately in Figures 5.2(b~d), both transmission dips and GDs undergo gradual changes. Optimal performance is observed at a 10 μm offset, as demonstrated in Figure 5.4. The transmission spectra are seen to shift (Figures 5.4(a, c)) in good qualitative agreement with the shifts occurring for GDs (Figures 5.4(b, d)).

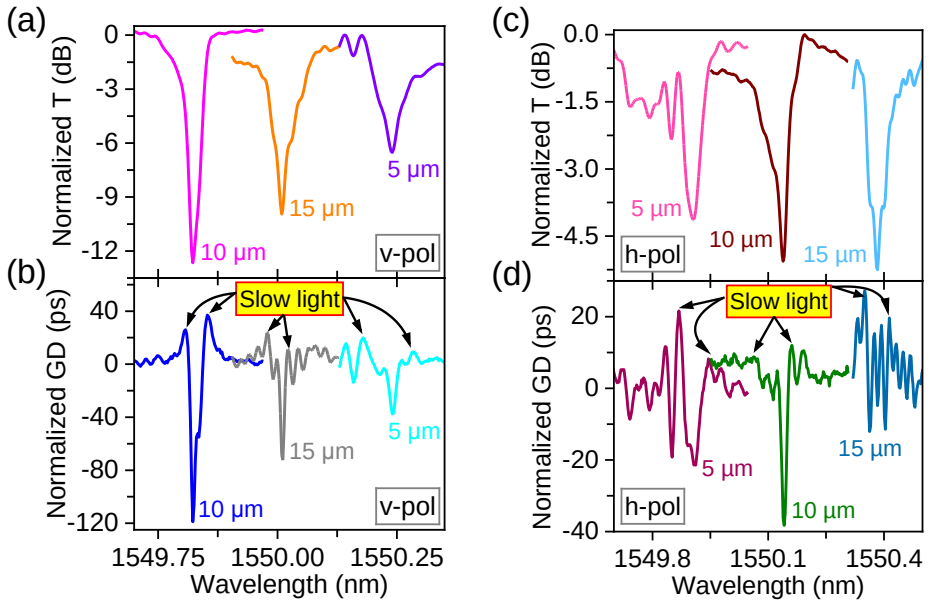

Figure 5.4 The measured transmission (T) spectra and GDs in T for WLBG at 5 μm, 10 μm, and 15 μm offsets. In v-polarization, the normalized transmission spectra (a) and GDs (b), whereas (c) and (d) display the normalized transmission spectra and GDs in horizontal polarization (h-polarization). Note that the slow-light regions are marked in (b) and (d), where the GDs of the SLPWG in WLBG are normalized to zero on the y-axes in order to better analyze the slow-light effect of the grating.

For vertical polarization (v-polarization), at offsets of 5 μm, 10 μm, and 15 μm, the measured transmission dips are separately 5.8 dB, 12.5 dB, and 8.6 dB, as shown in Figure 5.4(a). These dips are centered at resonant wavelengths of 1550.24 nm, 1549.83 nm, and 1550.01 nm. As can be seen from Figure 5.4(b) marked with arrows, at each resonant wavelength, there are two symmetric GD (i.e. pulse delays) peaks appearing at the band edges. The corresponding GD values on the left/right for the above-mentioned resonant wavelengths (i.e. 1550.24 nm, 1549.83 nm, and 1550.01 nm) are approximately 20 ps /9 ps, 24 ps /35 ps, and 22 ps /11 ps, respectively. For horizontal polarization (h-polarization), at offsets of 5 μm, 10 μm, and 15 μm, the measured transmission dips are 3.1 dB, 4.6 dB, and 4.7 dB, as depicted in Figure 5.4(c), with the resonant wavelengths of 1549.91 nm, 1550.15 nm, and 1550.38 nm, respectively. Adjacent to those resonant wavelengths, as depicted in Figure 5.4(d), the yielding peak GDs on the left/right are roughly 20 ps /8 ps, 8 ps /11 ps, and 27 ps /19 ps, also arising at the band edges but accompanied by more fluctuations. Note that the phase fluctuation in h-polarization is slightly stronger than in v-polarization. Those facts demonstrate the slow-light effects occur at the band edges, with the best effect emerging at the 10 μm offset in the v-polarization.

The performance of the WLBG is notably superior in v-polarization compared to h-polarization, indicating a higher sensitivity to v-polarization regardless of transmission dips and GDs. Importantly, GDs at a 10 μm offset exhibits larger values than those at 5 μm and 15 μm offsets, independent of v- and h-polarizations. The choice of offset is a compromise between 1) overlap between grating and SLPWG (closer the better); and 2) writing resolution limitation from the exposure lines overlapping with one another causing a loss in periodicity, hence offsetting the line allows interaction with the finer tip of the exposition which is better resolved. Therefore, the 10 μm offset exhibits a reasonable value and plays a pivotal role in transmission spectra and GDs, as will be discussed later, revealing an enhanced slow-light effect with a larger SDF.

The transmission and reflection spectra in v- and h-polarizations for WLBG with the offset of 10 μm measured by the Luna OBR 4600, is shown in Figure 5.5. As can be seen the WLBG achieves a distinct 12.5 dB transmission dip, centered at 1549.83 nm in v-polarization (Figure 5.5(a)). On the other hand, in h-polarization (Figure 5.5(b)), a 4.6 dB transmission dip is obtained at 1550.15 nm. Additionally, equally spaced sideband resonances around the fundamental resonance wavelength are observed, potentially resulting from the phase or amplitude of the grating RI change that is modulated periodically [137]. The complex spectra observed in reflection is caused by the

grating incoherent component scattering (phase noise of the grating) and potentially from a contribution of higher-order modes.

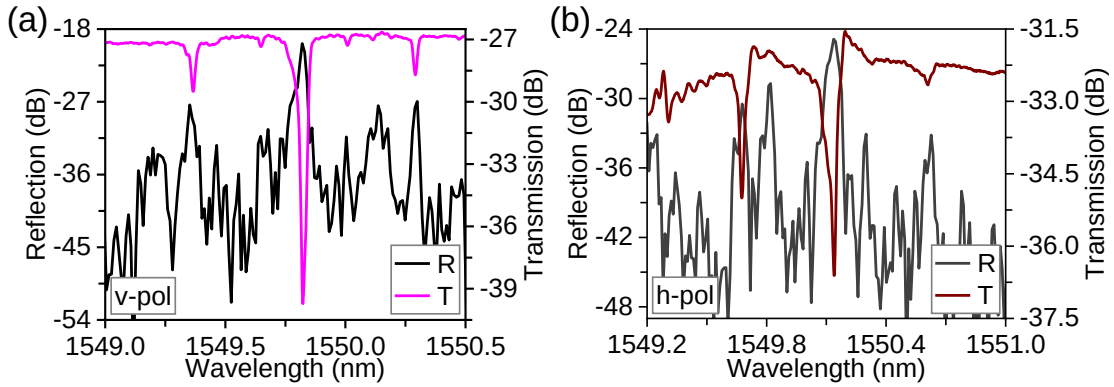

Figure 5.5 The measured transmission and reflection spectra of WLBG at a 10 μm offset are shown in (a) for v-polarization and (b) for h-polarization.

The Bragg condition [45] is described by

$$m\lambda_B = 2n_{\text{eff}}\Lambda \tag{5.1}$$

where λ_B is the Bragg wavelength, m is the grating order of 2, n_{eff} is the effective refractive index of 1.497 calculated using writing parameters of FSL, Λ is the grating period of 1.035 μm. Considering equation (5.1), we can get $m\Delta\lambda = 2\Delta n_{\text{B}}\Lambda$, where $\Delta\lambda$ is the difference in Bragg wavelengths of the two polarizations, Δn_{B} is the effective birefringence. The Bragg wavelength difference of 35 pm between v- and h-polarizations, with the Bragg wavelengths of 1549.83 nm and 1550.15 nm for the two polarizations, corresponds to an effective birefringence of 3.4×10^{-4}.

Figure 5.6 shows the transmission spectra (Figures 5.6(a) and 6(c)) and GDs in transmission (Figures 5.6(b) and 6(d)) for v- and h-polarizations with a 10 μm offset. For v-polarization, the GD exhibits an enhanced difference due to the reasonable offset of 10 μm, as shown in Figure 5.6(b). Near the band edges, the absolute value of the GD is approximately 143 ps, symmetric around 1549.83 nm. The scattering losses are also enhanced because of the slow-light propagation as the mode frequencies approach the band edges [138]–[140]. This may result in the GD peak asymmetry, as shown in Figure 5.6(b). The left and right GD peaks are centered at 1549.81 nm and 1549.86 nm, respectively. These peaks achieve approximately a -119 ps time advance and about 24 ps and 35 ps time delays. This indicates the appearance of both fast light and slow light. Additionally, the

FWHM bandwidth of the resonance at 1549.83 nm is 2.7 GHz, leading to a time-bandwidth product of 0.39 and 0.42 for the left and right GD peaks, respectively.

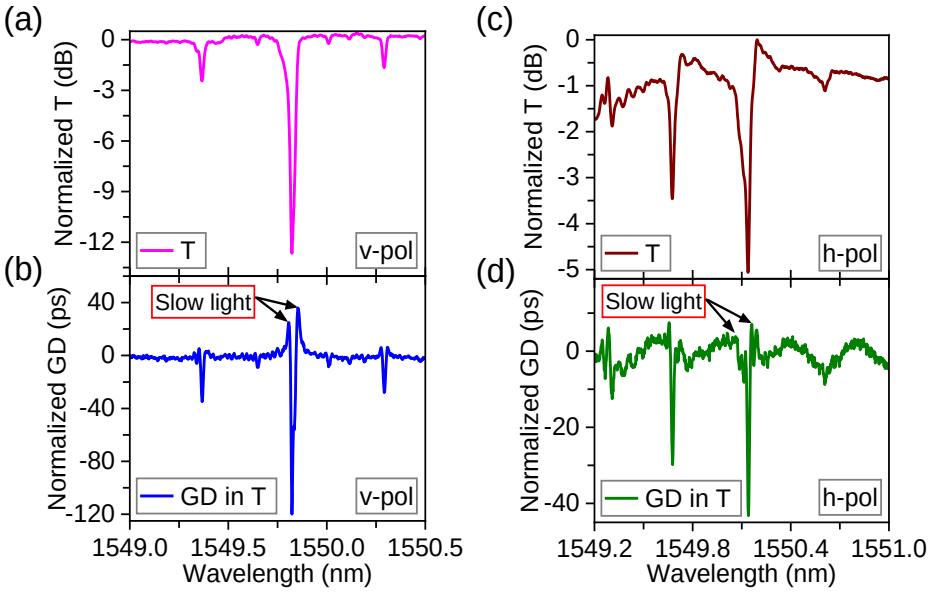

Figure 5.6 The measured transmission (T) spectra and GDs in T for WLBG at a 10 μm offset. In v-polarization, (a) displays the normalized transmission and (b) shows the normalized GD. In h-polarization, (c) presents the normalized transmission and (d) illustrates the normalized GD. Note that the slow-light regions are marked in (b) and (d), where the GDs of the SLPWG in WLBG are normalized to zero on the y-axes for a clearer analysis of the slow-light effect of the grating.

In h-polarization, the transmission and GD in transmission of the WLBG, as shown in Figures 5.6(c, d), are relatively smaller than in v-polarization. This is mainly caused by the lower strength of grating (κL), leading to weaker coupling between the forward and backward propagating modes. As a result, the reflection is weaker, resulting in a shallower transmission dip (Figure 5.6(c)). Consequently, this causes a smaller phase shift and thus a smaller group delay (Figure 5.6(d)). Therefore, the slow-light effect, represented as group delay in Figure 5.6(d), exhibits approximately an 8 ps time delay and a -40 ps time advance near the band edges. Moreover, a 2 GHz FWHM bandwidth of the resonance at 1550.15 nm is achieved, exhibiting a time-bandwidth product of 0.096 for both GD peaks. In addition, compared to the slow-light regions shown in Figures 5.6(b) and 5.6(d), the shape in v-polarization is relatively perfect shapes, while the imperfect shape in h-polarization are primarily influenced by κL.

The coupled-mode theory (CMT) is used to delve into the slow-light effects of the WLBG in v- and h-polarizations. Firstly, the maximum reflectivity, R_{max}, of the WLBG is calculated using equation (5.2), referring to the transmission dip strength, T, in unit of dB [45].

$$R_{max} = |\rho|^2 = 1 - 10^{-\frac{T}{10}} = \tanh^2(\kappa L) \tag{5.2}$$

where ρ and $|\rho|^2$ are the amplitude and power reflection coefficients, respectively. Herein, we can calculate the R_{max}, κ, and κL with the values of 94%, 42.4 m^{-1}, and 2.12 for a 50 mm long WLBG in v-polarization. Similarly, the values of 65%, 22.4 m^{-1}, and 1.12 are achieved for the same length WLBG in h-polarization. Therefore, the grating GDs, τ_g, can be calculated using the derivative of the phase, θ_t, derived from the amplitude transmission coefficient t, and described as [46]

$$\tau_g = -\frac{\lambda^2}{2\pi c}\frac{d\theta_t}{d\lambda} \tag{5.3}$$

Considering

$$t = \frac{\alpha}{\alpha\cosh(\alpha L) - i\hat{\sigma}\sinh(\alpha L)} \tag{5.4}$$

with $\alpha = \sqrt{\kappa^2 - \hat{\sigma}^2}$ the effective coupling coefficient and $\hat{\sigma} = \beta - \beta_B$, the phase-matching condition. The phase can then be extracted as:

$$\theta_t = \mathrm{atan}\left(\frac{\hat{\sigma}}{\alpha}\tanh(\alpha L)\right) \tag{5.5}$$

By combining equations (5.3) and (5.5), and evaluating at the peak delay which happens at $\alpha = i\pi$, for $\beta = \pm L^{-1}\sqrt{\pi^2 + (\kappa L)^2}$, the group delay is calculated as (Appendix B.3)

$$\tau_g \approx \frac{L}{v_w}\left(1 + \frac{(\kappa L)^2}{\pi^2}\right) \tag{5.6}$$

Using the definition of SDF, $S = \tau_g/\tau_w$, we have

$$S = 1 + \frac{(\kappa L)^2}{\pi^2} \tag{5.7}$$

where $\tau_w = L/v_w$ and v_w are the group delay and group velocity of the waveguide, respectively. It is clear that slow-down factor is a monotonically increasing function of κL. A larger κL results

in a stronger grating, leading to increased group delay and group index. Using CMT, the GDs can be calculated, and then the group index (GI), denoted as n_g, using the derived equation $n_g = c\tau_g/L$.

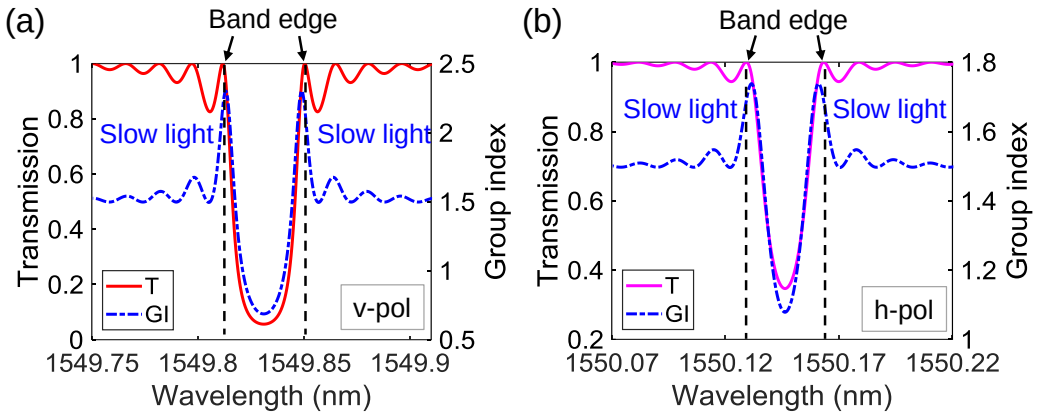

Figure 5.7 The calculated transmission spectra and group index at a 10 μm offset, are derived using the coupling constants (κL) obtained from the transmission measurements. In (a) for v-polarization with $\kappa L = 2.12$ and (b) for h-polarization with $\kappa L = 1.12$. Note that the slow-light regions are marked close to the band edges.

Figure 5.7 shows the transmission and GI for WLBG at a 10 μm offset in both v- and h-polarizations. As shown in Figure 5.7, close to the band edges, a slow-light effect emerges, symmetrically distributed with the resonant wavelengths. The maximum GIs near the band edges for v- and h-polarizations are approximately 2.3 (Blue curve in Figure 5.7(a)) and 1.7 (Blue curve in Figure 5.7(b)), respectively, which are derived using the coupling constants based on the measurement. It is worth noting that the GI at the edges of plot is 1.5 (Blue curves in Figures 5.7(a, b)), which is the GI of the waveguide without grating.

The SDF is employed to further compare the slow-light effects for WLGB with a 10 μm offset. The derived SDFs based on the GD measurements (GDs without normalization) and the GIs (Blue curves in Figure 5.7) are depicted in Figures 5.8 (a, b) for v- and h-polarizations, respectively. For v-polarization, the SDFs is 1.0003 derived from the measurement and the calculated value is 1.54, while the values for h-polarization are approximately 1.0001 and 1.16, respectively. Using equation (5.7), the CMT-estimated SDFs are separately 1.45 and 1.13 for v- and h-polarizations, with κL values of 2.12 and 1.12. These estimated results agree well with the calculation in Figure 5.7. The lower experimental SDFs are mainly due to the imperfectly implemented grating and the lower resolution during measurements, which results in phase fluctuations. Moreover, they might be ascribed to multiple losses during the WLBG fabrication by FSL direct-writing, in which the

measured propagation losses by OBR are roughly 1.16 dB/cm and 0.83 dB/cm for v- and h-polarizations, respectively. In addition, multiple reflections at the interfaces of fiber-sample facets (even using index matching oil), and system noise or losses (such as in connectors or the bent optical fibers) during measurement also could contribute to the SDF reduction.

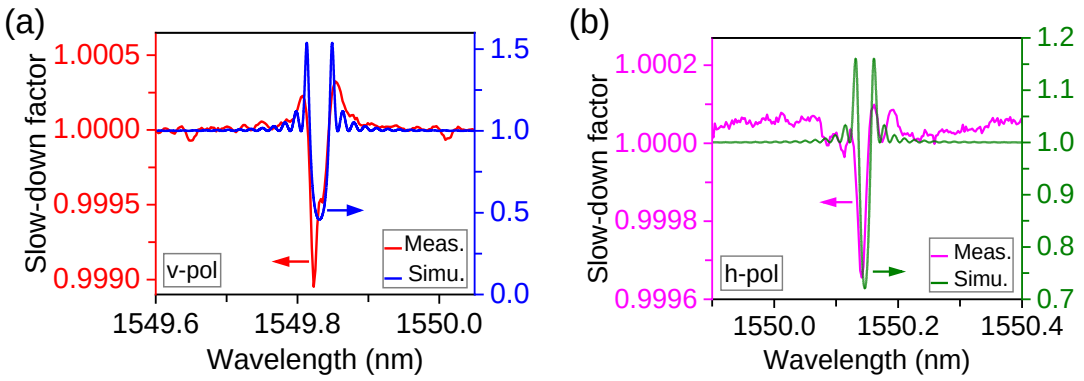

Figure 5.8 For WLBG with a 10 μm offset, the SDFs are derived from the GD measurements and simulated using GIs in (a) for v-polarization and (b) for h-polarization.

5.5 Conclusion

In conclusion, we have demonstrated a single-laser-pass and second-order WLBG with four offsets to exploit the slow-light effects near the band edges. For WLBG at a 10 μm offset, a best transmission dip of 12.5 dB is achieved with an enhanced GD up to 35 ps and a derived SDF of 1.54 in v-polarization. In contrast, the GD and derived SDF values in h-polarization are 11 ps and 1.16, respectively. These values could be improved by using either long Bragg gratings or short gratings through chemical etching. Grating dispersion may be used to create slow-wave optical structures, enabling high-efficiency light-matter interactions for potential applications, including: (1) photonic devices, such as photonic crystal waveguides to control light velocity for effective filtering and sensing in optical systems, and optical delay lines to buffer optical signals and synchronize data streams in high-speed communications, (2) hardened glass for cellphone screens to minimize reflection and optimize light transmission to enhance visibility and user experience since the grating structure is invisible, especially in bright conditions, (3) microfluidic devices to detect changes in refractive index for real-time monitoring of fluid properties, useful in chemical analysis and diagnostics, (4) biosensing to increase sensitivity by enhancing the interaction length between light and low-concentration biomolecules, aiding early disease detection and

environmental monitoring, (5) smart glass windows selectively filter or modulate light based on external conditions, improving energy efficiency and indoor comfort.

5.6 Funding

This work was funded by the Natural Sciences and Engineering Research Council of Canada (NSERC), through the New Frontiers in Research Funding Fund (NFRF) with project number NFRFE-2020-00355.

5.7 Author contributions

Q.C. conducted the optical characterization, including device polishing, experimental platform setup, measurements, data analysis, manuscript writing and revisions, as well as the literature review. J.-S.B., F.J., and Q.C. collaborated on the Bragg grating inscription using FSL. S.L. provided guidance on the derivation of the SDF formula and offered valuable comments on the manuscript. R.K. and M.S. led the research and secured the funding. All authors contributed to the manuscript by providing feedback and suggestions.

This chapter covers Objectives 3 and 4.

CHAPTER 6 ARTICLE 3: ENHANCED SLOW-LIGHT PHENOMENON IN DOT-BRAGG GRATINGS THROUGH OFFSET ENGINEERING

Qingtao Chen, Jean-Sébastien Boisvert, Foroogh Jafari, Mohammad S. Sharawi, Sébastien Loranger, and Raman Kashyap

Published in: Journal of Lightwave Technology

Submission date: Mar. 26, 2025

This article has been submitted in Journal of Lightwave Technology (Submission date: Mar. 26, 2025) and titled **"Enhanced slow-light phenomena in dot-Bragg gratings through offset engineering"**. The article explores enhanced slow-light effects in two types of waveguide dot-Bragg gratings, achieved through optimized writing parameters and offset engineering: Model I, based on a single-pass-laser waveguide (SLPWG), and Model II, utilizing a dual-pass-laser waveguide (DLPWG). Compared to Model I, Model II exhibited a deeper transmission dip and an increased slow-down factor (SDF), enabled by using both a lower laser repetition rate and adjusting the center distance in DLPWG, and optimizing the offset between dots and DLPWG. These adjustments reduced the sensitivity of dot positioning—observed in Model I—and improved the interaction between the dots and the waveguide in Model II. Compared to the dot-Bragg grating discussed in Article 1, the SDF values in Model I and Model II improved by 16% and 39%, respectively. Additionally, time-delay measurements in Model II, obtained from signal pulse traces at the reflection peak and edges, demonstrated a relative delay of 7 ps, indicating a slightly overestimated slow-light effect. The supplement of this article is given in Appendix C of this thesis.

Abstract: We demonstrate enhanced slow-light phenomenon in dot-Bragg grating (DBGs) inscribed by femtosecond laser (FSL) in bulk glass through offset engineering. Two types of first-order DBGs, Model-I and Model-II, are inscribed based on single-laser-pass waveguide (SLPWG) and double-laser-pass waveguides (DLPWG), respectively. In Model-I DBG, the effective light-guiding occurs in the shell region with a refractive index (RI) change of $\sim 2 \times 10^{-3}$, while the core region exhibits a smaller RI change less than 0.4×10^{-3}. The enhanced slow-light phenomena are

achieved at a 5 μm offset, yielding a transmission dip of 6.7 dB, a slow-down factor (SDF) of 1.21, and a maximum group delay (GD) of 33 ps. In Model-II DBG, the two-pass inscription combined with center distance adjustment in DLPWG enhances the core RI change by a factor of 2 over SLPWG, with a value of 0.8×10^{-3}, while the shell RI change decreases to ~1×10^{-3} due to the lower repetition rate. With offset optimization, the transmission dip in Model-II DBG nearly doubles, up to 12.5 dB at a 5 μm offset with a 5 μm center distance, leading to slow-light effect with an SDF of 1.45 and a maximum GD of 43 ps —representing an 87% improvement in transmission, and 20% and 30% improvements in SDF and GD, respectively, compared to Model-I DBG. In addition, a time delay of ~7 ps is obtained by comparing the detected signal pulse at the Bragg wavelength of Model-II DBG with the signal pulses at wavelengths tuned near the reflection edges, which represents an overestimated value for the slow-light effect. These results demonstrate that the two DBG models hold significant potential for optical filtering in communication and sensing, as well as in optical networks for data traffic management and dynamic reconfiguration of optical channels.

6.1 Introduction

Slow-light phenomena, in which the group velocity of light is reduced, have been performed in diverse media [141] at room temperature. These experiments have utilized large refractive index (RI) changes in photonic crystals [142], small RI changes in fibers [3] and transparent glass slides [42], [143]. These slow-light devices have garnered considerable attention due to their potential applications in optical communication [6], sensing [144], optical filters [145], and quantum technologies [146]. It shows potential features, including optical buffering [147] and precise signal delays [31], while they could contribute to applications in smartphone displays [85] and integration with photodiodes [148], enhancing performance across various optical systems.

Most silicon-based and photonic crystal slow-light devices rely on high-RI solid materials (RI change>1) to create multiple cavities or long periodic structures via cleanroom complex photolithography, effectively reducing group velocity [18]. In contrast, bulk glass-based Bragg gratings can be inscribed using a femtosecond laser (FSL), offering a cost-effective, rapid, simplified, and versatile alternative. This method enables 3D inscription and it not limited to photosensitive materials, making it applicable to polymers and crystals. Utilizing FSL techniques, some slow-light devices based on Bragg grating configurations (RI change: 10^{-4}~10^{-2}),

particularly those inscribed in fibers or bulk glass, have been recognized as effective tools for controlling group velocity [22], [42], [43]. These configurations typically function by periodically modulating the RI, forming a resonant peak escorted by two shoulder bands, where the group index increases, thereby generating slow light. In our previous work, the slow-light effects in bulk glass-based Bragg gratings, represented by the slow-down factor (SDF), exhibited a derived value of 1.54 in line-Bragg grating [43] with offset but only 1.04 in dot-Bragg grating (DBG) [42] with a specific offset value. Therefore, a comprehensive investigation of offset engineering in DBG is of paramount importance.

In this work, we explore enhanced slow-light phenomena in 75 mm long DBGs through offset engineering. Using FSL two-step inscription, we create two distinct DBG models with different offsets in bulk glass slides. Model-I DBG, based on a single-laser-pass waveguide (SLPWG) and offset adjustment, achieves a maximum transmission dip of 6.7 dB and an SDF of 1.21. However, the weakly guiding core in the SLPWG and the dot position can influence both the transmission dip and the slow-light effect as well. To address these limitations, Model-II DBG employs a double-laser-pass waveguides (DLPWG) method with a lower repetition rate and writing speed than the previous DBG [42]. By incorporating a precisely calibrated center-to-center distance (center distance, for short), the DLPWG shows a more symmetric cross-section and a twofold increase of RI change within the weakly guided core (compared to SLPWG), but a halved RI change in the primary light-guided shell due to the utilization of a lower repetition rate. With a carefully optimized offset, the dot sensitivity in Model-II DBG is minimized, enabling a maximum transmission dip of 12.5 dB and an SDF of 1.45, an improvement of 87% and 20% over Model-I DBG, respectively. Additionally, we investigate the time delay in Model-II DBG, which is measured to be approximately 7 ps, indicating an overestimation of the slow-light effect. These findings demonstrate that well-calibrated offsets and center distance can significantly enhance slow-light effects in DBG structures, enabling more efficient and tunable devices for next-generation optical systems.

6.2 Models and experiments

6.2.1 Two types of DBG models

The slow-light effect of Bragg gratings in bulk glass can be evaluated using a slow-down factor (SDF) [43], *S*, as follows:

$$S = 1 + \frac{(\kappa L)^2}{\pi^2}, \tag{6.1}$$

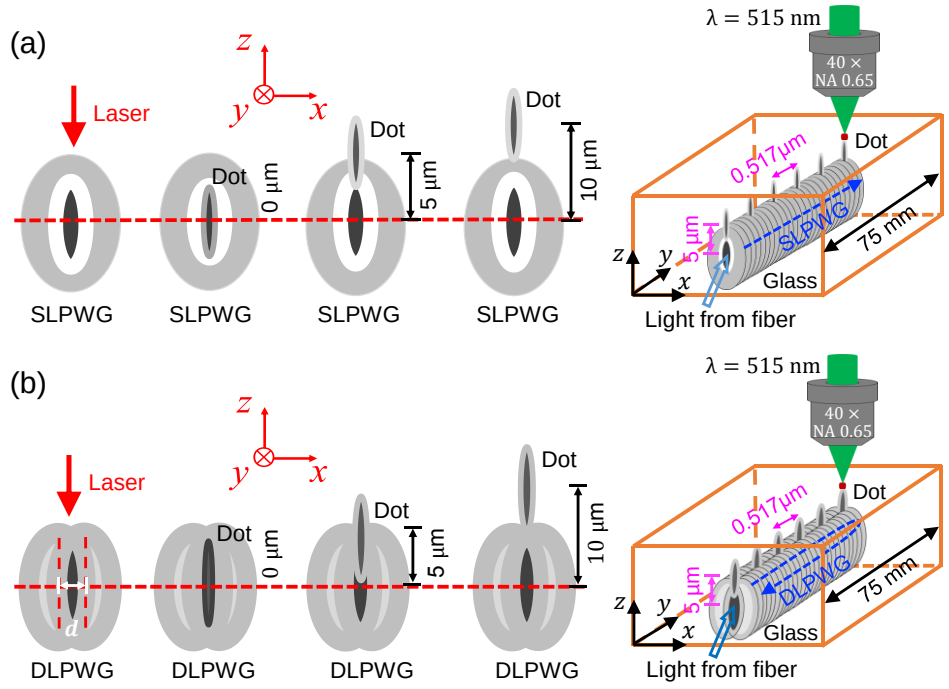

Figure 6.1 Schematic cross-sections of the two DBG models show three offsets between SLPWG or DLPWG and dots for (a) Model-I DBG, and (b) Model-II DBG. In Model-II, *'d'* denotes the center distance in the DLPWG with six values. Marked values are not to scale, and the inscription laser (red arrows) was incident from the top.

where κ and κL are the coupling coefficient and the coupling constant, respectively, with L as the length of the grating. Based on equation (6.1), we can conclude that a larger κL corresponds to a strong Bragg grating, resulting in a larger SDF and a narrower frequency band (if $(\kappa L)^2 \ll \pi^2$ [45]), which is ideal for precise optical filtering applications. However, the partially overlapping waveguides dot-Bragg grating (DBG) in [42] exhibited a weak structure, yielding a small SDF of 1.04. To exploit Bragg gratings with larger SDFs for increased light-matter interactions, we propose two DBG models with three different 'offset' values (0 µm, 5 µm, and 10 µm), as shown

in Figure 6.1. The 'offset' refers to the vertical z-axis between the waveguide and the dot (Figure 6.1). Model-I DBG (Figure 6.1(a)) is a single-laser-pass waveguide (SLPWG) DBG, while Model-II DBG (Figure 6.1(b)) is a double-laser-pass waveguides (DLPWG) DBG, incorporating six center distance (d: 0~5 μm, 1 μm step size) in DLPWG for each offset.

The DBGs were inscribed using a Pharos FSL system (laser wavelength: 1030 nm, pulse duration: 250 fs) with a frequency doubled to 515 nm by an Orpheus optical parametric amplifier, while the samples are translated by an Aerotech 3200 precision stage with three axes [108]. The low-iron soda-lime glass (Fisherbrand, 75 mm length×25 mm width×1 mm height) slides were used for DBGs inscription along the 75 mm directions. These glass slides offer high transparency, low absorption, cost-effectiveness, moisture and oxidation resistance, and scalability for optical applications such as telecommunications and optical sensing [149]. Unlike single-step waveguide Bragg gratings inscription via modulated burst method [75], [80], which is constrained by waveguide cross-section size or Bragg grating period, and a balance of precise FSL-writing parameters, our two-step process enhances flexibility. The waveguide is inscribed first, followed by the dot, allowing precise and adjustable Bragg grating periods.

6.2.2 Model-I DBG and Model-II DBG inscription

For Model-I DBG inscription: (1) A 75 mm long SLPWG was inscribed using an FSL with a 0.65 NA (numerical aperture) microscope objective, focusing 50 μm below the glass slide surface. The writing parameters included 100 mW laser power, a 606 kHz repetition rate, and 1 mm/s writing speed (i.e. the translating speed of the three-axis stage). Due to the non-ideal smoothness of the glass slide surface, variations in the glass slide's thickness, and the three-axis Aerotech 3200 precision stage not being perfectly level, the waveguide end facets have an approximately 10~20 μm difference. (2) The first-order dot-Bragg gratings were inscribed using a 100 mW laser power, a 5.51 kHz repetition rate, 2.85 mm/s writing speed, and a 50% duty cycle, yielding a 0.517 μm grating period, centered at the Bragg wavelength of ~1550 nm (based on the Bragg condition [45], with an effective refractive index of 1.498, derived from writing parameters.). To explore the effect of laser power on the transmission, four levels (100 mW, 300 mW, 500 mW, and 700 mW) were used for inscribing Bragg gratings, each with three different vertical offsets (0 μm, 5 μm, and 10 μm), adjusted by shifting the laser focus along the vertical directions (z-axis in Figure 1(a)).

For Model-II DBG inscription: (1) A 75 mm long DLPWG was inscribed using a 250-mW laser power with 60 μm focus depth, 202 kHz repetition rate, and 1 mm/s writing speed. The center distance (*d*) within the DLPWG varied from 0 μm to 5 μm (1 μm step size) to study overlap effects on grating transmission. (2) The first-order dot-Bragg gratings were inscribed atop each DLPWG with three offsets (0 μm, 5 μm, and 10 μm) (Figure 6.1(b)), using 100 mW laser power, a 5.51 kHz repetition rate, a 2.85 mm/s writing speed, and a duty cycle of 50%. This results in a 0.517 μm grating period and a Bragg wavelength of ~1550 nm.

6.3 Experimental results and discussions

6.3.1 RI changes of SLPWG and Model-I DBGs

The cross-section views of SLPWG and Model-I DBG with three offsets are measured by white light. The corresponding refractive index (RI) change (Δn) is calculated by

$$\Delta n = \frac{\Delta\phi\lambda}{2\pi h}, \tag{6.2}$$

where h is the effective affected height of the modified region, λ is the measurement wavelength of 632 nm, and $\Delta\phi$ is the phase change measured by "The Ripper" from PhotoNova Inc. [110]. The SLPWG features an oval-shaped core-shell cross section (Figure 6.2(a)), where the shell serves as the primary light-guided region with an RI change of $\sim 2 \times 10^{-3}$, while the core region, covering an area of $4 \times 11\ \mu m^2$, exhibits a weaker light-guided effect with an RI change of $\sim 0.4 \times 10^{-3}$. The formation of SLPWG is facilitated by thermal diffusion in the vertical direction and heat accumulation [55] at a 606 kHz repetition rate. The higher repetition rate also enhances the circular symmetry of SLPWG (Figures 6.2(a~b)), improving light guiding along the shell region. Additionally, setting the laser focusing point 50 μm below the glass slide surface contributes to more heat accumulation in the horizontal direction (x-axis), making the SLPWG cross-section more circular (inset of Figure 6.2(a)).

To successfully inscribe dot-Bragg gratings, it is essential to maintain an unsaturated RI change in the SLPWG. Thus, the dot inscription usually requires a much lower repetition rate than SLPWG inscription, as a higher or equal repetition rate may cause dot areas to approach or exceed the SLPWG, leading to potential saturation. After several adjustments, a repetition rate of 5.51 kHz is chosen for dot inscription in Model-I DBG with three offsets. When the offset is 5 μm (Figure

6.2(c)), the RI change (Figure 6.2(d)) in the shell region is ~1.8×10^{-3} (black curve, h=22 μm) and 1.6×10^{-3} (red curve, h=25 μm), while the core region exhibits a negative value of -5.4×10^{-5} due to the use of a very low repetition rate (5.51 kHz) for dot inscription. The negative RI change has a minimal impact on the total RI change values (i.e. the effective light-guided regions) of the Model-I DBG, and thus allows the DBG to exhibit a Bragg resonance. Moreover, the cross-sectional shapes, light-guided regions, and RI change profiles are nearly symmetric (Figures 6.2(a~d)).

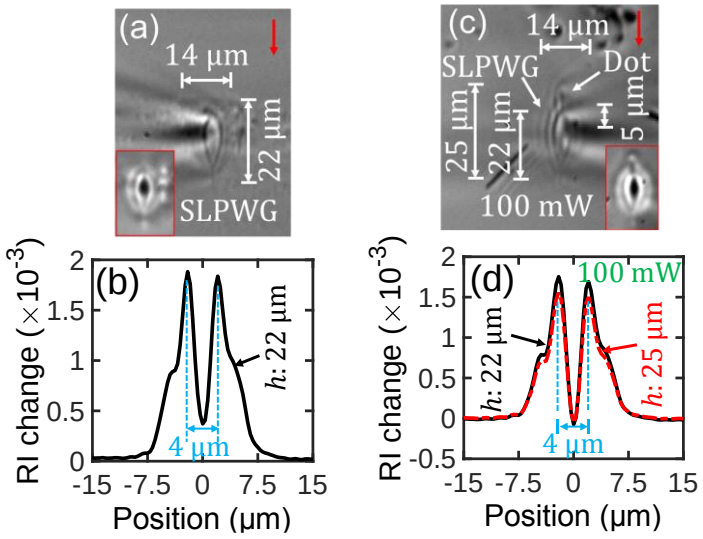

Figure 6.2 (a) Cross-section view and (b) RI change of SLPWG. Model-I DBG: (c) Cross-section view and (d) RI change at a 5 μm offset with 100 mW laser power for dot inscription. Note that the inscription laser (red arrows) was incident from the top.

Figure 6.3(a) presents the RI changes of Model-I DBG at three offsets under a 100 mW laser power for dot inscription. The RI change of the SLPWGs in Model-I DBGs is approximately 1.8×10^{-3} for h of 22 μm. However, the RI changes in Model-I DBG decreases significantly from 1.8×10^{-3} (h=22 μm) at 0 μm offset to 1.2×10^{-3} (h =33 μm, the combined effective length of SLPWG and dot) at 10 μm offset (Appendix C, Figure C.1). Figure 6.3(b) further compares RI changes for Model-I DBG at a 5 μm offset under four different laser powers (100 mW, 300 mW, 500 mW, and 700 mW) for dot inscription. The mean RI changes range from $(1.65\sim1.85) \times 10^{-3}$ for SLPWGs in Model-I DBGs and $(1.5\sim1.7) \times 10^{-3}$ for Model-I DBGs, as the laser powers varies from 100 mW to 700 mW (Appendix C, Figure C.2). Notably, these RI changes predominately occur in the shell regions (insets of Figure 6.3(b)), while the SLPWG size remains largely unchanged, with only slight variations in dot size. This suggests that the laser power has a relatively weak effect on dot

size and a minimal impact on RI changes. However, the core RI changes of SLPWGs gradually worsen as the laser power increases, with negative values ranging from -0.4×10^{-3} to -0.7×10^{-3} (Appendix C, Figure C.2). This could lead to a decrease or oscillation in the transmission and GD characteristics.

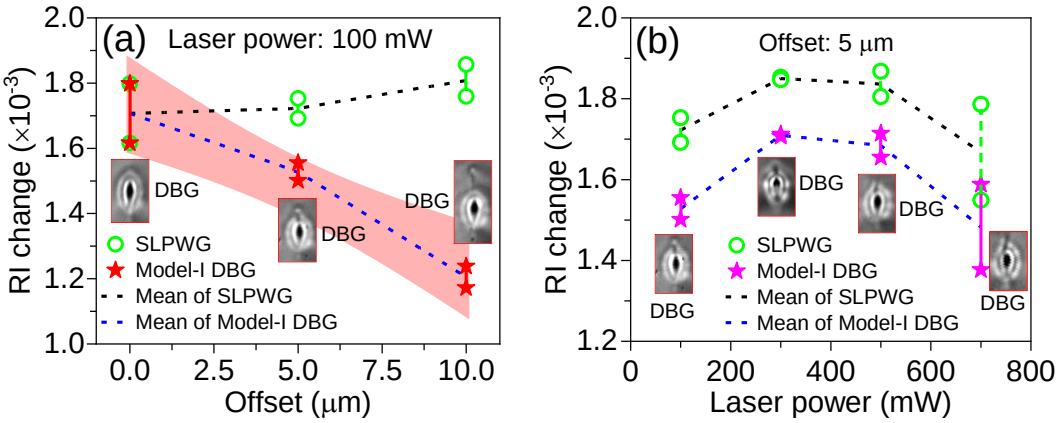

Figure 6.3 (a) RI change comparisons at three offsets and 100 mW laser power for dot inscription, with a confidence band around the fitting curve showing the impact of the effective affected height (h). (b) RI change comparisons at four laser powers for dot inscription at a 5 μm offset. Green circles and solid stars represent peak RI changes, typically occurring in the shell regions with effective light-guiding, as shown in the insets.

In summary, it is difficult to pinpoint a single "best" waveguide recipe for subsequent grating inscription, as almost all the recipes produce bright focal spots for light guiding. Therefore, further analysis combining spectrum measurement is essential to fully understand the influence of laser power and to select the most suitable recipe, excluding considerations of dot-SLPWG interactions (i.e. offset distance).

6.3.2 Spectrum and slow-light effect of Model-I DBGs

The spectrum and group delay (GD) of Model-I DBG are measured using the Luna OBR 4600 [43], with a polarization controller to adjust the incident light to vertical (v-pol) and horizontal (h-pol) polarizations. Index matching oil with an RI is used to minimize cavity reflections between the fiber and DBG facets.

Figure 6.4 compares the spectrum and GD of Model-I DBG (100 mW laser power for dot inscription, 5 μm offset) for both v-pol and h-pol. The DBG shows transmission dips of 6.7 dB (v-pol, 1549.80 nm) in Figure 6.4(a) and 4.2 dB (h-pol, 1549.82 nm) in Figure 6.4(b). GDs in

transmissions for v-pol and h-pol are shown in Figures 6.4(c~d), which indicate slow-light effects close to the band edges with GDs of 30 ps (v-pol, 1549.79 nm) and 33 ps (v-pol, 1549.82 nm), and 28 ps (h-pol, 1549.80 nm) and 25 ps (h-pol, 1549.83 nm). The GDs near the right band edges in Figures 6.4(c) and 6.3(d) are zoomed in partially, as shown in Figures 6.4(e) and 6.4(f), respectively. In addition, the fast-light effects are also observed at the Bragg wavelengths for both polarizations.

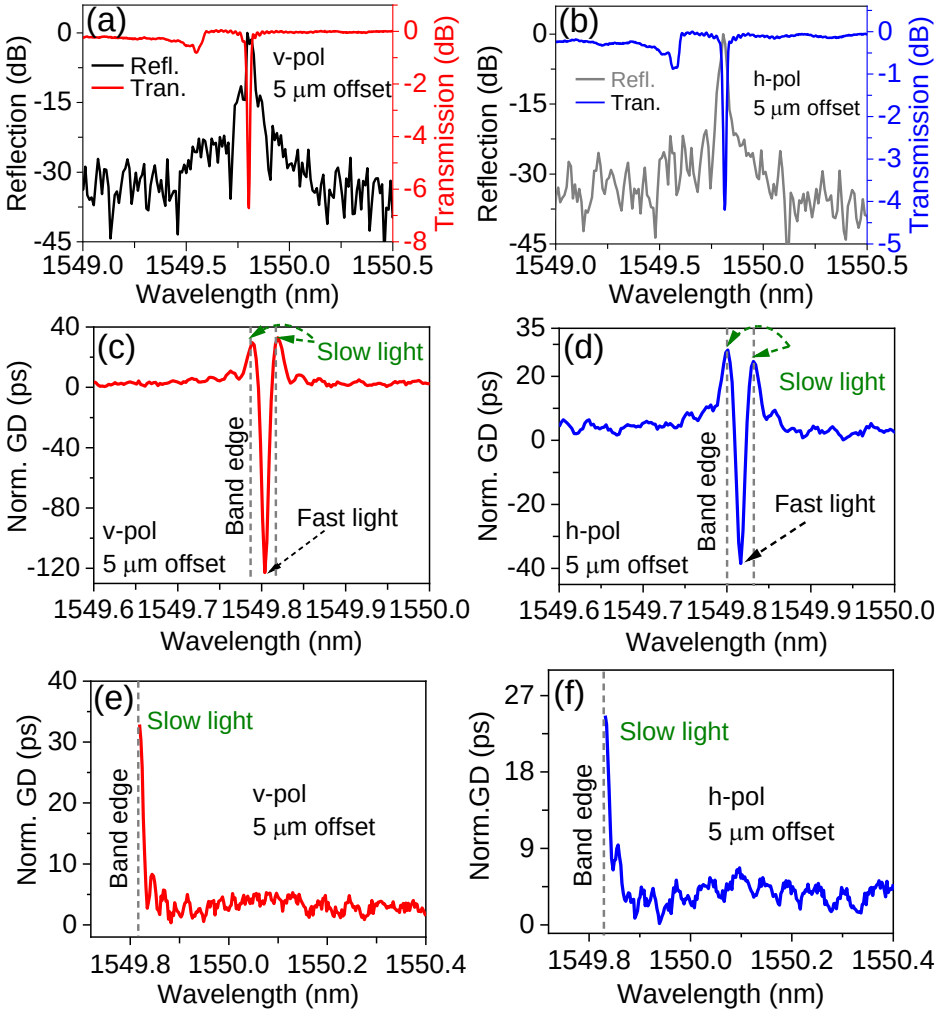

Figure 6.4 Model-I DBG spectrum and GD at a 5 μm offset and 100 mW laser power for dot inscription for both v-pol and h-pol. (a~b) The measured reflection and transmission spectra, (c~d) GDs in transmission, and (e~f) the partially zoomed-in graphs of the GDs from (c~d). Normalized y-axes are used to analyze the slow-light effect.

To address the offset impact on the slow-light effect, the transmission and GD of Model-I DBG are measured at offsets of 0 μm, 5 μm, and 10 μm. The values of SDF are obtained by Eq.(1) while

the coupling constant (κL) are calculated using the maximum reflectivity (R_{max}) equation [45] given by:

$$R_{max} = 1 - 10^{-\frac{T}{10}} = \tanh^2(\kappa L) \tag{6.3}$$

where T represents the transmission dip value in dB, L is the grating length of 75 mm. When the laser power is 100 mW for dot inscription, the SDFs at a 5 μm offset are increased by 7.1% (v-pol in Figure 6.4(a), Trans. dip of 6.7 dB, κ of 19 m^{-1}, κL of 1.41, and SDF of 1.21) and 2.8% (h-pol in Figure 6.4(b), Trans. dip of 4.2 dB, κ of 14 m^{-1}, κL of 1.10, and SDF of 1.11) compared to the offset at 0 μm (SDF values of 1.13 in v-pol and 1.08 in h-pol) in DBGs (Appendix C2, Figure C.3 and Table C.1). At a 10 μm offset, the transmission dips reduce to less than 1 dB (SDFs<1.03) for both polarizations.

To examine the impact of laser power on the spectrum and slow-light effect, the laser power is increased to 300 mW, 500 mW, and 700 mW for dot inscription at three offsets. At offsets of 0 μm, 10 μm, and 15 μm, most transmission dips in both polarizations are less than 1.1 dB (SDFs < 1.03) or absent, with exceptions in the v-pol such as 1.4 dB dips at 10 μm offset (300 mW) and 0 μm offset (500 mW), and a 1.9 dB dip at 10 μm (500 mW). Sideband resonances near main resonance wavelengths are also observed due to coupling or phase/amplitude changes in the grating.

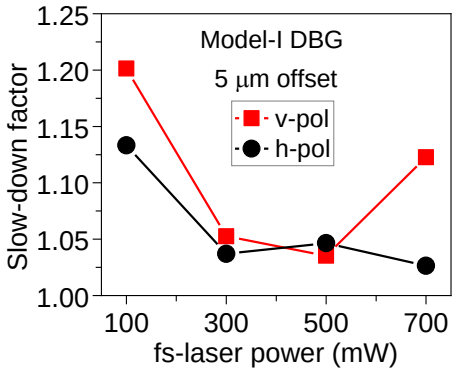

Figure 6.5 SDFs of model-I DBGs versus femtosecond laser (fs-laser) powers (100 mW~ 700 mW) for dot inscription at a 5 μm offset under v-pol and h-pol incident light.

To highlight that the 5 μm offset plays a vital role in enhancing transmission dips and slow-light effects (SDF using equation (6.3)) for Model-I DBG, when used the laser powers of 300 mW, 500 mW, and 700 mW for dot inscription. The measured transmission dips range from 1 dB to 4.6 dB in both v-pol and h-pol, centered at 1549.76 nm to 1549.82 nm (Appendix C, Figure C.4). The

summarized SDFs (Figure 6.5) shows a maximum of 1.21 at 100 mW in v-pol, decreasing to ~1.05 at 300 mW and 500 mW, and rising to 1.13 at 700 mW. In h-pol, the maximum SDF is 1.1 at 100 mW, then drops below 1.05 as the fs-laser power increases from 300 mW to 700 mW. These trends indicate that laser power affects the SDFs through κL, which depend on the transmission dip and the relative positions of the dots to SLPWGs.

6.3.3 RI changes of Model-II DBG

Based on the definition of SDF, a larger coupling constant (κL) results in a stronger grating, with deeper transmission dips and larger SDFs. From Model-I DBG, we observed that the relative positions of dots are sensitive to SLPWGs in DBGs, suggesting that multi-pass waveguide DBGs could offer stronger transmission dips. However, this may introduce additional modes, particularly when using bundle waveguides or waveguide arrays. In contrast, the double-laser-pass for waveguide (DLPWG) inscription along horizontal direction (x-axis in Figure 6.1(b)) could be a more favorable option for Model-II DBG. The double-laser-pass technique can increase the waveguide's cross-sectional area along the x-axis and reduce the sensitivity of the dot's relative position to the waveguide to some extent. However, if the center distance is too large, it may introduce additional modes or decrease the core RI change [42], which could further diminish the transmission dip of the Bragg grating. To address this, six center distances (0~5 μm, 1 μm step size) are used in DLPWG during FSL-inscribed Model-II DBG for each offset. This approach aims to: (1) optimize the cross-section area of waveguide for lessening the dependence of the dot's relative position on the waveguide, (2) increase the weakly core light-guided efficiency (e.g. increase the core RI changes from $\leq 0.4 \times 10^{-3}$ in Figures 6.2(b, d) to ~0.8×10^{-3} in Figures 6.6(b, d)), and (3) minimize the impact of side lobes in the resonant spectrum.

Given a higher repetition rate (606 kHz), it could increase the RI change of the waveguide (e.g. SLPWG). However, it may also reduce the material's photosensitivity at higher exposures, leading to cumulative heating or saturation, which is undesirable for subsequent strong grating inscription. Hence, the repetition rate is reduced from 606 kHz to 202 kHz for DLPWG inscription, while the laser power is increased from 100 mW to 250 mW. As a result, the RI changes in Model-II DBGs are slightly smaller (1×10^{-3}, Figures 6.6(b, d)) than that of Model-I DBGs (1.8×10^{-3}, Figures 6.2(b, d)) due to the larger h in DLPWG (Figures 6.6(a, c)). The primary light-guided regions in Model-II DBGs are predominantly situated along the shell sections, with the improved weak light-

guided regions of cores in DLPWG due to adjusted center distances. The RI change in core regions of Model-II DBGs (Figures 6.6(b, d)) reaches $\sim 0.8 \times 10^{-3}$, a twofold increase compared to SLPWG ($(0 \sim 0.4) \times 10^{-3}$, Figures 6.2(b, d)). This improvement is due to partially overlapping double shells (Figures 6.6(a, c)), which reduce non-light-guiding areas in the core. This forms several smaller non-light-guiding areas (insets of Figures 6.6(a, c) and Figures 6.7(a~b)), which enhances the overall light-guiding performance of DLPWGs in Model-II DBGs.

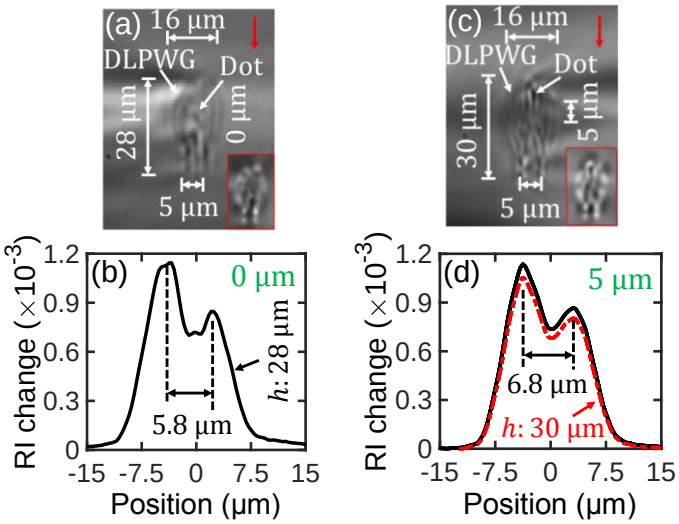

Figure 6.6 Model-II DBG with 100 mW laser power and 5.51 kHz repetition rate for dot inscription: (a) Cross-section view and (b) RI change at a 0 μm offset. (c) Cross-section view and (d) RI change at a 5 μm offset. Note that the inscription laser (red arrows) was incident from the top.

The mode profiles of SLPWG in Model-I DBG and DLPWG in Model-II DBG are estimated using the mode field diameter (MFD) and V-number (Appendix C, Figure C.5). The MFDs of SLPWG and DLPWG are 12.9 μm × 12.8 μm and 16.1 μm × 17.9 μm, respectively, with V-number values of 1.47, 2.53 and 1.88, 2.82. These values indicate that both waveguides can support the LP_{01} mode. However, due to the mismatch in MFD with the SMF28 fiber (which has a 10.5 μm MFD), transmission losses occur during the measurement. Additionally, during DLPWG inscription, prior exposures can reduce the material's photosensitivity for subsequent inscriptions, potentially resulting in a smaller modified cross-sectional area and a slightly reduced RI change, as indicated by the right peaks in the RI change profiles (Figures 6.6(b, d), left peak: the 1st inscription, and right peak: the 2nd inscription). Further, the horizontal distance (x-axis) between the peaks (5.8 μm and 6.8 μm, Figures 6.6(b, d)) exceeds the designed center distance of 5 μm, likely due to measurement errors or imperfections in the DLPWG inscription process.

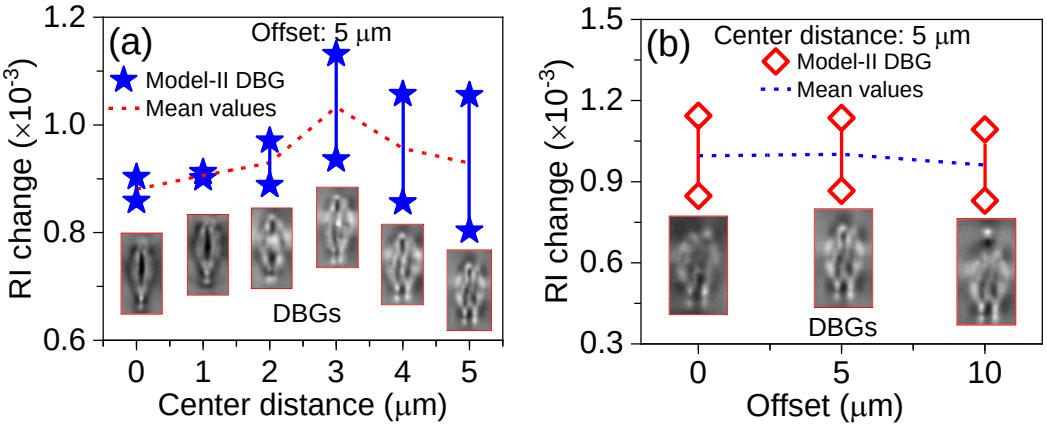

Figure 6.7 Model-II DBG with 100 mW laser power and 5.51 kHz repetition rate for dot inscription: (a) RI change comparisons at a 5 μm offset for six center distance in DLPWG. (b) RI change comparisons at a 5 μm center distance for three offsets. Note: Solid stars and red diamonds indicate peak RI changes in shell regions with effective light-guiding (see insets).

Figure 6.7(a) compares RI changes for Model-II DBG at a 5 μm offset with six different center distance, ranging from 0.8×10^{-3} to 1.1×10^{-3} (Appendix C, Figure C.6). The nearly perfectly symmetrical peaks are observed at 0 μm, 1 μm, and 2 μm center distance (insets of Figure 6.7(a)), while the symmetry deteriorates beyond 3 μm (insets of Figure 6.7(a)) attributed to imperfect overlap in two-pass inscription. Considering the prominent peaks (Figure 6.7(a)) at center distances of 3 μm, 4 μm, and 5 μm, we select 5 μm for a detailed analysis (due to its stronger resonance characteristics in DBG). Figure 6.7(b) presents RI change comparisons at offsets of 0 μm, 5 μm, and 10 μm. The peak RI changes reach ~1.2×10^{-3} for h of 28 μm in the DLPWG, but decreases to (1.15 and 0.9) $\times 10^{-3}$ for the combined affected heights of dots and DLPWGs (30 μm and 36 μm) (Appendix C, Figure C.7). The resonance characteristics of Model-II DBGs depend on the relative positions of dots: at 0 μm and 5 μm offsets (Figures 6.6(a, c), the dots appear unclear due to greater vertical heights of DLPWG. At a 10 μm offset, the dot becomes more distinguishable (inset of Figure 6.7(b)). Consequently, the Model-II DBGs with the aforementioned offsets (0 μm, 5 μm, and 10 μm) could exhibit resonance due to the DLPWG-dot interaction (inset of Figure 6.7(b)). In a word, further spectrum measurements of Bragg gratings are essential to identify the most suitable waveguide inscription recipe.

6.3.4 Spectrum and slow-light effect of Model-II DBG

The spectrum and GD characteristics of Model-II DBG, with six center distances (0~5 μm, 1 μm step size) in DLPWG at offsets of 0 μm, 5 μm, and 10 μm, are measured using the same setup as Model-I DBG. In addition to the main Bragg resonance, sideband resonances appear at shorter wavelengths, likely due to the coupling with the cladding modes, the periodic modulation of the phase or amplitude [137], or higher-order modes from the larger DLPWG area.

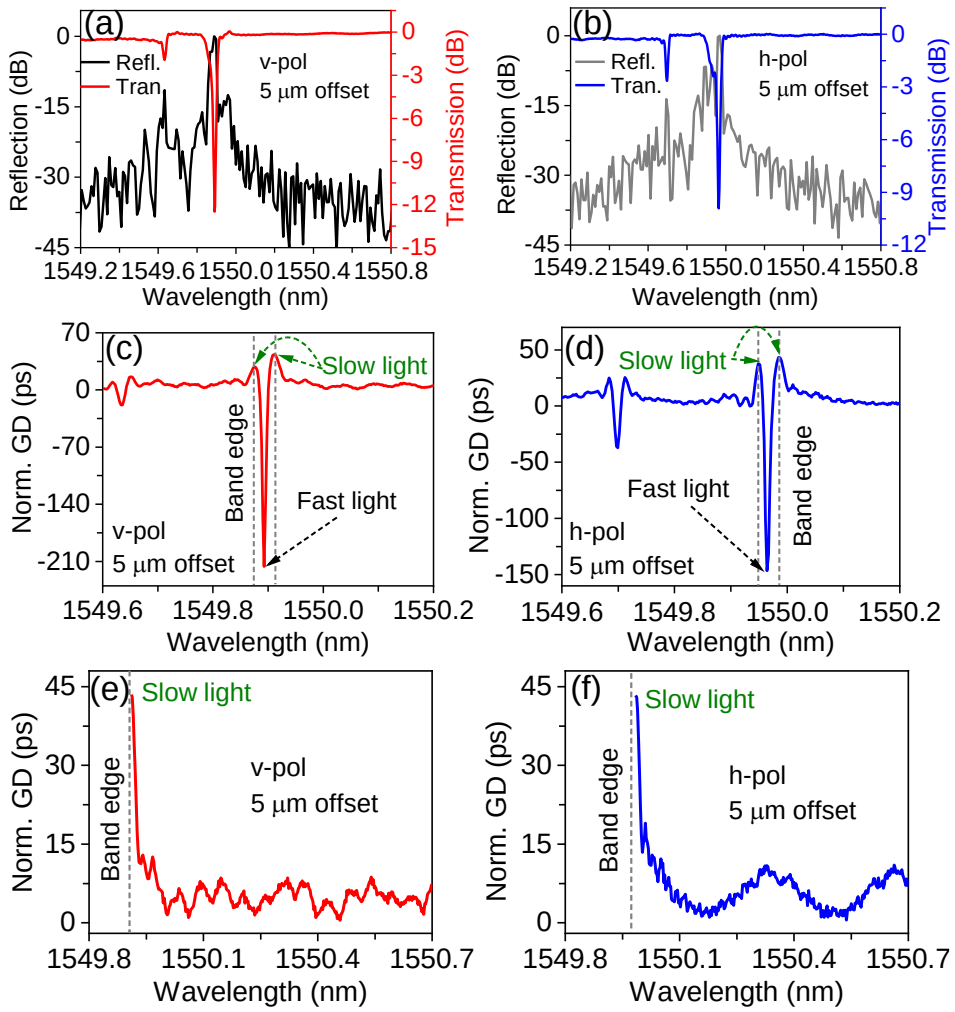

Figure 6.8 Model-II DBG spectrum and GD at a 5 μm offset, 5 μm center distance in DLPWG, and 100 mW laser power for dot inscription for both v-pol and h-pol. (a~b) The measured reflection and transmission spectra, (c~d) GDs in transmission, and (e~f)) the partially zoomed-in graphs of the GDs from (c~d). Normalized y-axes are used to analyze the slow-light effect.

At a 5 μm offset, Model-II DBGs with six center distances in DLPWG exhibit strong transmission, reflection, and slow-light effects. Moreover, the optimal spectral characteristics appear at a 5 μm

center distance for both v-pol and h-pol (Figure 6.8). In v-pol, a 12.5 dB transmission dip (Figure 6.6(a)) is observed at a Bragg wavelength of 1549.89 nm, with the κ and κL values of 28.2 m^{-1} and 2.2 (using equation (6.3)), while shows an SDF of 1.45 (using equation (6.1)). The slow-light effect (Figure 6.8(c)) shows GDs of 28 ps and 43 ps near the band edges, at wavelengths of 1549.875 nm and 1549.911 nm, respectively. In h-pol, a 10 dB transmission dip (Figure 6.8(b)) occurs at a Bragg wavelength of 1549.96 nm, with the κ and κL of 24.2 m^{-1} and 1.82, and an SDF of 1.34. The measured GDs in transmission (Figure 6.8(d)) show GDs of 36 ps and 43 ps at wavelengths of 1549.949 nm and 1549.985 nm, respectively, adjacent to the band edges, demonstrating slow-light effects. In addition, time advances at Bragg wavelengths in both polarizations indicate fast-light effects. The GDs near the right band edges in Figures 6.8(c) and 6.8(d) are zoomed in partially, as depicted in Figures 6.8(e) and 6.8(f), respectively. Meanwhile, the difference in Bragg wavelengths ($\Delta\lambda$) between v-pol and h-pol is 70 pm, corresponding to an effective birefringence (Δn_B) of 4.5×10^{-5}, calculated using $m\Delta\lambda = 2\Delta n_B \Lambda$ (derived using the Bragg condition[45] $m\lambda_B = 2n_{eff}\Lambda$, where m is the grating order of 1, λ_B is the Bragg wavelength, n_{eff} is the effective refractive index of 1.499 calculated using writing parameters of FSL, Λ is the grating period of 0.517 μm.).

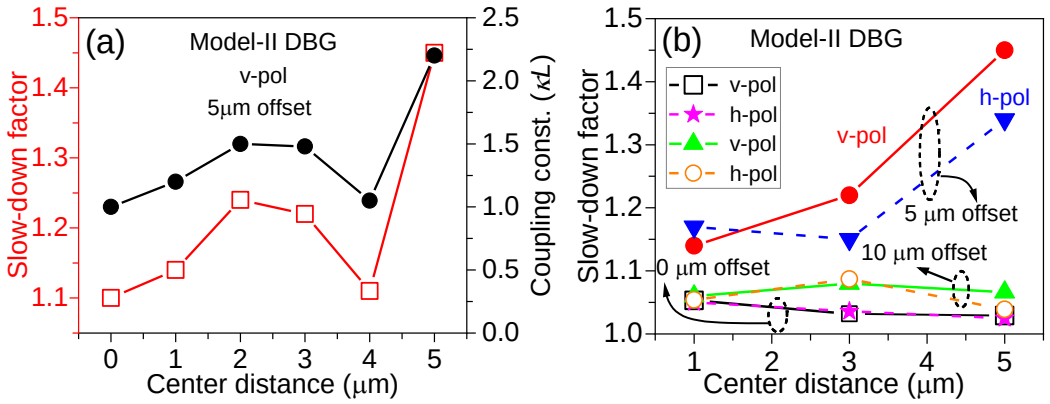

Figure 6.9 SDF comparisons of model-II DBGs: (a) at a 5 μm offset with six center distances (0~5 μm, 1 μm step size) in v-pol, and (b) at 0 μm, 5 μm, and 10 μm offsets, with center distances of 1 μm, 3 μm, and 5 μm in v-pol and h-pol.

Figure 6.9 shows the SDF distributions of Model-II DBG. As shown in Figure 6.9(a), the SDF generally increases with the rise of κL across the entire range, except at the 4-μm center distance (Appendix C, Figure C.8 and Table C.2). As seen in Figure 6.9(b), the SDFs remain below 1.1 at both 0 μm and 10 μm offsets, while the highest value is observed at a 3 μm center distance in h-

pol for 10 μm offset. Slightly lower SDFs appear at 3 μm and 5 μm center distances in v-pol at the same offset. For 5 μm offset, SDFs increase with center distance, reaching 1.45 (v-pol) and 1.34 (h-pol) at 5 μm (center distance), indicating a strong slow-light effect (Appendix C, Table C.3). This configuration is promising for filtering, signal processing, precision measurements, and pulse compression. However, higher SDFs may cause signal distortion and bandwidth limitations, requiring careful control. In contrast, smaller SDFs (1.0~1.1) indicate a weaker slow-light effect, which is preferable for systems where fast transmission and minimal signal distortion are critical, such as in WDM high-speed communication networks, where low delay is essential to maintain signal integrity [98].

6.3.5 Simulation of slow-down factor

The SDF (S) is the ratio of the Bragg grating group index (GI), n_g, to the waveguide GI, n_w, expressed as $S = n_g/n_w$. The GI is given by $n_g = c\tau_g/L$, where τ_g is the grating group delay and L is the length of the grating (Appendix C, Figure C.9). Near the transmission band edges, the S values are summarized in Table 6.1. Note the reasonably good agreement between the simulated and measured values for both the Model-I DBG and Model-II DBG structures. The calculations leading to the results in Table 6.1 are detailed in the simulation section (Appendix C, Figure C.10).

Table 6.1 Comparison of SDF metrics for Model-I and Model-II DBGs.

Name	**Model-I DBG**					**Model-II DBG**				
	Measurement				Sim.	Measurement				Sim.
Metrics	Tran. (dB)	κL	GD (ps)	SDF	SDF	Tran. (dB)	κL	GD (ps)	SDF	SDF
v-pol	6.7	1.41	33	1.21	1.25	12.5	2.2	43	1.45	1.54
h-pol	4.2	1.10	25	1.10	1.14	10	1.82	43	1.34	1.40

6.3.6 Time delay measurement of Model-II DBG

The time delay in Bragg gratings can be measured by observing signal pulse traces at different wavelengths of reflections [150]–[152]. Here, the time delay is observed by an oscilloscope with the experimental setup shown in Figure 6.10.

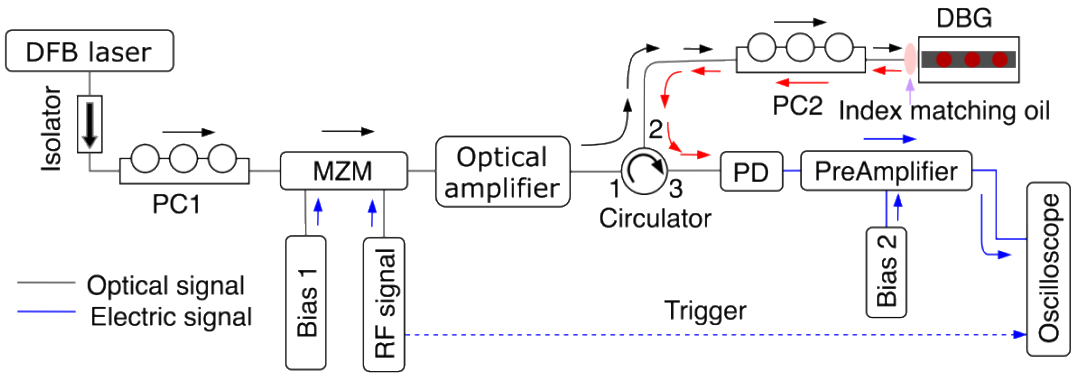

Figure 6.10 Experimental setup for the time delay measurement of Model-II DBG with a 5 μm offset and a 5 μm center distance in the v-pol (Figure 6.8(a), taking this one as an example for analysis). DFB laser: distributed-feedback laser, PC1 and PC2: polarization controller 1 and 2, MZM: Mach-Zehnder Modulator, DBG: dot-Bragg grating, PD: photodiode.

A tunable DFB single-frequency laser with an isolator generates a pulse signal, modulated by an MZM (130 MHz–14 GHz bandwidth) driven by a 2 GHz RF signal (modulation frequency, f_m) and a 1.6 V DC bias for linear operation. PC1 optimizes polarization for maximum MZM output. The modulated signal is amplified by an JDSU optical amplifier (i.e. erbium-doped fiber amplifier, EDFA) and sent to port1 of a circulator. After reflection by a Model-II DBG (adjusted via PC2), it exits port3 and is detected by a fast photodiode. The weak electrical signal is amplified by a wideband preamplifier (5 V, 60 mA) before being processed by an oscilloscope (12 GHz, 40 GSample/sec). A reference signal from the generator provides an external trigger. The modulated signal's bandwidth must be narrower than the Model-II DBG FWHM (full width at half maximum) to avoid the modulated signal leakage.

The detected signal pulse traces are obtained from the reflected modulated signal by the Model-II DBG through opto-electric conversion using the fast PD and are observed on an oscilloscope (Appendix C, Figure C.11). A time delay of ~7 ps is obtained (Figure 6.11) via comparing the signal pulse trace at the Bragg wavelength (1549.897 nm, red curve) and signal pulse traces at wavelengths tuned close to the reflection edges (1549.884 nm, black curve, or 1549.923 nm, green curve). Although this time delay is much smaller than those measured by the Luna OBR 4600, it is a relative value, reflecting an overestimated value for the slow-light effect, and is obtained when compared to the pulse traces at resonant wavelength rather than the actual out-of-band wavelength. The main reasons are: (1) OBR directly and accurately measures group delay, while Figure 6.10 indirectly measures delay through phase shifts in the reflected signal, which can be affected by

nonlinearities, signal processing, and bandwidth limitations. (2) MZM and oscilloscopes face bandwidth limitations, making it harder to capture fine delay details.

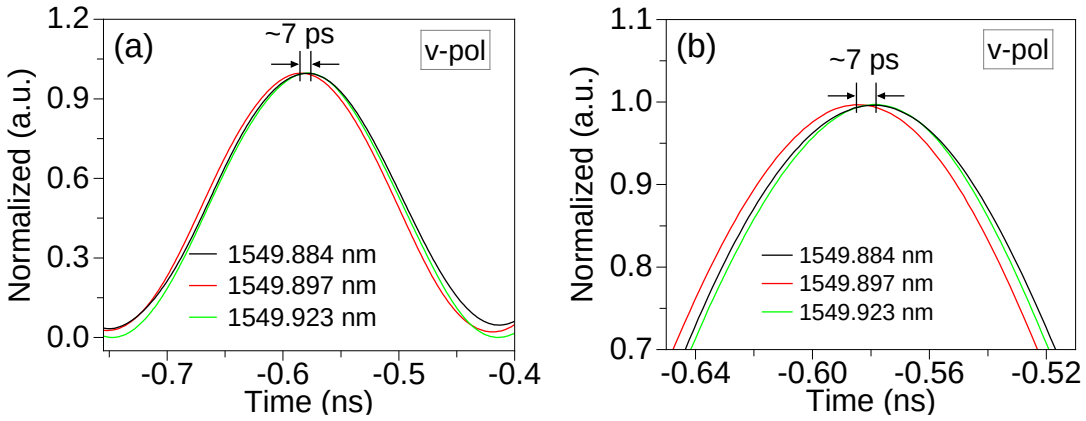

Figure 6.11 Detected signal pulse traces are obtained at wavelengths of resonance and reflection edges when a 2 GHz RF signal (f_m) at 10 dBm power is applied. (b) Partially zoomed-in views of detected signals.

Furthermore, a preamplifier is used after the fast PD to reduce oscilloscope background noise. However, both the preamplifier and optical amplifier increase jitter/oscillation of the detected signal. To mitigate this, six measurements were taken for each wavelength, averaging the results. The x-value differences at a chosen y-value were ≤0.1 ps, indicating a noise level much lower than the detected signal. Despite this, jitter still affects time delay accuracy. Additionally, ripples from spectral sidebands further complicate measurements but can be minimized using apodization techniques [45] or a high-resolution system.

6.4 Conclusion

In conclusion, offset engineering in dot-Bragg grating (DBG) significantly improves slow-light effects, as characterized by the slow-down factor (SDF) and group delay (GD). For Model-I DBG, a 5 μm offset with v-pol incident light yields a maximum SDF of 1.21 (Simulation: 1.25) and a 6.7 dB transmission dip. In Model-II DBG, a double-pass inscription technique enhances the small RI change in the core region of the DLPWG, achieving an SDF of 1.45 (Simulation: 1.54) and a 12.5 dB transmission dip with v-pol at a 5 μm offset and 5 μm center distance. Model-I and Model-II DBG achieve maximal GDs of 33 ps and 43 ps, respectively. Additionally, an overestimated value for the slow-light effect with a time delay of ~7 ps is achieved in Model-II DBG by comparing signal pulse traces at wavelengths of resonance and tuned near the reflection edges. Both DBG

types not only create slow-wave optical structures for slow-light operation, but also act as narrowband optical filters, selectively attenuating light at specific wavelengths while allowing others to pass through.

6.5 Funding

This work was funded by the Natural Sciences and Engineering Research Council of Canada (NSERC), through the New Frontiers in Research Funding Fund (NFRF) with project number NFRFE-2020-00355.

6.6 Acknowledgments

The authors thank Dr. Pascal Burasa for his assistance with the instruments, as well as Jianzhao Gou, Zhiyong Dong, and Dr. Yuxuan Xie for their valuable discussions on the true time delay measurements.

6.7 Author contributions

Q.C. conducted the optical characterization, including device polishing, experimental platform setup, measurements, data analysis, manuscript writing and revisions, as well as the literature review. Q.C. also conducted the Bragg grating inscription using FSL. J.-S.B., F.J., and S.L. offered valuable comments on the manuscript. R.K. and M.S. led the research and secured the funding. All authors contributed to the manuscript by providing feedback and suggestions.

This chapter covers Objective 5.

CHAPTER 7 GENERAL DISCUSSION

This chapter provides a general discussion of the overall results of this thesis. It summarizes the key findings and contributions (with interpretations), addresses the encountered problems and solutions, suggests directions for future research, and highlights the practical applications and significance of the research.

7.1 Key findings and contributions

The slow-light effect in waveguide Bragg gratings has been thoroughly investigated through theoretical design/simulation, FSL fabrication, and experimental measurements. The key findings and contributions are as follows:

(1) Slow-light effect in uniform Bragg gratings: Simulations indicate that a higher coupling constant generally leads to a larger slow-down factor (SDF).

(2) Novel partially-overlapping waveguide model: A novel waveguide model was successfully developed using FSL direct writing techniques in bulk glass slides, resulting in a refractive index (RI) change of 1.63×10^{-3}, a propagation loss of 0.2 dB/cm, and light guiding efficiency (i.e. the ratio of output power to input power, excluding Fresnel reflections, coupling loss, and propagation loss) up to 60%. This addressed the **first objective** effectively.

(3) Bragg gratings fabrication and characterization: Based on the novel waveguide model described in (2), two types of Bragg gratings were created. The weak dot-Bragg grating exhibited a smaller SDF of 1.04 with a 1.74 dB transmission dip, while the line-Bragg grating achieved an SDF of 1.12 and a transmission dip of 4.4 dB. The slow-light effects of these two Bragg gratings were analyzed using coupled-mode theory and Bloch's theorem, addressing the **second objective**.

(4) Offset in waveguide line-Bragg grating for enhancing slow-light effect: Unlike the overlapping waveguide-based line-Bragg gratings described in (3), this Bragg grating used a single-pass waveguide inscription with low repetition rate, achieving an RI change of 1.1×10^{-3} and an offset to enhance the slow-light effect. Combining theoretical and experimental studies, the optimal performance occurred at a 10 μm offset, resulting in a group delay of 35 ps and an SDF of up to 1.54 (calculated using the derived theoretical SDF formula---**the 3rd objective**), with a 12.5

dB transmission dip and a propagation loss of 1.16 dB/cm in vertical polarization. This addressed both **the third and fourth objectives**.

(5) Dot-Bragg grating with offset and center-to-center distance for slow light enhancement: Two types of dot-Bragg gratings were fabricated using single-pass and two-pass waveguide inscriptions, referred to as Model-I and Model-II, respectively, with RI changes of approximately 2×10^{-3} and 1×10^{-3}. Experimental measurements revealed enhanced slow light phenomena at a 5 μm offset for both models. The transmission dips were 6.7 dB with an SDF of 1.21 for Model-I DBG, and 12.5 dB with an SDF of 1.45 for Model-II DBG (with center-to-center distance adjustment in two-pass waveguide inscription), both centered at around 1550 nm. These results addressed the **fifth objective** of this thesis.

7.2 Problems and solutions

The slow-light effect in waveguide Bragg gratings inscribed in bulk glass slides by FSL was explored, revealing potential applications like enhancing light-matter interactions in photonic integrated devices, embedding sensors in cellphone screens, and integrating optical antennas into smart glass windows for real-time environmental monitoring. However, achieving the above results/findings was not without challenges, and several issues emerged throughout the research process. To address these, this thesis presents corresponding solutions, which are briefly discussed below.

(1) Optimal recipe exploration for novel waveguide inscription: To optimize the waveguide inscription process for high-efficiency light guiding, a careful selection of the writing parameters (such as laser power, repetition rate, writing speed, and focal spot positioning) was essential. Initially, high laser power and repetition rates were used with varying writing speeds to fabricate waveguides. However, larger cross-sectional waveguides resulted in the appearance of higher-order modes, as evidenced by white light measurement and V-number calculations. To address this, we reduced the laser power to 250 mW, set the repetition rate to 606 kHz, and achieved continuous, modified regions suitable for optical waveguiding.

We also explored the use of parallel adjacent two-pass inscription to improve light guiding efficiency. In this experiment, we varied the writing speed (5 mm/s, 10 mm/s, 15 mm/s, and 20 mm/s) and center distance values (6 μm, 8 μm, and 10 μm) to determine the optimal parameters for achieving the largest refractive index (RI) change. After phase change measurement using "The

Ripper™" and subsequent RI change calculations, we found that a writing speed of 5 mm/s and a center distance of 6 μm yielded the best results, as shown in Appendix A (A.1). The light guiding efficiency measured approximately 60% at this writing speed.

While further fine-tuning of the writing speed (e.g., from 0.1 mm/s to 5 mm/s in steps of 50 or 100 μm/s) was not conducted due to the significant workload involved, we also explored other inscription strategies. For example, a single-pass process with 1 mm/s writing speed, 500 mW laser power, and 101 kHz repetition rate successfully created a light-guiding waveguide. This waveguide served as a foundation for inscribing line-Bragg gratings with offsets, which exhibited excellent transmission dips and slow-light effects.

Further optimization of the single-pass process for waveguide was carried out with a writing speed of 1 mm/s, laser power of 100 mW, and repetition rate of 606 kHz, resulting in the successful creation of offset-enhanced Model-I dot-Bragg gratings. To enhance waveguide-dot interactions, we also achieved two-pass inscription waveguide (center distance adjustment from 0 to 5 μm, in step of 1 μm) with laser power of 250 mW, 1 mm/s writing speed, and 202 kHz repetition rate, resulting in the creation of offset-enhanced Model-II dot-Bragg gratings.

(2) Successful fabrication of Bragg gratings with deeper transmission dips: Building on the high light-guiding waveguide described in (1), dot- and line-Bragg gratings were inscribed using FSL inscription. A key consideration during this process is determining whether resonance, and thus a Bragg grating, can be achieved. Consequently, careful adjustment of writing parameters remains crucial. In general, the repetition rate for inscribing dot and line gratings is typically lower than that of the corresponding waveguides. After iterative calibration, the optimal writing parameters for dot gratings were found to be 100 mW laser power, 5.51 kHz repetition rate, 2.85 mm/s writing speed, and a 50% duty cycle (for a 1st-order Bragg grating with a period of 0.517 μm). For line gratings, the best parameters were 100 mW laser power, 20.2 kHz repetition rate, 1 mm/s writing speed, and a 50% duty cycle. The transmission dips were gradually enhanced by adjusting the offsets in both dot- and line-Bragg gratings. Given the sensitivity of dot positions in single-pass waveguide Bragg gratings, a two-pass waveguide design was implemented for dot-Bragg gratings, incorporating center distance adjustments in the waveguide to further enhance both the transmission dips and the slow-light effect.

Certainly, further fine-tuning of the writing speed (e.g., reducing it from 1 mm/s to 0.1 mm/s in steps of 100 or 200 μm/s) and adjusting the repetition rate for dot and line gratings would likely result in deeper transmission dips. However, these adjustments were not conducted due to the significant workload involved.

(3) Precise characterization of waveguide and Bragg grating metrics: During the waveguide characterization, the output power was typically very low. Possible causes for this include inscription quality issues, polishing problems at the end facets of the glass slides, loss between the fiber and end facets of the waveguides, or issues with spliced fibers or connectors. It is crucial to carefully check and rule out these factors with sufficient patience; otherwise, the effective light signal may be obscured by instrument noise. Additionally, intentional bending of the SMF28 fiber to form a small angle and using index-matching oil were employed to reduce potential loss.

For measuring the propagation loss of both waveguides and waveguide Bragg gratings, the cut-back method was initially used, with the sample being cut into four slabs using a diamond saw. This method allows for precise measurement of propagation loss based on the slope of insertion loss, although it is destructive and prevents reuse of the sample. Later, we used a Luna OBR to roughly estimate the propagation loss of Bragg gratings from the reflection data. However, this method typically overestimates the propagation loss by a factor of 4 to 6 compared to the cut-back method. Additionally, the coupling constant often affected spectrum measurements, particularly when adjusting the vertical and horizontal polarizations of the incident light using the polarization controller. The optimal transmission dips occurred either in the vertical or horizontal polarizations, requiring dozens or even hundreds of calibrations, in addition to a solid understanding of the underlying theory.

For group delay measurements, two methods were employed. The first involved directly obtaining values from the Luna OBR in the transmission or reflection spectrum. The second utilized a DFB laser diode, modulator, circulator, fast photodiode, and oscilloscope to capture the signal pulse traces from the reflection peak and its edges. However, the optical and electrical signals often exhibited fluctuations, either up and down or side to side, due to interference from the measurement system or instruments. To mitigate measurement errors, multiple measurements were taken for each wavelength, and the results were averaged. Despite this, the measured group delay still exhibited uncertainty, with overestimated values of 7 ps at different positions of the output signal

trace as observed on the oscilloscope. Ripples from sidebands in the reflection spectrum may also impact the oscillated signals, suggesting the need for a high-resolution system to improve measurement accuracy.

7.3 Practical applications and significance

This thesis explores the slow-light phenomena in bulk glass-based waveguide Bragg gratings, which demonstrate considerable potential for practical applications. These phenomena offer innovative solutions in various fields, from the integration of photonic devices into daily life to advancements in optical communication, sensing technologies, and integrated photonic systems. The key advantages of these technologies are outlined as follows:

(1) Real-world applications of slow light Bragg gratings: Further investigation into slow light Bragg gratings could lead to their application in real-world scenarios, enhancing signal processing, increasing sensitivity, and offering new methods for storing and transmitting information. For example, these devices could be integrated into ultra-large smart windows (transparent bulk glass) or paired with optical antennas for wireless communication, optical sensing, temperature regulation, or environmental monitoring.

(2) Influence of external factors on slow light behavior: It would be beneficial to study the effects of environmental factors, such as temperature, electric fields, and magnetic fields, on slow light phenomena in bulk glass-based waveguide Bragg gratings. Such research could contribute to the development of more stable slow light in both Bragg grating devices and metamaterial-based Bragg grating devices. Additionally, collaborating with experts in nanotechnology and quantum optics could accelerate the development of novel slow light devices for next-generation photonic applications.

CHAPTER 8 CONCLUSION AND RECOMMENDATIONS

8.1 Conclusion

This thesis focuses on the design, simulation, fabrication, and measurement of slow light in waveguide Bragg gratings, which are inscribed in bulk glass slides at room temperature using FSL direct writing techniques.

Chapter 1 introduces the motivation and objectives of the study.

Chapter 2 presents the theory of slow light along with its key metrics and simulates slow light phenomena in uniform Bragg grating. A review of relevant literature on slow light devices follows, with a discussion of the fabrication techniques, particularly FSL direct writing methods used throughout this research for waveguides and waveguide Bragg gratings. The potential applications of slow light devices are also highlighted in this chapter.

Chapter 3 describes the methodology used in this thesis, which covers the fabrication and characterization methods for the slow light devices (including three sections: waveguides, dot-Bragg gratings, and line-Bragg gratings) and outlines the structure of the articles that form the main body of the thesis.

Chapters 4 to 6 present the core content of the thesis, comprising three articles that explore slow-light effects in waveguide Bragg gratings (Objectives 1~5). These chapters detail the successful creation of novel waveguides (Objective 1) with Bragg gratings to achieve resonant characteristics (Objective 2). Offset engineering is applied in line-Bragg gratings to enhance the slow-light effect, as represented by the derived formula of slow-down factor (Objectives 3~4), while the center-to-center distance is optimized in dot-Bragg gratings, combined with offset engineering (Objective 5), to further improve the slow light performance.

The thesis concludes with a general discussion and conclusions in Chapters 7 and 8.

8.2 Recommendations for future work

In this thesis, the slow-light effects in waveguide Bragg gratings have been investigated based on FSL direct writing techniques within bulk glass slides. Building upon these findings, some

designed examples of waveguide Bragg gratings are presented in Appendix D, and various key areas for future research in this field are proposed as follows:

(1) Optimization writing parameters for higher efficiency waveguides: It would be valuable to explore and refine FSL writing parameters to create new straight waveguide structures exhibiting higher RI changes (on the order of 10^{-2}), while avoiding oversaturation in the waveguide before subsequent inscriptions for Bragg gratings. This optimization could reduce propagation losses in waveguides and enhance the light-matter interaction between the waveguide and gratings. As a result, it could yield Bragg gratings with deeper transmission dips and stronger slow-light effects, facilitating the development of more compact, efficient, and robust slow light devices for integrated photonics.

(2) Exploring bent waveguides with higher RI change: Another avenue of research involves expanding from straight waveguides to bent waveguides with higher RI changes, avoiding oversaturation. Investigating slow light in bent waveguide Bragg gratings which interact with other photonic devices, such as photoconductors, photodiodes, modulators, and amplifiers, leading to more advanced systems that improve overall performance.

(3) Increasing curvature of the bent waveguide for vortex light guiding: Further increasing the bending radius of the waveguide could enable the formation of vortex structures that guide vortex light. By creating vortex waveguide Bragg grating structures, one could realize enhanced light-matter interactions, potentially leading to novel slow-light effects with unique characteristics.

(4) Enhance measurement accuracy for time delay: To minimize or eliminate side lobes in the reflection or transmission spectra, apodization techniques could be applied during the inscription of new waveguide Bragg gratings. This approach may help in accurately measuring group delays, regardless of the method used, such as with the Luna OBR or fast photodiodes, thus improving device precision. Additionally, employing higher precision instruments to improve the accuracy of time delay measurements is another viable option.

REFERENCES

[1] R. R. Gattass and E. Mazur, "Femtosecond laser micromachining in transparent materials," *Nat. Photonics*, vol. 2, no. 4, pp. 219–225, Apr. 2008, doi: 10.1038/nphoton.2008.47.

[2] R. W. Boyd and D. J. Gauthier, *"Slow" and "fast" light*, vol. 43, no. C. Elsevier Masson SAS, 2002. doi: 10.1016/S0079-6638(02)80030-0.

[3] G. M. Gehring, R. W. Boyd, A. L. Gaeta, D. J. Gauthier, and A. E. Willner, "Fiber-Based Slow-Light Technologies," *J. Light. Technol.*, vol. 26, no. 23, pp. 3752–3762, Dec. 2008, doi: 10.1109/JLT.2008.2004883.

[4] T. Baba, "Slow light in photonic crystals," *Nat. Photonics*, vol. 2, no. 8, pp. 465–473, Aug. 2008, doi: 10.1038/nphoton.2008.146.

[5] C. Monat, M. De Sterke, and B. J. Eggleton, "Slow light enhanced nonlinear optics in periodic structures," *J. Opt.*, vol. 12, no. 10, p. 104003, 2010, doi: 10.1088/2040-8978/12/10/104003.

[6] R. W. Boyd, D. J. Gauthier, and A. L. Gaeta, "Applications of Slow Light in Telecommunications," *Opt. Photonics News*, vol. 17, no. 4, pp. 18–23, 2006, doi: 10.1364/opn.17.4.000018.

[7] J. B. Khurgin and R. S. Tucker, *Slow Light Science and Applications*. CRC Press, 2009.

[8] R. W. Boyd, "Material slow light and structural slow light: similarities and differences for nonlinear optics [Invited]: reply," *J. Opt. Soc. Am. B*, vol. 29, no. 9, p. 2644, Sep. 2012, doi: 10.1364/JOSAB.29.002644.

[9] M. SoljaČiĆ and J. D. Joannopoulos, "Enhancement of nonlinear effects using photonic crystals," *Nat. Mater.*, vol. 3, no. 4, pp. 211–219, Apr. 2004, doi: 10.1038/nmat1097.

[10] S. A. Schulz, L. O'Faolain, D. M. Beggs, T. P. White, A. Melloni, and T. F. Krauss, "Dispersion engineered slow light in photonic crystals: A comparison," *Journal of Optics*, vol. 12, no. 10. p. 104004, 2010. doi: 10.1088/2040-8978/12/10/104004.

[11] T. Datta, M. Sen, I. Loss, and T. F. Krauss, "Slow light in photonic crystal waveguides," *J. Phys. D. Appl. Phys.*, vol. 40, no. 9, pp. 2666–2670, 2007, doi: 10.1088/0022-3727/40/9/S07.

[12] A. Yariv, Y. Xu, R. K. Lee, and A. Scherer, “Coupled-resonator optical waveguide: a proposal and analysis,” *Opt. Lett.*, vol. 24, no. 11, pp. 711–713, Jun. 1999, doi: 10.1364/OL.24.000711.

[13] S. Mookherjea, J. S. Park, S.-H. H. Yang, and P. R. Bandaru, “Localization in silicon nanophotonic slow-light waveguides,” *Nat. Photonics*, vol. 2, no. 2, pp. 90–93, Feb. 2008, doi: 10.1038/nphoton.2007.278.

[14] K. L. Tsakmakidis, A. D. Boardman, and O. Hess, “‘Trapped rainbow’ storage of light in metamaterials,” *Nature*, vol. 450, no. 7168, pp. 397–401, 2007, doi: 10.1038/nature06285.

[15] S. Zhang, D. A. Genov, Y. Wang, M. Liu, and X. Zhang, “Plasmon-induced transparency in metamaterials,” *Phys. Rev. Lett.*, vol. 101, no. 4, pp. 1–4, 2008, doi: 10.1103/PhysRevLett.101.047401.

[16] P. Tassin, L. Zhang, T. Koschny, E. N. Economou, and C. M. Soukoulis, “Low-loss metamaterials based on classical electromagnetically induced transparency,” *Phys. Rev. Lett.*, vol. 102, no. 5, pp. 6–9, 2009, doi: 10.1103/PhysRevLett.102.053901.

[17] C. J. Chang-Hasnain and S. L. Chuang, “Slow and Fast Light in Semiconductor Quantum-Well and Quantum-Dot Devices,” *J. Light. Technol.*, vol. 24, no. 12, pp. 4642–4654, Dec. 2006, doi: 10.1109/JLT.2006.885767.

[18] M. L. Povinelli, S. G. Johnson, and J. D. Joannopoulos, “Slow-light, band-edge waveguides for tunable time delays,” *Opt. Express*, vol. 13, no. 18, pp. 7145–7159, 2005.

[19] P. C. Ku, C. J. Chang-Hasnain, and S. L. Chuang, “Slow light in semiconductor heterostructures,” *J. Phys. D. Appl. Phys.*, vol. 40, no. 5, pp. R93–R107, Mar. 2007, doi: 10.1088/0022-3727/40/5/R01.

[20] Z. Zhu, D. J. Gauthier, A. L. Gaeta, and R. W. Boyd, “Slow Light in Optical Waveguides,” no. September, 2008. doi: 10.1201/9781420061529.ch3.

[21] P. Jean, A. Gervais, S. LaRochelle, and W. Shi, “Slow Light in Subwavelength Grating Waveguides,” *IEEE J. Sel. Top. Quantum Electron.*, vol. 26, no. 2, pp. 1–8, Mar. 2020, doi: 10.1109/JSTQE.2019.2933788.

[22] G. Skolianos, A. Arora, M. Bernier, and M. Digonnet, “Slow light in fiber Bragg gratings

and its applications," *J. Phys. D. Appl. Phys.*, vol. 49, no. 46, p. 463001, Nov. 2016, doi: 10.1088/0022-3727/49/46/463001.

[23] A. Melloni, F. Morichetti, and M. Martinelli, "Optical Slow Wave Structures," *Opt. Photonics News*, vol. 14, no. 11, p. 44, 2003, doi: 10.1364/opn.14.11.000044.

[24] T. Baba and D. Mori, "Slow light engineering in photonic crystals," *J. Phys. D. Appl. Phys.*, vol. 40, no. 9, pp. 2659–2665, 2007, doi: 10.1088/0022-3727/40/9/S06.

[25] P.-C. Ku, "Semiconductor slow-light device," *PhD Diss. Univ. California, Berkeley*, pp. 1–192, 2003.

[26] R. C. Rumpf, "Advanced Electromagnetics: 21st Century Electromagnetics, Lecture #22 Slow Waves," 2020. https://empossible.net/wp-content/uploads/2020/01/Lecture-Slow-Waves.pdf

[27] R. W. Boyd, "Slow and fast light: Fundamentals and applications," *J. Mod. Opt.*, vol. 56, no. 18–19, pp. 1908–1915, 2009, doi: 10.1080/09500340903159495.

[28] L. V. Hau, S. E. Harris, Z. Dutton, and C. H. Behroozi, "Light speed reduction to 17 metres per second in an ultracold atomic gas," *Nature*, vol. 397, pp. 594–598, Feb. 1999, doi: 10.1038/17561.

[29] J. Marangos, "Slow light in cool atoms," *Nature*, vol. 397, pp. 559–560, 1999, doi: 10.1038/17475.

[30] M. S. Bigelow, N. N. Lepeshkin, and R. W. Boyd, "Observation of Ultraslow Light Propagation in a Ruby Crystal at Room Temperature," *Phys. Rev. Lett.*, vol. 90, no. 11, p. 113903, Mar. 2003, doi: 10.1103/PhysRevLett.90.113903.

[31] Y. Okawachi *et al.*, "Tunable all-optical delays via brillouin slow light in an optical fiber," *Phys. Rev. Lett.*, vol. 94, no. 15, pp. 1–4, 2005, doi: 10.1103/PhysRevLett.94.153902.

[32] C. Zeng and Y. Cui, "Rainbow trapping of surface plasmon polariton waves in metal-insulator- metal graded grating waveguide," *Opt. Commun.*, vol. 290, pp. 188–191, 2013, doi: 10.1016/j.optcom.2012.10.020.

[33] J. Goeckeritz and S. Blair, "Optical characterization of coupled resonator slow-light rib waveguides," *Opt. Express*, vol. 18, no. 17, p. 18190, Aug. 2010, doi:

10.1364/OE.18.018190.

[34] J. Poon, J. Scheuer, S. Mookherjea, G. T. Paloczi, Y. Huang, and A. Yariv, “Matrix analysis of microring coupled-resonator optical waveguides,” *Opt. Express*, vol. 12, no. 1, p. 90, 2004, doi: 10.1364/OPEX.12.000090.

[35] S. Mookherjea and A. Yariv, “Coupled resonator optical waveguides,” *IEEE J. Sel. Top. Quantum Electron.*, vol. 8, no. 3, pp. 448–456, May 2002, doi: 10.1109/JSTQE.2002.1016347.

[36] M. L. Cooper *et al.*, “Statistics of light transport in 235-ring silicon coupled-resonator optical waveguides,” *Opt. Express*, vol. 18, no. 25, p. 26505, Dec. 2010, doi: 10.1364/OE.18.026505.

[37] Z. Zhao, H. Zhao, R. T. Ako, J. Zhang, H. Zhao, and S. Sriram, “Demonstration of group delay above 40 ps at terahertz plasmon-induced transparency windows,” *Opt. Express*, vol. 27, no. 19, p. 26459, 2019, doi: 10.1364/oe.27.026459.

[38] T. Amemiya *et al.*, “Demonstration of slow-light effect in silicon-wire waveguides combined with metamaterials,” *Opt. Express*, vol. 27, no. 10, p. 15007, May 2019, doi: 10.1364/oe.27.015007.

[39] R. Halir *et al.*, “Subwavelength-Grating Metamaterial Structures for Silicon Photonic Devices,” *Proc. IEEE*, vol. 106, no. 12, pp. 2144–2157, Dec. 2018, doi: 10.1109/JPROC.2018.2851614.

[40] S. Yamasaki, T. Amemiya, Z. Gu, J. Suzuki, N. Nishiyama, and S. Arai, “Analysis of the slow-light effect in silicon wire waveguides with metamaterials,” *J. Opt. Soc. Am. B*, vol. 35, no. 4, p. 797, 2018, doi: 10.1364/josab.35.000797.

[41] A. Gervais, P. Jean, W. Shi, and S. LaRochelle, “Design of Slow-Light Subwavelength Grating Waveguides for Enhanced On-Chip Methane Sensing by Absorption Spectroscopy,” *IEEE J. Sel. Top. Quantum Electron.*, vol. 25, no. 3, pp. 1–8, May 2019, doi: 10.1109/JSTQE.2018.2885496.

[42] Q. Chen, J.-S. Boisvert, M. S. Sharawi, and R. Kashyap, “Bragg gratings with novel waveguide models fabricated in bulk glass via fs-laser writing and their slow-light effects,” *Opt. Express*, vol. 32, no. 1, pp. 188–204, 2024, doi: 10.1364/oe.509482.

[43] Q. Chen, J.-S. Boisvert, F. Jafari, M. S. Sharawi, S. Loranger, and R. Kashyap, "Offset-enhanced slow light in femtosecond laser-fabricated Bragg gratings," *Opt. Express*, vol. 32, no. 22, pp. 39257–39266, Oct. 2024, doi: 10.1364/OE.537736.

[44] R. M. De La Rue, "Slower for longer," *Nat. Photonics*, vol. 2, no. 12, pp. 715–716, Dec. 2008, doi: 10.1038/nphoton.2008.238.

[45] R. Kashyap, *Fiber Bragg Gratings*, 2nd ed. Academic Press, 2010.

[46] T. Erdogan, "Fiber grating spectra," *J. Light. Technol.*, vol. 15, no. 8, pp. 1277–1294, 1997, doi: 10.1109/50.618322.

[47] K. M. Davis, K. Miura, N. Sugimoto, and K. Hirao, "Writing waveguides in glass with a femtosecond laser," *Opt. Lett.*, vol. 21, no. 21, pp. 1729–1731, 1996, doi: 10.1364/ol.21.001729.

[48] K. Miura, J. Qiu, H. Inouye, T. Mitsuyu, and K. Hirao, "Photowritten optical waveguides in various glasses with ultrashort pulse laser," *Appl. Phys. Lett.*, vol. 71, no. 23, pp. 3329–3331, 1997, doi: 10.1063/1.120327.

[49] E. N. Glezer *et al.*, "Three-dimensional optical storage inside transparent materials," *Opt. Lett.*, vol. 21, no. 24, pp. 2023–2025, 1996, doi: 10.1364/ol.22.000422.

[50] E. N. Glezer and E. Mazur, "Ultrafast-laser driven micro-explosions in transparent materials," *Appl. Phys. Lett.*, vol. 71, no. 7, pp. 882–884, 1997.

[51] J. Qiu, "Femtosecond laser-induced microstructures in glasses and applications in micro-optics," *Chem. Rec.*, vol. 4, no. 1, pp. 50–58, 2004, doi: 10.1002/tcr.20006.

[52] V. R. Bhardwaj *et al.*, "Femtosecond laser-induced refractive index modification in multicomponent glasses," *J. Appl. Phys.*, vol. 97, no. 8, pp. 083102 (1–9), 2005, doi: 10.1063/1.1876578.

[53] D. M. Krol, "Femtosecond laser modification of glass," *J. Non. Cryst. Solids*, vol. 354, no. 2–9, pp. 416–424, 2008, doi: 10.1016/j.jnoncrysol.2007.01.098.

[54] S. M. Eaton *et al.*, "Heat accumulation effects in femtosecond laser-written waveguides with variable repetition rate," *Opt. Express*, vol. 13, no. 12, pp. 4708–4716, 2005, doi: 10.1364/opex.13.004708.

[55] S. M. Eaton *et al.*, “Transition from thermal diffusion to heat accumulation in high repetition rate femtosecond laser writing of buried optical waveguides,” *Opt. Express*, vol. 16, no. 13, pp. 9443–9458, 2008, doi: 10.1364/oe.16.009443.

[56] L. Shah, A. Y. Arai, S. M. Eaton, and P. R. Herman, “Waveguide writing in fused silica with a femtosecond fiber laser at 522 nm and 1 MHz repetition rate,” *Opt. Express*, vol. 13, no. 6, p. 1999, 2005, doi: 10.1364/opex.13.001999.

[57] A. M. Streltsov and N. F. Borrelli, “Study of femtosecond-laser-written waveguides in glasses,” *J. Opt. Soc. Am. B*, vol. 19, no. 10, pp. 2496–2504, 2002.

[58] J. Burghoff, S. Nolte, and A. Tünnermann, “Origins of waveguiding in femtosecond laser-structured LiNbO3,” *Appl. Phys. A Mater. Sci. Process.*, vol. 89, no. 1, pp. 127–132, 2007, doi: 10.1007/s00339-007-4152-0.

[59] J. Lapointe and R. Kashyap, “Laser Processed Photonic Devices,” in *Planar Waveguides and other Confined Geometries*, vol. 189, Springer, 2015, pp. 129–167.

[60] L. Li, W. Kong, and F. Chen, “Femtosecond laser-inscribed optical waveguides in dielectric crystals: A concise review and recent advances,” *Adv. Photonics*, vol. 4, no. 2, pp. 024002(1–29), 2022, doi: 10.1117/1.AP.4.2.024002.

[61] M. Heinrich *et al.*, “Evanescent coupling in arrays of type II femtosecond laser-written waveguides in bulk x-cut lithium niobate,” *Appl. Phys. Lett.*, vol. 93, p. 101111, Sep. 2008, doi: 10.1063/1.2981801.

[62] H. Zhang, S. M. Eaton, and P. R. Herman, “Low-loss Type II waveguide writing in fused silica with single picosecond laser pulses,” *Opt. Express*, vol. 14, no. 11, p. 4826, 2006, doi: 10.1364/oe.14.004826.

[63] J. Wu and X. Shu, “Multifunctional Line-by-Line Tilted Waveguide Bragg Gratings Directly Written by Femtosecond Laser,” *J. Light. Technol.*, vol. 42, no. 16, pp. 5639–5644, 2024, doi: 10.1109/JLT.2024.3394838.

[64] M. Thiel, G. Flachenecker, and W. Schade, “Femtosecond laser writing of Bragg grating waveguide bundles in bulk glass,” *Opt. Lett.*, vol. 40, no. 7, pp. 1266–1269, 2015, doi: 10.1364/ol.40.001266.

[65] H. E. Lazcano and G. V. Vázquez, “Low-repetition rate femtosecond laser writing of optical waveguides in water-white glass slides,” *Appl. Opt.*, vol. 55, no. 12, pp. 3268–3273, 2016, doi: 10.1364/ao.55.003268.

[66] K. Suzuki, V. Sharma, J. G. Fujimoto, E. P. Ippen, and Y. Nasu, “Characterization of symmetric [3 x 3] directional couplers fabricated by direct writing with a femtosecond laser oscillator,” *Opt. Express*, vol. 14, no. 6, pp. 2335–2343, 2006, doi: 10.1364/oe.14.002335.

[67] A. M. Streltsov and N. F. Borrelli, “Fabrication and analysis of a directional coupler written in glass by nanojoule femtosecond laser pulses,” *Opt. Lett.*, vol. 26, no. 1, pp. 42–43, 2001, doi: 10.1364/ol.26.000042.

[68] K. Minoshima, A. Kowalevicz, E. Ippen, and J. Fujimoto, “Fabrication of coupled mode photonic devices in glass by nonlinear femtosecond laser materials processing,” *Opt. Express*, vol. 10, no. 15, pp. 645–652, 2002, doi: 10.1364/oe.10.000645.

[69] W. Watanabe, T. Asano, K. Yamada, K. Itoh, and J. Nishii, “Wavelength division with three-dimensional couplers fabricated by filamentation of femtosecond laser pulses,” *Opt. Lett.*, vol. 28, no. 24, pp. 2491–2493, 2003, doi: 10.1364/ol.28.002491.

[70] S. M. Eaton, W. J. Chen, H. Zhang, and P. R. Herman, “Telecom-band directional couplers written with a high repetition rate femtosecond fiber laser,” *Opt. InfoBase Conf. Pap.*, vol. 18, no. 20, pp. 2174–2176, 2006.

[71] A. M. Kowalevicz, V. Sharma, E. P. Ippen, J. G. Fujimoto, and K. Minoshima, “Three-dimensional photonic devices fabricated in glass by a femtosecond oscillator,” *Springer Ser. Chem. Phys.*, vol. 79, no. 9, pp. 801–803, 2004.

[72] N. D. Psaila *et al.*, “Er:Yb-doped oxyfluoride silicate glass waveguide amplifier fabricated using femtosecond laser inscription,” *Appl. Phys. Lett.*, vol. 90, no. 13, pp. 131102(1–4), 2007, doi: 10.1063/1.2716866.

[73] S. Taccheo *et al.*, “Er:Yb-doped waveguide laser fabricated by femtosecond laser pulses,” *Opt. Lett.*, vol. 29, no. 22, pp. 2626–2628, 2004, doi: 10.1364/ol.29.002626.

[74] G. D. Marshall, M. Ams, and M. J. Withford, “Direct laser written waveguide-Bragg gratings in bulk fused silica,” *Opt. Lett.*, vol. 31, no. 18, pp. 2690–2691, 2006, doi: 10.1364/ol.31.002690.

[75] H. Zhang, S. M. Eaton, J. Li, and P. R. Herman, “Femtosecond laser direct writing of multiwavelength Bragg grating waveguides in glass,” *Opt. Lett.*, vol. 31, no. 23, pp. 3495–3497, 2006, doi: 10.1364/ol.31.003495.

[76] S. Nolte, M. Will, J. Burghoff, and A. Tuennermann, “Femtosecond waveguide writing: A new avenue to three-dimensional integrated optics,” *Appl. Phys. A Mater. Sci. Process.*, vol. 77, no. 1, pp. 109–111, 2003, doi: 10.1007/s00339-003-2088-6.

[77] S. Gross and M. J. Withford, “Ultrafast-laser-inscribed 3D integrated photonics: Challenges and emerging applications,” *Nanophotonics*, vol. 4, no. 1, pp. 332–352, 2015, doi: 10.1515/nanoph-2015-0020.

[78] F. Sima, K. Sugioka, R. M. Vázquez, R. Osellame, L. Kelemen, and P. Ormos, “Three-dimensional femtosecond laser processing for lab-on-a-chip applications,” *Nanophotonics*, vol. 7, no. 3, pp. 613–634, 2018, doi: 10.1515/nanoph-2017-0097.

[79] M. Ams, P. Dekker, S. Gross, and M. J. Withford, “Fabricating waveguide Bragg gratings (WBGs) in bulk materials using ultrashort laser pulses,” *Nanophotonics*, vol. 6, no. 5, pp. 743–763, 2017, doi: 10.1515/nanoph-2016-0119.

[80] H. Zhang, S. M. Eaton, and P. R. Herman, “Single-step writing of Bragg grating waveguides in fused silica with an externally modulated femtosecond fiber laser,” *Opt. Lett.*, vol. 32, no. 17, pp. 2559–2561, 2007.

[81] K. Zhou, M. Dubov, C. Mou, L. Zhang, V. K. Mezentsev, and I. Bennion, “Line-by-Line Fiber Bragg Grating Made by Femtosecond Laser,” *IEEE Photonics Technol. Lett.*, vol. 22, no. 16, pp. 1190–1192, Aug. 2010, doi: 10.1109/LPT.2010.2050877.

[82] J. Wu, R. Zhao, and X. Shu, “Line-by-Line Inscription of Waveguide Bragg Gratings in Bulk Glass Using Femtosecond Laser,” in *CLEO 2023*, 2023, p. JTu2A.13. doi: 10.1364/CLEO_AT.2023.JTu2A.13.

[83] P. Lu *et al.*, “Plane-by-Plane Inscription of Grating Structures in Optical Fibers,” *J. Light. Technol.*, vol. 36, no. 4, pp. 926–931, 2018, doi: 10.1109/JLT.2017.2750490.

[84] J. Harb, L. Talbot, Y. Petit, M. Bernier, and L. Canioni, “Demonstration of Type A volume Bragg gratings inscribed with a femtosecond Gaussian-Bessel laser beam,” *Opt. Express*, vol. 31, no. 10, pp. 15736–15746, 2023, doi: 10.1364/oe.483722.

[85] J. S. Boisvert, S. Loranger, and R. Kashyap, “Fs laser written volume Raman–Nath grating for integrated spectrometer on smartphone,” *Sci. Rep.*, vol. 13, no. 1, pp. 1–8, 2023, doi: 10.1038/s41598-023-40909-9.

[86] A. Theodosiou *et al.*, “Modified fs-Laser Inscribed FBG Array for Rapid Mode Shape Capture of Free-Free Vibrating Beams,” *IEEE Photonics Technol. Lett.*, vol. 28, no. 14, pp. 1509–1512, 2016, doi: 10.1109/LPT.2016.2555852.

[87] R. Osellame *et al.*, “Femtosecond writing of active optical waveguides with astigmatically shaped beams,” *J. Opt. Soc. Am. B*, vol. 20, no. 7, pp. 1559–1567, 2003, doi: 10.1364/josab.20.001559.

[88] M. Ams, G. D. Marshall, D. J. Spence, and M. J. Withford, “Slit beam shaping method for femtosecond laser direct-write fabrication of symmetric waveguides in bulk glasses,” *Opt. Express*, vol. 13, no. 15, pp. 5676–5681, 2005, doi: 10.1364/opex.13.005676.

[89] P. Roldan-Varona, D. Pallares-Aldeiturriaga, L. Rodriguez-Cobo, and J. M. Lopez-Higuera, “Slit Beam Shaping Technique for Femtosecond Laser Inscription of Enhanced Plane-by-Plane FBGs,” *J. Light. Technol.*, vol. 38, no. 16, pp. 4526–4532, Aug. 2020, doi: 10.1109/JLT.2020.2992568.

[90] G. Skolianos, A. Arora, M. Bernier, and M. J. F. Digonnet, “Slowing down light to 300 km/s in a deuterium-loaded fiber Bragg grating,” *Opt. Lett.*, vol. 40, no. 7, p. 1524, 2015, doi: 10.1364/ol.40.001524.

[91] G. Skolianos, M. Bernier, R. Vallée, and M. J. F. Digonnet, “Observation of ~20 ns group delay in a low-loss apodized fiber Bragg grating,” *Opt. Lett.*, vol. 39, no. 13, pp. 3978–3981, 2014, doi: 10.1364/ol.39.003978.

[92] G. Curatu, S. LaRochelle, C. Pare, and P.-A. Belanger, “Pulse shaping with a phase-shifted fiber Bragg grating for antisymmetric pulse generation,” in *Optical Pulse and Beam Propagation III*, Apr. 2001, vol. 4271, p. 213. doi: 10.1117/12.424698.

[93] N. K. Berger, B. Levit, B. Fischer, M. Kulishov, D. V. Plant, and J. Azaña, “All-optical temporal differentiator based on a single phase-shifted fiber Bragg grating,” *Conf. Proc. - Lasers Electro-Optics Soc. Annu. Meet.*, pp. 370–371, 2006, doi: 10.1109/LEOS.2006.279136.

[94] N. K. Berger, B. Levit, B. Fischer, M. Kulishov, D. V. Plant, and J. Azaña, "Temporal differentiation of optical signals using a phase-shifted fiber Bragg grating," *Opt. Express*, vol. 15, no. 2, pp. 371–381, 2007, doi: 10.1364/oe.15.000371.

[95] T. J. Kippenberg, S. M. Spillane, and K. J. Vahala, "Demonstration of ultra-high- Q small mode volume toroid microcavities on a chip," *Appl. Phys. Lett.*, vol. 85, no. 25, pp. 6113–6115, 2004, doi: 10.1063/1.1833556.

[96] I. V. Kabakova, C. M. de Sterke, and B. J. Eggleton, "Bistable switching and reshaping of optical pulses in a Bragg grating cavity," *J. Opt. Soc. Am. B*, vol. 27, no. 12, pp. 2648–2653, 2010, doi: 10.1364/josab.27.002648.

[97] J. Upham *et al.*, "Enhancing optical field intensities in Gaussian-profile fiber Bragg gratings," *Opt. Lett.*, vol. 39, no. 4, pp. 849–852, 2014, doi: 10.1364/ol.39.000849.

[98] G. P. Agrawal, *Fiber-Optic Communication Systems*, 4th ed. Wiley, 2012.

[99] E. M. Purcell, "Spontaneous emission probabilities at radio frequencies," *Phys. Rev.*, vol. 69, p. 681, 1946.

[100] G. Skolianos, A. Arora, M. Bernier, and M. J. F. Digonnet, "High Purcell factor in fiber Bragg gratings utilizing the fundamental slow-light mode," *Opt. Lett.*, vol. 40, no. 15, pp. 3440–3443, 2015, doi: 10.1364/ol.40.003440.

[101] H. Wen, M. Terrel, S. Fan, and M. Digonnet, "Sensing with slow light in fiber Bragg gratings," *IEEE Sens. J.*, vol. 12, no. 1, pp. 156–163, Jan. 2012, doi: 10.1109/JSEN.2011.2135343.

[102] H. Wen, G. Skolianos, S. Fan, M. Bernier, R. Vallee, and M. J. F. Digonnet, "Slow-light fiber-bragg-grating strain sensor with a 280-femtostrain/√Hz resolution," *J. Light. Technol.*, vol. 31, no. 11, pp. 1804–1808, 2013, doi: 10.1109/JLT.2013.2258658.

[103] A. Rosenthal, D. Razansky, and V. Ntziachristos, "High-sensitivity compact ultrasonic detector based on a pi-phase-shifted fiber Bragg grating," *Opt. Lett.*, vol. 36, no. 10, pp. 1833–1835, 2011, doi: 10.1364/ol.36.001833.

[104] J. Lapointe, "Fonctionnalisation des écrans de téléphones mobiles : des premiers dispositifs invisibles à l'amélioration de l'écriture par laser," Polytechnique Montreal, 2017.

[105] A. Roberge, “Fabrication of fiber Bragg gratings using femtosecond laser direct-writing techniques,” Polytechnique Montreal, 2022.

[106] S. Loranger, “Discovery and Correction of Spatial Non-Uniformity in Optical Fibers: Towards the Fabrication of Perfect Ultra-Long Fiber Bragg Gratings for Applications in Non-Linear Optics,” Polytechnique Montréal, 2018.

[107] J.-S. Boisvert, “L’écriture laser femtoseconde comme vecteur d’intégration de la photonique au téléphone intelligent,” Polytechnique Montréal, 2023.

[108] J.-S. Boisvert *et al.*, “Photosensitised PDMS for femtosecond laser writing,” *OSA Contin.*, vol. 3, no. 5, pp. 1334–1345, 2020, doi: 10.1364/osac.386533.

[109] M. Ams *et al.*, “Investigation of ultrafast laser-photonic material interactions: Challenges for directly written glass photonics,” *IEEE J. Sel. Top. Quantum Electron.*, vol. 14, no. 5, pp. 1370–1388, 2008, doi: 10.1109/JSTQE.2008.925809.

[110] A. Drouin, P. Lorre, J.-S. Boisvert, S. Loranger, V. L. Iezzi, and R. Kashyap, “Spatially resolved cross-sectional refractive index profile of fs laser–written waveguides using a genetic algorithm,” *Opt. Express*, vol. 27, no. 3, pp. 2488–2498, 2019, doi: 10.1364/oe.27.002488.

[111] M. Malinauskas *et al.*, “Ultrafast laser processing of materials: From science to industry,” *Light Sci. Appl.*, vol. 5, no. 8, pp. 3–5, 2016, doi: 10.1038/lsa.2016.133.

[112] G. Della Valle, R. Osellame, and P. Laporta, “Micromachining of photonic devices by femtosecond laser pulses,” *J. Opt. A Pure Appl. Opt.*, vol. 11, pp. 013001–013009, 2009, doi: 10.1088/1464-4258/11/1/013001.

[113] C. Florea and K. A. Winick, “Fabrication and characterization of photonic devices directly written in glass using femtosecond laser pulses,” *J. Light. Technol.*, vol. 21, no. 1, pp. 246–253, 2003, doi: 10.1109/JLT.2003.808678.

[114] J. Del Hoyo, P. Moreno-Zarate, G. Escalante, J. A. Valles, P. Fernandez, and J. Solis, “High-efficiency waveguide optical amplifiers and lasers via FS-Laser induced local modification of the glass composition,” *J. Light. Technol.*, vol. 35, no. 14, pp. 2955–2959, 2017, doi: 10.1109/JLT.2017.2705422.

[115] T. Toney Fernandez *et al.*, “Ion migration assisted inscription of high refractive index contrast waveguides by femtosecond laser pulses in phosphate glass,” *Opt. Lett.*, vol. 38, no. 24, p. 5248, 2013, doi: 10.1364/ol.38.005248.

[116] M. Hughes, W. Yang, and D. Hewak, “Fabrication and characterization of femtosecond laser written waveguides in chalcogenide glass,” *Appl. Phys. Lett.*, vol. 90, no. 13, pp. 2005–2008, 2007, doi: 10.1063/1.2718486.

[117] J.-S. Boisvert *et al.*, “Photosensitization agents for fs laser writing in PDMS,” *Sci. Rep.*, vol. 12, no. 1, pp. 1–10, 2022, doi: 10.1038/s41598-022-05366-w.

[118] T. Fukuda, S. Ishikawa, T. Fujii, K. Sakuma, and H. Hosoya, “Improvement on asymmetry of low-loss waveguides written in pure silica glass by femtosecond laser pulses,” *Opt. Fibers Passiv. Components*, vol. 5279, pp. 21–28, 2004, doi: 10.1117/12.520333.

[119] Y. Nasu, M. Kohtoku, and Y. Hibino, “Low-loss waveguides written with a femtosecond laser for flexible interconnection in a planar light-wave circuit,” *Opt. Lett.*, vol. 30, no. 7, pp. 723–725, 2005, doi: 10.1364/ol.30.000723.

[120] M. Khalid, G. Y. Chen, H. Ebendorff-Heidepreim, and D. G. Lancaster, “Femtosecond laser induced low propagation loss waveguides in a lead-germanate glass for efficient lasing in near to mid-IR,” *Sci. Rep.*, vol. 11, no. 1, pp. 1–12, 2021, doi: 10.1038/s41598-021-90249-9.

[121] D. Tan, X. Sun, Z. Li, and J. Qiu, “Effectively writing low propagation and bend loss waveguides in the silica glass by using a femtosecond laser,” *Opt. Lett.*, vol. 47, no. 18, p. 4766, 2022, doi: 10.1364/ol.470670.

[122] J. Lapointe *et al.*, “Nonlinear increase, invisibility, and sign inversion of a localized fs-laser-induced refractive index change in crystals and glasses,” *Light Sci. Appl.*, vol. 9, no. 1, pp. 1–12, 2020, doi: 10.1038/s41377-020-0298-8.

[123] A. Ghatak and K. Thyagarajan, *Introduction to Fiber Optics*. Cambridge: Cambridge University Press, 1998.

[124] A. Yariv and P. Yeh, *Photonics: Optical Electronics in Modern Communications*, 6th ed. Oxford University Press, 2006.

[125] M. Rubin, “Optical properties of soda lime silica glasses,” *Sol. Energy Mater.*, vol. 12, no. 4, pp. 275–288, 1985, doi: 10.1016/0165-1633(85)90052-8.

[126] Y. Sun *et al.*, “Peak wavelength and bandwidth tunable fiber Bragg grating notch filter induced by femtosecond laser point by point inscription,” *Opt. Commun.*, vol. 521, no. May, p. 128583, 2022, doi: 10.1016/j.optcom.2022.128583.

[127] Luna Innovations, “Using a Circulator to Make Insertion Loss Measurements in Transmission with the Optical Backscatter Reflectometer,” 2013. https://lunainc.com/sites/default/files/assets/files/resource-library/LT_TD_EN-FY1306_IL-in-Transmission-Using-the-OBR-with-Circulator_v5.pdf

[128] G. Rodriguez and S. M. Gilbertson, “Ultrafast fiber bragg grating interrogation for sensing in detonation and shock wave experiments,” *Sensors (Switzerland)*, vol. 17, no. 248, pp. 1–20, 2017, doi: 10.3390/s17020248.

[129] L. Poladian, “Group-delay reconstruction for fiber Bragg gratings in reflection and transmission,” *Opt. Lett.*, vol. 22, no. 20, pp. 1571–1573, 1997, doi: 10.1364/ol.22.001571.

[130] H. Wen, M. Terrel, S. Fan, and M. Digonnet, “Sensing With Slow Light in Fiber Bragg Gratings,” *IEEE Sens. J.*, vol. 12, no. 1, pp. 156–163, Jan. 2012, doi: 10.1109/JSEN.2011.2135343.

[131] C.-W. Chen *et al.*, “Calibration of a High-Resolution Slow-Light Fiber-Bragg-Grating Sensor for Temperature Measurements of Laser-Cooled Fibers,” *J. Light. Technol.*, vol. 42, no. 20, pp. 7391–7397, Oct. 2024, doi: 10.1109/JLT.2024.3416867.

[132] Y. Li, R. Wang, P. Luo, F. Chen, R. Zhou, and X. Qiao, “Sensitivity Enhancement of Fiber Accelerometer Based on Slow-Light Phase-Shifted Fiber Bragg Gratings in Single-Core and Multi-Core Fiber,” *J. Light. Technol.*, vol. 42, no. 8, pp. 3052–3058, Apr. 2024, doi: 10.1109/JLT.2024.3349521.

[133] M. Xu, P. Lei, Y. Bai, Z. Chen, and X. Xie, “Slow-light-enhanced Brillouin scattering with integrated Bragg grating,” *Opt. Lett.*, vol. 49, no. 8, pp. 2177–2180, Apr. 2024, doi: 10.1364/OL.520165.

[134] Y. A. Vlasov, M. O’Boyle, H. F. Hamann, and S. J. McNab, “Active control of slow light on a chip with photonic crystal waveguides,” *Nature*, vol. 438, no. 7064, pp. 65–69, Nov.

2005, doi: 10.1038/nature04210.

[135] T. F. Krauss, “Why do we need slow light?,” *Nat. Photonics*, vol. 2, no. 8, pp. 448–450, 2008, doi: 10.1038/nphoton.2008.139.

[136] J. Wu, R. Zhao, and X. Shu, “Strong line-by-line waveguide Bragg gratings inscribed in bulk glass using femtosecond laser,” *Opt. Laser Technol.*, vol. 180, no. July 2024, p. 111461, Jan. 2025, doi: 10.1016/j.optlastec.2024.111461.

[137] G. D. Marshall, R. J. Williams, N. Jovanovic, M. J. Steel, and M. J. Withford, “Point-by-point written fiber-Bragg gratings and their application in complex grating designs,” *Opt. Express*, vol. 18, no. 19, pp. 19844–19859, 2010, doi: 10.1364/oe.18.019844.

[138] S. Mazoyer, J. P. Hugonin, and P. Lalanne, “Disorder-induced multiple scattering in photonic-crystal waveguides,” *Phys. Rev. Lett.*, vol. 103, no. 6, pp. 1–4, 2009, doi: 10.1103/PhysRevLett.103.063903.

[139] L. O’Faolain *et al.*, “Loss engineered slow light waveguides,” *Opt. Express*, vol. 18, no. 26, p. 27627, Dec. 2010, doi: 10.1364/OE.18.027627.

[140] S. Ek, P. Lunnemann, Y. Chen, E. Semenova, K. Yvind, and J. Mork, “Slow-light-enhanced gain in active photonic crystal waveguides,” *Nat. Commun.*, vol. 5, no. 1, p. 5039, Sep. 2014, doi: 10.1038/ncomms6039.

[141] J. B. Khurgin, “Slow light in various media: a tutorial,” *Adv. Opt. Photonics*, vol. 2, no. 3, p. 287, Sep. 2010, doi: 10.1364/AOP.2.000287.

[142] Y. Hamachi, S. Kubo, and T. Baba, “Low dispersion slow light and nonlinearity enhancement in lattice-shifted photonic crystal waveguide,” *Conf. Quantum Electron. Laser Sci. - Tech. Dig. Ser.*, vol. 34, no. 7, pp. 1072–1074, 2008, doi: 10.1109/QELS.2008.4553172.

[143] D. Tan, K. N. Sharafudeen, Y. Yue, and J. Qiu, “Femtosecond laser induced phenomena in transparent solid materials: Fundamentals and applications,” *Prog. Mater. Sci.*, vol. 76, pp. 154–228, Mar. 2016, doi: 10.1016/j.pmatsci.2015.09.002.

[144] J. He, B. Xu, X. Xu, C. Liao, and Y. Wang, “Review of Femtosecond-Laser-Inscribed Fiber Bragg Gratings: Fabrication Technologies and Sensing Applications,” *Photonic Sensors*, vol.

11, no. 2, pp. 203–226, 2021, doi: 10.1007/s13320-021-0629-2.

[145] G. Lenz, B. J. Eggleton, C. K. Madsen, and R. E. Slusher, "Optical delay lines based on optical filters," *IEEE J. Quantum Electron.*, vol. 37, no. 4, pp. 525–532, 2001, doi: 10.1109/3.914401.

[146] R. W. Boyd, "Applications of Slow Light for Telecommunications and Quantum Information," in *Frontiers in Optics*, 2005, p. LWB5. doi: 10.1364/LS.2005.LWB5.

[147] R. S. Tucker, Pei-Cheng Ku, and C. J. Chang-Hasnain, "Slow-light optical buffers: capabilities and fundamental limitations," *J. Light. Technol.*, vol. 23, no. 12, pp. 4046–4066, Dec. 2005, doi: 10.1109/JLT.2005.853125.

[148] Q. Chen, X. Zhang, M. S. Sharawi, and R. Kashyap, "Advances in High–Speed, High–Power Photodiodes: From Fundamentals to Applications," *Appl. Sci.*, vol. 14, no. 8, p. 3410, Apr. 2024, doi: 10.3390/app14083410.

[149] J. Lapointe, F. Parent, E. Soares de Lima Filho, S. Loranger, and R. Kashyap, "Toward the integration of optical sensors in smartphone screens using femtosecond laser writing," *Opt. Lett.*, vol. 40, no. 23, pp. 5654–5657, 2015, doi: 10.1364/ol.40.005654.

[150] R. Kashyap and M. D. L. Rocha, "On the group delay characteristics of chirped fibre Bragg gratings," *Opt. Commun.*, vol. 153, no. 1–3, pp. 19–22, 1998, doi: 10.1016/S0030-4018(98)00212-0.

[151] S. Blais and J. Yao, "Photonic true-time delay beamforming based on superstructured fiber Bragg gratings with linearly increasing equivalent chirps," *J. Light. Technol.*, vol. 27, no. 9, pp. 1147–1154, 2009, doi: 10.1109/JLT.2008.929421.

[152] K. Qian *et al.*, "Tunable delay slow-light in an active fiber Bragg grating," *Opt. Express*, vol. 17, no. 24, p. 22217, 2009, doi: 10.1364/oe.17.022217.

APPENDIX A SUPPLEMENT OF ARTICLE 1: BRAGG GRATINGS WITH NOVEL WAVEGUIDE MODELS FABRICATED IN BULK GLASS VIA FS-LASER WRITING AND THEIR SLOW-LIGHT EFFECTS

A.1 Refractive index (RI) change of PO-WGs with 64 recipes

Given the maximum light guiding of PO-WGs, we explored 64 recipes realized by femtosecond laser (fs-laser) direct-writing, while the refractive index (RI) change is shown in Figure A.1. It can be seen that the biggest RI change is with the recipe of the repetition rate of 606 kHz, the power of 250 mW and the writing speed of 5 mm/s as shown in Figure A.1(a) while a little smaller RI change is demonstrated in Figure A.1(b).

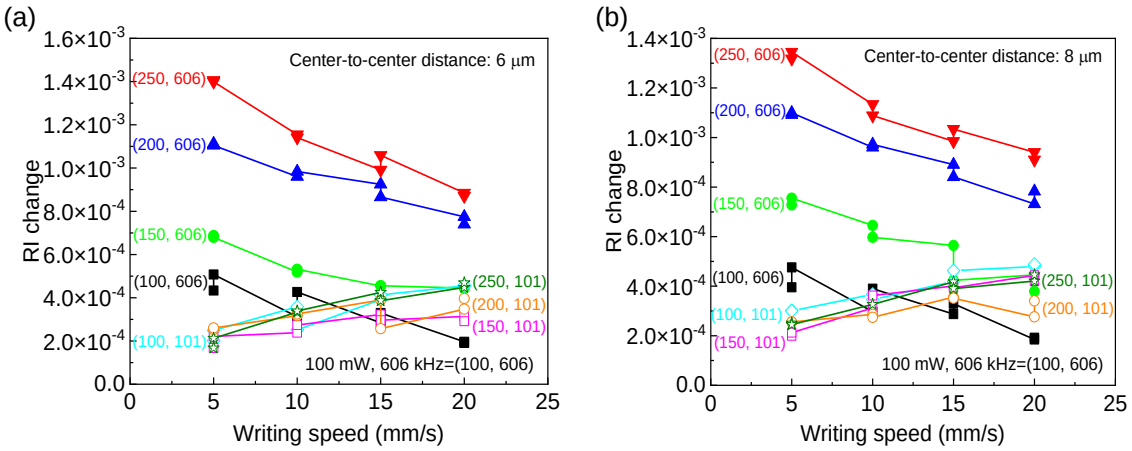

Figure A.1 RI change versus writing speed of 64 recipes for PO-WGs below the glass surface at 397 μm. (a) 6 μm and (b) 8 μm center-to-center distance.

A.2 Schematic of the propagation loss measurements

The propagation loss is obtained from the slope of insertion loss getting from the transmission spectrum measurements, and the corresponding experimental setups are shown in Figures A.2(a, b), which are used for source reference spectrum measurement (without any samples) and sample transmission spectrum measurement (with samples), respectively [A1].

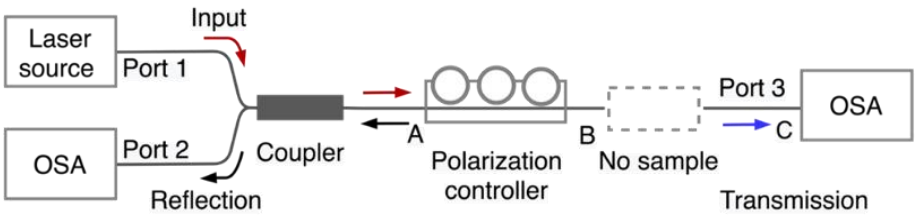

(a) Source reference spectrum measurement.

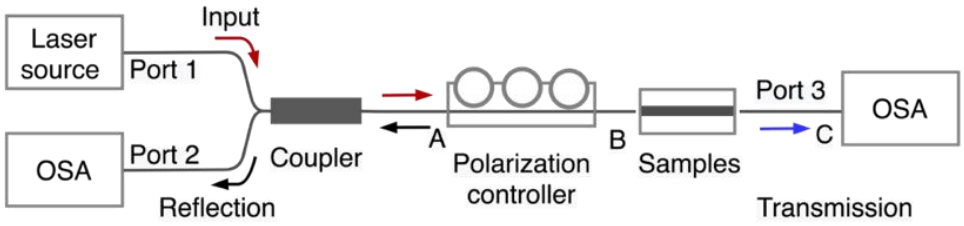

(b) Sample transmission spectrum measurement.

Figure A.2 Schematic of spectrum measurement setups for (a) source reference spectra with the power transmitted from fiber B to fiber C which is expressed as $P_{ref}(\lambda)$, and (b) sample spectra with the power transmitted from fiber B to fiber C which is indicated by $P_o(\lambda)$.

A.3 Schematic of setups for output power, light guided position, and near-field measurements

Schematic of setups for output power, light guided position and near-field measurements are illustrated in Figures A.3(a~c).

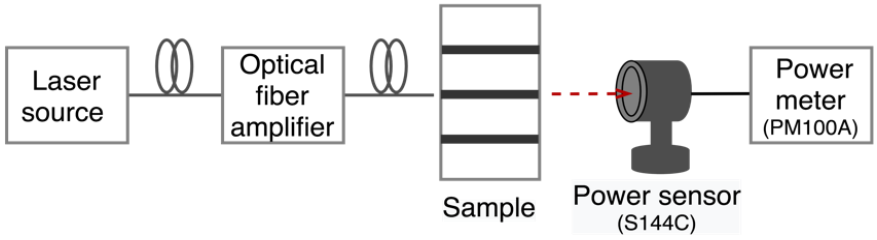

(a) Setup for output power measurement.

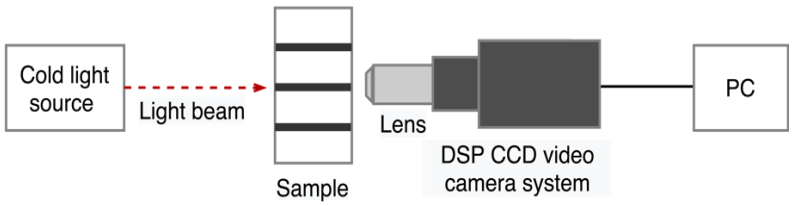

(b) Setup for light guided position measurement.

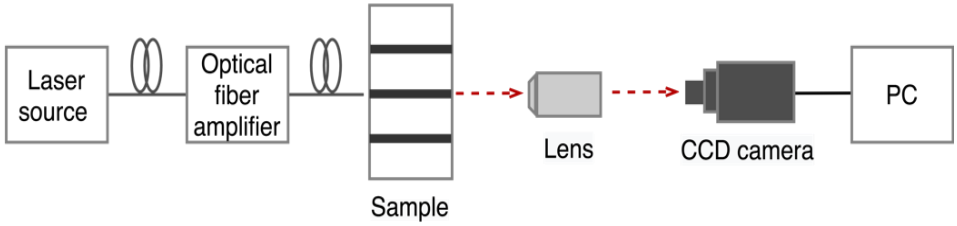

(c) Setup for mode near-field measurement.

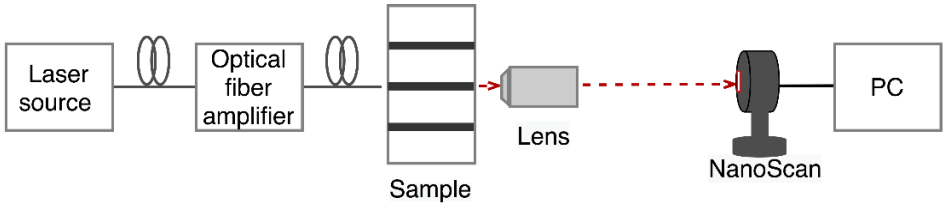

(d) Setup using NanoScan for mode field diameter (MFD) measurement.

Figure A.3 Schematic of setups for (a) output power, (b) light guided position, (c) mode near-field, and (d) mode field diameter (MFD) measurements.

The output power for waveguides and waveguides in Bragg gratings was measured by the experimental setup shown in Figure A.3(a). A 1550 nm laser source and an optical fiber amplifier were used to couple the light from single-mode fiber (SMF28) to waveguides. The input and output end-facets of waveguides were polished to reduce reflection loss. The S144C Integrating Sphere Power Sensor Head with InGaAs Detector and PM100A Handheld Optical Power and Energy Meter were employed to record the measured results. Figure A.3(b) shows the light guided position measured using the white light (Cold light source, intralux 6000-1) and CCD video camera system, while the results will be displayed by computer through the NI-MAX system. The near field was measured using the experimental setup as shown in Figure A.3(c). In addition to the laser source and an optical fiber amplifier, a lens and CCD camera were used to transit and record the near-field

profile, while the color images will be displayed by the monitor of a computer using NI-MAX system. The mode field diameter (MFD) measurement is presented in Figure A.3(d), where the NanoScan device was used in place of the CCD camera shown in Figure A.3(c). The MFDs of the waveguide or waveguide Bragg gratings can be determined by comparing the measured values to that of the standard SMF-28 fiber, which has an MFD of 10.4 μm.

A.4 V-number calculation for waveguides in Bragg gratings

The operation modes of dot-Bragg grating and line-Bragg grating can be estimated by V-number and the equation is given by [A2]

$$V = \frac{2\pi}{\lambda} r \sqrt{n_{core}^2 - n_{clad}^2} \qquad (A.1)$$

where the λ is the wavelength, r is the radius, n_{core} and n_{clad} are the refractive index of core and cladding parts.

Figure A.4 Side views of (a) PO-WGs (with dot) of dot-Bragg grating, and (b) DO-WGs of line-Bragg grating.

We assume that the working wavelength, λ, is 1550 nm, while the radii for PO-WGs of dot-Bragg grating are 4 μm and 6 μm along r_1 and r_2 direction shown in Figure A.4(a). Given the effective index with an estimated value of 1.49 by the writing parameters and the average RI change of 1.3×10^{-3} (Figure A.5(c)), so we can assume $n_{core,dot} = 1.49 + (1.3 \times 10^{-3})$ and $n_{clad,dot} = 1.49 - (1.3 \times 10^{-3})$. According to equation (A.1), we can get the two V-number values are $V_{1,dot} = 1.43$ and $V_{2,dot} = 2.14$, which are smaller than 2.405, so the dot-Bragg grating just works at LP_{01} mode.

For DO-WGs of line-Bragg grating, as shown in Figure A.4(b), the effective radii for r_3 and r_4 are 9.2 μm and 8.15 μm, the average RI change of 1.63×10^{-3} (Figure A.8(d)), while the core and cladding refractive indices are assumed as $n_{core,line} = 1.49 + (1.63 \times 10^{-3})$ and $n_{clad,line} =$

$1.49 - (1.63 \times 10^{-3})$, respectively. Similarly, the V-number can be calculated by equation (A.1) to be $V_{3,line} = 3.68$ and $V_{4,line} = 3.26$. Because those two values are all bigger than 2.405 but smaller than 3.832, so the line-Bragg grating works at LP_{01} and LP_{11} modes.

A.5 Experimental setup for transmission and reflection spectra measurements

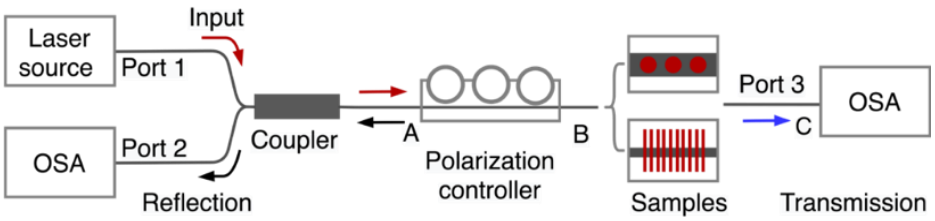

Figure A.5 Experimental setup for transmission and reflection measurements. The top is dot-Bragg grating and the bottom is line-Bragg grating. OSA: Optical Spectrum Analyzer.

A.6 Transmission and reflection spectra for PO-WGs line-Bragg grating

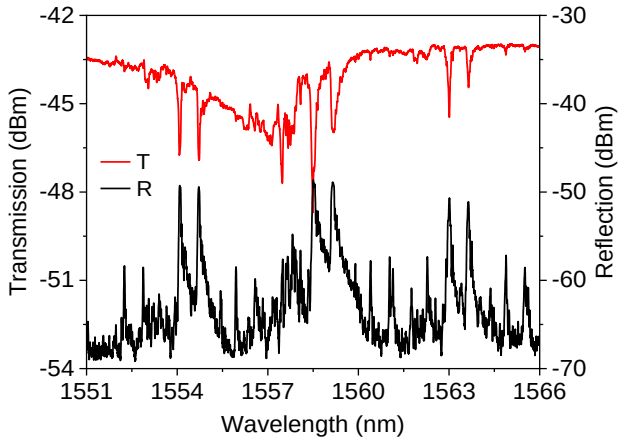

Figure A.6 Transmission (T) and reflection (R) spectra of PO-WGs line-Bragg grating.

A.7 Schematic of setup for group delay measurement

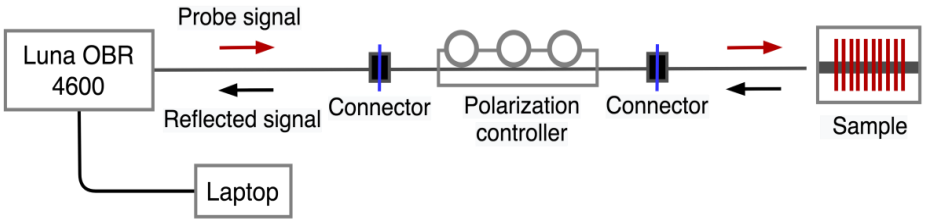

(a) Schematic of setup for group delay measurement in reflection.

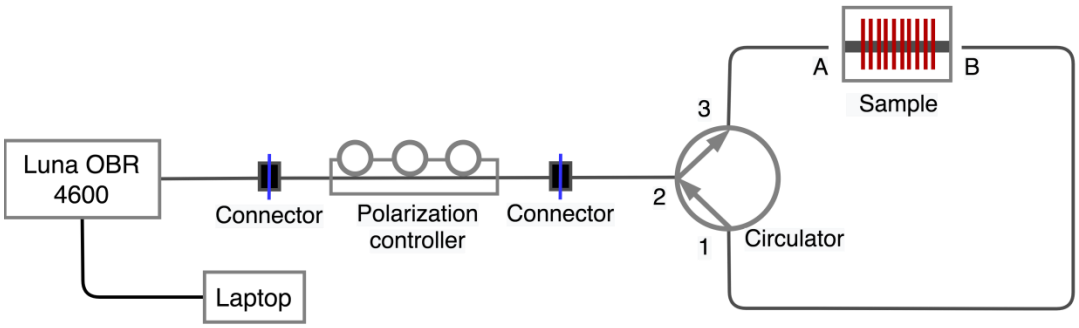

(b) Schematic of setup for group delay measurement in transmission.

Figure A.7 Schematic of setup to measure return loss (reflection and transmission [A3]) and group delay in (a) reflection and (b) transmission for line-Bragg grating by Luna OBR 4600 Optical Backscatter Reflectometer (OBR) with polarization controller. The gel was used to reduce reflections in between fiber and facets (e.g. A and B in (b)) of samples, while the measurement results were directly displayed and collected by the OBR control software from a laptop.

A.8 Bandgap calculation via Bloch's theorem and coupled-mode theory (CMT)

An example of 'bandgap' calculation for the line-Bragg grating, which operates at TM mode with a resonant wavelength of 1602.55 nm (Figure A.10(a)), utilizes both Bloch's theorem and coupled mode theory along with relevant explanations as follows. Figure 10(a) shows that the 'bandgap' based on Bloch's theorem seems to be smaller than the value obtained by CMT. This is because we employed the 'wavelength' as the 'unit', not frequency, such as $\omega\ [2\pi c/\Lambda]$, or $\omega\ [\pi c/\Lambda]$, or $\omega\ [c/\Lambda]$. Actually, the obtained bandgap by Bloch's theorem here (Other figures, Figure A.10(b) and Figures 7(a~b) are also the same) is not the actual value, because this value is affected by the 'unit' of the x-axis. One needs to notice that the obtained 'bandgap' by CMT actually is the bandwidth, i.e. the full width at first zeroes bandwidth of the reflection spectrum. The detailed calculation, accompanied by the relevant explanations, is outlined below.

(1) Applying Bloch's theorem, the wave propagation in our Bragg gratings can be equivalent to being guided in a periodic medium. The group delay (Figure A.8(a)) is calculated by the derivative of the Bloch wavenumber (K) with respect to frequency (ω), expressed as $\tau = L(\partial K/\partial\omega)$ [A4]. Subsequently, the bandgap here seems to be determined from the dispersion relation (Figure A.8(b)) as well, while it can be seen that the bandgap is approximately 8×10^{-3} pm. However, this value is not the actual bandgap, and the actual size of the bandgap is given by [A4]:

$$\Delta\omega_{gap} = \omega_0 \frac{4}{\pi} \sin^{-1} \left| \frac{n_2 - n_1}{n_2 + n_1} \right| \quad (A.2)$$

We assume that the refractive index for line grating stack and the gap are $n_1 = n_{eff} + \Delta n = 1.49 + 10^{-4}$ and $n_2 = n_{eff} - \Delta n = 1.49 - 10^{-4}$, and ω_0 corresponds to the central wavelength ($\lambda_0 = 1602.55$ nm) of the bandgap and here is $\omega_0 = \frac{2\pi c}{\lambda_0}$. Therefore, the bandgap, $\Delta\omega_{gap}$, is 1×10^{11} Hz, corresponding to 3 mm, not the values shown in Figure A.8.

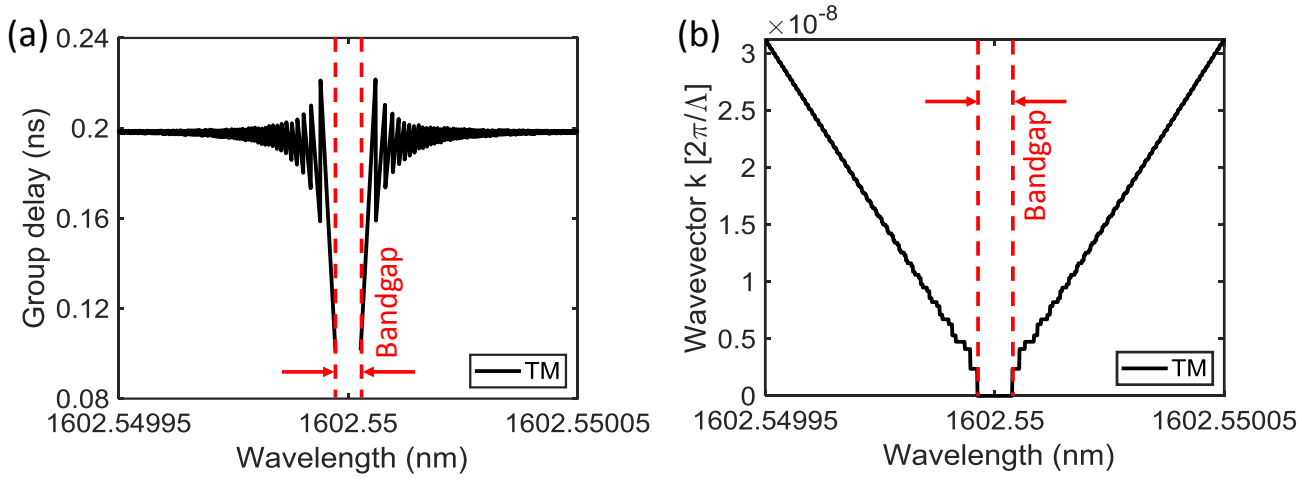

Figure A.8 The line-Bragg grating at TM mode and 1602.55 nm calculated by Bloch's theorem. (a) Group delay and bandgap, (b) Dispersion relation.

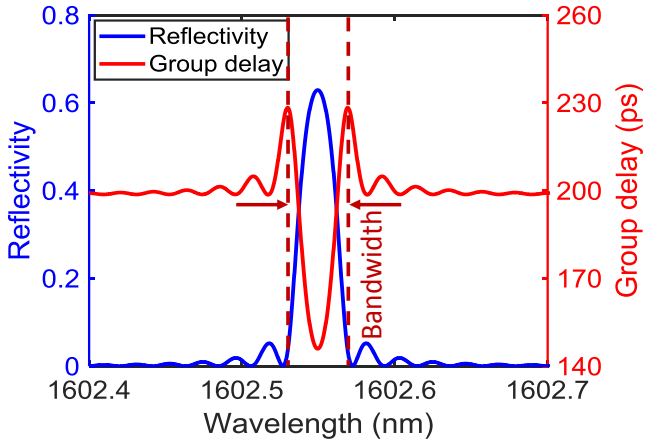

Figure A.9 The reflectivity and group delay of the line-Bragg grating at TM mode and 1602.55 nm computed by CMT. The bandgap can be estimated using the FWHM value.

(2) Utilizing coupled-mode theory (CMT), the group delay can be computed through the first derivative of phase (θ_ρ) derived from the amplitude reflection coefficient (ρ), expressed as $\tau =$

$-(\lambda^2/(2\pi c))(d\theta_\rho/d\lambda)$ [A5]:, as shown in Figure A.9 alongside the reflectivity. It is clearly to see that the bandwidth is approximately equal to 45 pm. Additionally, for our line-Bragg grating, with a coupling constant of κL=1.1, i.e. $(\kappa L)^2 \ll \pi^2$, the bandwidth also can be estimated as [A6]:

$$\mathrm{BW} \approx \lambda^2/(n_{eff}L) \tag{A. 3}$$

which results in a value of 43 pm.

(3) In conclusion, it is clearly found from (1) and (2) that the obtained 'bandgap' values are totally different based on the two methods.

A.9 References

[A1] S. Eaton, "Contrasts in thermal diffusion and heat accumulation effects in the fabrication of waveguides in glasses using variable repetition rate femtosecond laser," University of Toronto, 2008.

[A2] A. W. Snyder and J. D. Love, Optical Waveguide Theory. London: Chapman and Hall, 1983.

[A3] Luna Innovations, "Using a circulator to make insertion loss measurements in transmission with the optical backscatter reflectometer," 2013. https://lunainc.com/sites/default/files/assets/files/resource-library/LT_TD_EN-FY1306_IL-in-Transmission-Using-the-OBR-with-Circulator_v5.pdf, 2013

[A4] A. Yariv and P. Yeh, Photonics: Optical Electronics in Modern Communications, 6th ed. Oxford University Press, 2006.

[A5] T. Erdogan, "Fiber grating spectra," J. Light. Technol., vol. 15, no. 8, pp. 1277–1294, 1997, doi: 10.1109/50.618322.

[A6] R. Kashyap, Fiber Bragg Gratings, 2nd ed. Academic Press, 2010.

APPENDIX B SUPPLEMENT OF ARTICLE 2: OFFSET-ENHANCED SLOW LIGHT IN FEMTOSECOND LASER-FABRICATED BRAGG GRATINGS

B.1 V-number estimation

The V-number is defined as $V = (2\pi/\lambda)r\sqrt{n_{\text{core}}^2 - n_{\text{clad}}^2}$ [B1]. Here, λ is 1550 nm, while the radii for single-laser-pass waveguide (SLPWG) are 2 μm and 4.5 μm along r_1 and r_2 directions (Note that we just consider the effective light guiding position.), as shown in Figure B.1. Separately, the n_{core} and n_{clad} are $1.497 + (1.1 \times 10^{-3})$ and $1.497 - (1.1 \times 10^{-3})$, with 1.497 being the effective refractive index of SPWG calculated by the writing parameters of femtosecond laser and 1.1×10^{-3} being the average refractive index of SLPWG. Therefore, we can roughly obtain V_1 and V_2 with the values of 0.65 and 1.46, respectively, which supports the LP_{01} mode along r_1 and r_2 directions. In addition, the MFDs can also measured using the NanoScan (Appendix A.3(d)), with values of 24 μm and 22 μm along the effective radii of 2 μm and 4.5 μm, respectively. The measured MFD values are significantly larger than that of the SMF28 fiber (MFD=10.4 μm), indicating a greater mismatch between the SMF28 fiber and the SLPWG during the measurements.

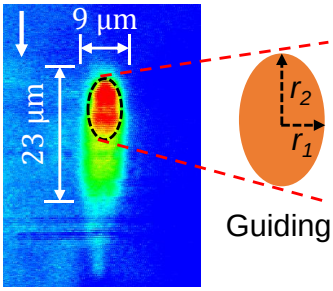

Figure B.1 The side view of SLPWG with an approximately oval-shaped light guided position measured by white light. The inset shows the effective enlarged light guiding position with the radii of r_1 and r_2.

B.2 Schematic of setups for grating spectrum and group delay measurements

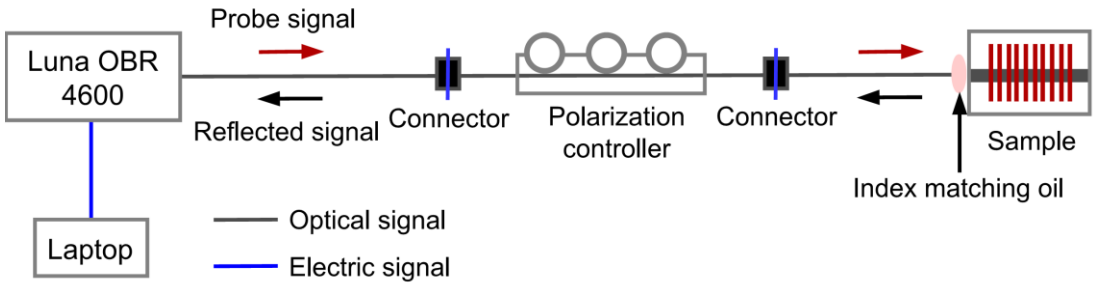

(a) Schematic of setup for reflection spectrum measurement.

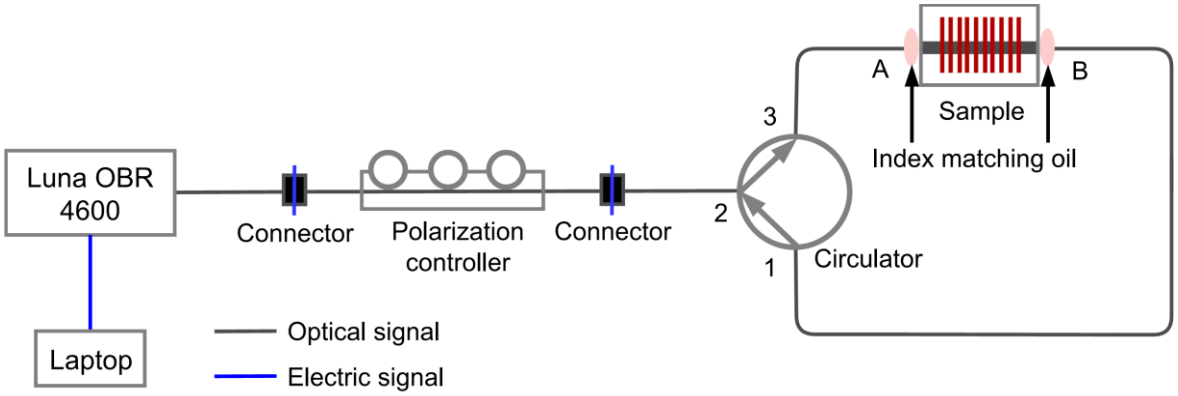

(b) Schematic of setup for transmission spectrum and group delay in transmission measurements.

Figure B.2 Schematic of setups for the measurements of (a) reflection and (b) transmission and group delay in transmission for line-Bragg grating by Luna OBR 4600 Optical Backscatter Reflectometer (OBR) [B2] with polarization controller. The index matching oil was used to reduce reflections in between fiber and facets (e.g. A and B in (b)) of samples, while the measurement results were directly displayed and collected by the OBR control software from a laptop.

B.3 Slow-down factor (SDF) derivation

The grating group delay (GD), τ_g, can be calculated using the derivative of the phase, θ_t, derived from the amplitude transmission coefficient, t, and described as [B3]

$$\tau_g = -\frac{\lambda^2}{2\pi c}\frac{d\theta_t}{d\lambda} \tag{B.1}$$

While the amplitude transmission coefficient, t, is given by

$$t = \sqrt{1 - r^2}$$

$$= \frac{\alpha}{\alpha \cosh(\alpha L) - i\hat{\sigma} \sinh(\alpha L)}$$
$$= \frac{\alpha^2 \cosh(\alpha L) + i\alpha\hat{\sigma} \sinh(\alpha L)}{\alpha^2 \cosh^2(\alpha L) + \hat{\sigma}^2 \sinh^2(\alpha L)}$$
$$= \mathrm{Re}(t) + i\mathrm{Im}(t) \quad (B.2)$$

The phase, θ_t, can be written

$$\theta_t = arctan\left(\frac{Im(t)}{Re(t)}\right)$$
$$= arctan\left(\frac{\alpha\hat{\sigma}\, sinh(\alpha L)}{\alpha^2\, cosh(\alpha L)}\right)$$
$$= arctan\left(\frac{\hat{\sigma}}{\alpha} tanh(\alpha L)\right) \quad (B.3)$$

In equation (B.2), r is the amplitude reflection coefficient

$$r = \frac{i\kappa \sinh(\alpha L)}{\alpha \cosh(\alpha L) - i\hat{\sigma} \sinh(\alpha L)} \quad (B.4)$$

where $\alpha = \sqrt{\kappa^2 - \hat{\sigma}^2}$ is the effective coupling coefficient, $\hat{\sigma} = \delta + \sigma = \beta - \beta_B + \sigma$. κ is the "ac" coupling coefficient, defined as $\kappa = \pi v \Delta n/\lambda$, where v is the fringe visibility, belonging to [0, 1], and Δn is the refractive index change, on the order of 10^{-3}. $\hat{\sigma}$ is a general "dc" self-coupling coefficient, δ is the detuning and defined as $\beta - \beta_B$. β is the propagation constant and equal to $2\pi n_{\text{eff}}/\lambda$, and β_B is the propagation constant and equal to $2\pi n_{\text{eff}}/\lambda_B$, where n_{eff} is the effective index of the core. σ is the "dc" coupling coefficient and equal to $2\pi\Delta n/\lambda$, L is the length of the grating, c is the speed of light, λ_B is the designed Bragg wavelength. Note that the power reflection coefficient here is $R = |r|^2$, while the maximum reflectivity for a Bragg grating is $R_{max} = \tanh^2(\kappa L)$.

In order to obtain the group delay, τ_{GD}, the several calculated steps are carried out as follows.

Step 1: Differentiate $\hat{\sigma}$ and α, with respect to λ, i.e. $\frac{d\hat{\sigma}}{d\lambda}$ and $\frac{d\alpha}{d\lambda}$

Therefore, the "dc" self-coupling coefficient can be written

$$\hat{\sigma} = \delta + \sigma$$
$$= \beta - \beta_B + \sigma$$

$$= \frac{2\pi n_{\text{eff}}}{\lambda} - \frac{2\pi n_{\text{eff}}}{\lambda_B} + \frac{2\pi \Delta n}{\lambda}$$

$$\approx \frac{2\pi n_{\text{eff}}}{\lambda} - \frac{2\pi n_{\text{eff}}}{\lambda_B} \tag{B.5}$$

Now, let's differentiate $\hat{\sigma}$, with respect to λ

$$\frac{d\hat{\sigma}}{d\lambda} = \frac{d}{d\lambda}\left(\frac{2\pi n_{\text{eff}}}{\lambda} - \frac{2\pi n_{\text{eff}}}{\lambda_B} + \frac{2\pi \Delta n}{\lambda}\right)$$

$$= -\frac{2\pi(n_{\text{eff}} + \Delta n)}{\lambda^2}$$

$$\approx \frac{2\pi n_{\text{eff}}}{\lambda^2} \tag{B.6}$$

Similarly, the α also can be differentiated with respect to λ

$$\frac{d\alpha}{d\lambda} = \frac{d}{d\lambda}\left(\sqrt{\kappa^2 - \hat{\sigma}^2}\right)$$

$$= \frac{1}{2\sqrt{\kappa^2 - \hat{\sigma}^2}} \frac{d}{d\lambda}(\kappa^2 - \hat{\sigma}^2)$$

$$= \frac{1}{2\sqrt{\kappa^2 - \hat{\sigma}^2}} \left(2\kappa \frac{d\kappa}{d\lambda} - 2\hat{\sigma}\frac{d\hat{\sigma}}{d\lambda}\right)$$

$$= \frac{1}{2\sqrt{\kappa^2 - \hat{\sigma}^2}} \left(\frac{-2\kappa\pi\nu\Delta n}{\lambda^2} + \frac{4\hat{\sigma}\pi(n_{\text{eff}} + \Delta n)}{\lambda^2}\right)$$

$$\approx \frac{\pi}{\lambda^2\sqrt{\kappa^2 - \hat{\sigma}^2}} (2\hat{\sigma} n_{\text{eff}} - \kappa\nu\Delta n)$$

$$\approx \frac{2\pi\hat{\sigma} n_{\text{eff}}}{\lambda^2\sqrt{\kappa^2 - \hat{\sigma}^2}}$$

$$= \frac{2\pi\hat{\sigma} n_{\text{eff}}}{\lambda^2 \alpha} \tag{B.7}$$

Step 2: Differentiate θ_t, with respect to λ, i.e. $\frac{d\theta_t}{d\lambda}$

Considering equations (B.3), (B.6) and (B.7), we have

$$\frac{d\theta_t}{d\lambda} = \frac{1}{1 + \left(\frac{\hat{\sigma}}{\alpha}\tanh(\alpha L)\right)^2} \frac{d}{d\lambda}\left(\frac{\hat{\sigma}}{\alpha}\tanh(\alpha L)\right)$$

$$= \frac{1}{1 + \left(\frac{\hat{\sigma}}{\alpha}\tanh(\alpha L)\right)^2} \left[\frac{\hat{\sigma}}{\alpha}\frac{d}{d\lambda}\left(\tanh(\alpha L)\right) + \tanh(\alpha L)\frac{d}{d\lambda}\left(\frac{\hat{\sigma}}{\alpha}\right)\right]$$

$$= \frac{1}{1+\left(\frac{\hat{\sigma}}{\alpha}\tanh(\alpha L)\right)^2}\left[\frac{\hat{\sigma}}{\alpha}(\operatorname{sech}^2(\alpha L))L\frac{d\alpha}{d\lambda}\right.$$

$$\left.+\left(\tanh(\alpha L)\right)\left(\frac{\alpha}{\alpha^2}\frac{d\hat{\sigma}}{d\lambda}-\hat{\sigma}\frac{d\alpha}{d\lambda}\right)\right]$$

$$\approx \frac{1}{1+\left(\frac{\hat{\sigma}}{\alpha}\tanh(\alpha L)\right)^2}\begin{bmatrix}\frac{\hat{\sigma}}{\alpha}(\operatorname{sech}^2(\alpha L))L\frac{2\pi\hat{\sigma}n_{\text{eff}}}{\lambda^2\alpha}\\ +\left(\tanh(\alpha L)\right)\left(\frac{\alpha}{\alpha^2}\left(-\frac{2\pi n_{\text{eff}}}{\lambda^2}\right)-\hat{\sigma}\left(\frac{2\pi\hat{\sigma}n_{\text{eff}}}{\lambda^2\alpha}\right)\right)\end{bmatrix}$$

$$= \frac{2\pi n_{\text{eff}}}{\lambda^2\alpha^3}\frac{L\alpha\hat{\sigma}^2\operatorname{sech}^2(\alpha L)-(\alpha^2+\hat{\sigma}^2)\tanh(\alpha L)}{1+\left(\frac{\hat{\sigma}}{\alpha}\tanh(\alpha L)\right)^2}$$

$$= \frac{2\pi n_{\text{eff}}}{\lambda^2\alpha^3}\frac{L\alpha\hat{\sigma}^2\frac{1}{\cosh^2(\alpha L)}-\kappa^2\frac{\sinh(\alpha L)}{\cosh(\alpha L)}}{1+\frac{\hat{\sigma}^2}{\alpha^2}\frac{\sinh^2(\alpha L)}{\cosh^2(\alpha L)}}$$

$$= \frac{2\pi n_{\text{eff}}}{\lambda^2\alpha}\frac{L\alpha\hat{\sigma}^2-\kappa^2\sinh(\alpha L)\cosh(\alpha L)}{\alpha^2\cosh^2(\alpha L)+\hat{\sigma}^2\sinh^2(\alpha L)}$$

$$= \frac{2\pi n_{\text{eff}}}{\lambda^2\alpha}\frac{L\alpha\hat{\sigma}^2-\kappa^2\sinh(\alpha L)\cosh(\alpha L)}{(\kappa^2-\hat{\sigma}^2)\cosh^2(\alpha L)+\hat{\sigma}^2(\cosh^2(\alpha L)-1)}$$

$$= \frac{2\pi n_{\text{eff}}}{\lambda^2\alpha}\frac{L\alpha\hat{\sigma}^2-\kappa^2\sinh(\alpha L)\cosh(\alpha L)}{\kappa^2\cosh^2(\alpha L)-\hat{\sigma}^2}$$

$$= \frac{2\pi n_{\text{eff}}}{\lambda^2\alpha}\frac{L\alpha-\frac{\kappa^2}{\hat{\sigma}^2}\sinh(\alpha L)\cosh(\alpha L)}{\frac{\kappa^2}{\hat{\sigma}^2}\cosh^2(\alpha L)-1}$$

$$= \frac{2\pi n_{\text{eff}}}{\lambda^2}\frac{L-\frac{\kappa^2}{\alpha\hat{\sigma}^2}\sinh(\alpha L)\cosh(\alpha L)}{\frac{\kappa^2}{\hat{\sigma}^2}\cosh^2(\alpha L)-1} \qquad \text{(B.8)}$$

Step 3: Group delay expression

Combing equations (B.1) and (B.8), the group delay is

$$\tau_g = -\frac{\lambda^2}{2\pi c}\frac{d\theta_t}{d\lambda}$$

$$= -\frac{\lambda^2}{2\pi c}\frac{2\pi n_{\text{eff}}}{\lambda^2}\frac{L-\frac{\kappa^2}{\alpha\hat{\sigma}^2}\sinh(\alpha L)\cosh(\alpha L)}{\frac{\kappa^2}{\hat{\sigma}^2}\cosh^2(\alpha L)-1}$$

$$= \frac{n_{\text{eff}}}{c} \frac{\frac{\kappa^2}{\alpha\hat{\sigma}^2}\sinh(\alpha L)\cosh(\alpha L) - L}{\frac{\kappa^2}{\hat{\sigma}^2}\cosh^2(\alpha L) - 1}$$

$$= \frac{1}{v_w} \frac{\frac{\kappa^2}{\alpha\hat{\sigma}^2}\sinh(\alpha L)\cosh(\alpha L) - L}{\frac{\kappa^2}{\hat{\sigma}^2}\cosh^2(\alpha L) - 1} \tag{B.9}$$

where $v_w = c/n_{\text{eff}}$ is the group velocity.

The peak delay occurs when $\alpha = i\pi$, $\beta = \pm L^{-1}\sqrt{\pi^2 + (\kappa L)^2}$, while considering the approximated value $\hat{\sigma} = \delta + \sigma \approx \beta - \beta_B \approx \beta = \pm L^{-1}\sqrt{\pi^2 + (\kappa L)^2}$ [B4]. Note the following equivalent relations: $\sinh(\alpha L) = \sinh(i\pi L) = i\sin(\pi L)$, and $\cosh(\alpha L) = \cosh(i\pi L) = \cos(\pi L)$. Therefore, we have

$$\tau_g = \frac{1}{v_w} \frac{\frac{\kappa^2}{i\pi\hat{\sigma}^2} i\sin(\pi L)\cos(\pi L) - L}{\frac{\kappa^2}{\hat{\sigma}^2}\cos^2(\pi L) - 1}$$

$$= \frac{1}{v_w} \frac{\frac{\kappa^2}{2\pi\hat{\sigma}^2}\sin(2\pi L) - L}{\frac{\kappa^2}{\hat{\sigma}^2}\cos^2(\pi L) - 1}$$

$$= \frac{1}{v_w} \frac{\frac{\kappa^2}{2\pi\hat{\sigma}^2}\sin(2\pi L) - L}{\frac{\kappa^2}{\hat{\sigma}^2}\cos^2(\pi L) - 1}$$

$$= \frac{1}{v_w} \frac{\kappa^2 \sin(2\pi L) - 2\pi\hat{\sigma}^2 L}{2\pi\kappa^2\cos^2(\pi L) - 2\pi\hat{\sigma}^2}$$

$$= \frac{1}{v_w} \frac{\kappa^2 \sin(2\pi L) - 2\pi\hat{\sigma}^2 L}{2\pi\kappa^2\cos^2(\pi L) - 2\pi\hat{\sigma}^2}$$

$$\approx \frac{1}{v_w} \frac{\kappa^2 L^2 \sin(2\pi L) - 2\pi L(\pi^2 + (\kappa L)^2)}{2\pi\kappa^2 L^2\cos^2(\pi L) - 2\pi(\pi^2 + (\kappa L)^2)}$$

$$= \frac{L}{v_w} \frac{\kappa^2 L \sin(2\pi L) - 2\pi(\pi^2 + (\kappa L)^2)}{2\pi[\kappa^2 L^2\cos^2(\pi L) - (\pi^2 + (\kappa L)^2)]} \tag{B.10}$$

Since $\sin(2\pi L) = 0$, $\cos^2(\pi L) = 1 - \sin^2(\pi L) = 1$, so we can simplify the equation (B.10) to be

$$\tau_g = \frac{L}{v_w} \frac{-2\pi(\pi^2 + (\kappa L)^2)}{2\pi[\kappa^2 L^2 - (\pi^2 + (\kappa L)^2)]}$$

$$= \frac{L}{v_w}\left(1 + \frac{(\kappa L)^2}{\pi^2}\right) \tag{B.11}$$

Using the definition of slow-down factor (SDF), $S = \tau_g/\tau_w$, and recall the waveguide group delay, $\tau_w = L/v_w$. Thus, we have

$$S = 1 + \frac{(\kappa L)^2}{\pi^2} \tag{B.12}$$

B.4 References

[B1] A. W. Snyder and J. D. Love, Optical Waveguide Theory. London: Chapman and Hall, 1983.

[B2] Luna Innovations, "Using a circulator to make insertion loss measurements in transmission with the optical backscatter reflectometer," 2013. https://lunainc.com/sites/default/files/assets/files/resource-library/LT_TD_EN-FY1306_IL-in-Transmission-Using-the-OBR-with-Circulator_v5.pdf, 2013

[B3] T. Erdogan, "Fiber grating spectra," J. Light. Technol., vol. 15, no. 8, pp. 1277–1294, 1997, doi: 10.1109/50.618322.

[B4] R. Kashyap, Fiber Bragg Gratings, 2nd ed. Academic Press, 2010.

APPENDIX C SUPPLEMENT OF ARTICLE 3: ENHANCED SLOW-LIGHT PHENOMENON IN DOT-BRAGG GRATINGS THROUGH OFFSET ENGINEERING

C.1 RI changes of SLPWG and Model-I DBG

The cross-sectional views of single-lass-pass waveguide (SLPWG) and Model-I DBG (dot-Bragg grating) with four offsets of 0 μm, 5 μm, and 10 μm are shown in Figures C.1(a~e), while the measured phase change by "The Ripper™" from PhotoNova Inc.[C1] and the calculated refractive index (RI) changes is shown in Figures C.1(e~h).

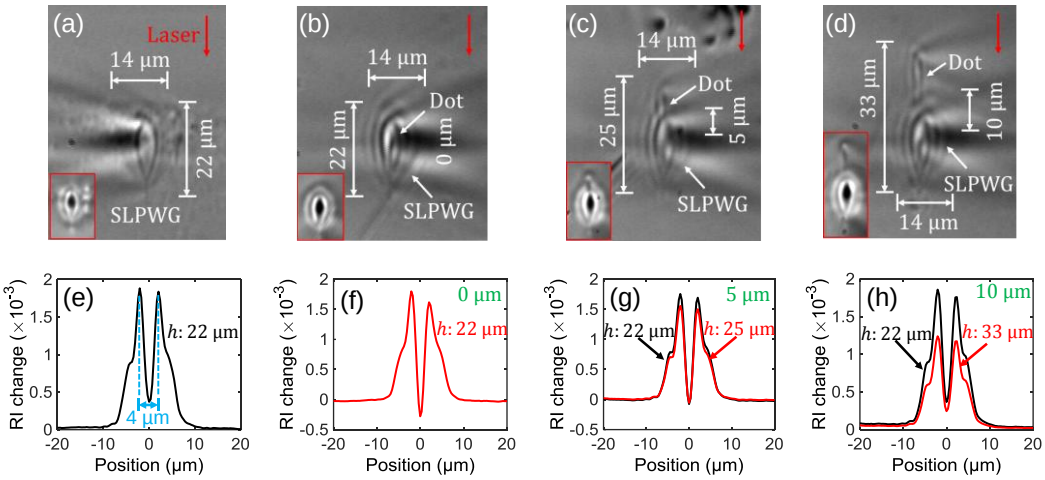

Figure C.1 Cross-sectional views at an inscribing laser power of 100 mW for (a) SLPWG, and model-I DBGs with offsets of (b) 0 μm, (c) 5 μm, and (d) 10 μm, where the corresponding RI changes are given from (e) to (h). The insets in the red boxes from (a)~(d) show the light-guided positions along the 'shell,' as measured by white light (measurement setup can be seen from Supplement in Ref. [C2]). Note that the RI changes decrease linearly with an increase in the effective affected height, h, as illustrated from (g) to (h), where the black curves correspond to the SLPWG heights of 22 μm, and the red curves correspond to the height (SLPWG and dot) values of 25 μm and 33 μm. The inscribing laser in (a~d) was incident from the top, as indicated by the red arrows.

The SLPWG shows an oval-shaped core-shell cross section (Figure C.1(a)). The primary light-guided region is in the shell region with an RI change of $\sim 2 \times 10^{-3}$, while the core region is a weaker light-guided effect with an RI change of $\sim 0.4 \times 10^{-3}$ (Figure C.1(e)). When the offset is 0 μm, as illustrated in Figure C.1(b), the RI change has a negative value about -2.8×10^{-4} (Figure

C.1(f)) in the core, due to the lower repetition rate used for the dot inscription. The negative RI change almost has little impact on the total RI change values (i.e. the effective light-guided regions) of the Model-I DBG, and thus allows the DBG to exhibit a Bragg resonance. If continuing to increase the offset to 5 μm (Figure C.1(c)), the RI change (Figure C.1(g)) in the shell region decreases from ~2×10^{-3} (black curves in Figure C.1(g), calculated using the effective affected height h=22 μm) to ~1.5×10^{-3} (red curves in Figure C.1(g), obtained using a combined effective affected height h=25 μm), while the core region has a negative RI change of -5.4×10^{-5}. When the offset is further increased to 10 μm (Figure C.1(d)), the RI change (Figure C.1(h)) in the shell is ~1.25×10^{-3}, calculated using h of 33 μm. At this point, the RI change in the core region is on the order 10^{-4}, similar to that of the SLPWG. Therefore, the Bragg resonance can be successfully achieved with 5 μm and 10 μm offsets. However, the RI change exhibits a more significant downward, reaching a value of 1.2×10^{-3} (Figure C.1(i)), due to the longer h of 33 μm when the offset is 10 μm (Figure C.1(d)).

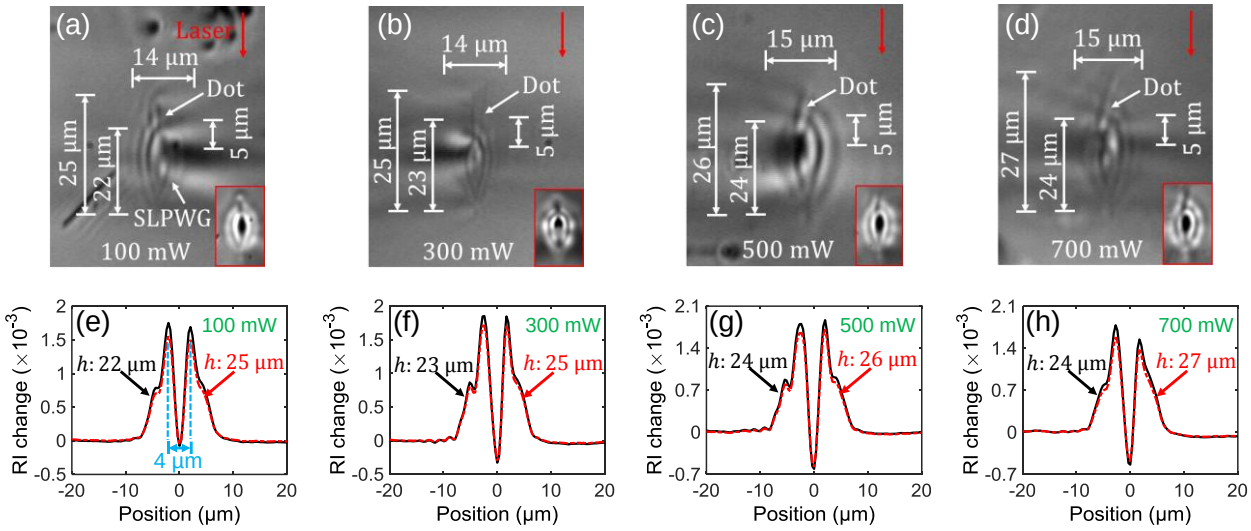

Figure C.2 Cross-sectional views of Model-I DBGs with offsets of 5 μm at inscribing laser powers of (a) 100 mW, (b) 300 mW, (c) 500 mW, and (d) 700 mW for dot inscription, where the insets display the light-guided positions measured by white light (The inscription laser (red arrows) was incident from the top). The corresponding RI changes are shown from (e) to (h). The effective affected height, h, plays a crucial role in influencing the RI change, as illustrated by the black curves for the SLPWG height and the red curves for the combined height (SLPWG and dot), as demonstrated from (e) to (h).

The impact of laser power on dot inscription, as it relates to the cross-sectional views and RI changes of Model-I DBGs, is also discussed for a 5 μm offset, as shown in Figure C.2. It is observed

that the size of the SLPWG itself remains largely unchanged (Figures C.2(a~d)), while the combined effective affected heights, h, experience a slight variation with laser powers of 100 mW, 300 mW, 500 mW, and 700 mW. This suggests that the laser power has a weaker effect on dot size when using a smaller repetition rate, as well as on the RI changes in the shell regions (Figures S2(f~h)), with values of $(1.5\sim1.9)\times10^{-3}$. Furthermore, there is minimal effect on the RI changes in the core regions, of order -10^{-4}, as illustrated in Figures C.2(f~h).

C.2 Model-I DBG spectrum and group delay

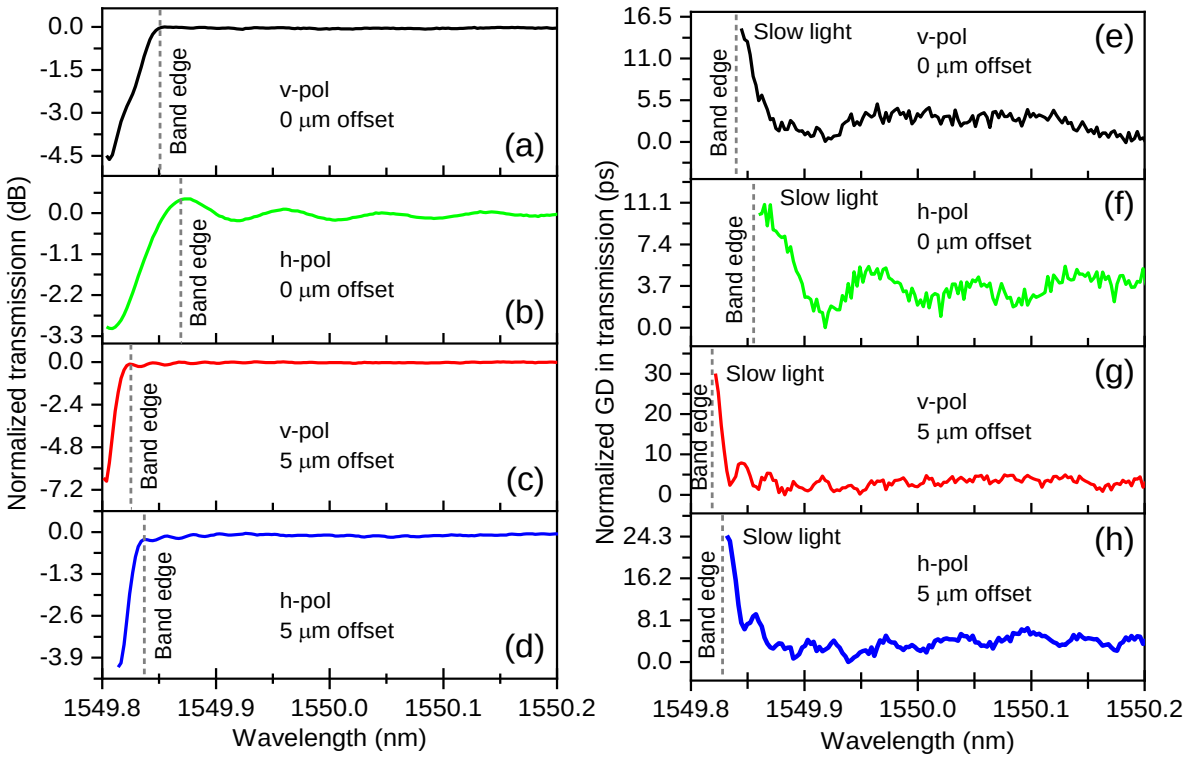

Figure C.3 Model-I DBG characteristics comparisons with 100 mW laser power for dot inscription. At 0 μm offsets, the transmission spectra are shown in (a) for v-pol and in (b) for h-pol. The spectra in (c) for v-pol and (d) for h-pol, with offsets of 5 μm. The measured GD in transmission at 0 μm offsets are shown in (e) for v-pol and in (f) for h-pol. For a 5 μm offset, the GDs are displayed in (g) for v-pol and in (h) for h-pol. Note that the y-axes are normalized to facilitate a better analysis of the slow-light effect, while the band edges are also given.

To address the offset impact to the slow-light effect in Model-I DBG. The reflection, transmission spectra, and group delays (GDs) for Model-DBG with offsets of 0 μm, 5 μm, and 10 μm were measured. Figure C.3 shows the normalized transmission spectra and the GDs near the band edges with the offsets of 0 μm and 5 μm. At 0 μm offsets, as shown in Figures C.3(a) and C.3(b), DBGs

achieve transmission dips of 4.6 dB and 3 dB, centered at 1549.81 nm, for both polarizations. The coupling coefficient (κ) and coupling constant (κL) are calculated by maximum reflectivity equation [C3], showing separately 15 m^{-1} and 1.12 for v-pol, and 12 m^{-1} and 0.86 for h-pol. The slow-light effects occur at the GD peaks, close to the band edges (Figures C.3(e) and C.3(f)), showing time delays of 15 ps and 11 ps at wavelengths of 1549.844 nm (v-pol) and 1549.865 nm (h-pol), respectively. The calculated slow-down factors (SDFs) are separately 1.13 and 1.08 for v-pol and h-pol. At 5 μm offsets, the slow-light effects also appear close to the band edges, where the detailed positions are marked in the normalized transmission spectra (Figures C.3(c~d)) and GDs (Figures C.3(g~h)). The calculated SDFs [C4] for v-pol and h-pol are 1.21 and1.11, which are increased by 7.1% and 2.8% compared to the values in DBGs with 0 μm offset. When the offset is increased to 10 μm with the same inscribed laser power of 100 mW for dot inscription, the transmission dips reduce to less than 1 dB (with SDFs less than 1.03) for both v-pol and h-pol.

Table C.1 Model-I DBG characteristics comparisons with 100 mw laser power for dot inscription.

Modes (Offset)	**Trans. (dB)**	**κ (m^{-1})**	**κL**	**GD (ps)**	**SDF**
v-pol (0 μm)	4.6	15	1.12	15	1.13
h-pol (0 μm)	3.0	12	0.86	11	1.08
v-pol (5 μm)	6.7	19	1.41	33	1.21
h-pol (5 μm)	4.2	14	1.10	25	1.11

To thoroughly investigate the influence of inscribed laser power on DBG spectrum and slow-light effect, we increased the laser power to 300 mW, 500 mW, and 700 mW for dot inscription. It is observed that, at offsets of 0 μm and 10 μm, most of the transmission dips in both the v-pol and h-pol are either less than 1.1 dB or absent. However, a few exceptions were noted, such as a 1.4 dB transmission dips at a 10 μm offset (300 mW) and a 0 μm offset (500 mW), as well as a 1.9 dB dip at a 10 μm offset (500 mW), all in the h-pol. Moreover, some sideband resonances were observed near the main resonance wavelengths, likely caused by phase or amplitude changes in the grating refractive index [C5].

It is important to highlight that the 5 μm offset plays a vital role in enhancing the transmission dips and slow-light effects when the inscribed laser powers are 300 mW, 500 mW, and 700 mW. The measured spectra and GDs at the 5 μm offset for these three laser powers are shown in Figure C.4.

The measured spectra (Figures C.4(a~f)) reveal the resonant behaviors of the DBGs in both v-pol and h-pol, with transmission dips ranging from 1 dB to 4.6 dB, centered around wavelengths of 1549.76 nm to 1549.82 nm. From GDs measured through transmission spectra, as can be seen from Figures C.4(g~l), almost all exhibit obvious slow-light effects. The only exception is the result in Figure C.4(l), where no evident slow-light effect is observed, potentially due to phase fluctuations.

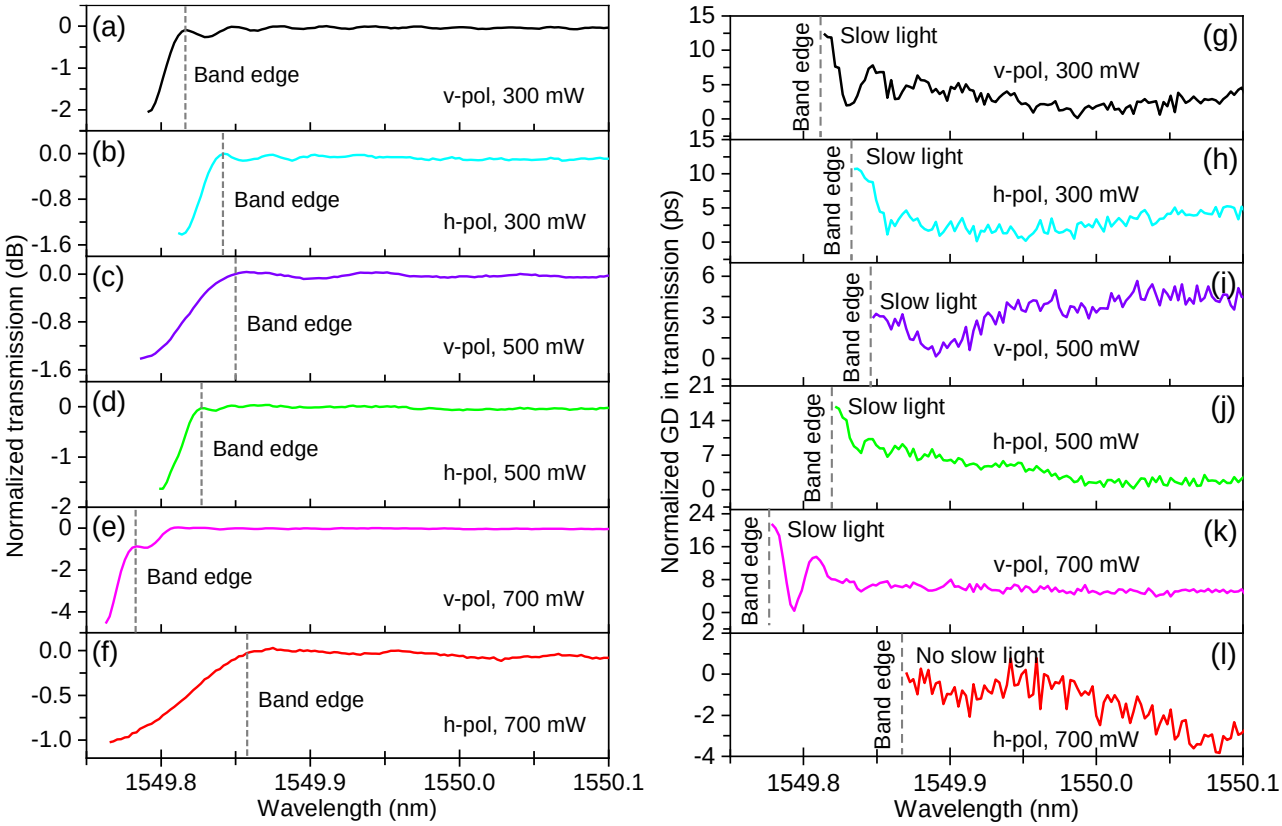

Figure C.4 The measured transmission spectra and GDs of Model-I DBGs with 5 μm offsets were recorded at the inscribed laser power of 300 mW, 500 mW, and 700 mW for dot inscription. The normalized spectra in (a), (c), and (e) are for v-pol, while in (b), (d), and (f) are for h-pol, respectively. The corresponding GDs are shown in (g), (i), and (k) are for v-pol, while in (h), (j), and (l) are for h-pol, respectively. Note that the normalized y-axes enable a clearer analysis of the slow-light effect.

When the laser power is 300 mW, the DBG exhibits a 2.1 dB transmission dip (Figure C.4(a)) centered at a resonant wavelength of 1549.79 nm in v-pol, with values for κ and κL of 9.6 m^{-1} and 0.72, respectively, leading to an SDF of 1.05. The corresponding GD in transmission (Figure C.4(g)) reveals a time delay 12 ps at 1549.82 nm, indicating a slow-light effect. In h-pol, a 1.4 dB transmission dip (Figure C.4(b)) also centered at 1549.82 nm is obtained, with κ and κL values of

7.8 m^{-1} and 0.58, respectively, yielding an SDF of 1.03 and a GD of 11 ps (Figure C.4(h)). As the laser power of 500 mW, the DBG achieves transmission dips of 1.42 dB at 1549.79 nm in v-pol (Figure C.4(c)) and 1.7 dB at 1549.79 nm in h-pol (Figure C.4(d)). The corresponding κ, κL, and SDF values are 7.8 m^{-1}, 0.59, and 1.035 for v-pol, and 8.6 m^{-1}, 0.65, and 1.043 for h-pol. The slow-light effects are observed with GDs of 3 ps in v-pol (Figure C.4(i)) and 17 ps in h-pol (Figure C.4(j)). When the laser power increases to 700 mW, the DBG exhibits a transmission dip of 4.6 dB at 1549.76 nm in v-pol (Figure C.4(e)), with κ, κL, and SDF values of 15 m^{-1}, 1.1, and 1.12. In h-pol, a 1 dB transmission dip is observed at 1549.83 nm (Figure C.4(f)), with κ, κL, and SDF values of 6.5 m^{-1}, 0.49, and 1.02. The slow-light effect is present in v-pol, with a GD of 21 ps at 1549.78 nm (Figure C.4(k)), but no slow-light effect is observed in h-pol (Figure C.4(l)). Furthermore, unforeseen jitter occurs in the vicinity of the GD peaks, which could be attributed to the coupling constants (κL).

C.3 Mode profile estimation

The mode profiles of SLPWG in Model-I DBG and DLPWG in Model-I DBG can be estimated using mode field diameter (MFD) [C6], given by

$$MFD = 2a\left(0.65 + \left(\frac{1.619}{V^{3/2}} + \frac{2.878}{V^{6}}\right)\right), \tag{C. 1}$$

where a is the effective radii of light guiding regions with values of $r_1 \approx 3.5$ μm and $r_2 \approx 6.0$ μm for SLPWG (Figure C.5(a)), and $r_3 \approx 6.0$ μm and $r_4 \approx 9.0$ μm for DLPWG (Figure C.5(b)), V is the normalized frequency (i.e. V-number) [C7], defined as

$$V = (2\pi/\lambda) r_{eff} \sqrt{n_{\text{core}}^2 - n_{\text{clad}}^2}\,. \tag{C. 2}$$

Here, the λ is 1550 nm and the r_{eff} represents the effective radius (r_1~r_4) of the light guiding cross-sections, respectively. The refractive indices, n_{core} and n_{clad}, are expressed as $n_{eff} + (\Delta n)$ and $n_{eff} - (\Delta n)$, where the effective refractive index, n_{eff}, is 1.498, and Δn is 1.8×10^{-3} for SLPWG and 1.0×10^{-3} for DLPWG.

Using equation (C.2), the V_1 and V_2 values are calculated to be 1.47 and 2.53, indicating that the SLPWG supports the LP_{01} mode along the r_1 direction and LP_{01}, LP_{11} modes along the r_2 direction. The MFD_1 and MFD_2, calculated using equation (C.1), are 12.9 μm and 12.8 μm, respectively.

Similarly, the values for V_3 and V_4 are 1.88 and 2.82, respectively, which means that the DLPWG supports the LP_{01} mode along the r_3 direction and both LP_{01} and LP_{11} modes along the r_4 direction. The corresponding MFD_3 and MFD_4 are 16.1 μm and 17.9 μm. Compared to the mode for SMF fiber with a 10.4 μm MFD, the mode profiles for SLPWG and DLPWG at 1550 nm, represented by their mode field diameters, are MFD_{SLPWG}= 12.9 μm × 12.8 μm (The measured values are 17 μm × 14 μm by NanoScan, Appendix A.3(d)) and MFD_{DLPWG}=16.1 μm × 17.9 μm (Measured by NanoScan with values: 22 μm × 19 μm), both larger than the SMF28, which could lead to increased transmission losses during coupling with SMF28 in coupling-in/out measurements. Furthermore, both waveguides show the potential for multimode operation. However, the SLPWG exhibits a more symmetric mode profile than the DLPWG, which could result in more nonlinear effects when used in communication systems. The mode field positions for Model-I and Model-II DBGs approximately correspond to the light guiding regions (indicated by the black dashed circles in Figure C.5), where the light intensity is distributed over a larger area in the DLPWG than in the SLPWG.

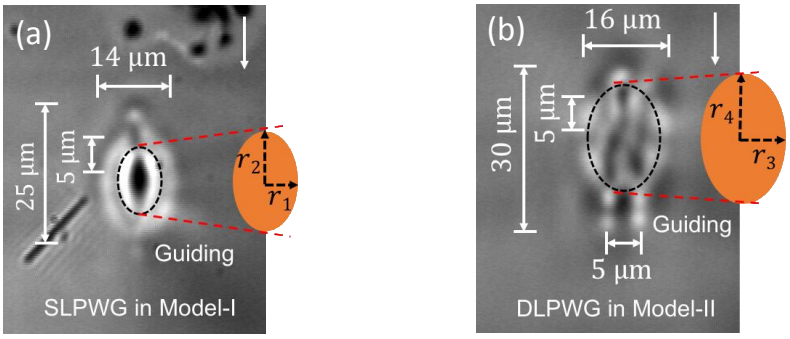

Figure C.5 The cross-sectional views of light guiding positions are measured by white light. (a) SLPWG in Model-I DBG (inset of Figure 6.2(c)), and (b) DLPWG in Model-II DBG (inset of Figure 6.5(c)). Note: (1) The insets show the effective enlarged light guiding positions with the radii of r_1~r_4. (2) The inscription laser (white arrows) was incident from the top.

C.4 RI change of Model-II DBG

Figure C.6 presents the cross-sectional views and RI changes of Model-II DBGs with 5 μm offsets at six center-to-center distances (center distances, for short) of 0 μm, 1 μm, 2 μm, 3 μm, 4 μm, and 5 μm. The results indicate that the weak light-guided regions in Model-I DBGs are improved to some extent in Model-II DBGs, with RI changes reaching approximately on the orders of ~1×10^{-3}.

Unlike the single oval-shaped core-shell shape structure seen in Model-I DBGs, the light-guided regions in Model-II DBGs are characterized by overlapping or partially overlapping double shells, as illustrated in the insets of Figures C.6(a~f). These overlapping regions reduce the non-light-guiding areas in the core, forming several smaller non-light-guiding areas (insets in Figures C.6(c~f)), which enhances the overall light-guiding performance of double-laser-pass waveguides (DLPWGs) in Model-II DBGs. It is worth noting that the double-laser-pass used for DLPWG inscription results in vertical differences between the two overlapping waveguides, as evidenced by the two distinct peaks in the RI change profiles shown in Figures C.6(g~l). In addition, the horizontal distances between the two peaks in the RI change profiles (Figures C.6(g~l)) are observed to be larger than the designed center distances shown in Figures C.6(a~f). This discrepancy may be attributed to measurement errors associated with the use of "The Ripper." Nonetheless, it highlights that the primary light-guided regions are predominantly situated along the shell sections.

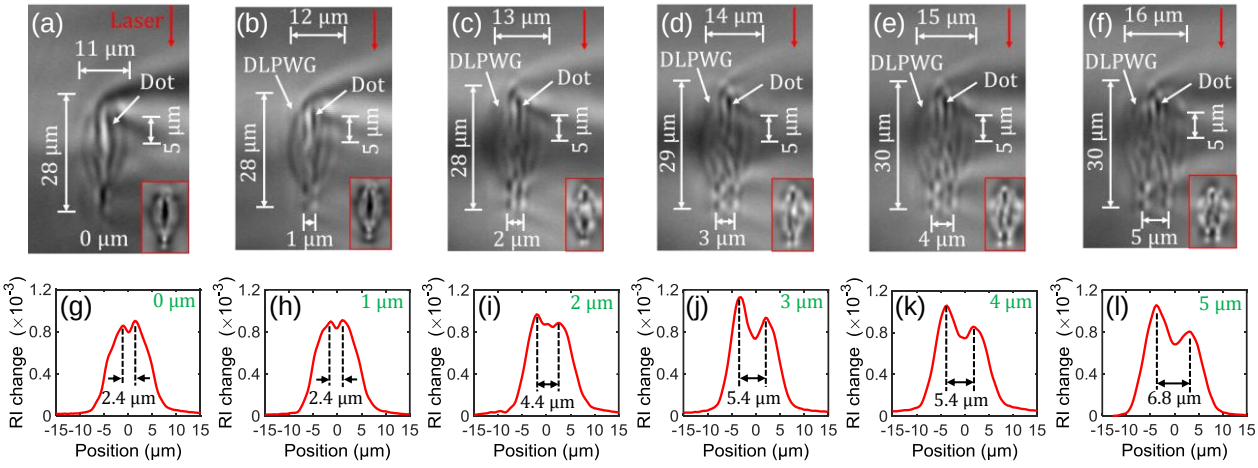

Figure C.6 Cross-sectional views of Model-II DBGs with 5 μm offsets and varying center distances in the DLPWG are shown in (a) 0 μm, (b) 1 μm, (c) 2 μm, (c) 3 μm, (c) 4 μm, and (d) 5 μm, with the corresponding RI changes displayed from (g) to (l). The insets from (a) to (f) reveal the light-guided regions, as measured via white light. Note that the inscription laser (red arrows in (a~f)) was incident from the top.

Considering the prominent peak RI changes observed in Figures C.6(j~l) at center distances of 3 μm, 4 μm, and 5 μm, we select the configuration with a 5 μm center distance for a detailed analysis to the offset engineering. This analysis is conducted using four offset values: 0 μm, 5 μm, and 10 μm. Figure C.7 illustrates the corresponding cross-sectional views and RI change profiles. It can be observed that the peak RI changes in Figures C.7(d~f) reach approximately 1.1×10^{-3} when

considering only the h of the DLPWG, which is 28 μm. However, the RI changes decrease to 1.0×10^{-3} and 0.9×10^{-3}, as indicated by the dashed red lines in Figures C.7(e~f), when taking into account the combined affected heights of 30 μm and 36 μm, respectively. The resonance characteristics of the Model-II DBGs are also affected by the relative positions of the dots. With offsets of 0 μm (Figure C.7(a) and 5 μm (Figure C.7(b), the visibility of the dots appears unclear due to the greater vertical heights of the DLPWGs. However, with a 10 μm offset, the dot becomes more distinguishable. Consequently, the Model-II DBGs with the aforementioned offsets (0 μm, 5 μm, and 10 μm) could exhibit resonances, which can be attributed to the interaction between the DLPWG and the dots.

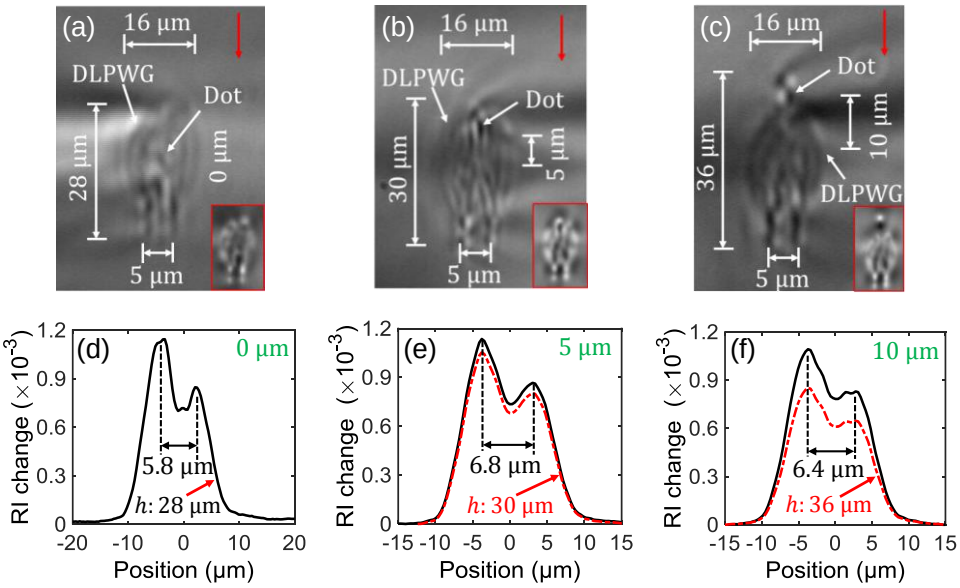

Figure C.7 At 5 μm center distances in DLPWGs, the cross-sectional views and RI changes of Model-II DBGs with offsets of (a) 0 μm, (b) 5 μm, and (c) 10 μm. From (d) to (f), the black curves of RI changes are obtained using the effective affected heights (h of 28 μm) of DLPWG, while the red ones are derived from the combined heights (DLPWG and dot). The insets from (a) to (c) show the light-guided positions as measured by white light, where the inscription laser (red arrows) was incident from the top.

C.5 Model-II DBG spectrum and group delay

For comparison, the slow-light effects are presented for Model-II DBGs with offsets of 5 μm and varying center distances from 0 to 5 μm, with a 1 μm step size in DLPWGs. Here, we primarily focus on analyzing the transmission spectrum and GD (in transmission) in v-pol due to the more

stable spectrum and GD than that of h-pol, as shown in Figure C.8. Note that laser power for dot inscription is 100 mW.

When the offset is 0 μm and 10 μm in the Model-II DBGs with six center distances in DLPWGs, almost all DBGs exhibit weak Bragg grating characteristics in v-pol and h-pol. The comparisons with the center distance values of 1 μm, 3 μm, and 5 μm are given in Table C.1. Note that the difference in Bragg wavelength between v-pol and h-pol is 70 pm with an effective birefringence of 4.5×10^{-5} when the offset is 10 μm and the center distance is 3 μm.

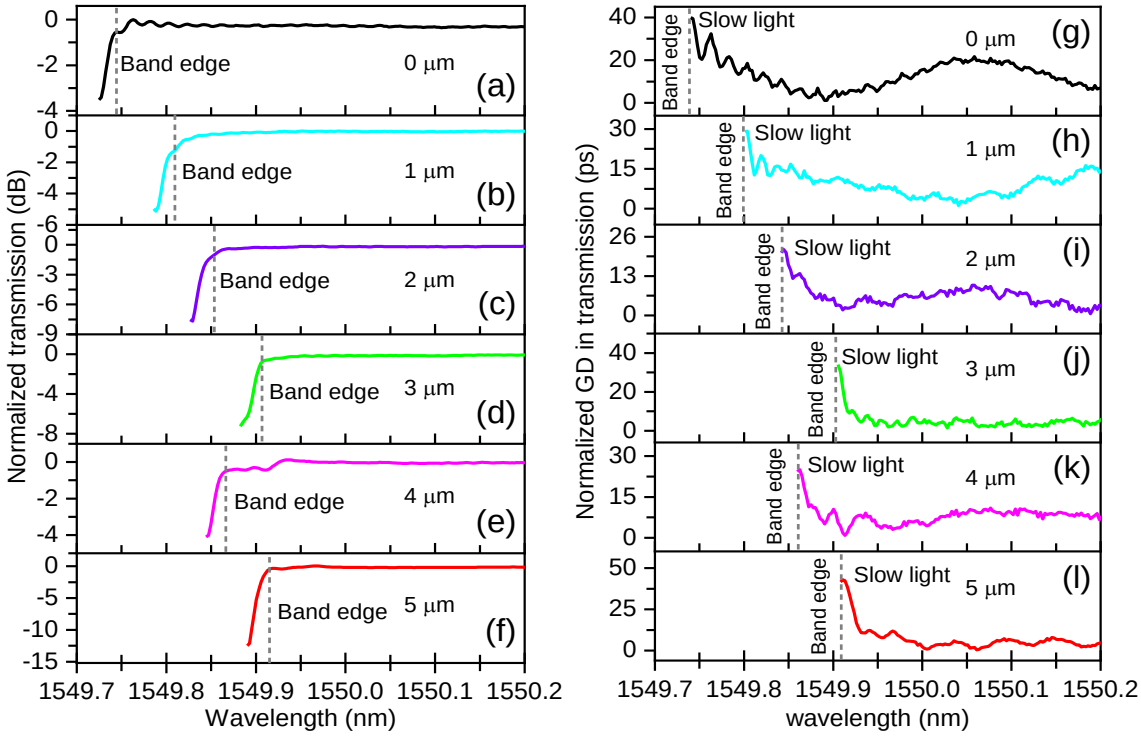

Figure C.8 Model-II DBG characteristics comparisons at a 5 μm offset and v-pol. The measured transmission spectra (a~f) and GDs (g~l) with six center distances (0 μm, 1 μm, 2 μm, 3 μm, 4 μm, and 5 μm) in DLPWGs. Note that the y-axes are normalized to facilitate a better analysis of the slow-light effect.

Table C.2 compares the GD and derived SDF of Model-II DBG for 5 μm offset and six varying center distances in the DLPWG at v-pol (Figure C.8), which shows more stable spectrum and GD characteristics than h-pol. It is evident that SDF increases with the rise of κL and the transmission dip, while the GD behaves somewhat differently due to the polarization effects of the incident light, as seen with a value of 39 ps at $\kappa L = 1$. Additionally, at 0 μm and 10 μm offsets, Model-II DBGs

exhibit weak Bragg characteristics, with 1~3.3 dB transmission dips in both polarizations across six center distances in DLPWG (Table C.3).

Table C.2 Model-II DBG characteristics at a 5 μm offset and six center distances in the v-pol.

Center distance	**Tran. (dB)**	**κ (m^{-1})**	**κL**	**GD (ps)**	**SDF**
0 μm	3.8	13.4	1.0	39	1.10
1 μm	5.1	16	1.2	29	1.14
2 μm	7.7	21	1.5	21	1.24
3 μm	7.2	19.7	1.48	35	1.22
4 μm	4.1	14	1.05	25	1.11
5 μm	12.5	28.2	2.2	43	1.45
0 μm	3.8	13.4	1.0	39	1.10

Table C.3 Model-II DBG characteristics comparisons at offsets of 0 μm and 10 μm.

Modes (Offset/Center distance)	**Tran. (dB)**	**κ (m^{-1})**	**κL**	**GD (ps)**	**SDF**
v-pol (0 μm, 1 μm)	2.1	9.6	0.72	11/7	1.053
h-pol (0 μm, 1 μm)	2.0	9.4	0.70	7/16	1.050
v-pol (0 μm, 3 μm)	1.3	7.5	0.57	6/2	1.032
h-pol (0 μm, 3 μm)	1.5	7.9	0.60	7/9	1.036
v-pol (0 μm, 5 μm)	1.2	7.1	0.53	6/8	1.029
h-pol (0 μm, 5 μm)	1.0	6.6	0.50	6/8	1.025
v-pol (10 μm, 1 μm)	2.2	10	0.75	14/15	1.060
h-pol (10 μm, 1 μm)	2.1	9.7	0.73	14/7	1.054
v-pol (10 μm, 3 μm)	2.9	11.5	0.86	16/18	1.080
h-pol (10 μm, 3 μm)	3.3	12.4	0.93	9/13	1.087
v-pol (10 μm, 5 μm)	2.6	10.8	0.81	22/16	1.066
h-pol (10 μm, 5 μm)	1.6	8.2	0.62	13/6	1.039

C.6 Simulation for group index

The group index (GI), $n_g = c\tau_g/L$, for Model-I and Model-II DBGs is derived from coupled-mode theory [C4], [C8], as shown in Figure C.9, where τ_g is the group delay of the Bragg grating (GD, $\tau_g = -(\lambda^2/2\pi c)(d\theta_t/d\lambda)$) and L is the length of the Bragg grating.

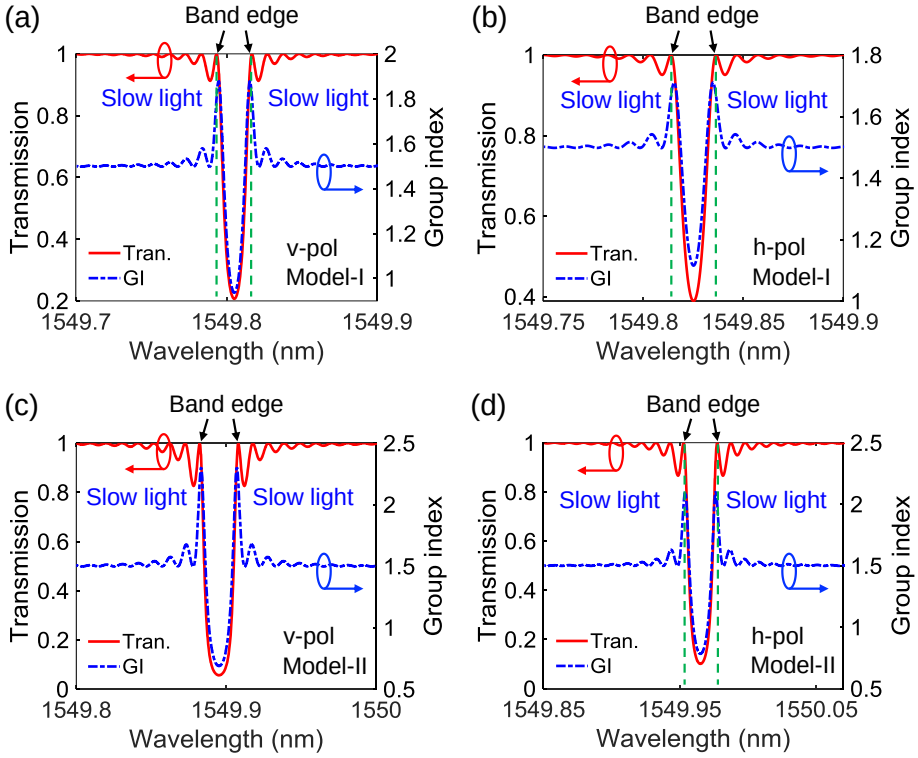

Figure C.9 Simulation of GIs and transmission spectra at a 5 μm offset for Model-I DBG in (a) v-pol and (b) h-pol, and for Model-II in (c) v-pol and (d) h-pol. Note that the coupling constants used for simulation are derived from the experimental results shown in Figures 6.3 and 6.6.

It can be observed that the GI for waveguide (SLPWG and DLPWG) itself, n_w, is 1.498, while the GIs are 1.88 (Figure C.9(a)) and 1.71 (Figure C.9(b)) for Model-I DBG in the v-pol and h-pol, respectively, and 2.30 (Figure C.9(c)) and 2.10 (Figure C.9(d)) for Model-II DBG in the v-pol and h-pol, respectively. Using the SDF definition $S = n_g/n_w$ (Note that the n_g is the group index (GI) of the Bragg grating), the corresponding *S* for Model-I and Model-II DBG are derived and shown in Figure C.10. As seen, the ratio, *S* for Model-I DBG, close to the band edges, is 1.25 in the v-pol (Figure C.10(a)) and 1.14 in the h-pol (Figure C.10(b)), respectively. For Model-II DBG, *S* is 1.54 (Figure C.10(c)) and 1.40 (Figure C.10(d)) in the v-pol and h-pol, respectively. The simulation values agree well with the experimental values, which were first obtained by the coupling constant

(κL) and then calculated using Eq. (1): 1.21 and 1.10 for Model-I DBG in v-pol and h-pol, and 1.45 and 1.34 for Model-II DBG in v-pol and h-pol.

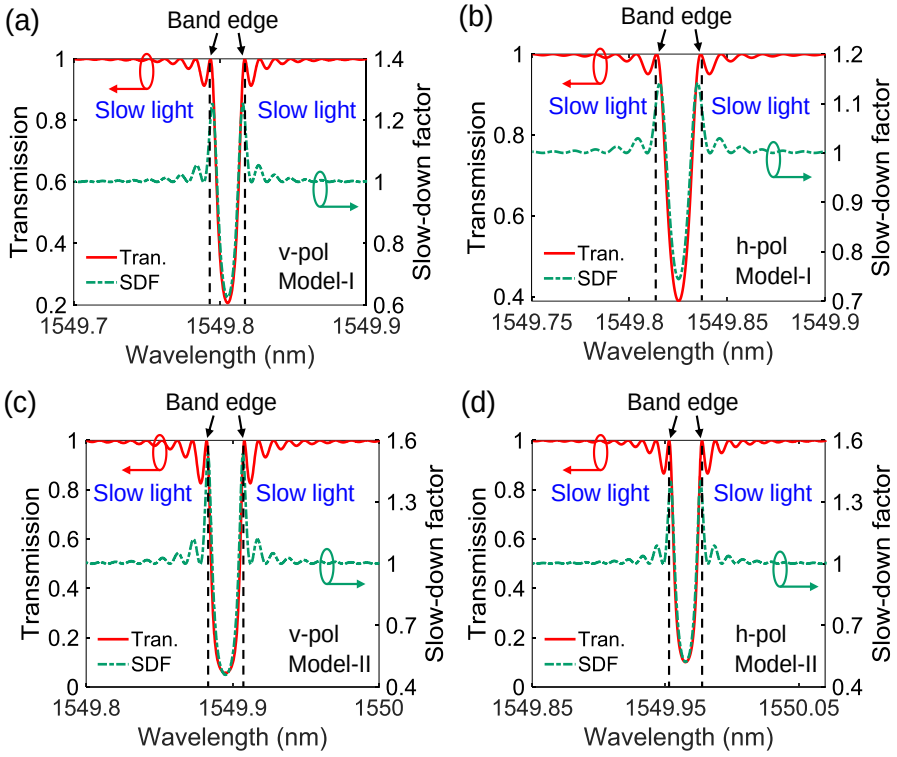

Figure C.10 Simulation of SDFs and transmission spectra at a 5 μm offset for Model-I DBG in (a) v-pol and (b) h-pol, and for Model-II in (c) v-pol and (d) h-pol. Note that the coupling constants used for simulation are derived from the experimental results shown in Figures 6.4 and 6.8.

C.7 Analysis for time delay measurement

The accurate reflection edge positions (A: 1549.883 nm, and C: 1549.920 nm) and peak (B: 1549. 897 nm) in Model-II DBG (Figure 6.6(a)) was measured using an optical spectrum analyzer (APEX technologies, 1.12 pm resolution), as shown in Figure 6.10(a), showing a reflection FWHM of ~4.5 GHz.

Note that sidebands near the reflection peak arise from imperfections of the grating period, RI non-uniformity, and polarization dependence of incident signal. Figures 6.10(b~d) show the DFB laser spectrum, modulated signal, and reflected modulated signal, respectively, where the DFB laser wavelength (Figure 6.10(b)) was calibrated via temperature control. The modulated signal (Figure 6.10(c)) has a center wavelength of 1549.896 nm (carrier signal, f_c) with sidebands at 1549.880 nm ($f_c - f_m$) and 1549.912 nm ($f_c + f_m$), forming a 4 GHz bandwidth. Figure 6.10(d) confirms

full reflection of the modulated signal by the Model-II DBG, with additional spectral sidebands adjacent to the two primary sidebands ($f_c - f_m$ and $f_c + f_m$) due to the grating's reflection spectrum.

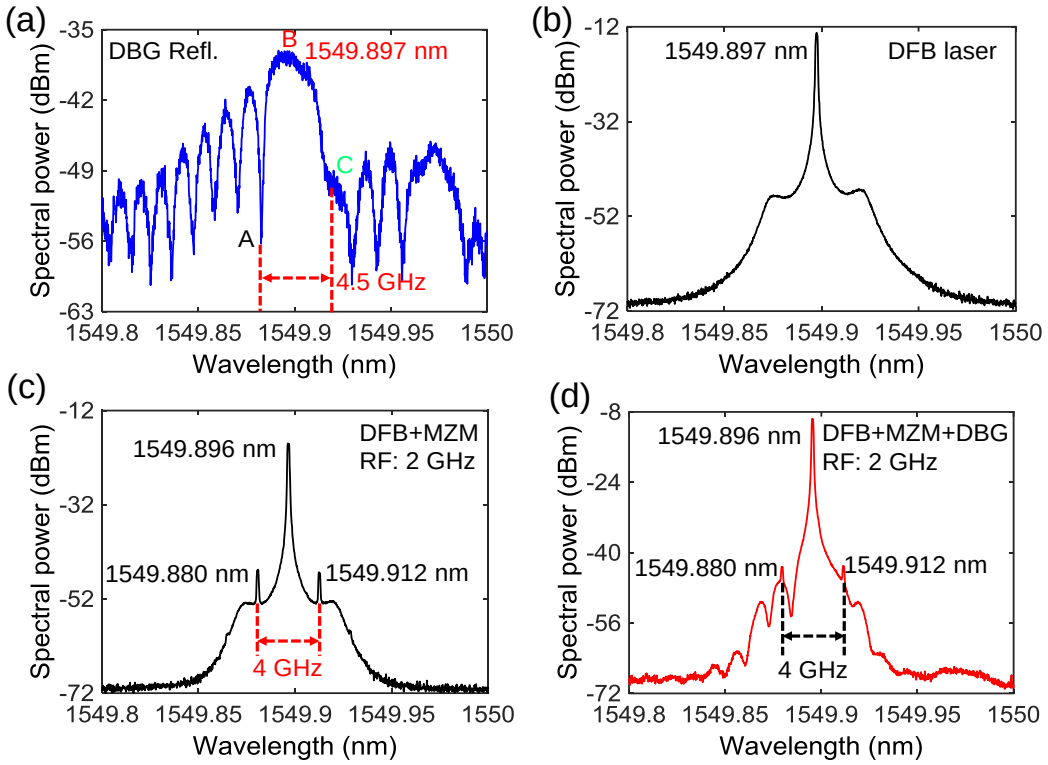

Figure C.11 (a) Reflection of Model-II DBG, centered at 1549.897 nm with a 4.5 GHz bandwidth at band edges. (b) DFB laser diode spectrum centered at 1549.897 nm. (c) Modulated signal, centered at 1549.896 nm (carrier signal, f_c), with a 2 GHz RF sinusoidal signal (modulation frequency, f_m) generated by a signal generator, producing a 4 GHz sideband range. (d) Reflected modulated signal from Model-II DBG, maintaining the 4 GHz sideband range.

The traces of the detected signal pulses are obtained from the reflected modulated signal by the Model-II DBG through opto-electric conversion using the fast PD and are observed on an oscilloscope grating. At wavelength of the resonance (point B, Figure C. 11(a)) and the reflection edges (points A and C, Figure C.11(a)), the resulting signal pulse traces (compared with the reference signal) are measured and shown in Figure 6.11.

C.7 References

[C1] A. Drouin, P. Lorre, J.-S. Boisvert, S. Loranger, V. L. Iezzi, and R. Kashyap, "Spatially resolved cross-sectional refractive index profile of fs laser–written waveguides using a genetic algorithm," Opt. Express 27(3), 2488–2498 (2019).

[C2] Q. Chen, J.-S. Boisvert, M. S. Sharawi, and R. Kashyap, "Bragg gratings with novel waveguide models fabricated in bulk glass via fs-laser writing and their slow-light effects," Opt. Express 32(1), 188–204 (2024).

[C3] R. Kashyap, Fiber Bragg Gratings, 2nd ed. (Academic Press, 2010).

[C4] Q. Chen, J.-S. Boisvert, F. Jafari, M. S. Sharawi, S. Loranger, and R. Kashyap, "Offset-enhanced slow light in femtosecond laser-fabricated Bragg gratings," Opt. Express 32(22), 39257–39266 (2024).

[C5] G. D. Marshall, R. J. Williams, N. Jovanovic, M. J. Steel, and M. J. Withford, "Point-by-point written fiber-Bragg gratings and their application in complex grating designs," Opt. Express 18(19), 19844–19859 (2010).

[C6] A. Ghatak and K. Thyagarajan, Introduction to Fiber Optics (Cambridge University Press, 1998).

[C7] A. W. Snyder and J. D. Love, Optical Waveguide Theory (Chapman and Hall, 1983).

[C8] T. Erdogan, "Fiber grating spectra," J. Light. Technol. 15(8), 1277–1294 (1997).

APPENDIX D EXAMPLES OF WAVEGUIDE BRAGG GRATINGS FOR FUTURE WORK

Slow-light behaviors in waveguide Bragg gratings, inscribed using FSL techniques in bulk glass at room temperature, offer a new perspective on slow light. This thesis demonstrates slow light and enhanced slow light in various Bragg gratings, with reliable and reproducible methods for theoretical calculations, writing parameters, and measurements, showing potential in photonics, optical communication, and sensing. However, further efforts are needed to fully realize the theoretical benefits and applications in the following waveguide Bragg grating models based on the aforementioned study to further enhance the slow-light effects:

(1) Enhanced RI change in line grating through BOE etching.

To investigate the impact of BOE (Buffered oxide etch (buffered HF): a mixture of 40% NH4F and 49% HF in a 6:1 ratio, with an etch rate ranging from 0.72 to 1 μm/min) on the diffraction effect, the inscribed line gratings (4 mm width ×4 mm length, laser power: 500 mW, repetition rate: 75.6 kHz, writing speed: 10 mm/s, grating period: Λ=2.088 μm) were etched for 2 hours. The experimental setup is shown in Figure D.1, with the diffraction patterns before and after BOE etching presented in Figure D.2.

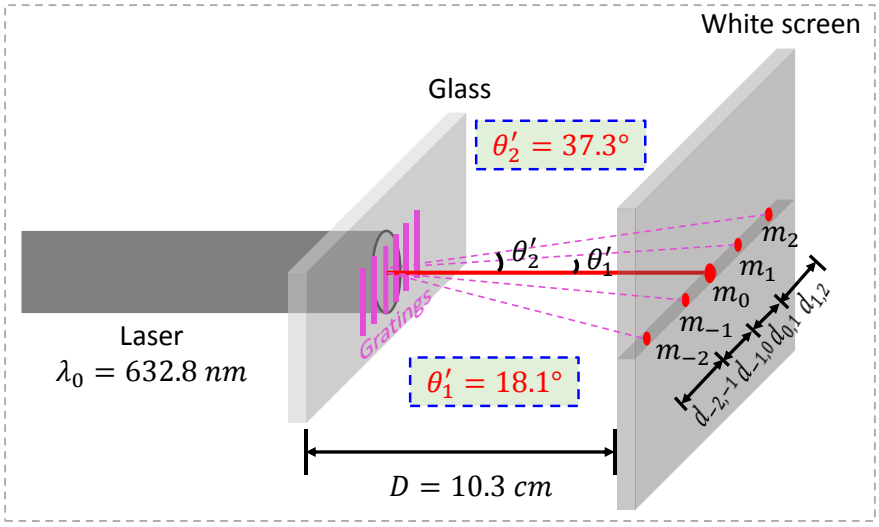

Figure D.12 The experimental setup for line grating diffraction measurement.

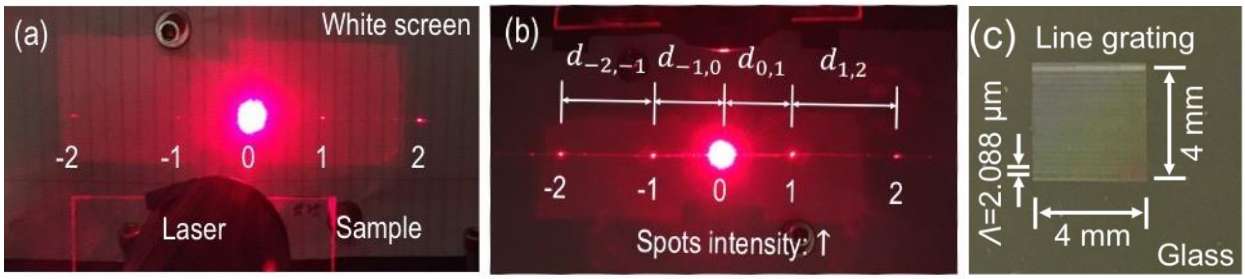

Figure D.2 Diffraction patterns of Line grating (a) before etching and (b) after 2 hours of BOE etching. (c) Top view of line grating after 2 hours of BOE etching.

It is evident that the intensity of the diffraction spots increases for the etched line gratings compared to the unetched ones. The first order and second order diffraction angles, θ_1' and θ_2' can be calculated using equations (D.1) and (D.2).

$$tan\theta_1' = \frac{d_{0,1}}{D} \tag{D. 1}$$

and

$$tan\theta_2' = \frac{d_{0,1} + d_{1,2}}{D} \tag{D. 2}$$

Here, $d_{0,1}$, $d_{1,2}$ are the distances between the fundamental and first order, second order diffraction spots, respectively. These measured values for $d_{0,1}$ and $d_{1,2}$are 3.25 cm (equals $d_{-1,0}$) and 4.6 cm (equals $d_{-2,-1}$). D is the distance from the line grating sample to the white screen for diffraction pattern projection, with a value of 10.3 cm. Using these values, the diffraction angles θ_1' and θ_2' are calculated to be 18.1 °and 37.3 °, respectively. It is also worth noting that the m_1, m_2, m_{-1}, m_{-2}, as shown in Figure D.1, represent the possible diffraction order numbers.

The schematic diagram of line grating diffraction for theoretical analysis is shown in Figure D.3. Based on Snell's law, $\sin\theta_1/\sin\theta_2 = \lambda_1/\lambda_2 = n_2/n_1$, and diffraction equation $\Lambda \sin\theta_1 = m\lambda_1$, where θ_1 and θ_2 are the first order and second-order diffraction angles, respectively, Λ is grating period of 2.088 μm, and $n_0 = n_2 = 1$ and $n_1 = 1.5$ are the refractive indices of air and glass.

Using these equations, the first-order diffraction angle θ_1 is calculated to be 11.9°, while the angle θ_{11} is 18° according to Snell's law when the order number $m = 1$. Similarly, for the second-order diffraction ($m = 2$), the diffraction angle $\theta_2 = 23.84°$, and the angle θ_{22} is 37.3°. These calculated angles closely match the experimental results.

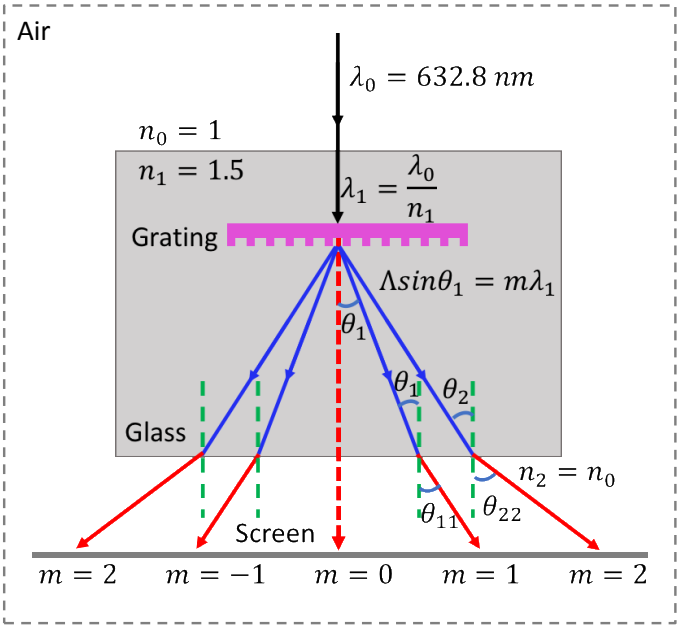

Figure D.3 Schematic diagram of line grating diffraction (before BOE etching) for theoretical analysis.

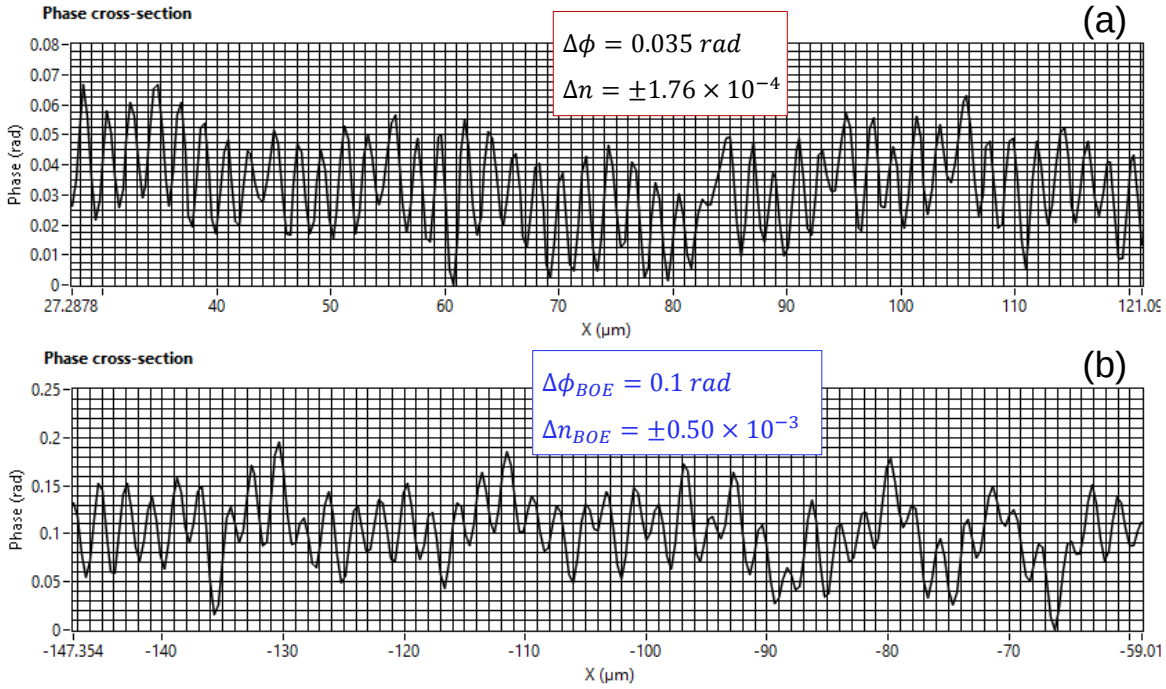

Figure D.4 Phase change and RI change of Line grating (a) before etching and (b) after 2 hours of BOE etching.

This measured phase changes by "The Ripper^{TM}" and the calculated RI changes are shown in Figure D.4. It can be observed that the phase change increases from 0.035 rad without BOE etching to 0.1 rad with BOE etching. The corresponding RI change increase from the order 10^{-4} to 10^{-3}, as shown in Figure D.4(a) and (b), respectively. This method could be extended in the future to etch line or dot Bragg gratings for enhanced RI changes and transmission characteristics.

For example, a second-order single-laser-pass waveguide (SLPWG) line-Bragg grating (Figure D.5(a), period $\Lambda = 1.044$ μm) was etched using BOE for 281 mins (Figure D.5(b)). It is evident that the periodic streaks of the line are clearly visible after BOE etching, but light guiding worsens due to the differences of the SLPWG end facets below the glass slide, which may result from the thickness of the glass slide itself or the FSL inscription system. Future work should focus on minimizing these end facet differences of SLPWG below the glass surface before BOE etching.

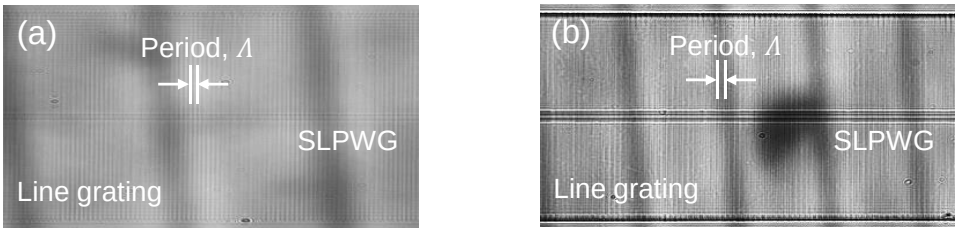

Figure D.5 Top view of SLPWG line-Bragg grating (a) before etching and (b) after 281 mins BOE etching. Note that (a) and (b) represent different positions of the SLPWG line-Bragg grating, shown here solely to illustrate the effect of BOE etching.

(2) Symmetrical offset-enhanced line-Bragg gratings with enhanced interactions between the SLPWG and line gratings.

Based on offset-enhanced line-Bragg gratings (Figure D.6(a)) described in Chapter 5, new line-Bragg gratings can be implemented with symmetrical line gratings that have offsets in the vertical direction, referred to as symmetrical offset-enhanced line-Bragg gratings (Figure D.6(b)). This inscription process involves two steps: (i) first, the single-laser-pass waveguide (SLPWG) is inscribed, and (ii) the subsequent line grating sections are inscribed. The offset adjustments are crucial for enhancing both the transmission dip and the slow-light effect. The schematic of the cross-sectional view for the symmetrical line grating is shown in Figure D.6.

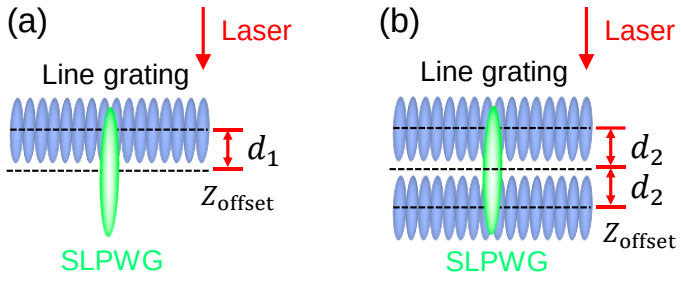

Figure D.6 Schematic cross-sections of (a) offset-enhanced line-Bragg gratings (Article 2, Chapter 5), and (b) symmetrical offset-enhanced line-Bragg gratings. Note that d_1 and d_2 represent the offsets along the z-axis, while the laser is incident from the top (indicated by the red arrow).

(3) Top semicircular SLPWG line-Bragg gratings and bottom semicircular SLPWG line-Bragg gratings.

Based on the circular light guiding mechanism in SLPWG, semicircular line gratings can be inscribed either at the top or bottom relative to the SLPWG. Note that the offset d along the z-axis is used to adjust the interaction between the SLPWG and the line gratings. Two types of semicircular line-Bragg grating models are shown in Figure D.7.

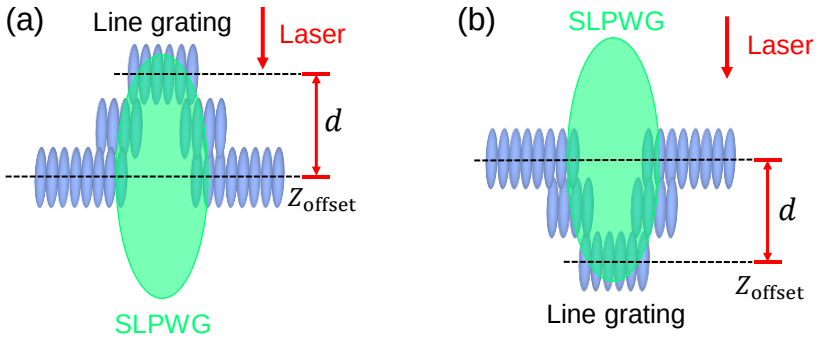

Figure D.7 Schematic cross-sections of (a) top semicircular SLPWG line-Bragg grating, and (b) bottom semicircular SLPWG line-Bragg grating. Note that d represents the offset along the z-axis, while the laser is incident from the top (indicated by the red arrow).

(4) DLPWG symmetrical-dot-Bragg gratings.

Based on the double-laser-pass waveguide (DLPWG) dot-Bragg gratings (Figure D.8(a)) described in Chapter 6, two types of dot-Bragg gratings can be proposed: bottom dot-Bragg grating (Figure D.8(b)) and symmetrical dot-Bragg grating (Figure D.8(c)), which are designed to adjust the dot-DLPWG interactions and enhance the transmission dips and slow-light effects. By combining adjustments to the offset between the dot and DLPWG along the z-axis, as well as the center-to-

center distance in the horizontal direction within the DLPWG, further increases in slow-light effects can be anticipated.

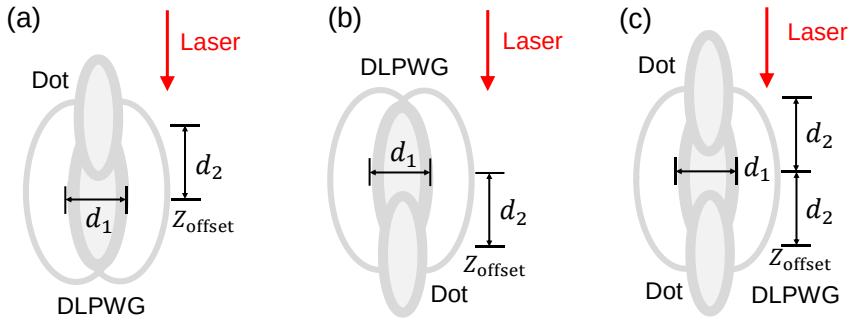

Figure D.8 Schematic cross-sections of (a) DLPWG dot-Bragg gratings (Article 3, Chapter 6), (b) DLPWG bottom-dot-Bragg gratings, and (c) DLPWG symmetrical-dot-Bragg gratings. Note that d_1 represents the center-to-center distance in DLPWG and d_2 is the offset along the z-axis, respectively, while the laser is incident from the top (indicated by the red arrow).

(5) Photonic crystal (PhC)-based SLPWG dot-Bragg gratings.

Based on the SLPWG dot-Bragg grating (Article 3, Chapter 6), PhC-based SLPWG dot-Bragg gratings can be designed with symmetrical PhCs relative to the SLPWG dot-Bragg grating, as shown in Figure D.9. The offset between the SLPWG and the dot is adjusted using d_1. The d_2 is kept such that the dot fully interacts with the shell of the SLPWG, while d_3 is further adjusted to enhance the interaction between the PhC and the SLPWG dot-Bragg grating. The slow-light effect can also be further enhanced depending on the positioning of the PhC (e.g., at the center and top, as shown in Figures D.9(a~b)).

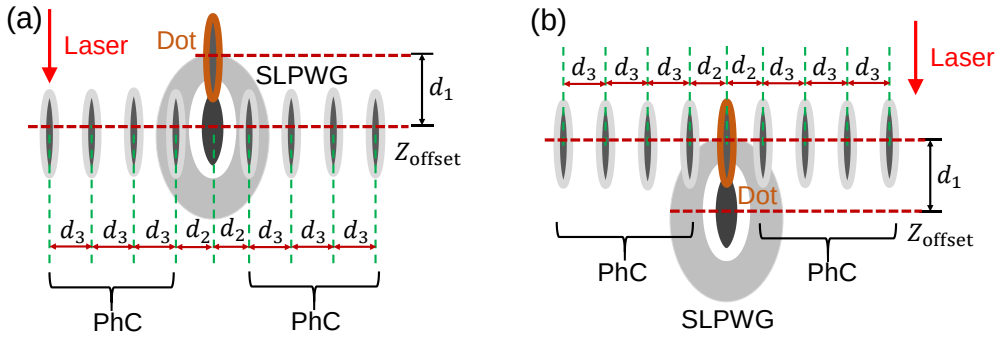

Figure D.9 Schematic cross-sections of PhC-based SLPWG dot-Bragg gratings, with the PhC located at (a) the center and (b) the top of the SLPWG dot-Bragg gratings. Note that the laser is incident from the top, as indicated by the red arrow.

APPENDIX E LIST OF PUBLICATIONS

1. Journal Articles Related to the Thesis

[1] **Qingtao Chen,** Jean-Sébastien Boisvert, Foroogh Jafari, Mohammad S. Sharawi, Sébastien Loranger, and Raman Kashyap, "Enhanced Slow-Light Phenomenon in Dot-Bragg Gratings Through Offset Engineering," Submitted to *Journal of Lightwave Technology*, Mar. 26, 2025.

[2] **Qingtao Chen,** Jean-Sébastien Boisvert, Foroogh Jafari, Mohammad S. Sharawi, Sébastien Loranger, and Raman Kashyap, "Offset-Enhanced Slow Light in Femtosecond Laser-Fabricated Bragg Gratings," *Opt. Express*, vol. 32, no. 22, pp. 39257–39266, Oct. 2024.

[3] **Qingtao Chen,** Jean-Sébastien Boisvert, Mohammad S. Sharawi, and Raman Kashyap, "Bragg Gratings with Novel Waveguide Models Fabricated in Bulk Glass via Fs-Laser Writing and Their Slow-Light Effects," *Opt. Express*, vol. 32, no. 1, pp. 188–204, Jan. 2024.

2. Conference Papers/Posters Related to the Thesis

[1] **Qingtao chen,** Jean-Sébastien Boisvert, Foroogh Jafari, Mohammad S. Sharawi, Sébastien Loranger, and Raman Kashyap, "Observation of Slow Light in Dot-Bragg Grating Waveguides Inscribed by Femtosecond Laser," Accepted by *Photonics North 2025* on Mar.18, 2025. (Oral presentation on May 20~23, 2025)

[2] **Qingtao chen,** Jean-Sébastien Boisvert, Foroogh Jafari, Mohammad S. Sharawi, Sébastien Loranger, and Raman Kashyap, "Slow-Light in Waveguide Dot-Bragg Gratings," *2025 STARaCom Poster Competition*, in École de technologie supérieure (ÉTS), Mar. 28, 2025, Montreal, Canada. (Poster presentation)

[3] **Qingtao chen,** Jean-Sébastien Boisvert, Foroogh Jafari, Mohammad S. Sharawi, Sébastien Loranger, and Raman Kashyap, "Enhanced Slow-Light Characteristics of Dot-Bragg Gratings," *The 1st Student Engineering Research Conference,* at Polytechnique Montreal, Mar. 26~28, 2025, Montreal, Canada. (Poster presentation)

[4] **Qingtao chen,** Jean-Sébastien Boisvert, Foroogh Jafari, Mohammad S. Sharawi, Sébastien Loranger, and Raman Kashyap, "Enhanced Slow-Light Characteristics of Dot-Bragg Gratings,"

The 8th Montreal Photonics Networking Event, in Polytechnique Montreal, Nov. 2024, Montreal, Canada. (Poster presentation)

[5] **Qingtao chen,** Jean-Sébastien Boisvert, Foroogh Jafari, Mohammad S. Sharawi, Sébastien Loranger, and Raman Kashyap, "Offset Influence on Slow Light Behavior in Femtosecond Laser Inscribed Bragg Gratings in Bulk Glass," *2024 Canadian Photonics Online Meetup (canPOM)*, Nov. 2024, Canada. (Online poster presentation)

[6] **Qingtao chen,** Jean-Sébastien Boisvert, Mohammad S. Sharawi, Raman Kashyap, "Impact of Position Offset on Characteristics of Waveguide Line-Bragg Grating Inscribed by fs-Laser in Bulk Glass," *The 7th Montreal Photonics Networking Event*, in École de technologie supérieure (ÉTS), Dec. 2023, Montreal, Canada. (Poster presentation)

[7] **Qingtao chen,** Jean-Sébastien Boisvert, Mohammad S. Sharawi, Raman Kashyap, "Dot-Bragg Grating with Novel Low-loss Waveguide Model Written via fs-Laser in Bulk Glass," *2023 Canadian Photonics Online Meetup (canPOM)*, Nov. 2023, Canada. (Online poster presentation)

[8] **Qingtao chen,** Jean-Sébastien Boisvert, Mohammad S. Sharawi, Raman Kashyap, "Slow-Light Effects of Bragg Gratings in Bulk Glass," *"2023 Innovation day" of SPIE student chapter (Polytechnique Montreal)*, Sept. 2023, Montreal, Canada. (Poster presentation)

[9] **Qingtao chen,** Jean-Sébastien Boisvert, Mohammad S. Sharawi, Raman Kashyap, "FS Laser Writing of 2nd-order Line-Bragg Grating," *The 6th Montreal Photonics Networking Event*, in École de technologie supérieure (ÉTS), December 2nd, 2022, Montreal, Canada. (Poster presentation)

[10] **Qingtao Chen,** Jean-Sébastien Boisvert, Mohammad S. Sharawi, Raman Kashyap, "FS Laser Writing of Waveguides with Bragg Gratings," *"2022 Innovation day" of SPIE student chapter (Polytechnique Montreal)*, Oct. 7, 2022, Montreal, Canada. (Best Poster Award)

[11] **Qingtao Chen,** Jean-Sébastien Boisvert, Mohammad S. Sharawi, Raman Kashyap, "FS Laser Writing of Waveguides with Bragg Gratings," *COPL 2022 Annual Conference*, Jun. 16, 2022, Montreal, Canada. (Poster presentation)

[12] **Qingtao Chen,** Jean-Sébastien Boisvert, Mohammad S. Sharawi, Raman Kashyap, "Femtosecond Laser Tailoring of Waveguides in Low-Iron Glass," *STARaCom Annual General Meeting*, May 18, 2022, Montreal, Canada. (Poster presentation)

3. Journal Articles not Related to the Thesis

[1] **Qingtao Chen,** Xiupu Zhang, Mohammad S. Sharawi, and Raman Kashyap, "Advances in High–Speed, High–Power Photodiodes: From Fundamentals to Applications," *Appl. Sci.*, vol. 14, no. 8, p. 3410, Apr. 2024.

[2] **Qingtao Chen**, Wenjing Fang, Yongqing Huang, Xiaofeng Duan, Kai Liu, Mohammad S. Sharawi, and Xiaomin Ren, "Uni-Traveling-Carrier Photodetector with High-Contrast Grating Focusing-Reflection Mirrors," *Appl. Phys. Express*, vol. 13, no. 1, p. 016503, Jan. 2020.

[3] Yuansen Shen, Huijuan Niu, **Qingtao Chen**, Liwen Wang, Kai Liu, Xiaofeng Duan, and Yongqing Huang, "Simulation of Mushroom-Typed Near-Ballistic MUTC-PD with Sub-THz Operational Bandwidth," Accepted by *Optica Applicata*, 2025.

[4] Huijuan Niu, Shuaiyang Zhang, Chuanxing Jiang, Tao Liu, **Qingtao Chen**, Jian Wei, Song Gao, Yongqing Huang, Xiaofeng Duan, and Chenglin Bai, "High-Responsivity, High-Power Waveguide Photodetector with Fabry-Pérot Cavity and Quasi-Dipole Doping for Sub-THz Applications," *Opt. Commun.*, vol. 577, no. November 2024, p. 131412, Mar. 2025.

[5] Shuaiyang Zhang, Huijuan Niu, **Qingtao Chen**, Yikang Zhang, Kai Liu, Xiaofeng Duan, and Yongqing Huang, "Theoretical Design of High Responsivity and High Output Power Sub-THz MUTC-PDs from Vertical to Waveguide Configurations," *Phys. Lett. A*, vol. 536, p. 130303, Mar. 2025.

[6] Jian Wei, Huijuan Niu, **Qingtao Chen**, Yuanhao Li, Yuxin Zhu, Yikang Zhang, Kai Liu, Xiaofeng Duan, and Yongqing Huang, "Research on PIN Photodetector with Novel Low-Loss Electrode (in Chinese)," *J. Liaocheng Univ. (Natural Sci. Ed.)*, vol. 38, no. 1, pp. 23–33, 2025.

[7] Haoyu Guo, Wenjing Fang, Tingting Wang, Xinye Fan, Jielong Pang, **Qingtao Chen**, Xin Wei, and Santosh Kumar, "High Q-factor Fano Resonances in a Double D-Type Metasurface based on Toroidal Dipole Bound States in the Continuum," *J. Opt.*, Dec. 2024.

[8] Jielong Pang, Wenjing Fang, Xinye Fan, **Qingtao Chen**, Haoyu Guo, Tingting Wang, Xin Wei, Chenglin Bai, and Santosh Kumar, "Polarization-Independent Tetramer Metastructure with Multi-Fano Resonances Governed by Quasi-Bound States in the Continuum," *Opt. Express*, vol. 32, no. 18, pp. 31905–31919, 2024.

[9] Yuanhao Li, Huijuan Niu, **Qingtao Chen**, Jian Wei, Xiaofeng Duan, Kai Liu, and Yongqing Huang, "Design of a Novel Coplanar Waveguide Fed Ku-Band Quasi-Yagi Patch Antenna (in Chinese)," *J. Liaocheng Univ. (Natural Sci. Ed.)*, vol. 37, no. 5, pp. 60–67, 2024.

4. Conference Papers not Related to the Thesis

[1] **Qingtao Chen**, Wenjing Fang, Yongqing Huang, Xiaofeng Duan, Kai Liu, Mohammad S. Sharawi, and Xiaomin Ren, "High Focusing-Reflection Subwavelength Gratings with Uni-Traveling-Carrier Photodetector for High Responsivity," in *Asia Communications and Photonics Conference (ACPC)*, 2019, p. S3D.4. (Oral presentation)

[2] Shuaiyang Zhang, Huijuan Niu, Chuanxing Jiang, Tao Liu, **Qingtao Chen**, and Chenglin Bai, "Responsivity Enhancement Using Fabry-Pérot Cavity for Zero-Bias Waveguide Photodiodes," in *2024 Asia Communications and Photonics Conference (ACP) and International Conference on Information Photonics and Optical Communications (IPOC)*, Nov. 2024, pp. 1–3.

[3] Shuaiyang Zhang, Huijuan Niu, **Qingtao Chen**, Kai Liu, Xiaofeng Duan, and Yongqing Huang, "High-Responsivity and High-Power Reconfigurable Uni-Traveling-Carrier Photodiodes: From Vertical to Waveguide Designs," in *2024 Asia Communications and Photonics Conference (ACP) and International Conference on Information Photonics and Optical Communications (IPOC)*, Nov. 2024, vol. 1, pp. 1–3.

[4] Jian Wei, Huijuan Niu, **Qingtao Chen**, Kai Liu, Xiaofeng Duan, and Yongqing Huang, "Investigating Novel Low-Loss Electrodes for PIN Photodetectors," in *2024 Asia Communications and Photonics Conference (ACP) and International Conference on Information Photonics and Optical Communications (IPOC)*, Nov. 2024, pp. 1–3.

[5] Liwen Wang, Huijuan Niu, **Qingtao Chen**, Kai Liu, Xiaofeng Duan, and Yongqing Huang, "High-Speed and High-Power Modified Uni-Traveling-Carrier Photodetector," in *2024 Asia Communications and Photonics Conference (ACP) and International Conference on Information Photonics and Optical Communications (IPOC)*, Nov. 2024, pp. 1–3.

[6] Yuansen Shen, Huijuan Niu, **Qingtao Chen**, Kai Liu, Xiaofeng Duan, and Yongqing Huang, "Design of Modified Mushroom-Type Near-Ballistic Uni-Traveling-Carrier Photodetectors," in *2024 Asia Communications and Photonics Conference (ACP) and International Conference on Information Photonics and Optical Communications (IPOC)*, Nov. 2024, pp. 1–3.